KU Leuven
Biomedical Sciences Group
Faculty of Medicine
Department of Imaging and Pathology
Division of Nuclear Medicine & Molecular Imaging

KU LEUVEN
DOCTORAL SCHOOL
BIOMEDICAL SCIENCES

MULTI-MODAL IMAGE ANALYSIS FOR SELECTIVE INTERNAL RADIATION THERAPY DOSIMETRY

Esmaeel Jafargholi Rangraz

Jury:
Promoter:
Professor Johan Nuyts
Co-promoters:
Professor Christophe M. Deroose
Professor Kristof Baete
Chair examining committee:
Professor Steven Dymarkowski
Chair public Defence:
Professor Michel Koole
Jury members:
Professor Marnix Lam
Professor Stephan Walrand
Professor Geert Maleux
Professor Patrick Dupont

Dissertation presented in partial fulfilment of the requirements for the degree of Doctor in Biomedical Sciences

October 2020

Personal acknowledgment

I still remember the first day I arrived in Leuven station on a cold and depressing night, a city where I knew no one, thousands of kilometers away from my wife, four years daughter, family, and friends. Now, I am writing these lines, in Leuven that I love the most, with my family and 11 years daughter and more friends than I had in my hometown.

I begin my adventure with lots of fears and hopes and continue with many peaks and valleys along the way; here it is, my dissertation, my nightmare, and my dream finished. During this fascinating but "I will never do it again" journey, I received a lot of help and support from many people who I would like to express my gratitude at the very beginning of this book. It wouldn't have been possible without any of you.

First of all, I would like to express my gratitude to *Professor Steven Dymarkowski* and *Michel Koole* for coordinating the reading committee and chairing the public defense. I gratefully acknowledge the internal jury juries, *Professor Geert Maleux*, and *Professor Patrick Dupont*, to join me on my path. Thank you very much for your guidance during my Ph.D. Your advice and comments increased the quality of this manuscript. I am deeply honored by the presence of *Professor Marnix Lam* and *Professor Stephan Walrand* as members of the jury. Thank you for the time you took to review my manuscript and for your critical and valuable input.

I would particularly like to express my gratitude to my promoters *Professor Johan Nuyts*, *Professor Christophe Deroose*, and *Professor Kristof Baete*, for giving me the possibility to perform research and theoretical and practical support that they have always manifested along with this work. During these years, you have not only shown great confidence in me, but you have also given me freedom and support in this project.

Special thanks to *Professor Nuyts* for allowing me to join his group, introducing me to the exciting field of nuclear medicine. Your continued enthusiasm has shown to me during my studies. In particular, detailed discussions over software design, outcome assessments, and critical appraisal have taught me many skills that I will endeavor to take forward into my future practice.

Professor Deroose inspired this work, and I am most grateful for all his support and encouragement throughout this work. I was honored when you invited me to analyze patient data; it was a big boost for my self-confidence every time. You are a conscientious scientist/physician and never missed any details. Thank you for many fruitful brainstorming sessions, honest feedback, and motivating me to do my best.

I want to express my most profound appreciation to *Professor Baete*, who put his unconditional trust and taught me to be more self-confident in what I do from the first moment I stepped into UZ Leuven. I thank you for sharing with me your extensive experience in the understanding of dosimetry. You believed that I could accomplish this journey. I am grateful for your talent in calming down every time I knocked on your door, panicking for something. You are indeed an extraordinary person, both intellectually and emotionally.

During my Ph.D., I was lucky to get excellent opportunities to interact and work with experienced and skillful professionals from different medical disciplines. A special acknowledgement goes to *Professor Geert Maleux* for being an endless source of knowledge on the evaluation and characterization of CBCT and for opening the door of the IRCC. I express my thanks to *Walter Coudyzer*, *Stijn De Buck*, *Professor Michel Koole*, *Professor Vincent Vandecaveye*, and *Frederik De Keyzer* for their expertise and cooperation, and for the lovely

chats, we had from time to time. You have often been closely involved in my research in various ways.

I express my gratitude to *Professor Koen Van Laere*, head of the department of the Nuclear Medicine, and personnel of the Nuclear Medicine department (UZ Leuven) for providing an existing environment for both research and pleasure. Instead of giving an exhaustive list, which risks being incomplete, I prefer to mention a few names. Thank you to *Wies Deckers* for solving the various computer-related and other practical problems that I encountered from time to time. You shared a passion for multi-modal image processing as well as dosimetry. A special thanks to *Christelle Terwinghe* for her incredible patience. You listened to the mountains of doubts I had during this work and uncovered the mysteries behind nuclear medicine. I want to thank the Nuclear Medicine department members involved in the pre-SIRT procedure (especially *Niloefar Ahmadi Bidakhvidi*) for their contributions, useful for my research.

I want to express my great gratitude to *Francine Reniers*, *Dr. Peter Vermaelen*, and *Nathalie Laurent*, who has been indispensable on many occasions. I could always count on your support.

Further, I genuinely thank all the present and past colleagues for the talks, events they've organized laughs in the lab and coffee room. I have enjoyed the many meetings and discussions we have had. *George*, you are an extensive scientist; thank you for your honest feedback and clean codes. *Ahmadreza*, you have helped me so much, I can never thank you enough! Thank you for introducing me to the new knowledge from the beginning of the Ph.D. and countless helpful discussions and new ideas whenever I needed them without asking for anything in return. *Rob*, *Masoud*, *Masoomeh*, and *Anna*, thank you for your moral support and pleasant company. *Marina*, thank you for your never-ending optimism. *Frederic*, *Matthew*, *Kathleen*, *Tao*, and *Koen*, it was fascinating to work alongside you. *Xikai*, our shared interest in SIRT dosimetry, has resulted in a strong collaboration.

Warm thanks to *Ahmed Radwan*, *Jeroen Bertels*, and *Mahdi Tabassian*, my office mates in MIRC, for being such generous support with my life in Leuven. You were always available for a drink and having time for a little chat whenever I struggled with the Ph.D., and my self-esteem was down. *Somayeh Akbari Saghezchi* and *Soha Sadat Mahdi*, thank you for all the exciting conversations.

I extend my appreciation to *Dries Christiaens (from BTG International Group)*, *Dominique Deloddere (from Sirtex Medical)*, and *Bryan Holvoet (from Quirem Medical)*, and *MIM software team* for sharing their knowledge and expertise. In particular, for inviting me to their meeting and symposium and the actual installation of their dosimetry software.

To my friends of the Iranian gang in Leuven and neighborhood :), *Nastaran & Ehsan*, *Sima & Hamed*, *Mehrnoosh & Mohammad*, *Solmaz & Hadi*, *Fariba & Saleh*, *Somayeh & Majid*, *Parinaz & Kaveh*, *Afsaneh & Amin*, *Maryam & Ahmadreza*, and *Matin*, ... for all the positive energy and strength that you always transmitted me along with this work. Thank you for making me still feel at home and for all the pleasant "Iranian" conversations. Thank you for making sure that I get a good dose of adventure and kabab at regular intervals. Little angels, *Tiam*, *Sorena*, *Mehrshid*, *Arvin & Arnika*, *Mehraeen*, *Bamdad*, and *Daniel*, you don't understand this yet, but you make my weekends so bright. Playing with you was worth more than 100 anti-depression pills.

To you, *Mohammad Sarshar*, for being always close, even a thousand miles away. You are proof that space won't break our 16-years-friendship. Thank you for filling almost every day my Telegram with dozens of useless but always hilarious memes.

Finally, words cannot express the thanks I owe to my extended (step) family who always supported me with their love and Skype calls:

از مهربانی، توجه و مراقبت همه عزیزانم سپاسگذارم.

I dedicate this thesis to the person dear to my heart, *Reyhaneh*, and my sweetheart, *Nila*, for getting me through the last six years, dealing with my periodic ups and downs, calming me down when I was too stressed. *Nila*, thank you very much for your beautiful cover design. You girls are my source of strength and making my life full of sunshine. I hope one day I can be of as much help to you as you were for me. Thank you for your unconditional love, support, and encouragement.

Summary

Liver cancer, whether primary or metastatic, represents a global public health priority due to its rising morbidity and mortality. Surgery is the procedure of choice for hepatic tumors, but many patients are not eligible for this treatment modality. Numerous novel therapeutic alternatives have been introduced over the last decades, depending on the tumor location, the stage of the disease, the age, and the general condition of the patients.

The role of external beam radiation therapy in liver cancer management remains restricted because of poor tolerance of normal liver parenchyma to radiation. One resolution would be following the Paul Ehrlich (1854-1915) proposal, *"we must learn to shoot microbes with magic bullets"*, to develop a radionuclide magic bullet to maximize the tumor irradiation while sparing healthy liver parenchyma as much as possible. The liver has an excellent blood flow mechanism; the contrast in blood supply between liver malignancies and the normal liver parenchyma, which is predominantly arterial and portal, respectively. Selective internal radiation therapy (SIRT) which is utilizing microspheres loaded with a high-energy β-emitting radioisotope (*e.g.* yttrium-90 or holmium-166) benefits from this mechanism; the microspheres target the tumors passively, when infused into the hepatic artery, and consequently deliver lethal tumor irradiation while sparing a significant portion of the non-tumoral liver tissue.

As mentioned before, despite the advantageous targeting of the targeted tumors, a fraction of the microspheres can be accumulated within the non-targeted tissues. So, in addition to the concept of effective treatment, based on the general rule of *"first, don't harm"*, preserving healthy tissue is also critical. In Europe, to perform a successful treatment, quantifying the tumor and non-tumor tissue irradiation is compulsory for treatment planning and for treatment verification. Because of a considerable inter- and intra-patient variation in tumor and liver tissue vascular anatomy, classical models that assume "the same relative tracer uptake in the tumor and the normal liver parenchyma in all patients" are over-simplistic for this task.

In each individual patient, **(i)** a careful treatment planning by employing a simulation workup to estimate the distribution of the therapeutic microspheres is essential since radionuclide therapies are historically prescribed in a (semi-)empirical manner and some evidence shows personalizing treatment planning could significantly enhance the therapeutic outcomes, and **(ii)** a more precise treatment evaluation is necessary to accurately determine the localization of the radionuclide in the patient's body and to identify potential adverse effects in terms of treatment efficacy and safety. The tumor and non-tumor irradiation are usually represented by absorbed dose or absorbed energy per unit of mass; this scheme is called dosimetry.

The existing dosimetric tools do not adequately extract all required information. The most commonly used method, initially developed for diagnostic applications in nuclear medicine, is widely accepted to be insufficient for internal radionuclide therapy due to several questionable assumptions: **(i)** the person is represented by a standard mathematical model, and the morphology of each person is not taken into account, **(ii)** activity is assumed to be distributed uniformly in the source organ (or sub-organ), and **(iii)** the absorbed doses are calculated only in the organ (or sub-organ) tissue level.

In contrast, voxel-level dose calculation addresses the patient-specific morphology and

activity heterogeneity. This personalized dosimetry approach can guarantee that healthy tissue irradiation does not lead to unacceptable toxicity and confirm tumor coverage. Voxel-level dose estimation also could be employed in treatment planning to determine a maximum injectable activity tailored for each patient based on healthy tissue tolerance criteria and tumor dose coverage. One drawback of voxel-level dosimetry is the requirement for sophisticated image registration and segmentation to obtain detailed information about activity distribution and the patient's liver and tumor anatomy.

The objective of this study was to develop a personalized dosimetric tool that answers the needs of SIRT for hepatic tumors. In this manuscript, a quantitative multi-modal image processing framework for SIRT was developed, evaluated, and applied to improve dose prediction for treatment planning, and evaluation of the treatment. The design of our procedure enables the treatment team to practice voxel-level dosimetry in a busy clinical routine. The largest part of this study was dedicated to developing registration and segmentation techniques for reporting an accurate and comprehensive absorbed dose distribution in clinically relevant volumes of interest.

List of abbreviations and symbols

^{131}**I** iodine-131.

^{142}**Pr** praseodymium-142.

^{166}**Ho** holmium-166.

^{169}**Yb** ytterbium-169.

^{177}**Lu** lutetium-177.

^{18}**F** fluorine-18.

^{188}**Re** rhenium-188.

^{226}**Ra** radium-226.

^{32}**P** phosphor-32.

^{89}**Y** yttrium-89.

^{90}**Sr** strontium-90.

^{90}**Y** yttrium-90.

^{90}**Zr** zirconium-90.

^{99}**Mo** molybdenum-99.

^{99}**Tc** technetium-99.

^{99m}**Tc** technetium-99m.

[^{177}**Lu**]**Lu-DOTA-TATE** [^{177}Lu]Lu-DOTA^{0},Tyr^{3}-octreotate.

[^{18}**F**]**FDG** 2-[^{18}F]fluoro-2-deoxy-D-glucose.

[^{68}**Ga**]**Ga-DOTA-TATE** [^{68}Ga]Ga-DOTATyr^{3}-octreotate.

[^{99m}**Tc**]**Tc-MAA** technetium-99m macro-aggregated albumin.

aHD average Hausdorff distance.

BCLC Barcelona clinic liver cancer.

BECT bremsstrahlung emission computed tomography.

BED biological effective dose.

BrIDA [^{99m}Tc]Tc-mebrofenin.

BSA body surface area.

CBCT cone-beam CT.

cDVH cumulative dose-volume histogram.

ceCT contrast-enhanced CT.

CNN convolutional neural network.

CT computed tomography.

D_{VOI} mean dose to the VOI.

DICOM digital imaging and communications in medicine.

DVH dose-volume histogram.

DWI diffusion weighted image.

Dx_{VOI} the minimum absorbed dose that x% of the VOI received.

EASL European Association for the Study of the Liver.

EBRT external beam radiation therapy.

ECOG Eastern Cooperative Oncology Group.

eLSF estimated lung shunt fraction.

EUD equivalent uniform dose.

FANC Federal Agency for Nuclear Control; Belgian radiological protection competent authority.

FOV field of view.

FSU independent functional subunit.

HA hepatic artery.

HCC hepatocellular carcinoma.

HR hazard ratio.

HU Hounsfield units.

IA injected activity.

ICC intrahepatic cholangiocarcinoma.

LET linear energy transfer.

LPT liver perfusion territory.

Lratio left LPT volume ratio.

LSF lung shunt fraction.

LtoW left LPT to entire liver volume.

MC Monte Carlo.

mCRC metastatic colorectal cancer.

MDT multi-disciplinary tumor board.

mHD maximum Hausdorff distance.

MI mutual information.

MIRD medical internal radiation dose.

MLEM maximum-likelihood expectation maximization.

MM metastatic melanoma.

mNET metastatic neuroendocrine tumor.

MR magnetic resonance.

MWA microwave ablation.

NET neuroendocrine tumor.

NTCP normal tissue complication probability.

NTV non-tumor volume.

OS overall survival.

OSEM ordered subset expectation maximization.

PET positron emission tomography.

PFS progression-free survival.

PM partition method.

PPV positive predictive value.

PRRT peptide receptor radionuclide therapy.

PV portal vein.

PVE portal vein embolism.

QoL quality of life.

RE radioembolization.

REILD radioembolization-induced liver disease.

RFA radiofrequency ablation.

RILD radiation-induced liver disease.

ROI 2D-region of interest.

Rratio right LPT volume ratio.

RTC randomized controlled trial.

RtoW right LPT to entire liver volume.

RV relative volume.

SIRT selective internal radiation therapy.

SPECT single photon emission computed tomography.

SSD sum of the squared differences.

SUV Standardized Uptake Value.

$T_{1/2}$ half-life.

T/N ratio tumor to normal tissue activity concentration ratio.

TACE transarterial chemoembolization.

TARE transarterial radioembolization.

TCP tumor control probability.

TOF time-of-flight.

TPR true positive ratio.

TV tumor volume.

UZ Leuven University Hospitals Leuven.

Vdiff volume difference.

VOI volume of interest.

Vx_{VOI} volume percentage of the VOI that receive at least x Gy.

Table of contents

Chapter 1

Introduction

1.1 Liver, cancer and treatments

1.1.1 The liver

The liver is one of the most complex organs and the largest solid organ in the abdomen. A healthy liver, generally, has a volume of 1 to 3 litres. It is located in the upper-right quadrant of the abdominal cavity. Specifically, this organ is encompassed by the heart and the right lung lobe from above (with the diaphragm as a physical barrier), by the stomach, and the pancreas and the spleen from the left, by the small intestine, the colon and the right kidney from below, and by the chest and the ribcage from the right and front (see figure 1.1-A). The liver has a dual blood supply: **(1)** it receives 75% of its blood from the portal vein (PV) arising from the confluence of the mesenteric and splenic vein, which drain blood from the stomach, intestines and spleen and **(2)** the rest from the hepatic artery (HA) branching from the celiac artery, which arises from the aorta (see figure 1.1-B and C) [1]. It follows that the former is nutrient-rich but oxygen deprived, and the latter is oxygen-rich.

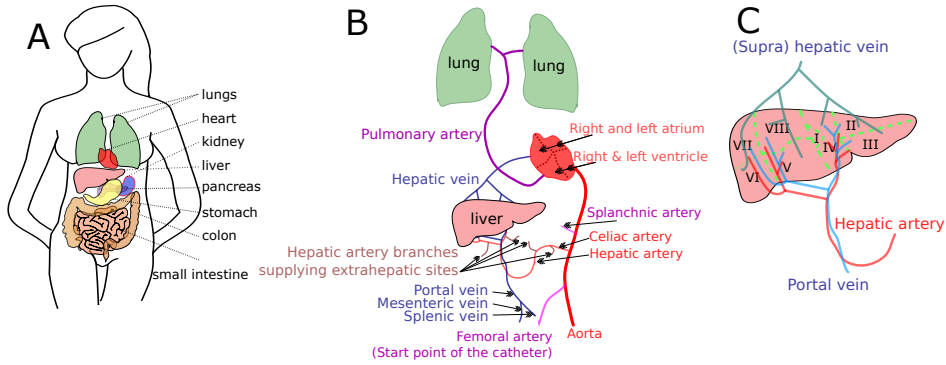

*Figure 1.1: **[A]** liver position in the body; there are some adjacent organs which sometimes have very similar density compared to the liver, which could make it difficult to distinguish them in some internal imaging modalities. **[B]** a schematic of the blood flow of the liver, **[C]** the liver consists of 8 segments which can be considered parallel in blood flow and functionality.*

This organ, as the interface between the digestive and the circulatory system (see figure 1.1-B), has an important role in filtering what is digestive system product prior to passing through the rest of the body. One of the primary functions of the liver is to process the nutrients resulting from the digestion of food. First, the liver receives the metabolic substrates (nutrients, drugs, hormones, toxins, alcohol, etc) from the intestines via the

PV. Then, the liver breaks down the molecules, and eliminates and neutralizes toxic substances. Finally, the liver's blood flow carries away the blood with the metabolites into the inferior vena cava using three major hepatic veins (left, right, and intermediate), and the liver's bile flow carries away some of the waste products in the bile through the biliary system. Additionally, the liver stores some vitamins, iron, and glucose.

The liver is composed of many different cell types which are divided into parenchymal cells (hepatocytes) and non-parenchymal cells (*e.g.* Kupffer cells, endothelial cells, fat storing cells, and pit cells). Histologically, the liver consists of five tissue systems: **(1)** vascular system, **(2)** hepatocytes and hepatic lobule, **(3)** hepatic sinusoidal cells, **(4)** biliary system, and **(5)** stroma. The hepatic lobule is the anatomical unit of the liver. The hepatic lobule is described as a hexagonal region of parenchyma which surrounds a central vein. On the other hand, the hepatic acinus is known as the smallest independent functional subunit (FSU) of the liver. The hepatic acinus is a cluster of hepatocytes oriented around the afferent vascular system.

Diseases typically target one of the liver components. The most common liver diseases are infections from hepatotropic viruses, fatty liver, alcohol damage, poisoning, drug damage, and finally cancer [2]. Liver dysfunction can be divided based on morphology in three basic categories:

1. extensive necrosis
2. cirrhosis (chronic liver scars, which are a source of impaired liver function)
3. hepatic dysfunction without apparent necrosis.

Fortunately, the liver has some exceptional characteristics:

- First, it has a high regenerative capability which is why liver resection, where macroscopic lesions are removed together with surrounding healthy tissue, can be a successful treatment.
- Also, the liver is a parallel organ, and it could be considered as a set of FSUs, similar to kidney [3]. Liver can be divided into eight segments based on the blood supply. In other words, each liver segment has an independent blood supply, blood outflow, and biliary drainage. These segments can be considered as functionally self-standing. So, in case of disease, if one removes or reduces function of the affected liver segments, the other segments can still carry out the liver function. In this situation, the other segments of the liver will grow to compensate for the lost liver volume.
- The last property is that it has an enormous functional reserve; the liver can adequately perform even if roughly up to 75% of the liver is impaired or resected [4].

1.1.2 Liver segments

The liver is divided into eight segments based on its function/blood supply, according to the Couinaud classification [5]. Each of these segments receives its own primary branches of the PV and HA. The most used indication for dividing the liver into these functional compartments is the position of the branches of the portal and sus-hepatic veins. The segments can be grouped in a superior part (segments VII, VIII, IVa, and II) and an inferior part (segments VI, V, IVb, and III). The liver also consists of left lobe (segments II, III, IV, and ± I) and right lobe (V, VI, VII, VIII, and ± I) that can be visually split using the middle hepatic vein.

The anatomy of the hepatic arterial bed has a high degree of variation. The "classic standard anatomy" appears in about three-quarters of the population (see figure 1.1;B): The common HA originates from the celiac trunk (which arises from the aorta), which becomes the proper HA after branching off the gastrointestinal artery. The common HA itself bifurcates into the left and right hepatic arteries. Then, the arterial branching pattern corresponds to the anatomy of the liver segments; the right HA splits into the right anterior and posterior hepatic arteries and left HA divides into sub-branches that

supply liver segments II and III. The blood flow of the segment IV is somewhat special; its hepatic branch can arise from the left, right, or proper HA.

Sometimes, a HA branch arises from a root other than the proper HA, which is called "aberrant". These aberrant arteries could be a substitute for the usual HA which is called a "replaced" HA. An "accessory" branch of the HA is the second type of aberrant artery; in this case in addition to this branch, the normal proper HA exists. Michels published a detailed classification of HA in 1966 which was revised later by several authors [6]. One of the latest studies observed "standard anatomy" in 77.2% of the 1200 evaluated cases. The rest had a replaced or accessory left HA(5.5%), replaced or accessory right HA (9.7%), replaced or accessory for both left and right hepatic artery (2.1%), common HA from the superior mesenteric artery (2.9%), common HA from the aorta (0.6%); in 2.1% of the cases the variation did not fit in the classical classification [7]. Anatomical variation is common and can be identified using early arterial phase computed tomography (CT) or magnetic resonance (MR) angiography, or cone-beam CT (CBCT) imaging (see section 1.2.1.3).

1.1.3 Liver cancer and the current status of its management

Cancer is a generic term for a group of diseases in which a population of cells is growing rapidly and uncontrollably inside an organ and forms a mass, called tumor. Furthermore, cancerous tumors can spread to other body parts and grow beyond the boundary of its origin. According to the World Health Organization, cancer is the second cause of death worldwide after cardiovascular diseases. Cancer that develops in the liver (hepatic cancer) is the fourth most common leading cause of cancer-related mortality globally after lung, colorectal, and stomach cancer [8].

Liver malignancies may start from liver cells (primary liver tumors) or can reach the liver from another origin (secondary liver tumors or liver metastases), predominantly from organs drained by the PV (*e.g.* the colon, small bowel, stomach, and pancreas), or without PV drainage (*e.g.* breast and lung). Liver malignancies, whether primary or metastases, have a high incidence and constitute a significant cause of morbidity and mortality worldwide [8]. A balance of improving the quality of life (QoL) and maintaining lifespan is desirable in the management of liver cancer. In terms of disease-free survival, treatments can be curative or tumor controlling. Early detection of liver tumors improves the chances for successful curative therapy. Sometimes, successful tumor controlling treatment can later enable the tumor to be treated with curative options (*e.g.* downstaging approach). Liver cancer treatments can also be categorized into two groups: systemic treatment, which acts on the whole body, and locoregional treatments, which exclusively target the organ of interest or a specific volume.

Here, the main treatment options for liver cancer management are briefly reviewed. Liver cancer management requires a multi-disciplinary approach which depends on many factors like the cancer classification, the tumor type, the number of tumors and their distribution, cancer stage (*e.g.* the Barcelona clinic liver cancer or BCLC staging system, see section 1.1.4.1), overall condition of the liver (*e.g.* cirrhosis), preceding treatments, etc:

- **Partial hepatectomy:** Surgical resection of the solitary liver tumor with a margin of tumor-free tissue. It is the traditionally preferred treatment since this treatment is acknowledged as a potentially curative option which offers a long term survival. However, it is suitable for only a minority of patients with liver cancer. For instance, selecting the surgery depends on the tumor burden, localization of the tumor (*e.g.* if the tumor is located close to some critical structures, like the portal and sus-hepatic veins), presence of an extrahepatic tumor, the number of involved segments, and functionality of the liver "remnant". In patients with non-cirrhotic liver, preserving a future liver remnant of 20–30% of the initial liver volume can take over the normal function of the liver through an increase in volume (hypertrophy) [9].
- **Liver transplantation:** Liver transplantation consists of removing the entire liver and replacing it by a donor liver. Only a small portion of the patients suffering from

primary or secondary liver tumors are eligible for liver transplantation. The number of lesions, size of the lesions, PV invasion, and extrahepatic tumor involvement are taken into account when considering this treatment option [10].

- **Systemic chemotherapy:** When the cancer is diffused all over the body, systemic chemotherapy is an option. Nonetheless, using this treatment will not only lead to the destruction of tumor cells, it will also affect a significant amount of healthy cells, which is frequently associated with systemic toxicity.
  Currently, chemotherapy is a standard first-line therapy in some tumor types, *e.g.* metastatic colorectal cancer (mCRC), metastatic breast cancer, and high grade metastatic neuroendocrine tumor (mNET). In some other liver cancers, chemotherapy has poor results, *e.g.* hepatocellular carcinoma (HCC) and metastatic melanoma (MM) [2].
- **Targeted therapy:** This type of treatment aims at specific molecules that participate in the genesis or maintaining of a cancerous state and tumor growth. The most used drugs can be categorized into three classes: **(i)** kinase inhibitors, *e.g.* tyrosine kinase inhibitors such as sorafenib and sunitinib which target the VEGF pathway involved in angiogenesis, erlotinib which targets EGFR involved in uncontrolled cell division, and imatinib which targets c-KIT and platelet-derived growth factor receptor; serine or threonine kinase inhibitors such as everolimus which targets mammalian target of rapamycin or mTOR; **(ii)** hormonal agents such as somatostatin analogues and estrogen (receptor) inhibitors; **(iii)** monoclonal antibodies such as bevacizumab which targets VEGF, and cetuximab which targets EGFR involved in cell growth [11].
- **Local ablation:** Local ablation intends to destroy the tumor without resection and is as an alternative strategy for relatively small hepatic tumors resulting in limited parenchyma loss, not only to achieve local tumor control but also to downstage the tumor and render the patient a surgical candidate. It can be done percutaneously under radiological guidance or during laparoscopy.
  Ablating the tumor can be carried out using a wide range of techniques [11]: **(1)** hyperthermia techniques: radiofrequency ablation (RFA) or microwave ablation (MWA), **(2)** hypothermia techniques (*e.g.* cryoablation), **(3)** percutaneous ethanol injections.
  From this minimally invasive treatment list, percutaneous ethanol injection has been used more frequently in the past, but now is considered to be inferior to RFA/MWA, which is the most used modality today.
- **Transarterial (chemo)embolization:** Transarterial chemoembolization (TACE) and transarterial embolization consists of administering beads, bland or with a chemotherapeutic payload, via the tumor-feeding vessels and blocking these vessels to induce ischemia and deliver a high concentration of a chemotherapeutic drug in the vicinity of the tumor. TACE has shown a survival benefit in two small randomized controlled trials (RTCs) in HCC [12, 13]. However, there are some complications like post-embolization syndrome, (fatal) liver failure, gastrointestinal bleeding, and liver abscesses. The beads employed in TACE are typically sized above 100 µm. So the HA is blocked much more upstream, with a higher potential embolizing effect (*e.g.* more ischemia). More side effects are reported for TACE compared to other transarterial embolization techniques in which smaller beads are used (*e.g.* radioembolization) [14].
- **External beam radiation therapy:** Traditionally, the role of external beam radiation therapy (EBRT) in liver cancer management is limited due to the low tolerance of the healthy liver parenchyma to the fractionated dose, radiosensitivity of the adjacent organs, and motion of the tumor (mainly respiratory). In fact, the treatment field in traditional EBRT was usually large, and it led to a large area of the liver with significant radiation exposure, which can cause radiation-induced liver disease (RILD), also called radiation hepatitis. Alternatively, three-dimensional conformal radiation therapy or 3D-CRT has been recently introduced to deliver a high absorbed dose to the tumor while sparing the normal liver parenchyma and kidney from high absorbed doses. This technique is mostly applicable to focal

tumors. Modern adaptations of EBRT like intensity-modulated radiation therapy or IMRT (using pencil beams to enhance the precision of the radiation dose) and image-guided radiation therapy or IGRT (guiding the dosing by imaging techniques to improve radiation accuracy), and stereotactic body radiation therapy or SBRT (ablation of intrahepatic and intrapulmonary tumors) are under investigation [15].

– **Selective internal radiation therapy (SIRT):** This technique refers to the delivering of radioactive microspheres labelled with yttrium-90 (^{90}Y) or holmium-166 (^{166}Ho) through the HA. Although beads are delivered through the HA in both TACE and SIRT, their macro-embolic effects are different. Larger particles used in TACE (larger than 100 μm) occlude tumor feeding vessels. On the other hand, vessel occlusion is not the intent with SIRT; much smaller microspheres (25–35 μm) are employed in SIRT to reach the tumor micro-vasculature.
These microspheres contain a high energy β-emitter that will emits electrons with a relatively short range of energy absorption (see section 1.5.4). SIRT can achieve a highly localized irradiation of the tumor. SIRT or transarterial radioembolization (TARE) will be discussed in detail elsewhere in this manuscript.

1.1.4 Primary liver tumors

As described above, liver can be the host of either primary hepatic tumors or metastases. Although metastatic tumors are the more common cause of cancerous liver involvement, primary liver cancer is the fifth most prevalent cancer in the world, and it is the second most common cause of cancer-related mortality worldwide [2]. HCC is the most frequent type of primary hepatic cancer; the other major primary liver cancers are intrahepatic cholangiocarcinoma (ICC), mixed tumors (HCC-ICC) and angiosarcoma. HCC-ICC is usually an aggressive tumor and the prognosis is lower than in patients with a pure HCC or pure ICC [16, 17]. Angiosarcoma and HCC-ICC have a low incidence and are not addressed in this manuscript.

1.1.4.1 HCC

HCC, which arises from hepatocytes, is the most widespread primary liver malignancy (around 90% of the cases), which generally arises within a cirrhotic liver [18]. HCC incidence has more than doubled over the past two decades and it is still increasing [19]. Unfortunately, this type of cancer has a poor prognosis due to its aggressive nature and diagnosis, which is rarely in an early stage. Around 70 % of the HCCs are not resectable at the time of diagnosis. In case of early detection, a 5-year survival rate of 50-70% is reported after resection, liver transplantation, or local ablation. On the other hand, a 1-year survival of only 11% is observed in very late stage diagnosis [18].

HCC encompasses a broad spectrum of patients with different possible treatment options. Hence, the BCLC staging [20], which is currently the baseline for HCC treatment divides patients into five sub-groups (see table 1.1) based on:
(1) the Child-Pugh score; a scoring system to measure the severity of chronic liver disease. This score is defined based on five clinical measures: total bilirubin, serum albumin, international normalized ratio (INR), presence of ascites (fluid in peritoneal cavity), and presence of hepatic encephalopathy. Child-Pugh is scored A-B-C, with optionally the number of points scored (e.g B or B7).
(2) the Eastern Cooperative Oncology Group (ECOG) performance; a scale used to assess how a patient's disease is progressing. ECOG score is defined as:

– **PS0:** fully active and capable of all pre-disease activities,
– **PS1:** restricted in heavy physical work but able to carry out light work,
– **PS2:** capable of all self-care but not of any work activities, up and about more than half the day,
– **PS3:** in bed or a chair for more than half the day, capable of only limited self-care,
– **PS4:** completely disabled and need complete care, and
– **PS5:** dead.

stage	ECOG	Child-Pugh	other conditions
0 (very early)	PS 0	CP A	single tumor $\leq$ 2cm
A (early)	PS 0	CP A or B	single or up to 3 tumors $\leq$ 3cm
B (intermediate)	PS 0	CP A or B	large multi-tumors
C (advanced)	PS 1 or 2	CP A or B	portal invasion, extrahepatic spread
D (terminal)	PS 3 or 4	CP C	severe liver damage

Table 1.1: BCLC staging system

The choice of therapy is challenging and requires a multi-disciplinary approach, and depends on the patient's age, concomitant disease, liver function, cancer stage, pattern, location and dimensions of the intrahepatic tumor distribution, vessel invasion, portal hypertension, and extrahepatic tumor burden [18]. Recently, tumor ablation modalities [21], targeted therapy with sorafenib [22], TACE [23], SIRT [24], *etc.* have been reported to be safe and effective for non-resectable HCC tumors.

Intra-arterial embolization therapies, including TACE, and SIRT, are mainly used as a tumoristatic treatment and can be used as a bridge to liver transplantation. Specifically, TACE has recently become a standard of care for unresectable intermediate or advanced HCC tumors. Currently, SIRT is an emerging treatment for unresectable HCC, which aims to enhance overall survival (OS) while avoiding complications, limiting treatment side-effects and improving QoL. This treatment has been shown to be a safe and promising alternative for patients with HCC, but RTCs have shown a median survival comparable to TACE (*e.g.* SARAH, SIRveNIB, SORAMIC trials, see section 1.6.2). Accordingly, in recent guidelines, SIRT has been introduced as an alternative treatment for HCC cancer (see section 1.6.4).

1.1.4.2 ICC

ICC is the second major hepatic primary cancer (between 5 and 10 % of the primary hepatic malignancies) [1]. ICC is a malignancy of the intrahepatic bile ducts of the liver and tends to spread with local infiltration. The leading causes of ICC are biliary tract disease (sclerosing cholangitis), diabetes, viral hepatitis, and cirrhosis [25]. Usually, ICC has a rapid mass forming growing pattern and poor diagnosis. So, this cancer is typically diagnosed in advanced stages with large masses [26].

Despite the recent advancement in diagnosis and treatment, the prognosis of patients suffering from ICC remains poor because these tumors are clinically silent, and patients typically present at an advanced stage. So, most ICC tumors are usually incurable, poorly responding to the treatments, and they commonly spread to other organs [11]. There are few studies about using SIRT for ICC, however, data from a phase 2 clinical trial proposed combined chemotherapy (cisplatin and gemcitabine) and SIRT as an emerging treatment for these tumors [27]. Recently, a systematic review analyzing 203 patients from 12 studies showed a median survival of 15.5 months, which is higher than the survival of either systemic chemoembolization or TACE alone [28]. Also, TACE has been shown to have a partial response in one-quarter of the patients [1]. A retrospective multi-center study analyzing 58 patients with unresectable and chemorefractory ICC treated with SIRT showed an improvement in median OS when a personalized activity prescription was used compared to widely used body surface area method (5.5 vs 14.9 months; p-value < 0.001) [29]. They concluded that personalized activity prescription should be performed when employing SIRT for patients with ICC.

1.1.5 Metastatic liver tumors

Half of the patients with primary malignancies that develop distant metastases will develop metastases in the liver [11]. Liver metastases can arise from a variety of primaries with different characteristics. The liver is the predominant site of metastatic spread from primary tumors located in organs drained by the PV that irrigates the liver, with the

liver sinusoidal vessels being the first microvascular bed encountered, *e.g.* mCRC and mNETs. Liver metastases can although originated from organs which are not drained by the PV, *e.g.* breast, lung, and MM.

Liver metastases can be solitary but are often multiple lesions, and sometimes their borders are poorly defined. Most of the hepatic metastases are clinically silent and sometimes the detection can be challenging. These metastases are associated with advanced stage and have a poor prognosis in most tumor types. Similar to primary liver cancer, surgical resection and/or ablation is the best treatment available for liver metastasis, but patients should meet some conditions to be eligible for partial hepatectomy. Dependent on the tumor type, systemic therapy (with FOLFOX or FOLFIRI) or radiofrequency ablation is preferred, but transarterial treatments (*e.g.* TACE and SIRT) are relatively new and promising options [11].

1.1.5.1 mCRC

Colorectal carcinoma is a very common cause of liver metastases and around one-third of colorectal cancer patients have already developed liver metastases at the time of diagnosis and in total liver metastases occur in around half of colorectal carcinoma cases. Also, in one out of three advanced colorectal cancer patients, the liver is the only target of the metastases [30].

Locoregional embolization techniques, especially SIRT, are increasingly being used used for tumor downstaging. SIRT with resin microspheres is approved by the FDA for mCRC. Saxena *et al.* report a systemic review of SIRT for 979 patients with unresectable mCRC employing data from 20 studies. They stated that SIRT is a safe and effective option for this population [31]. The median OS was 12 months. A partial response has been observed in 31% of the cases, and time to hepatic progression was 9 months. This modality is mentioned in the guidelines of the European Society for Medical Oncology (ESMO) to prolong the time to tumor progression in selected patients [32].

When using SIRT in combination with chemotherapy, an 8-month improvement in liver-specific progression-free survival (PFS) can be achieved compared to chemotherapy alone [33]. Two recent studies showed that addition of SIRT to the chemotherapy, FOLFOX, (may) improve the resectability of the previously unresectable mCRCs [34, 35]. Another recent study also confirmed that hepatic resection could be considered as a treatment option after combined SIRT and FOLFOX in the first-line management of liver-dominant mCRC [36]. Initial investigations and trials on this type of tumor show that patient selection and treatment planning in SIRT is a crucial step to have a significant survival benefit, and without careful consideration, adding SIRT to chemotherapy does not show a survival benefit. This will be discussed in more detail in section 1.6.

1.1.5.2 mNET

This type of liver metastases stems from primary neuroendocrine tumors arising within a variety of organs like the small intestine, colon/rectum, pancreas, lung, and rarely other sites within the body. NET is a rare tumor, comprising less than 1% of all malignancies and up to 75% of these patients will develop liver metastases [37]. Surgical resection can be indicated for mNET patients if at least 90% of the tumor volume could be safely removed. Unfortunately, between 10-20% of the mNET tumors are resectable [38]. Disease-free survival for mNET patients after resection ranged from 42 to 46 months [39].

SIRT has been described to be safe and effective for mNET patients, as well as to improve the QoL significantly [39]. In a meta-analysis of 435 mNET patients from 12 studies, SIRT was described as an effective alternative option with a high response rate at three months; 86% of the patients showed a complete or partial response [40]. Also, a 5-year survival of 50.1% after SIRT was reported in mNET [41].

Braat *et al.* analyzed hepatotoxicity of SIRT with resin microspheres in patients who were previously underwent peptide receptor radionuclide therapy (PRRT), another type of radionuclide therapy which is a standard treatment now [42]. They concluded SIRT as

a safe treatment with rare REILD occurrence with an OS of 3.5 years. Similarly, SIRT with QuiremSpheres was reported as a safe and efficient treatment for patients previously treated with PRRT [43]. In a recent large international, multi-center retrospective study, SIRT was shown as a safe and effective treatment for even heavily pre-treated, progressive, and large mNET [44]. They reported a disease control rate of 91% in progressive patients.

1.1.5.3 MLM

Melanoma is a malignancy arising from melanocytes that are usually occurring in the skin but can also occur in the eye and in mucosal tissue. For ocular melanoma, even after the treatment of the primary tumor, half of the patients will develop metastases, mostly in the liver. Without any treatment, patient survival after diagnosis of melanoma liver metastasis ranges only from 3 to 12 months in the era before immune- and targeted therapy [45].

Most of the patients suffering from MM are not a candidate for surgery. TACE and SIRT are an option in unresectable MM. A recent study on 22 MM patients demonstrated that SIRT as the first-line treatment is safe with a promising outcome; the median OS was 18 months [46]. A systematic review of SIRT for unresectable MM proposed SIRT as a promising treatment for MM management with only mild side effects [45]. In this analysis, 255 patients from 12 studies were analyzed. The median OS was 10 months, and one-year OS was 35%. Partial response and stable disease were observed in 20% and 57% of the patients.

1.2 Medical imaging in SIRT workflow

Non-invasive medical imaging is a broad discipline. Here, we briefly discuss the the SIRT imaging that are used in clinical practice. Anatomical imaging modalities, *e.g.* CT, CBCT, and MR imaging are generally employed within the SIRT workflow for detecting the tumor, and defining the liver and liver lobes or segments. On the other hand, hybrid functional/anatomical imaging is usually performed for pre-treatment simulation ([^{99m}Tc]Tc-MAA-SPECT/CT), treatment verification (^{90}Y-BECT and ^{90}Y-PET imaging), and tumor detection and response evaluation ([^{18}F]FDG-PET/CT and [^{68}Ga]Ga-DOTA-TATE-PET/CT imaging).

1.2.1 Anatomical imaging

1.2.1.1 CT

CT imaging performs three-dimensional imaging of the body, which has become increasingly important in clinical practices. CT images are used in different tasks, such as diagnosis, treatment evaluation, and patient follow-up. The conception of CT imaging began in the late 1960s; Godfrey Hounsfield and Allan Cormack were honored with the Nobel Prize in Medicine in 1979 for designing the first CT.

Modern CT cameras acquire a set of 2D slices of the body with a sufficient spatial resolution for extracting clinically relevant information. The CT system is mounted in a gantry with a cylindrical patient opening of around 80 cm. A patient table, with sub-mm accurate positioning controlled by the computer, is used to position the patient. An X-ray source rotates inside the gantry. For each position of the source, a collimated fan beam of X-rays is sent through the patient. The detector, which is collimated with an anti-scatter grid to stop the X-rays unless they are coming directly from the focal spot of the X-ray tube, measures the intensity (energy) of the X-rays (see figure 1.2-A). From these measurements, a stack of 2D images representing the linear attenuation coefficients inside the patient's body can be created.

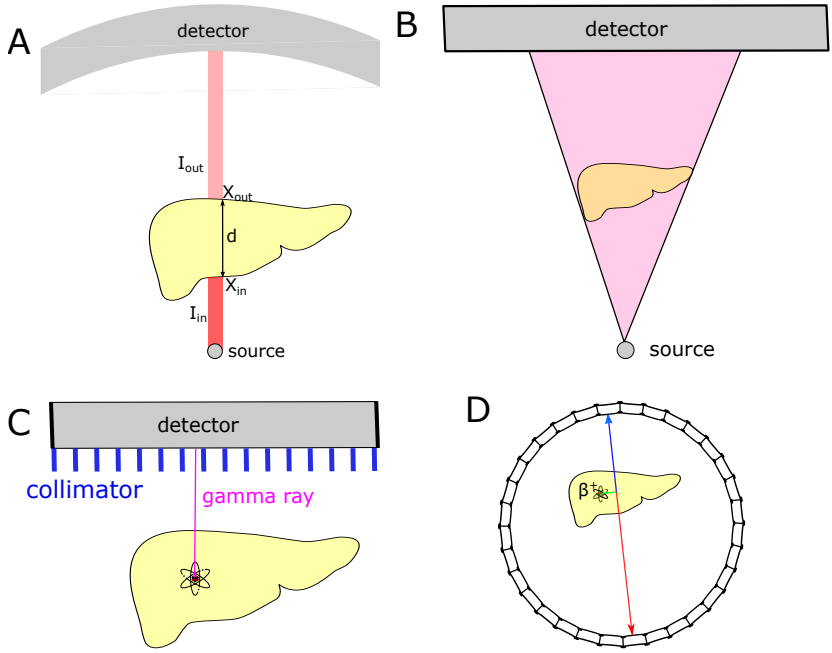

*Figure 1.2: An illustration of [**A**] computed tomography of the liver: X-ray beam intensity generated by the source is attenuated within its path through the liver, [**B**] a c-arm CBCT camera with flat detector and a source rotating around patient body, [**C**] a SPECT camera which measures the emitted photons with a perpendicular path to the detector by using a parallel hole collimator, [**D**] a PET camera which measures two photons travelling in opposite directions (blue and red lines) that are emitted as a result of a positron annihilation. In time-of-flight PET (TOF-PET), the time difference between the detection of these two photons is used to reduce the uncertainty regarding the position of the annihilation.*
*The X-ray source and detector rotate around the patient in CT [**A**] and CBCT [**B**] imaging, and in [**C**] the gamma camera also rotates around the patient. No rotation is needed for the PET system [**D**].*

Spiral or helical CT scanning is another technique in which the X-ray tube and detector rotate around the patient, while the patient table is moved at a constant speed, to create a helical trajectory of the system around the patient. This allows to reduce the scan time and provide a more detailed image.

The linear attenuation coefficient (μ) is a function of tissue density and X-ray energy. As illustrated in the figure 1.2, when the tissue is not uniform, then the relation between I_{out} and I_{in} is described by:

$$I_{out} = I_{in} \times e^{-\int_{x_{in}}^{x_{out}} \mu_x dx} \tag{1.1}$$

where, I_{in} and I_{out} denote the intensity of the generated X-ray beam and the output X-ray beam.

Then, a 3D image of linear attenuation coefficients is reconstructed from the acquired set of 2D X-ray projection images. The reconstructed linear attenuation coefficient in each voxel is usually rescaled to Hounsfield units (HU), also called CT number. HU is defined as a linear transformation of the measurement by setting -1000 HU to the attenuation of the air and 0 HU to the attenuation of the water:

$$\text{CT number(HU)} = \frac{\mu - \mu_{\text{water}}}{\mu_{\text{water}} - \mu_{\text{air}}} \times 1000 \tag{1.2}$$

The liver has a more or less uniform CT number (54-60 HU), which is very close to the CT number of the neighboring soft tissues (*e.g.* heart and kidney), hepatic vessels, and malignancies. This makes distinguishing them challenging in CT imaging.

1.2.1.2 Contrast-enhanced CT

Contrast medium (also known as contrast agents, contrast media, or contrast material) is typically used in x-ray, ultrasound, CT, and MR to increase contrast inside the body. Usually, contrast medium is employed to distinguish particular structures or tissues. These materials temporary modify the characteristic of selected areas (tissues/organs) which is detected in the imaging. For example, iodinated contrast agents injected intravenously are used to enhance CTs. As described above, the HU of a tissue depends on its density. So, administering iodine with an atomic number of 53, which is higher than most soft tissues within the body, produces an image contrast by modifying the density of the enhanced tissues.

Contrast-enhanced CT (ceCT) scans are helpful in imaging liver lesions and for mapping of the HA, because they enhance contrast between the liver parenchyma and tumors or vessels, respectively [47]. In this technique, an iodine-containing contrast agent is injected into the blood flow before the CT acquisition. This agent, by modifying the blood density, increases the X-ray attenuation of different tissues, which enhances the hypervascular tissues in the final reconstructed image. Different tissues have a variable contrast uptake rate due to a different arrival time of the contrast agent within the arterial and venous networks and different amounts of blood in the tissue. For liver imaging, the enhancement of the arterial and venous vessels, liver parenchyma, and tumors is dependent on the contrast agent concentration and the total amount of administered iodine and finally on the time between injection and imaging.

As mentioned previously, liver tumors are supplied mostly by the HA, while the normal liver parenchyma blood flow depends more on the PV. So, by performing the CT at different timepoints after contrast administration (so-called image phases), the contrast between different tissue types in the images can be optimized. In liver imaging, **(i)** native (pre-contrast), **(ii)** arterial phase for imaging the arteries (15-20 second after injection), **(iii)** late-arterial phase (which is also called early venous phase) to enhance the portal vein and image hypervascular liver lesions (35-40 second after injection), and **(iv)** hepatic phase or late portal phase (70-80 second after injection) enhance the liver parenchyma through blood supply by the portal vein are widely used. Most hepatic tumors have a pronounced hypervascularity, leading to a fast wash-in and washout of the contrast agent. So, early phase CTs (*i.e.* early or late arterial phase) provide better image quality in terms of distinguishing tumors and normal liver parenchyma (see section 1.6.4). The tumor detection rate of ceCT is reported to be about 70%, which is similar to non-enhanced MR and inferior to contrast-enhanced MR (90%) [47]. The utilization of ceCT in detection of small hepatic malignancies (*e.g.* tumors smaller than 1 cm) is usually challenging due to low contrast uptake.

1.2.1.3 Cone-beam CT

Cone-beam CT (CBCT) imaging is generally used in the angiography suite for performing intratreatment CT imaging in order to obtain a 3D mapping of the vascular anatomy. This new technique has been increasingly integrated into complex intra-arterial liver treatments (*e.g.* SIRT, and TACE) over the past decade. In CBCT imaging, an X-ray source and an array of detectors rotate 180 to 360 degrees around the patient in a single scan without any bed movement. Compared to the conventional or spiral CT techniques, in CBCT instead of a collimated fan-shaped beam, a cone-shaped X-ray beam is used (see figure 1.2-B) and the remnant beam is captured on a flat two-dimensional (2D) detector. Because of the cone shaped X-ray beam and 2D detector, an entire volume can be reconstructed from an acquisition by a single rotation.

Due to the different geometry and the absence of an effective anti-scatter grid, these images are not as quantitative as CT images. Usually, the reconstructed images have

a range of -1000 to +3000 in an arbitrary unit which are rescaled to provide high/low contrast in different tissues similar to CT images (*i.e.* air and water/soft tissue having values close to -1000 and 0, respectively). CBCTs have a limited field of view (FOV) which often results in tissue being outside the FOV. For example, in abdominal imaging, sometimes the entire liver is not in the FOV and often the liver is truncated in the image.

Dual-phase CBCT imaging consists of two succeeding rotations of the C-arm, to perform early arterial and late arterial (early venous) phase imaging, after contrast injection of contrast medium through a catheter within the HA, to provide 3D visualization of the arteries and the parenchyma they perfuse. During intra-arterial liver treatment planning, CBCT imaging can be used for the tumor detection and identification of feeding arteries, tumor hypervascularity, tumor perfusion coverage, and extrahepatic enhancement [48]. Also, the contrast-enhanced CBCT is performed to make images of the liver perfusion territories, which will be used to decide where to put the catheter during the treatment session or to verify if the intended catheter position will produce the desired results [49]. To provide this information, CBCT imaging is considered to be superior to other techniques such as digital subtraction angiography or diagnostic CT (which uses intravenous instead of intra-arterial contrast injection).

CBCT imaging is particular valuable in the following cases: **(1)** when part of the tumor in one lobe is vascularized by the contralateral HA (*e.g.* vascular supply of segments I and IV are highly variant within patients and may be supplied by aberrant arteries) [50, 51], **(2)** when a single liver segment is perfused by more than one HA branch, **(3)** when non-standard liver segments exist because of bulky tumors or extensive previous treatments (*e.g.* tumor ablation, surgery, etc), **(4)** when a super selective procedure is planned that is increasingly mentioned as an alternative curative treatment in some circumstances (see section 1.5.2).

A recent study shows the usefulness of CBCT in tumor and liver perfusion territory (LPT) definition compared to MR for HCC patients [52]. In addition to LPT definition, some studies showed the additional value of CBCT in SIRT for detecting extrahepatic deposition and/or tumor and normal liver perfusion definition [53, 54]. This information can be used to embolize additional vessels or to reposition the catheter during the work-up.

1.2.1.4 Magnetic resonance imaging

MR imaging is another frequently used imaging modality, which provides better soft tissue contrast than CT imaging. Superior soft tissue contrast is beneficial in the detection and characterization of hepatic malignancies. MR imaging relies upon the magnetic properties of the protons inside hydrogen nuclei, which is abundant in human tissue. These protons behave like small bar magnets. In normal circumstances, without a (strong) external magnetic field, protons spin with their axes randomly aligned in the body (net magnetization = 0). In an MR scanner, the majority of protons align parallel to the strong magnetic field (B0), achieving a longitudinal magnetization state. Radiofrequency (RF) pulses are used to excite these protons, forcing a majority into an non-parallel alignment to the B0 field (excited state) and to spin in sync with each other, *i.e.* in phase. This creates a transverse magnetization component, which is perpendicular to the axis of the main magnetic field. When the RF pulses are stopped, the excited spins start to lose energy, causing them to relax and return to their resting state and emitting a radio wave. A receiver antenna (phased array coil) is used to detect this radio wave, as an analog signal, which is then converted to a digital signal, and reconstructed into an image using Fourier transforms on a dedicated computer system. Excited protons can decay in a T1 relaxation (spin-lattice or longitudinal relaxation), where the energy is lost to the molecular lattice with recovery of the longitudinal magnetization component. T2 relaxation (spin-spin or transverse relaxation), is typically faster than T1 and occurs due to a dephasing of spins and loss of the transverse magnetization component. T2* relaxation occurs much faster and results from both T2 effects and local inhomogeneities of the main magnetic field. By adjusting certain MR acquisition parameters, *e.g.* echo time (TE), repetition time (TR), and flip angle (FA), the resulting image may be weighted for one

type of decay or another, *e.g.* T1, T2, or T2*. The rate of each type of decay depends on the tissue in which the spins are located, resulting in different signal patterns from different tissue types. MR scanners can use a variety of RF pulses, for different purposes. A typical MR acquisition will use multiple RF pulses in succession to achieve a higher signal to noise ratio, or a different type of image contrast, *e.g.* T2*, DWI, MRA, fMRI, etc.

Some MR sequences are very sensitive to noise and are prone to artefacts. MR is considered superior to CT imaging in liver evaluation because of the possibility of tissue characterization based on different contrast enhancement techniques and the possibility to perform different MR sequences:

- **T1-weighted MR**: this basic MR sequence investigates the T1-relaxation time, which is defined as the time that is needed to achieve 63% of the realignment in the direction of the external magnetic field. T1-weighted MR is beneficial in assessing the liver parenchyma tissue for fatty infiltrates. Both benign and malignant hepatic malignancies, cysts, and hemangioma (a benign hepatic tumor) usually have low signal intensity in T1-weighted images. So, this modality is useful for detecting abnormal liver tissue, but distinguishing between malignant liver tumors and other lesions is challenging.
- **T2-weighted MR**: this sequence evaluates the relaxation pattern of the spins perpendicular to the external magnetic field. This sequence is usually used for detecting liver tumors, especially when the fat-subtraction technique is used. By suppressing the fat signal, the contrast between the lesion and hepatic tissue will increase. Due to high signal of liquids in T2, cysts are very bright.
- **Diffusion weighted image (DWI)**: this subtype T2-weighted sequence computes the ease of free random motion of water molecules in each voxel. This modality could evaluate the cellularity of the tissue (*e.g.* highly cellular tumors). The diffusion weighted MR sequence is a valuable tool to differentiate small liver hemangioma and cyst from liver malignancies by assessing the cellularity of the tissues [55]. So, DWI enables identifying small lesions that are sometimes challenging in T2-weighted images. Some studies showed that DWI is superior to CT images for evaluating the tumor size and hypervascularity of the tumors [56].

Similar to CT imaging, contrast enhancement techniques using gadolinium-based contrast agents, are also available in MR imaging. These agents change the magnetic properties of the blood (*i.e.* the relaxation times), which improve the visual contrast of the hypervascular tissues. Pre-contrast, late arterial, portal venous and delayed phase, and especially, early arterial phase MR imaging (*e.g.* T1-weighted) and DWI sequences are crucial for liver tumor detection [57]. Contrast-enhanced and DWI-MR are the current gold standard for detection of small liver tumors (see section 1.6.4).

1.2.2 Molecular imaging

Radioactivity refers to the emission of radiation from unstable atomic nuclei. Radionuclides are unstable because of an excess of neutrons, protons or energy. Most radionuclides have different decay possibilities that can be followed to reach a final stable state, each with its own probability, which is called the branching ratio. The amount of radioactivity is usually expressed in the unit of becquerel (Bq), which is equivalent to one disintegration or transformation per second, which represents the number of decayed radioactive atoms per unit of time. The half-life ($T_{1/2}$) of a radionuclide is the amount of time after which the number of radionuclides has been reduced by half.

For example, β^- emission is the result of a transformation of a neutron into a proton and an electron (also emits an antineutrino), which is released with a certain amount of kinetic energy. β^- emission may produce a daughter nucleus in an excited state. The daughter nucleus can reach the ground state through different processes (*e.g.* γ decay, which is emitting the excitation energy in the form of one or more γ photons).

Molybdenum-99 (^{99}Mo) decays to the metastable state of technetium-99m (^{99m}Tc; which is the most common radionuclide used in nuclear medicine) by undergoing β^- decay. Then, technetium-99m decays to technetium-99 (^{99}Tc) by emitting a photon of 140 keV with a branching ratio of 89% (see figure 1.3-A).

Positron emission is another mode of decay (β^+ decay) in which a proton is transformed into a neutron and a positron (also emits a neutrino). At that point, the positron will be annihilated very quickly (on the order of hundreds of picoseconds) by interaction with an electron. The mass of these two particles is then converted into energy in the form of two photons with an energy of 511 keV, that are emitted in opposite directions ($\sim$ 180 degrees). One of the commonly used radionuclides decaying through positron emission is fluorine-18 (^{18}F) (see figure 1.3-B).

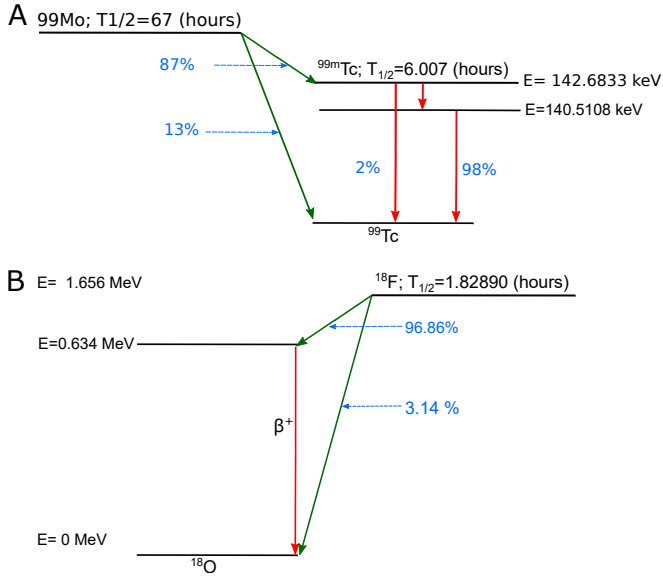

*Figure 1.3: Decay scheme of [**A**] technetium-99m and [**B**] fluorine-18*

The first gamma camera was developed in 1957 by Hal Anger to image the distribution of a gamma emitting radionuclide within the body. Most of the modern gamma camera still use the same principles. Modern single photon emission computed tomography (SPECT) and positron emission tomography (PET) are widely used in clinical practice for diagnostic purposes and are able to provide the quantification of the radioactivity concentration in absolute values. Nuclear imaging can have higher sensitivity compared to MR and CT imaging, depending on tumor type and tracer used, but on the other hand, these imaging modalities have relatively low spatial resolution and there is a lack of anatomical information in the images.

1.2.2.1 SPECT

In SPECT, a gamma-camera acquires 2D projections of the emitted gamma rays from a photon emitting radionuclide distribution. The detectors of the SPECT camera acquire projections from a 180 or 360 degree orbit around the patient with equal angular step. During SPECT acquisition, the detectors record the photons that fall within a selected energy window around one or more photopeak energies of the radionuclide. As illustrated in figure 1.2-C, the detectors are usually collimated using a parallel hole collimator in order to capture only the photons with a travelling path perpendicular to the detector. This collimation is crucial for the reprojection step in the reconstruction of the projection data.

Then, these 2D projections are reconstructed to a 3D volume using analytical, *e.g.* filtered back projection or (FBP), or iterative, *e.g.* maximum-likelihood expectation maximization (MLEM), reconstruction methods. The objective is to determine the activity distribution that produces the measured projections. In iterative reconstruction, the algorithm starts from an initial guess. In each step, the image projections obtained from the activity distribution of the previous step are compared to the measured projections. Based on the determined deviation, the activity distribution is updated. These steps are repeated until the difference between the calculated projections and the measured ones becomes sufficiently small. In some cases, regularization during image reconstruction is performed.

To provide absolute quantification, SPECT images should also be corrected for attenuation of the radiation within the body, collimator blurring, and scattering of gamma rays within the object. To perform attenuation correction, the tissue density distribution within the object should be provided. In hybrid imaging (combining nuclear medicine and radiology modalities, described in section 1.2.3), this information can be obtained from CT images by converting the value of these images into a linear attenuation coefficient map. The correction for the scatter photons is usually performed by using one or more additional energy windows alongside the primary photopeak energy window. By assuming that the counts in this additional energy window are representative for the scatter component in the main energy window, a scatter subtraction can be applied or the scatter component can be taken into account by the reconstruction method used. After these corrections, the provided image represents counts per volume per time unit. A calibration can be performed to convert the recorded count rate in each voxel to an absolute value (Bq or Bq/ml) using a volume or system sensitivity calibration factor obtained from a phantom scan [58].

Limited spatial resolution in SPECT imaging is a source of so-called partial volume effect [59]. This effect results in a more blurry image with underestimation of the activity concentration in small volumes (*e.g.* small hot spots relative to a cold background) with spill over of counts to the neighboring region. In this case the total counts are preserved in the reconstructed image but the object appears to be larger with lower activity concentration than the actual concentration. On the contrary, a cold spot relative to a hot background will be reconstructed smaller with higher apparent activity concentration.

1.2.2.2 PET

A PET camera is designed to detect a pair of photons that are emitted as the result of positron-electron annihilation. These photons are detected within a narrow time interval called the coincidence timing window (current systems use a coincidence timing window of about 4 to 10 ns). These photons are travelling in opposite directions each with an energy of 511 keV, as illustrated in figure 1.2-D. A modern PET camera has multiple rings containing small scintillation detector units surrounding a bed. Within an acquisition, the patient is moved through the gantry in one or multiple bed positions. Also, there are PET cameras that have a continuous bed motion. In contrast to a SPECT camera, a PET camera does not require a physical collimator because the coincidence detection in opposite detectors of the photon pair is used to define a line including the position of the annihilation. The path between these two detectors is referred to as a line of response. If two photons from two different annihilations are detected in the coincidence timing window, a so-called random event occurs, which can degrade the image accuracy. Scatter is another source of error which is the case when two photons of the same event are detected, but the line of response does not include the annihilation site because of a scattered trajectory of at least one of the annihilation photons. The distance which a positron travels through matter before it annihilates is called positron range and depends on the initial kinetic energy (*e.g.* the average positron range of yttrium-90 and fluorine-18 are approximately 1 and 0.64 mm, respectively) [60]. The positron range leads to a loss of spatial resolution.

Reconstruction of PET images is usually performed by employing an iterative method with attenuation and scatter correction. Scatter correction in PET can be performed by

different techniques, *e.g.* subtracting the simulated scatter contribution to the measured data (*e.g.* by Monte Carlo simulation). Estimating random events can be performed by using an additional delayed coincidence timing window [61].

One advantage of modern PET cameras is the time-of-flight (TOF) technique. After the annihilation of the positron, the two photons are travelling different path lengths before reaching the detector crystal. Differences in path length correspond to a difference in detection time between the two photons. By using this information, one can estimate a probability distribution for the position of the annihilation along the line of response. This additional information per detected true annihilation event results in less noise in the reconstructed image [62].

1.2.3 Hybrid imaging

The clinical use of hybrid or dual-modality imaging in nuclear medicine [63, 64] began around 2000 with the first commercial SPECT/CT system, the GE Discovery VG Hawkeye, and PET/CT system, the FE Discovery LS. Modern hybrid scanners combine the advantage of functional imaging (*e.g.* PET or SPECT) with the advantage of the anatomical imaging (*e.g.* CT or MR) within one examination to improve the diagnostic power. The anatomical component can also be used to improve the functional imaging quantification accuracy through attenuation and scatter correction. Low-dose CT is sufficient when the goal of dual-modality imaging is solely attenuation correction and anatomical localization for detected lesions. Therefore, the use of low-dose, non contrast-enhanced CT is performed in most of the SPECT/CT workflows. But for high dose CT, often with administration of iodinated contrast agents, might be relevant for diagnostic purposes and precise organ identification.

In dual-modality imaging, accurate image alignment is possible if the spatial coordinates of the modalities have been aligned using a geometric calibration step, and if functional and anatomical data are acquired while the patient maintains the same position during both acquisitions. However, since the duration of functional imaging usually takes about 30 minutes, mis-registration can occur because of respiratory, cardiac, and arbitrary patient motion. And on top of that, the weight of the patient might change the normal support position of the bed in between both acquisitions. Some modern PET/MR cameras acquire both modalities simultaneously, which eliminates the possible inter-acquisition alignment error but does not eliminate intra-acquisition motion effects.

1.3 Radionuclide therapy - therapeutic nuclear medicine

Nuclear medicine has been practiced in Belgium since the late 1940s and became a dynamic disciplines of medicine. Nuclear medicine became a separate medical specialty by Royal Decree, in March 1985. This clinical speciality utilizes unsealed radioactive substances for assessing different physiological functions (diagnostic), treating specific tumors (therapeutic), for clinical and research purpose. These unsealed radioactive materials (if considered a drug called a radiopharmaceutical) consist of a chemical agent (vector molecule) which is labelled with a radionuclide.

In 1900, Alexander Graham Bell suggested the idea of accumulating radioactivity near or within the tumor to treat them, which is still the key of brachytherapy (brachy is a Greek term meaning short-range). This concept was materialized in 1901 by using radium-226 (^{226}Ra) for treating tuberculous skin lesions. The therapeutic facet of nuclear medicine has evolved over decades after the discovery of the tracer principle by George de Hevesy in the 1920s. While the fundamental theory behind radionuclide therapy stays the same, this field developed slowly but surely in the form of a number of established clinical radionuclide therapies and promising treatments in preclinical development [65].

Radionuclide therapy results in high absorbed dose to key cellular molecules, which historically were thought to be only DNA, but proteins and lipids have been recently discovered to be vectors of the irradiation effect. This will lead to cell death or impaired

cell growth, causing tumors to shrink or stop growing. This radiation will also partially irradiate normal cells but these have a better ability to repair themselves, whereas tumor cells are more radiosensitive because of their rapid cell division. EBRT is the most commonly used type of radiotherapy. EBRT treats a limited region around the tumor by irradiating it with high energy photons and is more suitable for a limited target volume. On the other hand, targeted radionuclide therapy is most often a systemic therapy, akin to other systemic therapies, which consists of administrating non-sealed radionuclides (as radiopharmaceutical or medical device) into the blood circulation, which will lead to whole body coverage. It is a potentially effective modality to treat tumors which have spread within the body.

In targeted radionuclide therapy, the radiopharmaceuticals have a high affinity for tumor cells (guided by *e.g.* antigens, receptors, physical properties) to transfer high and lethal radiation energy to the lesion which can cause partial or complete ablation of the tumor. A good candidate therapeutical radiopharmaceutical should:

1. accumulate as much as possible into malignant lesions,
2. have as low accumulation in normal tissue as possible,
3. irradiate the tumor cells with an energy which is adequate to impairment of key molecules of the malignant cells (*e.g.* DNA) with limited irradiation of adjacent normal tissue

A good choice of the vector molecule or vehicle dictates the first two properties, while the last one depends mostly on the characteristics of the radionuclide.

To release sufficient energy to impact the tumor cells, the therapeutic radionuclide should have a good linear energy transfer (LET). The LET is the amount of energy transferred to the tissue by an ionizing particle per unit of distance (unit: keV/µm). Theoretically, radionuclides with dense dose deposition pattern (*i.e.* short penetration into the tissue; higher LET) and an adequate half-life in respect with the kinetics of the biodistribution are desired for radionuclide therapy. The most commonly used type of particle for radionuclide therapy is β emission (*e.g.* electron), but other types like α particle emission are useful as well.

One of the attractive features of targeted radionuclide therapy is the possibility of imaging a predicted distribution within the body of the therapeutic agent using the therapeutic radiopharmaceutical itself (in much lower quantities than for therapy) or using a vehicle similar to the therapeutic radiopharmaceutical, but labelled with a diagnostic radionuclide. This is called the "theranostic" aspect of radionuclide therapy. The non-invasive imaging and potential to predict the internal distribution of therapeutic radionuclides is an advantage over many other systemic therapies (*e.g.* chemotherapy). These images can be acquired before the treatment to predict efficacy or toxicity and also allow to tailor the treatment to the specific situation of the patient. For predictive imaging, a radionuclide with γ radiation or positron emission is preferred because it can be detected externally with clinically useful precision.

1.3.1 β^-mitters in radionuclide therapy

β^- emitters with useful physical characteristics (half-life, energy, ...) are used in targeted radionuclide therapy, to ensure that they have a good balance between therapeutic and side effects. So, practically, the β^- emitters like rhenium-188 (^{188}Re), lutetium-177 (^{177}Lu), holmium-166, and yttrium-90 are good choices in targeted radionuclide therapy. Notably, their path length is adequate to provide a good dose coverage to both small and bulky tumors, and can also be effective in poorly vascularized tumors because of the crossfire effect (irradiating the site of accumulation and a number of cells diameters around it). By using β^- emitters, most of the effective radiation is delivered within 2-4 mm of the source with practically no irradiation effect one centimeter away.

The emission of the β^- particles typically takes place when the ratio of neutrons to protons in the nucleus is too high. A redundant neutron is then transformed into a proton

which stays in the nucleus and an electron is expelled. The energy of the expelled β^- particle is radionuclide specific; the radionuclide defines the characteristics of the expelled particle (*e.g.* kinetic energy, penetration range, and the energy that can be deposited into the surrounding tissue).

Along with iodine-131 (^{131}I), yttrium-90 is one of the most widely used radionuclides in therapeutic nuclear medicine due to several advantageous characteristics:

1. **advantageous half-life**: the physical half-life of the radionuclide is an important consideration in nuclear medicine. If the physical half-life is too short, most of the energy will release before the acticity has reached the tumor. Conversely, to limit radiation exposure in the surrounding of patients, and provide sufficient energy deposition to impair the tumor, the use of radionuclides with too long half-life in therapeutic nuclear medicine is not preferred.
2. **limited need for radio-protection:** it is a virtually pure β^- emitter with limited radiation outside the patient, so radio-protection measures to be taken by the patient, the caregivers and people around are limited.
3. **favourable chemistry:** its chemical properties allow to attach it to many carriers.
4. **near-ideal energy features:** the average energy of β^- emissions from yttrium-90 is 0,9367 MeV with a mean and a maximum tissue penetration range of 2.5 and 11 mm.

Commercial therapeutic applications of yttrium-90 are available in forms of (1) ^{90}Y-ibritumomab tiuxetan (trade name: Zevalin®) radio-immunotherapy targeting CD20 for non-Hodgkin's lymphoma, (2) ^{90}Y-DOTA-TOC peptide receptor radionuclide therapy for mNET, (3) ^{90}Y glass or resin microspheres for hepatic malignancies.

1.3.2 Absorbed dose

The mathematical concept of internal energy deposition calculations (in terms of absorbed dose) was first published by Marinelli and Quimby *et al.* in 1948 [66]. However, the first study which implemented this computation to tailor a prescription for thyroid cancer treatment with iodine-131 was not successful, due to a large margin of error [67]. More precise image reconstructions as a result of mathematical, computer, and camera technology advancement enabled more accurate dose measurements.

Absorbed dose of a VOI, *i.e.* a lesion or (a part of) an organ, is defined as the amount of energy deposited within a unit of mass:

$$D_{\mathrm{VOI}}[\mathrm{Gy\ or\ J/kg}] = \frac{\text{deposited energy within a VOI [J]}}{\text{mass of the VOI [kg]}}, \tag{1.3}$$

Absorbed dose is a fundamental quantity of interaction between ionizing radiation and the tissue. Absorbed dose is widely used as a parameter to predict treatment effects (the efficacy and safety of a treatment), by ensuring the delivery of projected adequate absorbed dose to the treatment volume (sufficient tumor absorbed dose and safe healthy tissue absorbed dose).

The unit of absorbed dose is gray (Gy), which is equivalent to J/kg. By definition, to determine an absorbed dose for a volume of interest (*e.g.* organ, tissue, or voxel), we must calculate the deposited energy and the mass. The definition of activity concentration is an essential step for energy calculation together with the knowledge of the radionuclide, the energy of the emitted radiations, and the penetration pattern within the tissue. The same approach is used for protection against radiation in diagnostic nuclear medicine, but the absorbed dose in these applications is much lower, and dose assessment is applied only to lessen the risk of stochastic radiobiological effects. This so-called "internal dosimetry method" is different from the dosimetry of radiation from external sources and cannot be measured directly. This indirect approach relies on biodistribution modelling and quantitative imaging of the activity. Therefore, internal dosimetry sometimes needs to rely

on assumptions. For this purpose, different methodologies exist which use assumptions to make the calculations feasible, with different levels of detail and accuracy. This range is quite wide, from assuming a uniform absorbed dose to the entire treated organ and applying the so called medical internal radiation dose (MIRD) formalism to calculate a mean absorbed dose, to small level dosimetry using Monte Carlo (MC) calculations to estimate sub-voxel dose distributions (see figure 1.4).

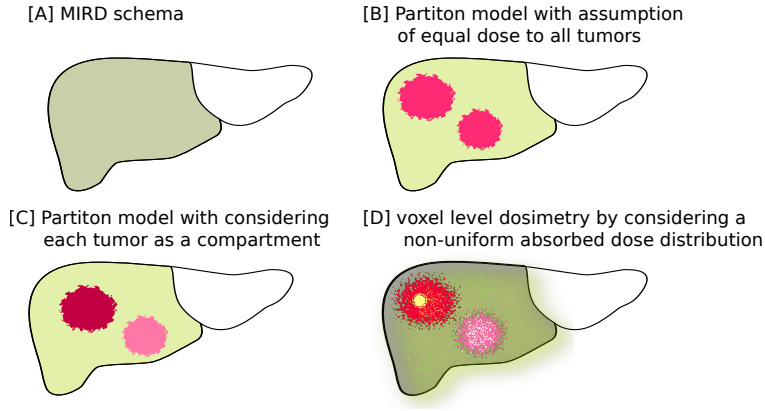

*Figure 1.4: Schematic of different levels of dosimetry **[A]** MIRD scheme; a uniform dose to the entire perfusion territory (tumor and healthy tissue) is used to calculate the injected activity, **[B]** partition method with two compartments of tumor and healthy tissue in a single perfusion territory, **[C]** partition method with three compartments; healthy tissue of the perfusion territory, tumor one and tumor two, and **[D]** voxel-level dosimetry considering the heterogeneity of the absorbed dose at the voxel-level*

1.3.2.1 MIRD schema

Since 1968, the MIRD committee of the Society of Nuclear Medicine [68] has proposed different dose calculation systems which have been widely accepted in internal dosimetry for many years. This schema was intended for diagnostic nuclear medicine and for estimating absorbed doses to the average patient. In the MIRD scheme, the body consists of source organ/regions that accumulate activity. Then, by assuming uniform activity within the source region and uniform absorbed dose to the target region, an average absorbed dose within the target region is calculated for a standard model of an individual [69]:

$$\bar{D}(r_k \leftarrow r_h) = \tilde{A}_h S(r_k \leftarrow r_h), \tag{1.4}$$

where r_k and r_h denote target and source organ, respectively. $\tilde{A}_h$ is cumulated activity, and $S(r_k \leftarrow r_h)$ is so-called S-value or S-factor, which is a conversion factor representing the mean absorbed dose in the target region caused by a unit of cumulated activity in source organ. Up to now, 26 MIRD pamphlets and 20 MIRD dose estimate reports addressed internal dose models, S-factors for the combination of different radioactive and biological decays and different source and target organs, equations, and techniques.

1.3.2.2 Other dosimetry methods

During the past decades, some new methods have been investigated to increase the accuracy of dosimetry by addressing some fundamental assumptions of the MIRD schema: **(1)** uniform distribution of the activity, **(2)** uniform dose in the target region, **(3)** anatomical deviation from models that are used to derive S-values.

To move forward from model-based dose calculation to personalized dosimetry, one needs to tackle different problems: **(i)** provide the anatomy of the volumes of interest,

e.g. normal organs, healthy tissues, lesions, ..., **(ii)** computation of cumulated activity which is traditionally done by serial measurements and/or kinetic modelling, **(iii)** translating the deposited energy to the absorbed dose in a defined VOI. For the latter, recently several new absorbed dose calculation methods have been introduced like: **(1)** adapted MIRD schema by modifying the formalism for patient-specific volume calculation, **(2)** convolutional dose point kernels derived from MC simulation to convert cumulated activity to a local absorbed dose (see figure 1.5), **(3)** fully MC methods to simulate all radiation paths through the patient's body.

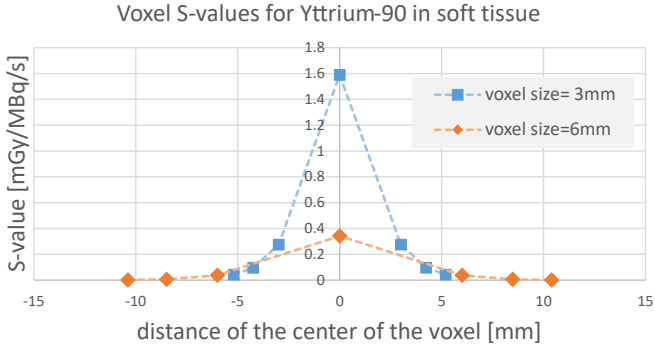

Figure 1.5: Comparison of the S-values for yttrium-90 for two voxel sizes (3 mm and 6 mm), the points correspond to voxels (-1,-1,-1), (0,-1,-1),(0,0,-1),(0,0,0),(0,0,1),(0,1,1), and (1,1,1) when the source activity is placed in the (0,0,0) [70]; available online: `http://www.medphys.it/down_svoxel.htm`

1.3.2.3 Dose-effect relationship

Post-treatment absorbed dose along with **(1)** radiation type **(2)** tissue radiosensitivity and **(3)** the dose rate is used to analyze the dose-effect relationship. To compare an irradiation induced by different modalities considering above mentioned parameters, a biological effective dose (BED) formalism is widely used. To account for the impact of the non-uniformity of the delivered absorbed dose, an equivalent uniform dose (EUD) formalism has been introduced [71, 72].

In a given treatment modality, to compare different scenarios, the other three factors are invariable, and absorbed dose plays an important role. The correlations between absorbed dose and radiation-induced effects on normal tissues and tumor could be compared when the same modality (*e.g.* EBRT and glass or resin microsphere) is used. So, this parameter is sometimes used to compare different treatment sessions and identify safety and efficiency criteria for a given treatment modality for an identical organ. Normal tissue complication probability (NTCP) and tumor control probability (TCP) are radiobiological models either inherited from EBRT or obtained from SIRT patients that describe the relationship between absorbed dose and liver toxicity (see figure 1.6-A) and tumor response (see section 1.7.7), respectively [71, 73, 74]. Figure 1.6-B illustrates the relationship between tumor absorbed dose and metabolic tumor response for mCRC.

In radionuclide therapy, absorbed dose levels are in the order of tens to hundreds of grays, and the absorbed dose is one of the parameters which is used to evaluate the tumor irradiation and healthy tissue safety. TCP and NTCP curves allow to find the balance between deterministic effects on the tumor and healthy tissue, *e.g.* from the NTCP curve, one can identify the D50, *i.e.* the dose that induces a 50% probability of normal tissue complication. In the TCP curve, one can find the probability that this dose will provide tumor control.

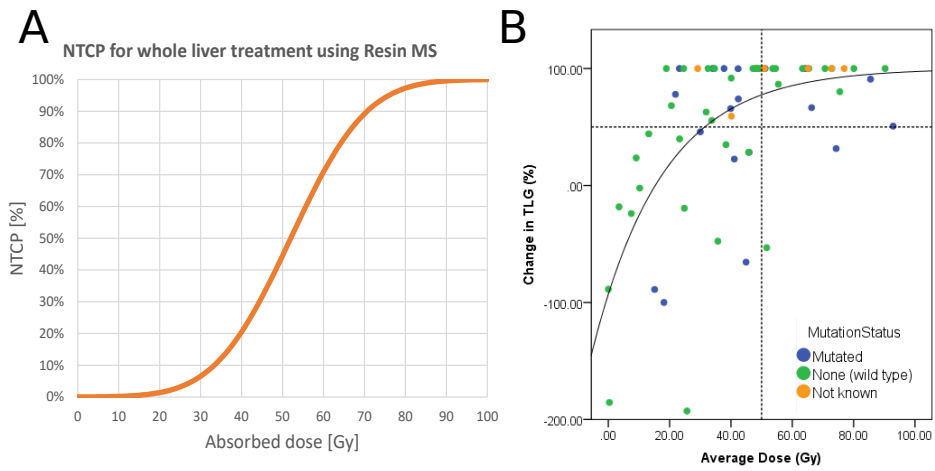

*Figure 1.6: **[A]** Adapted from [74, 75], a model of normal tissue complication probability of liver toxicity (grade 2 of so-called common terminology criteria for adverse events, version 4) versus non-tumoral liver absorbed dose **[B]** Adapted from [76], with permission: the dose-response for all lesions follows the expected relationship when measuring response with change in TLG; a 50 Gy cut-off (dashed line) corresponds to a significant response in all but two evaluated lesions.*

1.4 A historical perspective on SIRT

The exceptional vascularity of hepatic tumors has been studied since the early 1950s, with continued interest through the 1980s. Bierman demonstrated that liver tumors receive blood mainly from the HA, not the PV, in 1951 [77], and Breeds reaffirmed this discovery later in 1954 [78]. Disclosure of unique liver blood flow led to the development of various intra-arterial liver treatment modalities:

- trans-arterial embolization consists of blocking the hepatic artery flow using embolic agents
- trans-arterial chemotherapy is the use of a chemotherapeutic agent released from embolic agents
- SIRT or radioembolization, which deposits radiation selectively into tumor.

The first reported human administration of ^{90}Y-microspheres to address liver malignancies was performed by Ariel in 1965 after they observed resistance of liver cancer to contemporary EBRT and available chemotherapy. In this study, ceramic microspheres with a diameter of 50 $\pm$ 10 µm, labelled with yttrium-90 were infused into the aorta at the level of the celiac axis [79]. The distribution of the radionuclide was determined by a photo-scan[1] using ytterbium-169 (^{169}Yb) as a suitable γ emitter attached to the microspheres. They also reported the delivery of microspheres to non-target organs, which they related to some side-effects.

In the following years, many studies aimed at fine-tuning the technical aspects like **(1)** catheterization techniques (*e.g.* properly accessing the hepatic vasculature and optimizing the infusion position); **(2)** so-called "skeletonization" which is isolating the main vascular trunk by ligating or coiling all hepatic artery side-branches; **(3)** device characteristics (*e.g.* adapting the microsphere diameter and material); **(4)** performing a simulation by imaging radiolabelled albumin particles before treatment to predict the distribution of the therapeutic microspheres; **(5)** the use of post-treatment imaging to confirm the activity

[1] To obtain a photo-scan, a radiation probe moved along several horizontal lines and the output was plotted as dots on a paper

accumulation after treatment which has been acknowledged from early studies [80]; and **(6)** the methodology to estimate the activity to be administered (*e.g.* paying attention to activity accumulation within target tumors and organs at risks such as the non-tumoral liver tissue and extrahepatic sites).

The latter stresses the importance of accounting for the non-uniform activity deposition within the liver in pre- and post-treatment assessments. This challenge has been known since the very early SIRT studies by Blanchard *et al.* (1967) and is still relevant in modern SIRT:
"The difficulty in assessing the actual mass of tissue exposed has presented another problem in calculating dosimetry. Therefore, in the data presented here, dose has been expressed as the amount of radiation delivered in millicuries[2] *rather than the radiation absorbed in rads*[3]*. Hence, what might seem to be a relatively high dose delivered may be, in fact, a low dose absorbed if the tissue mass exposed is large."* [81]

1.5 SIRT concept

As mentioned before, application of EBRT is restricted for liver cancer because the normal liver parenchyma is one of the most radiosensitive organs, which makes liver parenchyma prone to radiation-induced injury. SIRT, which is using non-biodegradable (or very slowly biodegradable) microspheres as vehicles labelled with a β emitter (yttrium-90 or holmium-166), avoids this problem by a selective/super-selective irradiation of the tumor, and notably sparing of the normal liver tissue to some extent. This selective irradiation has several aspects:

1. **blood-flow selectivity:** as normal liver parenchyma and tumor have a dual blood supply (from PV and HA, respectively), administering the microspheres within the appropriate branch of HA results in higher activity concentration in tumoral than in the non-tumoral tissue (see section 1.1.2).
2. **anatomical selectivity:** the liver consists of separate blood draining regions (liver segments). So, it is possible to irradiate only selected liver segments. Also, the liver is a parallel organ and in case of damage to some liver segments due to high activity deposition, the other liver segments can preserve sufficient liver function (see section 1.1.2).
3. **radioactive selectivity:** short penetration and high LET of the used radionuclide leads to a very local irradiation (see section 1.3.1).

SIRT has a complex, logistically and technically demanding workflow. This multidisciplinary treatment modality involves different professionals and expertise, including interventional radiology, nuclear medicine, medical physics, hepatology, surgical and medical oncology, and radiation safety management.

1.5.1 Blood-flow selectivity and hepatic vascularization

SIRT consists of administering millions of microspheres labelled with a β-emitter radionuclide using a micro-catheter via the HA vascular tree. For this direct access to the hepatic arterial circulation, typically, a femoral artery catheterization is performed under fluoroscopic guidance.

The normal liver parenchyma acquires its blood mostly via the PV. In total, approximately 10-15% of the total blood volume is hepatic blood; 60-80% of the hepatic blood is delivered from the gastrointestinal tract through the PV and the rest from the systemic circulation through the HA [82].

Hepatic malignancies are capable of stimulating the growth of new blood vessels with a ∼20-400 times higher density than in normal hepatic parenchyma [83]. These extra

[2] a non-SI unit of radioactivity equivalent to 37 MBq
[3] a unit of radiation absorbed dose equivalent to 0.01 Gy

vessels are developed to supply the tumor with the oxygen and nutrients needed to spur further growth. Hepatic malignancies (either primary or secondary small tumors bigger than 3mm) receive their blood predominantly from the HA, which carries nutrient-rich and oxygenated blood (see figure 1.7).

When administering the microspheres via the tumor feeding HA branch, this difference in blood supply leads to a tumor to normal tissue activity concentration ratio (T/N ratio) around 5, but which can be as high as 25 in extreme cases. A ratio less than two is considered as a poor tumor vascularization and can lead to relatively poor SIRT outcome. SIRT exploits these properties to deliver an effective dose to the liver malignancies with limited irradiation to the normal liver tissue and without significant systemic side effects. This high dose to the liver tumor can provide a lethal dose to tumor cells and demolish crucial tumor vascular flow, which can result in tumor death and necrosis.

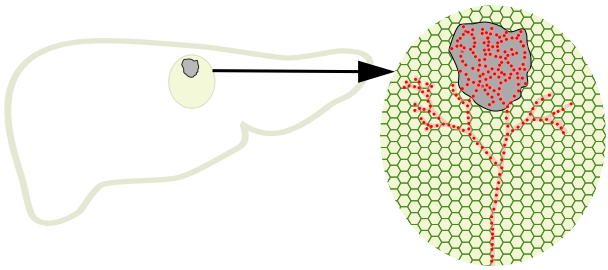

Figure 1.7: Illustration of a hypervascular tumor with a higher number of microspheres (red dots) trapped in the the tumor (gray area) compared to normal liver parenchyma (green area).

1.5.2 Anatomical selectivity and SIRT strategies/catheterization

SIRT can be performed at different levels of selectivity regarding liver blood vessel anatomy (see section 1.1.2) based on the treatment goal (see figure 1.8). Selective or super-selective irradiation of the tumor is obtained by choosing proper positions within the HA tree and providing an optimized amount of injected activity (IA) for each catheter position. This offers the possibility of patient-specific treatment to maximize efficacy and minimize the risk of normal liver complications. The following levels of selectivity are often considered:

- **whole liver treatment:** if there is tumoral involvement in both liver lobes and within multiple segments, the whole liver needs to be targeted. Administration can be performed by proximal catheterization (*e.g.* via proper HA) but whenever possible separate injection in the left and right HA is recommended.
- **lobar treatment:** when the tumor is situated in a single liver lobe the microspheres are injected only in the branch of the HA feeding the involved liver lobe.
- **segmental treatment:** when all the tumoral lesions are located in the same liver segment, selective catheterization of the HA branch feeding this segment will lead to only a small fraction of the healthy liver parenchyma being irradiated. If sufficient liver reserve, both the tumor and healthy liver can be treated to ablative doses.
- **radiotumorectomy:** in the presence of a single tumoral lesion, the tumor-feeding branch of the HA can be supraselectively catheterized, leading to activity delivery virtually exclusively to the tumor with minor involvement of the healthy liver.
- **hybrid treatment strategies:** in the case of multifocal bilobar disease, the treatment team can administer different activities within different branches of the HA, which perfuse the involved segments and/or lobes. This bilobar treatment can be performed in a single session or in two consecutive sessions.

There is always a tendency to avoid bilobar or whole liver treatment whenever possible, to spare non-tumoral tissue as much as possible. In case of a lobar or segmental strategy, the radiation damage induces a decrease in liver function within the treated volume, and an increase in liver function within the spared volume(s) [84]. This may have implications for subsequent treatments like resection of the treated liver segment or lobe.

In 55% of the European centers, sequential left and right lobe SIRT is preferred with a time interval of a month between sessions. Single session bilobar treatment is the favored modality in 38% of the centers, and only 5% of the centers mostly perform a whole liver approach trough injection of the common HA [85].

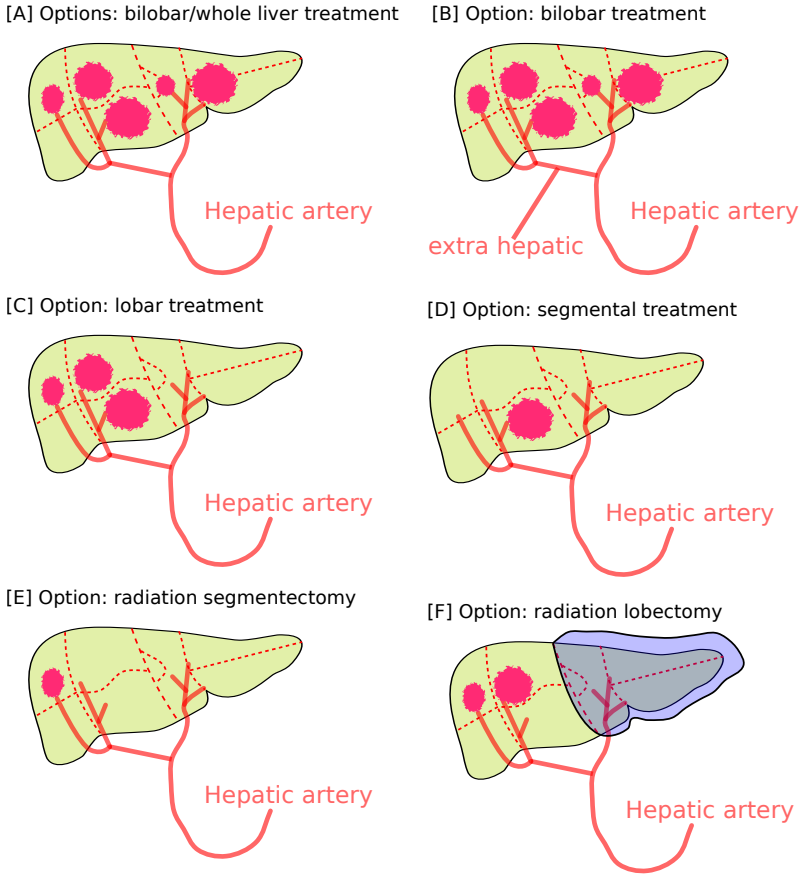

Figure 1.8: Schematic of different SIRT strategies ***[A]*** *diffuse tumors in both lobes; SIRT can be performed using bilobar treatment or whole liver administration.* ***[B]*** *diffuse tumors in both lobes; only bilobar treatment could be performed. Because of the existence of a branch of the hepatic artery supplying an extrahepatic site, a whole liver approach is not possible.* ***[C]*** *tumors in only one lobe, candidate for a lobar treatment.* ***[D]*** *tumor is limited to a single segment, segmental administration can be performed.* ***[E]*** *tumor in a small segment with a possibility of a super-selective approach, ideal for radiation segmentectomy.* ***[F]*** *a schematic of right-sided radiation lobectomy, leading to downstaging of the tumors in the right lobe and hypertrophy of the left lobe (purple area).*

1.5.2.1 Radiation segmentectomy

Radiation segmentectomy is a special case of segmental treatment, which is widely accepted as a curative approach in hepatic malignancies (especially in HCC). This technique consists of administrating a large amount of activity into a small portion of the liver, typically a single segment, which fully contains the tumor, often to a high extent [86]. By increasing the IA while minimizing the perfusion volume, a very high absorbed dose can be achieved in the tumoral area. In this approach, a substantial portion of the non-tumoral liver tissue in this LPT is sacrificed to obtain a very high tumor absorbed dose (as high as >1000 Gy), which is enough to ensure complete tumor ablation. One advantage of radiation segmentectomy over other ablative techniques is its ability to ablate tumors regardless of their size, geometry, orientation, and distance from large vessels.

Radiation segmentectomy is discussed in several studies as an ablation technique for large hypervascular, well-defined tumors with a clearly definable arterial supply, which are not suitable for typical curative treatments because of the tumor location or patient comorbidities [87]. This is only applicable when the lesion is located in an independent draining region of the hepatic artery with no or very limited leakage. This method has been shown to yield good results like complete tumor ablation or serving as a bridge to resection or transplantation [88].

In this scenario, the role of CBCT (see section 1.2.1.3) is crucial to **(i)** provide volumetric analysis for dosimetry, **(ii)** verify complete tumor coverage, and **(iii)** ensure complete coverage of the tumor margin. In radiation segmentectomy, CBCT is considered as the gold standard and a preferred modality for volume definition [53, 89].

In a recent retrospective study by Padia *et al.* [90], radiation segmentectomy was compared to segmental TACE. In total, 101 and 73 patients were treated with SIRT and TACE, respectively. Both treatments were safe with low reported toxicity. The overall complete response rate was significantly better for SIRT (84% versus 58%, p-value<0.001). Also, SIRT showed a better performance in terms of median PFS (18.8 versus 9.0 months, p-value=0.002) and OS (39.9 versus 34.8 months, p-value<0.001) [91].

1.5.2.2 Radiation lobectomy

Radiation lobectomy is another technique in which a lobar SIRT (usually in the right liver lobe) is applied when the entire lobe has a high tumor burden. In radiation lobectomy, the absorbed dose is not as high as in radiation segmentectomy and the non-tumoral liver parenchyma is not ablated. Still, the dose to non-tumoral liver is sufficient to produce liver atrophy in the treated lobe and compensatory hypertrophy in the contralateral lobe. This technique is beneficial for patients who are candidates for liver surgery, except when they have a too small future liver remnant [92]. Classically, a PV embolization is used to induce contralateral lobe hypertrophy, but this treatment has no direct anti-tumoral effect. With radiation lobectomy, the tumor is actively treated, preventing growth and inducing downstaging. Several studies demonstrated contralateral lobe hypertrophy of up to 57% in three months after radiation lobectomy with a promising response rate in the treated lobe [93, 94].

The optimal dose to non-tumoral liver to be used in radiation lobectomy is not well known. The mechanism of hypertrophy is still not entirely elucidated at the molecular level. Some studies suggests that the reduction in liver function (similar to surgery or PV embolization) as a result of non-tumoral liver dose in lobar SIRT leads to contralateral liver hypertrophy [95]. In this study, a sub-group analysis showed that in large lesions (> 100 ml), tumor dose relates to the liver hypertrophy.

1.5.3 Microsphere embolization

In SIRT, the microsphere embolization is dependent on the diameter of the microspheres, with a diameter typically ranging from 20 to 40 µm; according to the package insert for resin microsphere, the size of the microspheres are validated, as more than 90% of the

particles should have a diameter in the range of 32.5 ± 2.5 µm. The size is such that the microspheres are small enough to go quite distally in the arterial tree, up to the level of the precapillary arterioles, but large enough not to go through the capillary bed of the liver [96].

Upon administration of the microspheres, clusters of microspheres are lodged in the vascular plexus adjacent to or within the tumor. The microspheres have a high mechanical and chemical stability and are not degraded and will remain permanently in the case of glass or resin microspheres. The term radio**embolization** is somehow a misnomer because the treatment effect mostly relies on radiation with little contribution of the disruption of blood supply due to the embolism caused by the microspheres. Unlike most of the other transarterial treatments (*e.g.* transarterial embolization, TACE), the clusters of microspheres do not cause an important micro-embolic effect.

1.5.4 Physical properties of yttrium-90

The mechanism for tumor irradiation in SIRT is β particle radiation. By far the most used device for SIRT are yttrium-90 containing microspheres. Ytterbite is a mineral that has been discovered for the first time in 1787 in a mine near Ytterby in Sweden. This mineral comprises several elements; one of them was a formerly unknown metal, which was named yttrium. Commercially, yttrium-90 is produced either by neutron bombardment of yttrium-89 (^{89}Y) in a nuclear reactor or by a chemical separation from the parent isotope strontium-90 (^{90}Sr).

Yttrium-90 has a physical half-life of 64.0416 ± 0.0312 hours (2.6684 ± 0.0013 days)[4], which means that 94% of the energy will be delivered within 11 days after administration. Yttrium-90 mainly disintegrates by β^- emission to stable zirconium-90 (^{90}Zr) (see figure 1.9) with some other low-probability decay pathways [97]:

1. In 99.983% of decays, an electron is emitted with a maximum kinetic energy of 2278.7 keV, and an average energy of 926.7 keV ± 0.8 keV.
2. In 0.0000014% of decays, there is an emission of a 2186 keV gamma ray.
3. In 0.017% of decays, an electron is emitted with a maximum energy of 519.1 keV, and an average energy of 163.7 keV. In this case, the zirconium-90 nucleus is left in an excited state with an energy of 1760.7 keV above the ground state. Sometimes, the de-excitation process to the stable state of zirconium-90 via internal conversion results in an internal pair production (e^- and e^+) with a very small branching ratio of (31.86 ± 0.47) $\times 10^{-6}$. The resulting positron-annihilation photons have been successfully used for ^{90}Y-TOF-PET imaging and quantification [96, 98, 99].

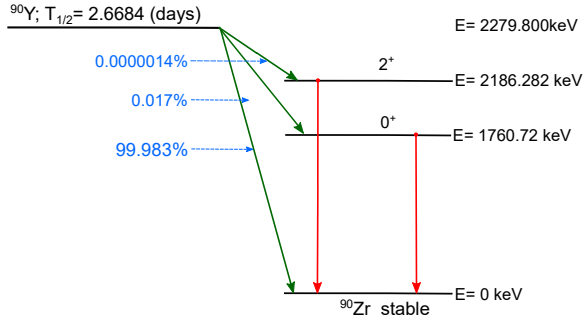

Figure 1.9: Yttrium-90 decay scheme

[4] http://www.lnhb.fr/nuclides/Y-90_com.pdf

As mentioned before, yttrium-90 decay virtually does not include primary gamma emission, but like many other β emitters, secondary high energy photons are created by bremsstrahlung interaction of the β particles along their pathway within the tissue. This emitted bremsstrahlung has a broad energy spectrum from 20 keV to 2.278 MeV. Some portion of these photons will travel through the patient body and can be imaged using a SPECT camera to verify the deposition of the microspheres after treatment witch is called bremsstrahlung emission computed tomography (BECT). Due to its broad energy spectrum, quantification of these images is challenging [100] and requires advanced MC simulation. So, for post-treatment dosimetry, modern TOF-PET images are considered superior compared to BECT.

As outlined above, the range within soft tissue of electrons emitted by yttrium-90 is low; the average and maximum soft tissue penetration of the electrons are 2.5 and 11 mm, respectively. A typical hepatocyte, the main functional cell of the liver, has a polygonal shape with a side of approximately 25-40 µm [101]. So, the approximate average penetration of yttrium-90 is 60-100 cells, and the maximal range of the electrons is about 275-450 cells. Therefore, the kinetic energy of the electrons emitted by each lodged microsphere is deposited in a limited number of surrounding cells. So, this so-called cross-fire effect, to some extent, can be beneficial for bulky tumor but most of the energy deposits with very high peaks in the very close vicinity of the sphere. As a result, the absorbed dose in SIRT is considered to be much less homogeneous compared to EBRT.

1.5.5 SIRT dosimetry

1.5.5.1 MIRD formalism for SIRT

Because of the unique characteristics of the microspheres, the MIRD schema (see section 1.3.2.1) can be tailored for SIRT by using some assumptions:

1. Permanent trapping of the microspheres in the precapillary arterioles, which simplifies the calculation of the cumulated activity.
2. Complete deposition of the energy of the IA within each catheter tip position in a pre-defined perfusion territory, which implies that $S(r_k \leftarrow r_h) = 1$ for h=k for perfusion territory and otherwise $S(r_k \leftarrow r_h) = 0$.

Thus, an activity of 1 GBq delivers about 49.38 Gy per kg of soft tissue:

$$\begin{aligned}\bar{D} &= \frac{\text{energy}}{\text{mass}} = \frac{\int_0^\infty \dot{D}dt}{\text{mass}} = \frac{\int_0^\infty A_t \bar{E} dt}{\text{mass}} = \frac{\bar{E} \times \int_0^\infty A_0 \times e^{-\ln(2)/T_{1/2}t} dt}{\text{mass}} = \frac{\bar{E} \times A_0 \times T_{1/2}}{\text{mass} \times \ln(2)} \\ &= \frac{(926.7[\text{keV}] \times 1.602 \times 10^{-16}[\text{J}]/[\text{keV}]) \times (1 \times 10^9[\text{Bq}]) \times (64.0416 \times 60^2[\text{sec}])}{1[\text{kg}] \times \ln(2)} \\ &= 49.38 \frac{\text{J}}{\text{kg}}\end{aligned} \tag{1.5}$$

Where $\bar{D}$ and $\dot{D}$ are the mean dose and dose rates, respectively; A_0 and A_t are the activity within the VOI at the time administration and at time t, respectively; $\bar{E}$ is the average energy of the β; and $T_{1/2}$ denotes the half-life of yttrium-90.

So, in each VOI, a mean absorbed dose could be derived by applying the calculated conversion factor:

$$\bar{D}_{VOI[Gy]} = 49.38[Gy.kg/GBq] \times \frac{\text{activity in the VOI [GBq]}}{\text{mass of the VOI [kg]}} \tag{1.6}$$

1.5.5.2 Partition model for SIRT

The partition method (PM) is based on the MIRD formalism that has been redesigned for SIRT and estimates the absorbed dose by assuming a uniform absorbed dose in tumor(s) and non-tumoral compartments of the LPT. Hence, on top of the assumptions discussed in the previous subsection, it is assumed that in each LPT, the tumor(s) and non-tumoral tissue receive a uniform absorbed dose which can be defined by the fractional activity uptake of each compartment:

$$D_{\text{comp}} = 49.38 \times \frac{\text{IA} \times FU_{\text{comp}}}{V_{\text{comp}}} \tag{1.7}$$

$$\text{where, } FU_{\text{comp}} = \frac{A_{\text{comp}}}{A_{\text{total}}}, \tag{1.8}$$

where, D_{comp}, FU_{comp}, V_{comp}, and A_{comp} are absorbed dose, fractional uptake, volume and activity of the compartment and A_{total} is the total IA.

For practical reasons, the fractional uptake in each compartment is usually derived from the ratio between activity concentration between tumor compartment(s) and non-tumoral compartment, which is called tumor to normal tissue activity concentration ratio (T/N ratio):

$$T_j/N = \frac{\frac{A_{T_j}}{V_{T_j}}}{\frac{A_{NT}}{V_{NT}}} \Rightarrow \frac{A_{T_j}}{A_{NT}} = T_j/N \times \frac{V_{T_j}}{V_{NT}} \tag{1.9}$$

Then,

$$\begin{aligned} FU_{T_j} &= \frac{A_{T_j}}{\sum_i (A_{T_i}) + A_{NT}} \\ &= \frac{\frac{A_{T_j}}{A_{NT}}}{\sum_i (\frac{A_{T_i}}{A_{NT}}) + 1} \\ &= \frac{T_j/N \times \frac{V_{T_j}}{V_{NT}}}{\sum_i (T_i/N \times \frac{V_{T_i}}{V_{NT}}) + 1} \\ &= \frac{T_j/N \times V_{T_j}}{\sum_i (T_i/N \times V_{T_i}) + V_{NT}} \end{aligned} \tag{1.10}$$

And

$$\begin{aligned} FU_{NT} &= 1 - \sum_j FU_{T_j} \\ &= 1 - \sum_j \frac{T_j/N \times V_{T_j}}{\sum_i (T_i/N \times V_{T_i}) + V_{NT}} \\ &= 1 - \frac{\sum_j (T_j/N \times V_{T_j})}{\sum_i (T_i/N \times V_{T_i}) + V_{NT}} \\ &= \frac{V_{V_{NT}}}{\sum_i (T_i/N \times V_{T_i}) + V_{NT}} \end{aligned} \tag{1.11}$$

Where T_j/N, A_{T_j}, V_{T_j}, and FU_{T_j} denote the tumor to normal activity concentration ratio, total activity, volume and fractional uptake of the tumor T_j, and $A_{T_{NT}}$, $V_{T_{NT}}$, and $FU_{T_{NT}}$ denote the total activity, volume and fractional uptake of the non-tumoral compartment.

1.5.5.3 Voxel level dosimetry

In voxel level dosimetry, the reconstructed activity map is converted into an absorbed dose distribution from which the dose inhomogeneity can be computed on a small scale. To compare different SIRT procedures, this spatial dose information is usually represented by a dose-volume histogram (DVH), which is often transformed into cumulative dose-volume histogram (cDVH) [102].

A DVH describes a frequency distribution of dose values within a pre-defined VOI, *e.g.* target volume or any other critical structure. A cDVH summarizes the absorbed dose distribution within a VOI. This graph visualizes the fraction of the total defined volume (*e.g.* tumor, non-tumor and total liver/LPT) that receives a specific minimum absorbed dose.

Dose distribution is usually interpreted by using different DVH parameters like $\mathrm{Dx}_{\mathrm{VOI}}$ (minimum absorbed dose to x% of the VOI voxels, *e.g.* $\mathrm{D50}_{\mathrm{NTV}}$), or $\mathrm{Vx}_{\mathrm{VOI}}$ (percentage of the VOI receiving at least x Gy, *e.g.* $\mathrm{V120}_{\mathrm{TV}}$), or mean absorbed dose ($\mathrm{D}_{\mathrm{VOI}}$; area under the curve of DVH). Radiobiological models are used to find the relation between these DVH parameters and clinical outcome. The aim is to quantify the biological effect of dosimetry parameters on an expected outcome like tumor control (tumor control probability; TCP) or normal liver toxicity (normal tissue complication probability; NTCP).

Different methods for converting activity maps to dose distributions have been introduced in the literature: **(a)** MC simulation, which reflects tissue density heterogeneity and random interaction between particle and tissue, **(b)** dose-point kernel, which considers cross-fire effects, and **(c)** local deposition method, which is simply multiplying each voxel activity by a conversion factor.

Direct Monte Carlo: When images of the attenuation coefficients and of the activity distribution are available, MC simulation (*i.e.* a general model of particle transport accounting for random interactions with the body) can be used to compute an accurate patient-specific absorbed dose distribution. Monte Carlo codes are available, like Electron Gamma Shower (EGS), Monte Carlo N-particle (MCNP), PENetration & Energy Loss of Positrons and Electrons (PENELOPE), FLUktuierende KAskade (FLUKA), and finally Geant4 Application for Tomographic Emission (GATE) (which is more tailored for nuclear medicine imaging) [103].

Dose point kernel convolution: MC simulation is complex and computationally time-consuming. Because the liver is a uniform medium, the conversion could be speeded up by employing MC to pre-compute the effect of the activity in a voxel to the other voxels and apply it as convolution to all the liver voxels. The result of the simulation is a convolution kernel that describes the mean absorbed dose to a target voxel per radioactive decay within a source voxel.

Generally, the main drawback of this model is neglecting the gradients of the density of the voxels which could be very important in case of substantial density heterogeneity (*e.g.* air-soft tissue or bone-soft tissue) which is not the case in SIRT; where liver and surrounding tissues have a more or less similar density.

There are some dose point kernels publicly available for yttrium-90 in soft tissue (see figure 1.5) [70, 104]. MIRD Pamphlet 17 defined voxel-based dosimetry using this method [105].

Local deposition method: In the local deposition model, it is assumed that the energy of the β particles released by the microspheres in each voxel is deposited within the same voxel. Here, the absorbed dose in each voxel can be easily determined by multiplying the activity or activity concentration by a constant scale factor. It is claimed that this method is even more accurate than dose point kernels. Because of the limited

resolution of the gamma cameras, the measured activity is already blurred a lot, which spreads the dose out similarly or even more than the convolution with the dose point kernels [106]. Mikell *et al.* found that for a voxel size of a typical SPECT image, MC, dose point kernel and local deposition model obtained nearly identical results [107].

1.5.6 Microspheres available for clinical SIRT

In the previous section, the properties of the radionuclide contained within the microspheres have been discussed. Here, different microspheres available for use in patients are described. As discussed in section 1.3, an ideal therapeutic agent in SIRT should have the following characteristics:

- a density close to blood density for optimal distribution
- a spherical shape to overcome cluster formation within peripheral arteries
- uniform size of 25-30 μm which is a fundamental characteristic for trapping within tumor precapillary arterioles with an average diameter of 15-35 μm
- easy labeling with β emitters with sufficient specific activity (activity per sphere) and low free radionuclide. No release of the radionuclide from the microspheres. No impurities.
- no long-lived radionuclide contaminants.
- biocompatibility and in vivo stability and retention until complete decay.

There are two different categories of microspheres commercially available for SIRT: **(1)** microspheres labelled with holmium-166 (QuiremSpheres- Quirem Medical B.V., Deventer, Netherlands) **(2)** resin (SIR-spheres - SIRTeX Inc, North Sydney, Australia) and glass (TheraSpheres- Boston Scientific, Natick, MA, USA) microspheres labelled with yttrium-90. In addition to these commercial devices, some other radionuclides, including phosphor-32 (^{32}P) [108], rhenium-188 (^{188}Re) [109], iodine-131 (^{131}I) [110], and praseodymium-142 (^{142}Pr) [111] have been developed, but they have not received CE market approval yet. Table 1.2 provides information about these three microspheres together with technetium-99m macro-aggregated albumin ([^{99m}Tc]Tc-MAA), which is usually used for treatment simulation (see section 1.7.3).

Glass and resin microspheres are very stable with virtually no degradation during patient life; for the resin microspheres, a level of up to 50 kBq/L in blood and urine has been reported; a six week in vitro discharge of less than 0.13% was reported for the glass microspheres. On the other hand, QuiremSpheres degrade more during the patient's life; its stability is around 93.5% in human plasma after 72 h.

When comparing QuiremSpheres with glass or resin microsphere, the difference in half-life is an important parameter. The $T_{1/2}$ for holmium-166 and yttrium-90 is quite different (26.8 versus 64.1 hours), leading to higher initial dose rate for holmium-166 when giving a similar absorbed dose, which could have a radiobiological impact.

One of the main differences between the resin and glass microspheres is the difference in the activity per sphere (specific activity), which is approximately 50 times higher for the glass microspheres. This means a ∼50 times lower number of microspheres will be administered into the patient for an equivalent absorbed dose. This higher number of administered resin microspheres can result in a mild to moderate embolic effect, which potentially enhances the risk of stasis during administration. Sometimes this phenomenon could also result in reflux and/or a large residual activity in the vial because there is not enough vascular space in the perfused volume to administer all prescribed spheres. On the other hand, the resin microspheres will produce a more uniform irradiation which is considered as an advantage in some circumstances. Recently, the FLEXdose delivery program was introduced for the resin microspheres to offer a variety of ordering options. In this new delivery system, rather than a fixed vial activity (3.6 GBq), 4 other activity levels are provided for 1-, 2-, 3- or 4- day pre-calibrated delivery choices. This directly has an influence on the specific activity of the microsphere and as a result the number of administered microspheres for the same amount of activity.

Table 1.2: Characteristics of different microspheres and [^{99m}Tc]Tc-MAA particles

Name	[^{99m}Tc]Tc-MAA	SIR-spheres	TheraSpheres	QuiremSpheres⋆
radionuclide	technetium-99m	yttrium-90	yttrium-90	holmium-166
max β emission (Mev)	-	2.28(100%)	2.28(100%)	1.77 (49%), 1.85 (50%)
gamma emission (keV)	141 keV (89%)	2 × 511 keV (32E-4%)	2 × 511 keV (32E-4%)	80.6 (6.8%)
half-life (hours)	6	64.1	64.1	26.8
mean tissue penetration	-	2.5 mm	2.5 mm	3.2 mm
imaging	SPECT	BECT or PET	BECT or PET	SPECT or MR
radionuclide location	surface	surface	matrix	matrix
matrix material	MAA	Resin (polymer)	Glass	Poly (L-lactic acid) (PLLA)
biodegradability	biodegradable	non-biodegradable	non-biodegradable	biodegradable
density (gr/ml)	1.1	1.6	3.2	1.4
mean diameter (range) µm	31.3 [10, 100]	32 [20, 60]	25 [20, 30]	30 [15, 60]
specific activity (Bq/sphere)	-	50⋆⋆	2500	450
available activity (GBq)	as needed	3.6⋆⋆	from 3 to 20	maximum 3 vials (each up to 12 GBq)
number of instilled particles	0.15 million	50 million	1.2 million(3GBq)	33 million
embolic effect	mild	mild-moderate	mild	mild-moderate
CE mark	-	2002	2014	2015

⋆ QuiremScout utilizes the same microsphere as QuiremSpheres with lower specific activity for treatment simulation instead of the [^{99m}Tc]Tc-MAA. It received CE mark in 2019.

⋆⋆ recently introduced FLEXdose: 5 different activity levels; 10.0, 7.8, 6.0 , 4.6, and 3.6 GBq whether the vial is 4-, 3-, 2- or 1-day pre-calibrated or delivered on calibration day

It has been shown that the optimum size and specific activity for each microsphere is something between the resin and glass design [112], which has been the target in the design of the new generation of the microspheres (QuiremSpheres). Besides, it seems reasonable (although not yet confirmed in literature) that fewer infused microspheres with higher specific activity is favored to cure small tumors. On the other hand, a larger number of spheres ensures sufficient irradiation coverage for bulky tumors. Besides some side-effects related to the embolic effect of the resin microspheres, recent studies showed comparable OS of the resin and glass microspheres for treating patients suffering from different stages of HCC [113] and mNET [114].

Also, some studies showed inconsistent non-tumoral distribution patterns; a lower number of administered glass microsphere provides less uniform irradiation, which produces very different microscopic radiobiology effects compared to the resin microspheres. This results in very different non-tumoral liver safety and tumor efficacy dose thresholds published for the glass and resin microspheres [73].

It is worthwhile to mention that one should be careful about the shelf-life of the glass microspheres when interpreting these results. The shelf-life is 1 and 15 days for the resin and glass microspheres, respectively. This indicates that the specific activity of the resin microsphere is fixed in different treatments, while the specific activity of the glass microsphere decreases based on the physical half-life of yttrium-90. Consequently, if an amount of glass microspheres was injected into a patient after 15 days, the specific activity would be around 51 Bq, which is comparable to the fresh resin microsphere.

Another variation between these two kinds of microspheres is the difference in density. The glass spheres have a higher density (3.6 gr/ml), which is substantially higher than blood density (1.05 gr/ml) and is assumed to result in a more non-uniform distribution compared to the resin microsphere with a density of 1.6 gr/ml. This non-uniformity could conceivably lead to non-uniform lodging in tumor vascular bed [115]. Additionally, the density of glass microspheres is higher than that of protein-based [^{99m}Tc]Tc-MAA particles (1.1 gr/ml), which are used for the simulation of the treatment. Therefore, this could be a reason for potential discrepancies between [^{99m}Tc]Tc-MAA and resin microsphere distribution patterns [116].

Also, due to the lack of considerable gamma-emission and the absence of free yttrium-90, which could transfer to body fluid system, patients can be sent home shortly after treatment with minimal precautions compared to many other radionuclide therapies. On the other hand, having no primary gamma radiation makes imaging of yttrium-90 distribution inside the body challenging.

1.6 Clinical trials, certifications, and guidelines

1.6.1 Certifications

Glass and resin microspheres obtained FDA approval for treating unresectable HCC in 1999, and for treating unresectable liver metastases in 2002, respectively. They also received European conformance (CE) certification in 2006 and 2002, respectively. From this point, this modality grew fast and has been used widely to treat liver malignancies in different clinical settings in the past two decades.

1.6.2 randomized controlled trials

A number of RTCs have evaluated SIRT for the treatment of various liver cancers. Table 1.3 provides information about selected RTCs, with various endpoints studied such as QoL, PFS and OS. None of these large RTCs did showed a statistically significant benefit for the primary endpoint over the control treatment. But the tumor response rate and treatment-related adverse events and rate of progression in the liver were found to be better for SIRT arms, in various trials. Questionable patient selection and IA prescription methods are frequently considered as the main reasons for these trials to be negative [117].

Table 1.3: Selected large RTCs for the resin microspheres, comparing the treatment results of SIRT (+chemo) with chemo alone

trial	NTC number	patient number	tumor type	arm1 SIRT(+chemo)	arm2 (chemo)	primary outcome measure	secondary outcome measures
[118]	NCT00739167	134	HCC	SIRT (n=68)	TACE (n=66)	**QoL:** improvement of Qof in many features	-
SIRveNIB [119]	NCT01135056	360	HCC	SIRT (n=182)	sorafenib (n=178)	**OS:** 8.8 vs. 10.0 months (p=0.36); **HR (arm1 vs. arm2):** 1.1 (95% CI, 0.9-1.4; p= 0.36)	**PFS:** 6.3 vs. 5.2 months (p=0.01); **TRR:** 23.1 vs. 1.9% (P<0.001)
SARAH [24]	NCT01482442	380	HCC	SIRT (n=184)	sorafenib (n=196)	**OS:** 8.0 vs. 9.9 (p=0.18); **HR (arm1 vs. arm2):** 1.15 (95% CI, 0.94-1.41; p= 0.18)	**PFS:** 4.1 vs. 3.7 months (p=0.76); **TRR** (complete or partial): 36 vs. 23%
SORAMIC [120]	NCT01126645	424	HCC	SIRT+ sorafenib (n=216)	sorafenib (n=208)	**OS:** 12.1 vs. 11.4; **HR (arm1 vs. arm2):** 1.01 (95% CI, 0.81-1.25; p= 0.9529)	**HR in patients without cirrhosis:** 0.46 (P=0.02)
SIRFLOX [33]	NCT00724503	530	mCRC	SIRT+ mFOLFOX6 (n=267)	mFOLFOX6 (n=263)	**PFS:** 10.7 vs. 10.2 months (P=0.551); **HR (arm1 vs. arm2):** 0.93 (95% CI, 0.77-1.12; p= 0.43)	**ORR:** 76.4 vs. 68.1 % (P<0.05)
FOXFIRE [121]	-	364	mCRC	SIRT+ mFOLFOX6 (n=182)	mFOLFOX6 (n=182)	**OS:** 18.8 vs. 29.4 months (p=0.712)	**PFS:** 9.9 vs. 9.5 months ; **ORR:** 67.6 vs. 61.0%
FOXFIREGlobal [121]	NCT01721954	209	mCRC	SIRT+ mFOFOX (n=105)	mFOLFOX (n=104)	**OS:** 25.9 vs. 25.0 months (p=0.43)	**PFS:** 11.8 vs. 11.2 months (P<0.05)

TRR: tumor response rate; **ORR:** overall response rate, **CI:** confidence interval

A combined analysis of FOXFIRE, SIRFLOX , and FOXFIRE-Global trials (549 patients receiving chemotherapy and SIRT; 554 patients receiving chemotherapy alone) showed that adding SIRT to the first-line chemotherapy for patients with mCRC did not improve the outcome regarding the primary endpoint, OS (22.6 versus 23.3 months; p-value=0.61), with hazard ratio (HR) 1.04 (95% CI, 0.90-1.19; p-value=0.61) [121]. Objective response over the complete study duration was in favor of the SIRT arm (72% versus 63%; p-value=0.0012). The study concluded that to further define the role of SIRT in mCRC, careful patient selection and studies investigating the role of SIRT as consolidation therapy after chemotherapy were needed.

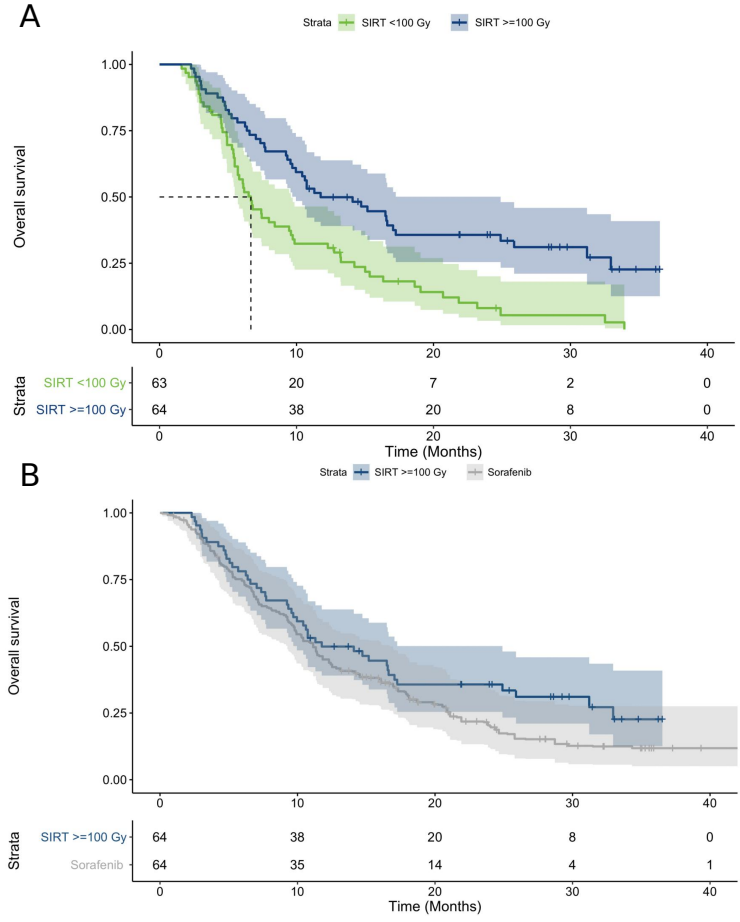

*Figure 1.10: Adapted from [122], with permission: Kaplan-Meier curves [**A**] OS of the patients in the SIRT arm for whom dosimetry was available (n=127) with tumor dose break down at the 100 Gy level. [**B**] matched comparison of OS between patients in the SIRT arm with documented dose >100 Gy to a matching set of patients from the sorafenib arm. This shows that when the tumor absorbed dose is sufficient, SIRT can lead to a survival benefit compared to sorafenib.*

The role of SIRT in multi-focal HCC has been the subject of the SARAH, SIRveNIB, and SORAMIC trials. These trials compared SIRT and sorafenib, which is the standard of care chemotherapy for advanced HCC. There was no difference in OS, but SIRT had fewer attributable high-grade adverse events with improved QoL. Some further investigations pointed out that the non-dosimetric prescription method is one of the primary sources of failure of these trials [123, 124]. A report [122] showed that in the group of patients

in the SARAH trial with reported pre-treatment tumor dose estimation (n=127), OS was considerably longer in patients with a predicted tumor dose (based on [^{99m}Tc]Tc-MAA-SPECT) of more than 100 Gy compared to patients with low predicted tumor dose. Also, when comparing patients in the SIRT arm with a predicted tumor dose of more than 100 Gy to a matched comparison sub-group of the sorafenib arm, the median OS was significantly higher for SIRT arm (22.5 versus 17.9 months), the HR was 0.74 (95% CI: 0.51-1.04, p-value=0.09). Median PFS is also in favor of the SIRT arm with a predicted tumor dose greater than 100 Gy (10.05 versus 6.91 months). Figure 1.10 shows the survival curves for these groups of patients in the SARAH trial.

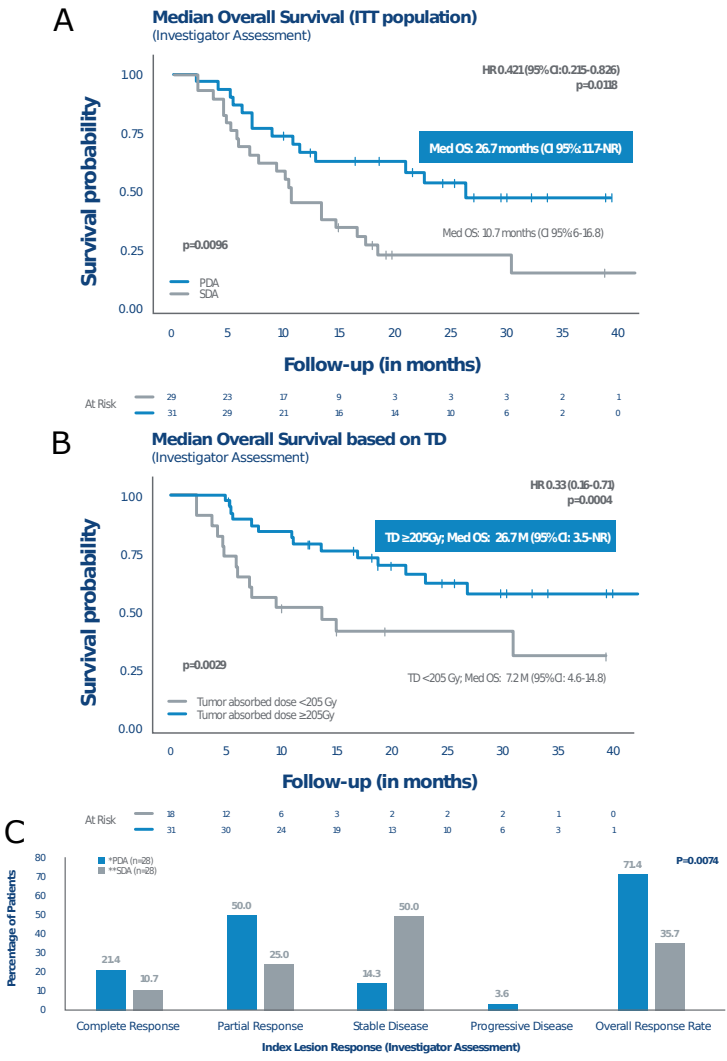

Figure 1.11: Initial results of DOSISPHERE-01 trial [125] from `www.bostonscientific.com`*: Kaplan-Meier curves [**A**] OS for the patients treated with IA prescription based on tumor dose is significantly higher than patients with standard IA prescription. [**B**] OS after SIRT according to tumor dose break down shows a better survival for patients who received more than 205 Gy than in patients with a tumor dose below 205 Gy. [**C**] EASL tumor response at three months in dosimetric arm (PDA) and standard arm (SDA).*

DOSISPHERE-01 is another RTC[5] which compared glass microsphere treatments with optimized individualized tumor dosimetry with standard treatment planning in unilobar HCC patients with at least one tumor larger than 7 cm [126]. As illustrated in figure 1.11, the initial results showed that prescribing an IA based on a predicted tumor dose of at least 205 Gy to the index lesion ("dosimetric arm") compared to classical MIRD-based lobar treatment ("standard arm") leads to a better median OS (26.7 versus 10.7 months, p-value=0.0096); HR:0.42 (95% CI, 0.215-0.826, p-value=0.012). The study also showed a better OS for those patients with an actual tumor absorbed dose of more than 205 Gy comparing to the patients with a lower tumor dose (26.7 versus 6.0 months, p-value=0.0029); HR:0.34 (95%CI: 0.15-0.74, p-value=0.0063). This study has as primary end point the response rate of the index lesion at month 3 according to European Association for the Study of the Liver (EASL) criteria. The overall response rate was higher in the dosimetric arm than in the standard arm (71.4% versus 35.7%; p-value=0.0074). The study also observed higher complete and partial responses and less stable or progressive disease in the dosimetric arm compared to the standard arm.

1.6.3 Large-scale international, national, and single center studies

Here, a few international (European), national (the UK and US), and single-center (Chicago) studies providing result in large cohorts are described:

- **ENRY (European Network on RE with ^{90}Y Resin Microspheres):** A European evaluation of the survival after resin microsphere SIRT in 325 HCC patients reported a median OS of 12.8 months which varied significantly by disease stage (see figure 1.12). The authors claimed that SIRT provided a substantial impact on the disease course, including in patients with advanced disease with few treatment options available [127].
- **UK National program for SIRT for mCRC:** This study evaluate the current SIRT practice (both resin and glass microspheres) in UK [128]. The results showed a median OS of 7.6 months and a median PFS of 3 months in 399 patients. They also reported a high-grade adverse event rate of 8%.
- **MORE study (US experience):** MORE was a retrospective analysis of the outcome of 606 patients with unresectable mCRC treated with resin microspheres. A report of this long-term follow-up study after the death of 574 patients showed a median OS of 10.0 months. The authors claimed that this was evidence of a favorable survival benefit [129].
- **A message from Chicago:** Northwestern Memorial hospital is one of the leaders in implementing SIRT in liver cancer management. In 2014, the treatment team reported their twelve-year experience with SIRT for mCRC in 214 patients. They reported a median OS of 10.6 months after first SIRT procedure [130]. They also reported their 15-year experience of SIRT in 1000 HCC patients [131]. In Child-Pugh A patients, censored OS for BCLC A, BCLC B, BCLC C were 47.3, 25.0, and 15.0 months, respectively. In Child-Pugh B patients, censored OS for BCLC A, BCLC B, BCLC C were 27, 15.0, and 8.0 months, respectively. About 5% and 11% of the patients developed grade 3/4 albumin and bilirubin toxicities. Based on experience in 1000 HCC patients, SIRT was adopted as a primary treatment for HCC in their center in 2018 .

These studies show that SIRT can be considered as a promising alternative in selected patient groups.

[5] https://clinicaltrials.gov/ct2/show/NCT02582034

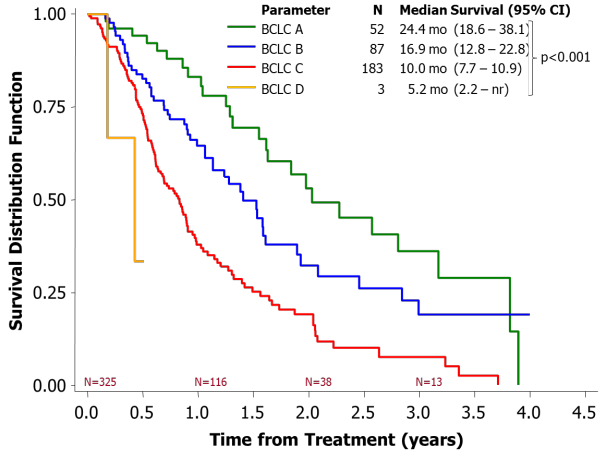

Figure 1.12: Adapted from [127, 132], with permission: Kaplan-Meier OS curves of patients with HCC treated with resin microsphere SIRT stratified by BCLC stage.

1.6.4 SIRT in the guidelines

Several prospective and retrospective studies suggested SIRT as a safe and effective alternative for the management of hepatic malignancies. This was reflected in different guidelines:

- **ESMO- European Society for Medical Oncology (HCC), 2018:** This guideline mentioned the use of SIRT in some circumstances: patients with liver-confined disease and excellent liver function who could not be considered for TACE or systemic therapies. For patients with small tumors waiting for liver transplantation, SIRT was suggested to be used instead of TACE [133].
- **ESMO (mCRC), 2016:** SIRT was noted as a good alternative for potential resection candidates with a small future liver remnant. Also, it was mentioned that SIRT should be considered for patients with liver-only disease who are not a candidate for chemotherapy [32].
- **NCCN- (US) National Comprehensive Cancer Network (HCC), 2017:** SIRT was mentioned as an alternative treatment for unresectable HCC [134].
- **NICE- (UK) National Institute for Health and Care Excellence (HCC), 2013:** SIRT was mentioned for patients with unresectable liver-predominant disease with a good liver function who are not suitable for ablative treatments. NICE also encouraged clinicians to enter patients into ongoing RTCs [135].
- **AASDL- American Association for the Study of Liver Diseases (HCC), 2018:** Lobar SIRT was suggested for appropriate resection candidates with small future liver remnant; this technique has been shown to treat the tumor and at the same time enhance the healthy liver volume in the non-treated lobe. This treatment modality also was mentioned as an alternative for TACE for large tumors and in case of portal vein invasion [136].
- **APASL- Asian Pacific Association for the Study of the Liver (HCC), 2017:** SIRT was noted as an evolving and promising option that can complement or replace TACE [137].
- **EASL- European Association for the Study of the Liver (HCC), 2018:** The effect of SIRT in tumor control was described. Also, for patients who are not eligible for surgery, SIRT could be performed for patient preparation and to improve the liver condition to be reconsidered for hepatic surgery. This is mostly due to its ability to induce hypertrophy in the liver lobe contralateral to the target [18].

1.7 SIRT procedure

A typical outline of the SIRT diagnostic-therapeutic path includes several steps:

1. pre-therapy tumor evaluation
2. patient selection
3. pre-treatment work-up
4. clinical evaluation by multi-disciplinary tumor board and therapy planning
5. therapy procedure
6. post-treatment evaluation
7. follow-up and response monitoring

These steps will be discussed in detail in the following sub-sections.

1.7.1 Pre-therapy tumor evaluation

Liver metastases usually are diagnosed through non-invasive imaging at diagnosis or in the follow-up of a primary tumor. Further procedures to provide information on which the treatment plan will be based upon may include: additional imaging of the liver tumors (ultrasound, MR), imaging of other body parts (to identify primary tumors and/or metastases) including nuclear medicine imaging, biopsies, blood tests (liver function, other organ function, tumor marker).

Cross-sectional imaging, *e.g.* CT, MR, whole-body PET with 2-[^{18}F]fluoro-2-deoxy-D-glucose ([^{18}F]FDG), and somatostatin receptor PET with [^{68}Ga]Ga-DOTA-TATE, is usually performed before treatment to evaluate the volume and condition of liver parenchyma, the hepatic vasculature, intrahepatic tumor characterization, as well as presence and extent of extrahepatic lesions.

MR sequence	HCC	hypervascular metastases
T1	variable	hypointense
T1 (arterial)	heterogeneous hyperintense	hyperintense
T1 (venous)	iso- or hypointense	iso- or hypointense
T1 (delayed)	variable (most often hypointense)	hypointense
T2	variable (most often hyperintense)	marked hyperintense
DWI	slightly hyperintense	hyperintense

Table 1.4: Appearance of hypervascular liver tumors on different MR sequences

The vascularity of malignant lesions plays a critical role in SIRT. Hepatic malignancies generally receive their blood supply from the HA, but they can be either hypovascular or hypervascular when compared to the surrounding liver parenchyma. Liver metastases from colorectal carcinoma, lung, gastric, and breast cancers are commonly hypovascular, while hepatic metastases from kidney, thyroid, neuroendocrine cancers, and melanoma are usually hypervascular [138]. Following ablation (radiofrequency, microwave, and cryoablation), the tumors can be avascular, and post chemotherapy or chemoembolization, tumors can be isovascular [139].

– **Hepatic metastases and ICC:** For patients with metastatic tumors or intrahepatic cholangiocarcinoma, a baseline CT, usually using contrast-enhancement, is preferred for the assessment of some tumor types. In CT imaging, most of the hepatic lesions are slightly hypo-attenuating in non-contrast enhanced and portal phase enhanced imaging. A multi-phase ceCT can be used to assess tumor hypervascularity and washout; for better visualization, a late arterial phase for hypervascular and a portal venous phase for hypovascular tumors is preferred.
Also, [^{18}F]FDG-PET imaging may be performed for lesion detection [140]. A higher

signal in [^{18}F]FDG-PET can be examined to locate the intra- and extrahepatic malignancies, determine their size, discriminate viable tumor cells from a necrotic part and evaluate treatment response. The most common ways for automatic lesion definition on PET are thresholding using a fraction (*e.g.* 40 or 50%) of the maximum Standardized Uptake Value (SUV), adaptive thresholding, or applying a relative threshold after background subtraction [141].
Sometimes MR imaging is performed to evaluate liver metastases. Some of the hepatic metastases (*i.e.* hypervascular metastasis) show hyper- or hypointense signals on different MR sequences (see table 1.4).

- **HCC:** In patients with HCC, contrast-enhanced MR or CT is preferred for tumor evaluation, with MR being superior over CT [142].
  The MR examination generally consists of T1 and T2 and DWI. An increased signal in DWI reflects the hypercellularity of the tumor. Contrast-enhanced T1 and DWI are the most important MR sequences for HCC tumor assessment (see table 1.4).
- **mNET:** For patients with grade 1 or 2 mNET metastases, [^{18}F]FDG-PET is inferior due to low FDG-avidity in the majority of lesions. [^{68}Ga]Ga-DOTA-TATE is currently the best PET tracer for this tumor type.

1.7.2 Patient selection

SIRT is generally known as a well-tolerated treatment with a low frequency of serious adverse events [143]:

- post-embolization syndrome, which consists of **(1)** immediate short-term abdominal pain in 25% of the patients which caused by transient hepatic ischemia and is linked to a higher number of administered microspheres, **(2)** slight fever for several days in 5% of the cases, and **(3)** fatigue (in half of the patients) and mild nausea (in 20% of the patients) for up to 10 days after therapy.
- rare non-target radiation-related complication, like stomach or duodenal ulcers, cholecystitis, pancreatitis, abdominal wall pain (with even necrosis), due to dose deposition from microspheres that followed arterial branches into these sites.
- radioembolization-induced liver disease (REILD) due to irradiation and inflammation of the normal liver parenchyma.
- microsphere radiation pneumonitis due to substantial lung shunt.

Careful patient selection is imperative in SIRT to achieve a safe and efficient outcome. Patient selection for SIRT demands a multi-disciplinary investigation on two different levels: **(1)** initial clinical evaluation: the patient's general condition, physical examination, laboratory results, and imaging findings, and **(2)** analyzing the pre-treatment work-up result, using angiography, [^{99m}Tc]Tc-MAA-SPECT, and planar imaging. Hence, the ultimate confirmation of the eligibility of the patient for SIRT treatment will be after pre-treatment work-up.

Absolute contraindications for SIRT include:

- decompensated cirrhosis
- insufficient baseline liver function
- significant extrahepatic disease which determines the patient's prognosis
- a life expectancy of fewer than three months
- pregnancy
- any contradiction regarding intra-arterial treatment in general
- uncorrectable risk of activity accumulation in gastrointestinal tract based on vascular anatomy or [^{99m}Tc]Tc-MAA scan
- uncorrectable lung shunt fraction (LSF) leading to a dose of more than 30 Gy (single session) or 50 Gy (split session) based on the planar image after [^{99m}Tc]Tc-MAA injection
- history of prior external beam radiation therapy to the liver

Besides these absolute exclusive contraindications, some aspects should be considered for each patient to tailor the treatment process:

- tumor burden: excessive tumor involvement (*e.g.* more than 70% of the liver mass especially in diffuse bilateral involvement can be a relative contraindication.
- tumor hypervascularity: for tumor tumors with no hypervascularity, radiation segmentectomy is an option
- Bile duct occlusion or incompetent papilla (biliary stents or Whipple procedure)
- significant intractable or refractory ascites
- previous extensive chemotherapy

1.7.2.1 PVE dilemma: contraindication or indication?

PVE, resulting from a direct tumor invasion into the portal vein, is a significant concern in patients with HCC. It occurs in one-third of the patients. Compared to HCC patients without portal vein invasion, patients with PVE have shortened survival; *e.g.* when supportive care was provided, OS of 2 to 4 month was reported for HCC patients with PVE, which was shorter than 10 to 24 month OS in HCC patients without PVE [144]. Sorafenib is the current standard of care for these patients.

Previously, the existence of PVE was considered as a relative (sometimes absolute) contraindication to SIRT because of the high perceived risk of liver infarction or decompensation due to loss of arterial and venous flow. Recently, because of the limited microembolic effect, in particular of glass spheres, SIRT has been reported to be both safe and effective for patients with PVE, which can also result in re-vascularization of the portal vein [145]. When considering SIRT for these patients, detailed dosimetry, including absorbed dose to the PVE as an additional compartment, could be beneficial for patient selection, therapy planning, and treatment evaluation.

1.7.2.2 Considering the QoL and cost-benefit in patient selection

Generally, in oncology, treatments are evaluated in terms of efficacy (tumor respons, survial) and toxicity. Nevertheless, for up to 95% of the patients who have advanced cancer, the QoL is at least as important as the life expectancy, especially in a non-curative setting [146]. For example, a study comparing TACE and SIRT for HCC patients, concluded that SIRT resulted in a significant increase in several QoL features [118]. Besides QoL, in cost-effect comparison, SIRT has been shown to induce a lower total lifetime cost compared to sorafenib for HCC in the UK (£21,441 versus £34,050, respectively) and conventional transarterial chemoembolization in the US ($31,000 versus $48,000, respectively). Rognoni *et al.* suggested an expected global saving of about 7 million euro in 5 years by progressive increased utilization rates of SIRT over sorafenib [147].

1.7.3 Pre-treatment work-up

The first phase after identifying a patient as potential candidate for SIRT is the pre-treatment work-up, which will serve as the basis for the treatment planning. This consists of two essential imaging studies: **(a)** an angiography to investigate the gross vascular anatomy and to evaluate tumor perfusion. During this angiography, the sites where the catheter will be positioned in the arterial tree during microsphere injection are identified. In many cases, some vessels are embolized in order to isolate the arterial supply to the liver from other structures. This is often followed by a valuable new modality, dual-phase contrast-enhanced CBCT imaging showing the perfusion territory of each catheter position and indicating the hyper- or hypovascular nature of the tumors, **(b)** administration of [^{99m}Tc]Tc-MAA particles at each proposed catheter position followed by planar imaging and SPECT/CT to predict the intra- and extrahepatic distribution of the microspheres. The combination of [^{99m}Tc]Tc-MAA simulation and hepatic angiography can be used for:

- confirming the appropriateness of SIRT for the patient
- finding the best treatment strategy (bilobar, lobar, segmental, supra-selective)
- identifying the configuration of the liver-feeding vessels
- confirming the hypervascularity of the tumors by visual tumor blush on angiographic images and high density areas on CBCTs
- optimizing the catheter tip position and coiling to assure more favorable tumor coverage, optimal normal liver parenchyma sparing and minimal deposition of the activity in extrahepatic sites
- visualizing the potential shunt to the gastrointestinal tract via tiny accessory arteries using angiography, CBCT and [^{99m}Tc]Tc-MAA-SPECT/CT
- assessing the microsphere uptake in the tumors and non-tumoral liver parenchyma, which can serve as the basis for IA planning

Because rapid revascularization of these vessels can occur, the treatment team should try to perform the treatment as close as possible to the pre-treatment work-up to avoid unexpected extrahepatic activity uptake. Generally, this angiography aims to detect the best catheter tip position in the work-up and therapy session for maximal tumor coverage and sparing as much as possible the non-tumoral liver and extrahepatic sites. A contrast-enhanced CBCT is beneficial for identifying incomplete tumor perfusion and/or extrahepatic perfusion. CBCT imaging is used in 78% of the European centers to verify tumor coverage (67%), extrahepatic deposition assessment (5%), and extract volumetric information (30%) [85].

After careful analysis of the arterial perfusion and determination of the proper catheter position(s) during the angiography, with or without CBCT, [^{99m}Tc]Tc-MAA particles (with density and average size close to resin microspheres; see table 1.2) are administered slowly at the selected catheter tip positions matched to planned draining regions, to simulate the biodistribution of therapeutic microspheres.

Thereafter, the patient is transferred as quickly as possible to the nuclear medicine department, and without much delay (preferably within less than one hour [148]) a planar image and SPECT/CT are performed to determine the extent of activity deposition in organs at risks (non-tumoral liver tissue, lung, extrahepatic intra-abdominal sites), and tumor coverage. Sticking to this time-frame is important to avoid an overestimation of the LSF [148] and to a lesser extent to avoid free technetium-99m uptake in thyroid and stomach, which may result in a misinterpretation of hepatopulmonary and gastrointestinal shunting; activity uptake in thyroid and stomach can be suppressed by giving intravenous perchlorate [149]. Usually, a planar (anterior / posterior) scintigraphy of the trunk is performed to measure the LSF. To calculate the LSF, total counts inside regions of interest drawn over the lungs and the entire liver are combined using the geometric mean of the anterior and posterior views of the planar image. A planar-based shunt calculation (which is shown to overestimate the lung shunt [150–152]) is usually used for activity planning as described in section 1.7.4. If the observed LSF might be due to excessive [^{99m}Tc]Tc-MAA degradation (*e.g.* scan several hours after injection), a new simulation can be envisioned [153, 154].

However, the accuracy of the prediction made using [^{99m}Tc]Tc-MAA, is uncertain. Possible reasons for a mismatch between [^{99m}Tc]Tc-MAA and therapeutic microspheres are:

- the irregular shape of the [^{99m}Tc]Tc-MAA that is different from the therapeutic spheres
- the discrepancy between [^{99m}Tc]Tc-MAA and microsphere size and size distribution; the small [^{99m}Tc]Tc-MAA particles can go further in the vascular tree and the smallest fraction of the [^{99m}Tc]Tc-MAA size distribution can potentially pass through the liver capillary bed:
  - resin microspheres have a size range of 20 to 60 µm; more than 90% of the microspheres in the vial have a size between 30 to 35 µm.

  - for the [^{99m}Tc]Tc-MAA particles, ∼20% of them are smaller than 20 µm; ∼45% and ∼20% of them have a size in the range of [20, 30] and [30, 40] µm, respectively; and ∼15% of the particles are bigger than 40 µm [155].
- the number of simulation particles and the number of administered microspheres are markedly different, the number of administered resin microspheres is in the order of 300 times higher than the number of injected [^{99m}Tc]Tc-MAA particles
- the in vivo stability, in particular in the arterial tree with its high blood pressure, is much less for [^{99m}Tc]Tc-MAA than for therapeutic microspheres, with clinically significant impact on LSF if measured at several hours interval [148, 156]
- the infusion rate of [^{99m}Tc]Tc-MAA is operator-dependent and can be different from the microspheres administration rate
- catheter tip positioning can be different between simulation and therapy session
- catheterization close to an arterial bifurcation or small arterial branch [157], with preferential flow in one branch during simulation and in the other branch during treatment
- temporary vessel spasm during pre-treatment work-up
- extent of tumor burden [158] with better agreement on bigger tumors

On the other hand, the value of [^{99m}Tc]Tc-MAA simulation in SIRT treatment planning has been shown in several studies. Strigari and Flamen reported a good correspondence between [^{99m}Tc]Tc-MAA and resin microsphere distribution of 80% and 100% of the cases, respectively [75, 159]. This correlation was confirmed later by Kao *et al.* for tumor dose determination [160, 161].

1.7.4 Therapy planning

Based on the result of the pre-treatment work-up and treatment intent of the tumor board, treatment planning can be conceptually performed in different settings:

- **salvage setting:** SIRT performed in patients with liver-limited or liver-dominant tumors to prolong the time to tumor progression.
- **adjuvant or consolidation setting:** SIRT used in the first- or second-line together with a primary treatment (*e.g.* chemotherapy) to impact the few remaining cells.
- **neoadjuvant setting:** SIRT conducted prior to surgery in potential resection candidates. In some patients with small functional liver residual volume, practicing SIRT can induce contralateral liver hypertrophy. Plus, for patients initially unfit for surgery due to tumor extent, SIRT may be employed for downstaging the tumor. These two approaches aim to increase the possibility of resection.
- **curative setting:** In hypervascular tumors with potential super-selective catheterization (*i.e.* tumor(s) in a single small LPT), SIRT could be considered as a curative option. In this setting, [^{99m}Tc]Tc-MAA needs to confer a high tumor uptake/absorbed dose, near-complete tumor coverage, and limited pre-defined LPT without significant activity leakage. In cirrhotic HCC patients, this can be complemented with a liver transplantation, which can be considered as a complete cure.

Radiation pneumonitis is one of the most serious reported complications of SIRT, which may cause impairment of respiratory function and can be lethal. The general assumption to avoid radiation pneumonitis, adapted from EBRT, is to keep the mean lung dose below 30 Gy for a single treatment and below 50 Gy for the accumulated absorbed dose in multiple SIRT; in resin microsphere's package insert, instead of using a criterion based on the estimated lung absorbed dose, LSF is used to **(1)** reduce the prescribed IA by 20% and 40% when the LSF is between 10 and 15 % and between 15% and 20%, respectively; **(2)** consider SIRT contraindicated for patients with a LSF>20%. The current gold standard for predicting lung absorbed dose before treatment is planar

[^{99m}Tc]Tc-MAA scintigraphy without accounting for attenuation or scatter effects. However, it has been confirmed that this method is conservative and the resulting estimated lung absorbed dose exaggerates the real lung dose [162] due to tissue overlap, lack of attenuation correction and neglecting of differences in tissue density between lung and liver tissue, the use of an estimated lung mass instead of the actual mass of the lung [163], and time-dependent degradation of the [^{99m}Tc]Tc-MAA particles.

Historically, IA planning has been performed using pragmatic methods, which have been designed to be safe for an average patient with an average liver according to historical data. Consequently, the use of these pragmatic methods has produced a wide range of outcomes, from under-dosing the tumor to overdosing the non-tumoral liver. So, this approach can have a high risk of hepatotoxicity in patients with decreased liver volume because of surgical resection. These pragmatic methods have been criticized by experts for many years and have been replaced by more scientific and patient-tailored methods.

Currently, the number of centers performing patient specific IA determination is increasing. Some centers take into consideration the viability of tumor, patient condition, and a specific desired therapy outcome (*e.g.* tumor ablation, radiation segmentectomy, tumor down-staging, etc) by planning to meet a target dose to the tumor or not to exceed the safety limit of the non-tumoral liver dose. In calculating the absorbed dose, T/N ratio is one of the key parameters. An estimation of T/N ratio, which can be easily obtained from several regions of interest (ROIs) over the [^{99m}Tc]Tc-MAA-SPECT image, could give a first estimate of the selective accumulation of activity within the tumor. Some authors consider a ratio of 2.0 (or sometimes 1.0) as an predictor for therapy outcome [159, 164].

Voxelized dosimetry for IA prescription is still under investigation. In this method, one can verify the heterogeneity of absorbed dose in each compartment by analyzing some DVH parameters corresponding to an IA. Multi-modal voxelized dosimetry is in a research phase, which uses a combination of morphological and functional imaging and image processing techniques (*i.e.* image registration and segmentation) to extract clinical relevant data from images performed before treatment, and to simulate the irradiation and its heterogeneity within different defined VOIs (various tumors, LPT). This method still requires large trials to set optimized dose limits (*i.e.* explore dose-effect relationships), which could be different from patient to patient based on factors affecting the tumor compartment (tumor type, tumor stage) and factors affecting the non-tumoral liver compartment (presence of cirrhosis, liver function, previous therapies) and finally the aim of the treatment.

A patient-tailored IA prescription for each of the selected branches of HA is the art of balancing many aspects like patient condition (clinical, imaging and laboratory data), liver condition (*e.g.* previous radical chemotherapy or SIRT, liver cirrhosis), treatment goal (extension of overall survival, prolong the time to progression, tumor downstaging or reducing the tumor burden while preserving the functional capacity of non- tumoral liver parenchyma, or palliation of the symptoms), and tumor characteristics (tumor type, tumor load, tumor distribution, and anatomy of the tumor-feeding vessels). Several methods are outlined in guidelines, resin microsphere package insert, recommendations, and literature for an optimal IA calculation. A European questionnaire among interventional radiologist in 2018 reported that in 80 and 16% of the centers, the body surface area (BSA) and empirical methods are used for calculating the prescribed IA for resin microspheres [85]. Also, 36% of the centers practiced PM in their clinical workflow.

1.7.4.1 Empirical method

This method has been developed for resin microspheres in 1989 [165] and is currently abandoned. This is the crudest method as it prescribes a fixed IA which depends only on the tumor burden.

With the empirical method, a standard activity based on the tumor burden in the liver is recommended; for a tumor involvement of more than 50% of the liver, the IA is 3.0 GBq; for 25–50% tumor involvement, 2.5 GBq; and for less than 25% tumor involvement,

2.0 GBq. This activity must be decreased by 20% and 40% in the case of a LSF of 10-15% and 15-20%, respectively. To split the IA in the right and left lobe injection, it is proposed to administer 30% of the planned IA into the artery feeding the left lobe and the rest into the artery feeding the right lobe.

Disadvantages:

- Historically, this method was designed to choose the safest and most effective IA planning. Later, this technique was shown to expose patients to the risk of unnecessary REILD or tumor under-dosage. Kennedy *et al.* reported radioembolization-induced liver disease (REILD) in 28 of 680 RE treatments by employing resin microspheres. From these 28 treatments, 75% of the treatments were planned using the empirical method [166].
- It restricts the IA up to 3 GBq. In some patients, an IA of more than 3 GBq can be applied safely with a better tumor control.
- It determines the IA just by considering fractional tumor involvement, *e.g.* the actual size of the tumor and the liver are not taken into account. Also, the physician has no control over the dose in any VOI.
- Total calculated IA is divided into liver lobes based on their (assumed) volumes (not their tumor involvement or intralobar activity distribution); it is not designed for prescribing IA for other LPTs, *e.g.* liver segments.

1.7.4.2 BSA method

This pragmatic method, which prescribes an IA based on anthropometric parameters (patient weight and height) together with tumor load, was developed to overcome high toxicity, which was observed in a lot of patients when using the empirical method. In the BSA method, a hypothetical liver volume is derived based on the patient body surface area [167], which was used together with the lung shunt fraction and tumor burden to prescribe an IA:

$$\mathrm{IA}_{\mathrm{BSA}}[GBq] = \Big(\mathrm{BSA}[m^2] - 0.2 + (\text{tumor involvement})\Big) \times (\text{LPT volume fraction}) \times (\text{lung shunt modifier}), \tag{1.12}$$

where tumor involvement is the fraction of the tumor in the defined volume (liver or LPT, when the latter is used, this is called modified-BSA) and BSA is the body surface area of the patient in m^2 which is calculated using the Dubois formula [168]:

$$\mathrm{BSA}[\mathrm{m}^2] = 0.20247[\frac{m^{1.275}}{kg^{0.425}}] \times \mathrm{height}[\mathrm{m}]^{0.725} \times \mathrm{weight}[\mathrm{kg}]^{0.425} \tag{1.13}$$

Similar to the empirical method, it is advised to decrease this IA by using a lung shunt modifier of 80% and 60% in the case of a lung shunt fraction of 10-15% and 15-20%, respectively.

A modified version of BSA, in form of lookup tables, was used in SIRFLOX, FOXFIRE, and FOXFIRE-global trials [169], where similar to the basic BSA method, prescribed IA is increased in proportion to the BSA of the patient and reduced based on LSF. In basic BSA, prescribed IA is first increased linearly with tumor involvement; but in this more conservative approach, for a given body surface area of the patient and LSF, prescribed IA is first increased with the increase of tumor involvement from 0 to 50% but for a tumor involvement above 50%, it is gradually decreased (see figure 1.13).

Advantages:

- It is relatively simple and user-friendly.
- The method is moderately safe.

– There is a large historical dataset describing the clinical use of this method.

Disadvantages:

– This method estimates the size of the liver from the body surface area; the concept of this method is based on a moderate correlation (r^2=0.46) that has been found between the body surface area (BSA) and total liver volume in a study in 2002 [167]. The actual volume of the liver is readily measured from CT or MR images and can be used instead. With the availability of anatomical imaging techniques, subjecting patients to a pragmatic method to estimate the size of the liver is highly questionable.
– This method limits the IA to the patient body surface area; the essential component of the formula is body surface area (for a standard human, body surface area is 1.73 m^2); so, large patients with small liver receive a relatively high dose to the liver; for patients who had liver resection before, there is a high risk for liver toxicity [170, 171].
– The physician has no control over absorbed dose in the lungs and healthy liver tissue and tumor in each liver lobe/segment. It is not corrected for intrahepatic distribution of the microspheres (*e.g.* T/N ratio)
– Total calculated IA is divided over different defined VOIs based on their volumes (not their tumor involvement or therapy activity distribution). It is not optimal for patients with unilobar disease.

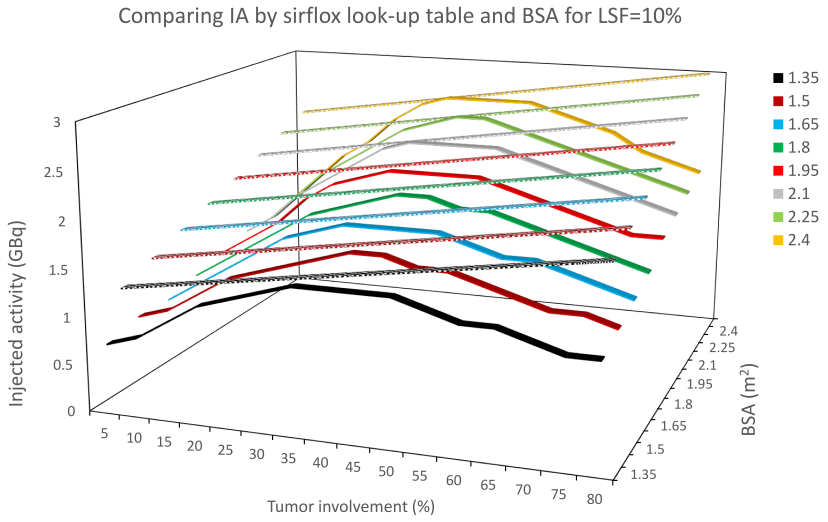

Figure 1.13: Representation of the injected activity recommended by the BSA method and SIRFLOX lookup table for an LSF of less than 10% as and different body surface area as a function of tumor involvement. For almost all bins, there is a reduction of injected activity for SIRFLOX look-up table compared to classical BSA.

Although there are some patient-specific parameters included in the BSA formula, nuclear medicine experts do not acknowledge this approach as an optimized treatment planning because it is based on anthropometric parameters and does not represent the patient-specific clinically relevant parameters, *i.e.* T/N ratio and the actual achieved doses. This may sacrifice the efficiency for safety for a large population of the patients. For example, Bernardini *et al.* observed no correlation between the BSA-based prescribed

IA and T/N ratio or tumor burden [172]. In a similar study, Lam *et al.* did not find a correlation between the BSA-based IA calculation and whole liver dose [171].

One general misconception is that "the BSA method is conservative, *i.e.* that it can only lead to under-treatment, never to over-treatment." BSA will be safe in many cases. Still, the assumption of correlation between the body surface area and liver weight may also result in liver toxicity, if the liver or tumor uptake deviate from the "average" patient (*i.e.* for tall patients with small liver, small cirrhotic liver, previous liver resection). Sangro *et al.* reported a 22.7% incidence of REILD for 75 patients treated with the BSA method (13% severe and 5% fatal) [173]. After adapting the prescription strategy (10-20% IA reduction), their subsequent 185 patients experienced a significantly lower REILD disease incidence of 5.4% (2.2% severe and 0.5% fatal; p-value=0.0001).

1.7.4.3 MIRD method

The MIRD method is the simplest dosimetric method. It takes into account the dose that is deposited by the IA in the targeted volume. Compared to the BSA method, in the MIRD method, the actual liver/LPT volume obtained from CT or MR is employed to control the mean absorbed dose to the total liver/LPT, by assuming a uniform activity distribution. So, it disregards the heterogeneity of the activity within the perfused territory and does not make a distinction between the tumoral and non-tumoral compartment. The MIRD calculation assumes that the activity uptake in the tumor and non-tumor compartment is identical and perfectly uniform. By implementing these assumptions into the basic MIRD methodology, one can calculate an IA corresponding to the desired absorbed dose to the total LPT:

$$\begin{cases} mIA_{\text{liver}} = \dfrac{D_{\text{planned,liver}} \times \text{mass}_{\text{liver}}}{49.87} \\ MIA_{\text{lung}} = \dfrac{D_{max,lung}}{49.87 \times LSF} \\ IA_{\text{MIRD}} = min(mIA_{\text{liver}}, MIA_{\text{lung}}) \end{cases} \tag{1.14}$$

where MIA_{lung}, mIA_{liver} and IA_{MIRD} are the maximum IA based on the safety limit of the calculated lung dose ($D_{max,lung}$) by assuming a lung mass of 1 kg, minimum IA based on the calculated liver dose ($D_{\text{planned,liver}}$), and IA based on the MIRD method, respectively.

Sangro *et al.* proposed an activity concentration of 0.8 GBq/l to the entire liver (tumoral and non-tumoral) which is correspondent to an approximate 40 Gy for the entire liver as the safety threshold to prevent REILD for resin microspheres, which can be used in MIRD method [173].

Advantages:

- Compared to the pragmatic methods (*i.e* empirical and BSA method), it is more "personalized" by providing control over clinically relevant parameters, *i.e.* the mean absorbed dose to the lungs and liver which has a more scientific explanation.
- It has no theoretical limits on the amount of IA.
- This dosimetry method does not rely on [^{99m}Tc]Tc-MAA as a surrogate of the microspheres within the liver parenchyma and tumor(s), which could be considered a limitation when a potential discrepancy between MAA and therapeutic microspheres is suspected (*e.g.* small or diffuse tumors).

Disadvantages:

- It considers a uniform therapeutic microsphere activity distribution within the liver and neglects the actual spatial dose distribution of an individual patient; it assumes that T/N ratio=1. So, the physician does not have control over the tumor and normal liver parenchyma absorbed dose.

The MIRD method is simple and has recently received a lot of attention. But the main weakness here is the fact that it does not take into account the preferential accumulation of microspheres in the tumor, which is the biological rationale for SIRT. The MIRD method implies a fixed T/N ratio of 1 for all lesions and all patients. The idea of incorporating the T/N ratio in the MIRD schema was the next step forward into the personalized dosimetry (see next section).

1.7.4.4 Partition method

The PM is a dosimetric approach that takes into account the differential uptake between the tumor and non-tumoral liver and was proposed in 1996 by Ho *et al.* [164]. This method assumes uniform uptake within each compartment. By applying this method, the physician has oversight over the tumor and non-tumor liver absorbed dose. This method is a considerable step forward in treatment planning. This method is also based on the MIRD model and has been validated in a series of studies [73, 102]. Although this method has been designated as the preferred method for treatment planning, it has some drawbacks like reliance on the T/N ratio calculation method and the correlation between [^{99m}Tc]Tc-MAA and therapeutic microsphere distribution.

In the PM, the first step is calculating some parameters like the tumor and non-tumoral liver volume (on CT, MR, baseline PET, or sometimes [^{99m}Tc]Tc-MAA-SPECT), T/N ratio, and LSF. The next step is calculating the fractional activity uptake of each compartment (*i.e.* tumor and non-tumor in each LPT):

$$\begin{cases} \mathrm{FU}_{\mathrm{non-tumor}} = (1 - LSF)\left(\dfrac{m_{\mathrm{non-tumor}}}{m_{\mathrm{non-tumor}} + \mathrm{T/N} \times m_{\mathrm{tumor}}}\right) \\ \mathrm{FU}_{\mathrm{tumor}} = (1 - LSF)\left(\dfrac{\mathrm{T/N} \times m_{\mathrm{tumor}}}{m_{\mathrm{non-tumor}} + \mathrm{T/N} \times m_{\mathrm{tumor}}}\right) \end{cases} \tag{1.15}$$

Here, $\mathrm{FU}_{\mathrm{non-tumor}}$ and $\mathrm{FU}_{\mathrm{tumor}}$ denote fractional accumulated activity in healthy liver and tumor. Then, by making a decision for a safe absorbed dose threshold for the lung and non-tumoral tissue and an absorbed dose criterion for an efficient treatment for the tumor, the maximum and minimum IA can be calculated using the MIRD schema:

$$\begin{cases} MIA_{\mathrm{non-tumor}} = \dfrac{D_{max,non-tumor} \times m_{\mathrm{non-tumor}}}{49.87 \times FU_{\mathrm{non-tumor}}} \\ mIA_{\mathrm{tumor}} = \dfrac{D_{min,tumor} \times m_{\mathrm{tumor}}}{49.87 \times FU_{\mathrm{tumor}}} \\ MIA_{\mathrm{lung}} = \dfrac{D_{max,lung}}{49.87 \times LSF} \end{cases} \tag{1.16}$$

Here, MIA_{x} and mIA_{x} denote maximum and minimum IA based on the maximum and minimum calculated dose to theVOI x ($D_{max,x}$, $D_{min,x}$); m_{x} and FU_{x} are the mass and fractional activity uptake of VOI x, respectively.

In this strategy, historically, a dose of 40 Gy to the non-tumoral liver compartment was considered a safe dose limit. This dose limit has been adapted from EBRT to avoid inducing fibrosis in non-tumoral liver tissue. Because of the differences between SIRT and EBRT (*e.g.* dose rates and uniformity of the absorbed dose), it is recommended by several authors to perform further careful evaluations about non-tumoral absorbed dose limit for SIRT. A non-tumoral absorbed dose limit of less than 80 Gy (70 Gy in cirrhotic livers) was proposed in resin microsphere package insert, but absorbed dose of 70 Gy (50 Gy in cirrhotic liver) is discussed in the literature as the maximum acceptable non-tumor liver absorbed dose [73, 174]. For glass microspheres, higher absorbed dose criteria for tumor (*e.g.* 205 Gy for HCC) and non-tumoral (*e.g.* 97 Gy for 50% probability of NTCP) were recommended by several authors [73].

If the maximum IA for the lung and non-tumoral tissue are both greater than the minimum IA for the tumor compartment, there is a therapeutic window, and every

activity in this interval could be selected, based on non-dosimetric considerations as explained previously. Otherwise, the safety limit to lung or liver will determine the final IA. One of the drawbacks of this method are the technical problems dealing with quantification of the dosimetric parameters in case of multifocal liver involvement and ill-defined tumors.

It is also important to consider that the LSF is overestimated, especially when planar imaging is applied. By using the MIRD and PM as originally proposed, any overestimation in LSF will directly affect the dose and activity calculation of both lungs, tumor and non-tumoral liver. So, in some centers for the calculation of IA for tumor and non-tumoral limits ($MIA_{\text{non-tumor}}$ and MIA_{tumor}), an LSF of 0% is used, *i.e.* it is assumed that all administered activity would be deposited into the liver.

Advantages:

- It is more "personalized" than previous methods and as a dosimetry based method has a more scientific basis; The physician has control over the mean absorbed dose to the lungs, liver, and tumor(s).
- It can be easily extended to additional compartments: **(1)** predict absorbed dose in every compartment which is defined by the physician can be calculated (*e.g.* liver lobes/segments, PVE), and **(2)** as individual tumors can be defined as an independent compartment, a tumor-by-tumor based absorbed dose calculation is feasible.
- It has no theoretical limits on the amount of IA.

Disadvantages:

- It assumes that [^{99m}Tc]Tc-MAA is a realistic microsphere surrogate and has the same T/N ratio and LSF as ^{90}Y-microspheres.
- It hypothesizes uniform yttrium-90 activity within each compartment, which is not necessarily true.
- Any imprecision in image registration/segmentation could directly influence the calculated absorbed doses and prescribed IA. This is particularly important when compartments are delineated on one modality and transferred to another modality, with potentially very important effects in small lesions.
- The calculations are too complex in some cases to be implemented in the clinical routine, *e.g.* it needs a liver and tumor segmentation either on anatomical or functional imaging, so it is unsuitable for tumors with ill-defined margins or diffuse metastatic disease.

Calculating the T/N ratio is one of the main challenges in the PM, and there is no standardized technique to do so [175]. Frequently, T/N ratio is represented on [^{99m}Tc]Tc-MAA-SPECT image using:

$$T/N = \frac{A(tumor)}{A(non-tumor)} \tag{1.17}$$

Where A(tumor) and A(non-tumor) are the mean of the activity concentration in (*i.e.* in Bq/ml or counts/ml), which are usually measured using several pre-defined tumoral and non-tumoral VOI or 2D-region of interest (ROI) in the [^{99m}Tc]Tc-MAA-SPECT space. This calculation depends on the ROI/VOI definition method, the skills of the expert, and deviates from tumor to tumor in case of multiple tumors. The applied method to calculate T/N ratio has a considerable variation between different operators. These methods can be classified into two different approaches: (1) thresholding the activity to avoid manual segmentation and deal with diffuse and small tumors, (2) drawing some 2D ROIs:

- Gulec *et al.* used max tumor counts and average liver counts [176] for thresholding.

- Flamen *et al.* use the VOIs from thresholding the [^{18}F]FDG-PET for defining the tumor ROIs and three circular VOIs with a diameter of 2 cm to define the tracer concentration in the non-tumoral liver volumes [159].
- Campbell *et al.* threshold [^{99m}Tc]Tc-MAA-SPECT with a level for which the tumor volume would be close to the volume of pre-defined tumors on a diagnostic contrast-enhanced CT [177].
- Kao *et al.* segment the tumor manually on each transaxial slice of the activity map [178].
- Arbizu *et al.* manually define ten identical ROIs (five as tumoral and five as non-tumoral) [179].
- Garin *et al.* proposes using combined anatomical and functional information to extract tumor regions, both in a phantom study and patient evaluation [180, 181].

Another possibility is a fully anatomical tumor segmentation on CT, MR, or CBCT. The disadvantage of the fully morphological process is a potential underestimation of the tumor dose due to registration error or in the case of necrosis (including this portion in the tumor compartment). On the other hand, a fully functional method on [^{99m}Tc]Tc-MAA-SPECT is prone to result in an overestimation of the tumor dose due to neglecting hypovascular tumor areas because they do not show increased [^{99m}Tc]Tc-MAA uptake. In addition, there is a possibility of mislabeling a high uptake area within the non-tumoral liver tissue as tumor. Also, this method faces problems arising from the partial volume effect and the difficulty of setting a fixed threshold level for all tumors. To deal with the latter, some adaptive thresholding methods haven been proposed in the literature [182].

When there are multiple tumors, there are even more substantial discrepancies in the implementation of the PM. There is no consensus on calculating the T/N ratio for tumor-specific dosimetry. The most used technique in the PM consists of extracting mass of the tumor and non-tumoral compartment in anatomical space (*e.g.* CT or MR) and estimating T/N ratio separately by using sample ROIs over different tumors on [^{99m}Tc]Tc-MAA-SPECT. This facilitates the use of the PM in clinical practice, but inevitably introduce a larger uncertainty in T/N ratio estimation. According to Mikell *et al.* these effects can create a large uncertainty (factor of ~ 2.5) in estimating T/N ratio estimation for glass microspheres [183].

1.7.5 Therapy procedure for resin microsphere

On the day of treatment, the following steps are performed: patient preparation and lab tests (liver, renal, and hematological checkup), activity preparation, catheterization, activity administration and (if possible) post-administration activity verification, and post-treatment imaging. The administration set is typically delivered a day before to the nuclear medicine department. For resin microspheres, this set, which is designed to optimize the radiation safety and administration and handling process, contains:

1. one (or sometimes two) vial(s) carrying 3 GBq $\pm$ 10% of ^{90}Y-microspheres calibrated at 23 h GMT in pyrogen-free water, which can be used up to one day after calibration,
2. a so-called V-vial that should be used for preparing the prescribed IA. This vial allows maximal retrieval of its contents by using an inserted needle
3. an acrylic holder of the V-vial,
4. a syringe shield which should be used during injected activity preparation,
5. connecting tubes and needles.

The IA, prescribed by a nuclear medicine physician, is prepared by a technologist in the laboratory following the manufacturer's instruction and local radio-pharmacy regulations at a time as close as possible to the time of administration. First, the prescribed IA is taken out of the vial received from the manufacturer using a reentrant type radionuclide calibrator or activity meter. Then, it is placed into a V-vial, that, for the administration,

will be shielded by a plastic delivery box to minimize radiation exposure. The accuracy of the activity calibration in this step is paramount because it can affect all quantitative measurements and delivered absorbed doses. A typical activity calibration is performed by measuring the bremsstrahlung production, which may vary with container geometry, container material, placement and thickness, the volume, and homogeneity of the source. It is the task of the medical physics expert to calibrate and control the quality of the used equipment, such as the radionuclide calibrator or activity meter [184, 185].

For resin microspheres, the delivered activity is provided by the company with an accuracy that is claimed to be within 10%. A study shows a difference of 20% between on-site activity measurement of the V-vial and the vendor claimed activity of the shipping vial [186]. According to the recommendation of the American Association of Physicists in Medicine on dosimetry, there could be a deviation of up to 26% between measured and manufacturer indicated activity [153]. So, further study is required to evaluate cross-calibration with regard to a primary laboratory [187].

The administration step consists of repositioning the catheter at the same positions within the HA tree as during the pre-treatment work-up. Extra angiography mapping is performed to verify the catheter positioning. This also allows to assess the possible development of arteriovenous anastomoses in the time window between pre-treatment work-up and the therapeutic procedure; further coil embolization can be performed, if needed. The intra-arterial infusion of the therapeutic microspheres is performed under fluoroscopic guidance with attention to sphere reflux. After slow administration of the prepared activity, 20 cc saline is flushed to wash the whole path (vial, catheter, ...). To determine the extent of the residual activity after administration, the radiation exposure of the set from an equal distance (30 cm from center of the box) is measured before and after administration and the relative value can be taken as a measure for the residual activity.

One hour after treatment, the patient is moved to a hospital room for an over-night stay, in line with local radiation regulations. Careful clinical follow-up is required in the first six weeks to diagnose potential side effects caused by extrahepatic activity deposition and REILD.

1.7.6 Post-treatment evaluation

For patient safety and treatment verification, post-treatment imaging should be performed to visualize the deposition of the microspheres after treatment and to identify possible accumulation of the activity in non-target organs as a verification of the pre-treatment prediction of the activity distribution.

Historically, it was suggested to perform a "SPECT" scan that has been setup to detect bremsstrahlung radiation with an energy of 50 keV or more that is emitted because of interaction between β particles and the soft tissue in 2.23% of the electrons. Making a quantitative reconstruction of a BECT acquisition is challenging and usually not performed in a routine clinical setting for a number of reasons: **(1)** the continuous energy spectrum of the bremsstrahlung photons and lack of photopeak which makes the energy window based scatter and attenuation correction very challenging, **(2)** uncertainty of the source position of the β^- emission; before releasing the bremsstrahlung, the β particles have traveled up to a few millimeters, and **(3)** pronounced collimator septa penetration of the high energy photons. Therefore, these images are usually used qualitatively to visually verify the placement of the microspheres in the liver and to look for potential extrahepatic deposits. Together with a low-dose CT scan, localization of BECT is much easier.

Quantitative imaging of the actual distribution of the spheres can, on the contrary, be performed using ^{90}Y-TOF-PET imaging. This assessment allows to determine the actual delivered doses on the tumors and healthy liver. Optimizing a ^{90}Y-PET procedure is not trivial: **(i)** the count rate is very low as there are only 32 internal pairs produced per million events with related Poisson noise; **(ii)** for a certain PET detectors (*e.g.*

LSO based crystals), the natural radioactivity inside the detector material will be non-negligible and this will influence the count rate. But it has been shown that by using the TOF technique, quantitative imaging of the distribution of the microspheres is feasible with acceptable accuracy and high resolution. Post-treatment imaging is performed in almost all European centers (93%) by performing ^{90}Y-BECT/CT (53%), ^{90}Y-PET imaging (34%), and stand alone ^{90}Y-BECT (19%) [85].

Some authors proposed advanced reconstruction methods mostly by utilizing MC modelling to reach an error level of less than 10% in ^{90}Y-BECT phantom imaging [73]. On the other hand, a multi-center study (QUEST) shows that dosimetry based on ^{90}Y-TOF-PET imaging is reproducible. Generally, ^{90}Y-TOF-PET imaging is widely accepted to be superior to clinical ^{90}Y-BECT imaging in different aspects like spatial resolution, clinical availability, and sufficient accuracy to perform post-treatment dosimetry.

1.7.7 Follow-up

Follow-up imaging is recommended usually after one to three months and every three months thereafter to evaluate the treatment, to consider additional SIRT procedures, or to alter treatment strategies. The response to SIRT in hepatic tumors could be assessed by employing imaging findings, evaluating tumor markers, and pathology results. Several methodologies have been established to determine the tumor response:

1. **Anatomical response evaluation methods:** Response Evaluation Criteria in Solid Tumors methods (RECIST [188], RECIST 1.1 [189], and mRECIST [190]) or EASL [191] are widely used for assessing tumor response. The mRECIST uses the single largest diameter of the viable tumor, which is defined as the tumor with hyperenhancement in the arterial phase. This method is currently the standard of radiological response assessment in HCC. This method is primarily based on ceCT or T1 contrast-enhanced MR imaging. Some authors suggested the usefulness of other MR sequences for HCC response evaluation [192].
2. **Functional assessment (EORTC [193], PERCIST [194]), or apparent diffusion coefficient -ADC- change:** For liver metastases and ICC, evaluating the tumor response based on [^{18}F]FDG-PET has been proposed in several studies. Some authors claimed that this monitoring technique is superior to anatomical evaluation because a tumor cell viability can be heavily impaired before anatomical size changes are present and it allows to distinguish massive necrotic areas more readily [195–198].

On follow-up imaging, different levels of response can be documented [199]:

1. **complete response:** the disappearance of all target lesions,
2. **partial response:** decrease of the tumor beyond a predefined threshold compared to the baseline image,
3. **progressive disease:** increase of the tumor beyond a predefined threshold compared to the baseline image or appearance of new lesions,
4. **stable disease:** any case that does not qualify for either of the above conditions.

Response evaluation follow up is performed by using CT and MR, PET/CT, and PET stand alone in 72, 72, 35, and 2% of the European centers, respectively [85].

1.8 Objective and main contributions

The main aim of this Ph.D. project is to develop a patient-specific and precise dose-prediction and dose-measurement method along with the development of the steps how to achieve this in clinical practice by employing advanced imaging and image processing methods.

For optimal use of information from images performed before and after SIRT, we developed and evaluated a new methodology for registering all these images to a common space. This so-called meta-image is used for multi-modality liver and tumor segmentation using contrast-enhanced MR, CT, CBCT, or [^{18}F]FDG-PET, and for LPT segmentation using CBCT. To our best knowledge, this is the first attempt to study the application of CBCT based LPT definition in SIRT dosimetry.

Before treatment, voxelized dosimetry is performed to estimate the absorbed dose to different VOIs (*i.e.* LPTs, tumors, normal liver parenchyma) in different scenarios (*i.e.* different IA). This information provides useful dosimetric details (*e.g.* mean absorbed dose, DVH parameters), which can facilitate a safe and efficient treatment strategy and IA prescription based on predicted absorbed dose to the tumor and healthy liver parenchyma. We also focused on assessing the predictive power of [^{99m}Tc]Tc-MAA simulation by comparing these predictions to actual delivered dose distributions measured with quantitative ^{90}Y-PET.

1.8.1 Outline

This manuscript is organized as follows:

- In **chapter 2**, the overview of our proposed workflow for multi-modal image analysis is described, and an example of prospective pre-treatment dose estimation and post-treatment dosimetry report are provided.
- **Chapter 3** describes the validation of the registration and segmentation workflow. The emphasis of this validation is on the multi-modal liver segmentation and definition of the LPTs using CBCT. We also investigate the registration accuracy for SIRT dosimetry.
- **Chapter 4** reports our result of a quantitative comparison between pre-treatment dose estimation and post-treatment dose verification. In this study, we used CBCT images to delineate the tumor and LPTs. Then the correlation between pre- and post-treatment dose assessments are provided using different dosimetric parameters.
- **Chapter 5** discusses some interesting clinical cases. We present some examples to highlight the importance of the multi-modal image analysis in SIRT dosimetry.
- **Chapter 6** concludes and summarizes all discussed methods and results and clarifies how our framework could be further extended to facilitate accurate SIRT in clinical routine.

Chapter 2

Investigation of the SIRT workflow in UZ Leuven

Over sixteen years that SIRT has been practiced in University Hospitals Leuven (UZ Leuven), more than 440 patients have been treated with ^{90}Y-microspheres. This treatment modality, together with [^{177}Lu]Lu-DOTA-TATE, has emerged as the primary therapeutic procedure within the nuclear medicine department, with 61% of the total therapeutic nuclear medicine sessions since 2004 till the end of 2019 (see figure 2.1).

Over the years, some investigations have been performed in UZ Leuven to optimize the SIRT workflow:

- **advanced imaging:** UZ Leuven is one of the pioneers in implementing advanced imaging techniques to optimize the treatment:
  (a) since 2009, SPECT/CT is used form imaging the [^{99m}Tc]Tc-MAA distribution and post-therapy bremsstrahlung imaging.
  (b) a two-phase contrast-enhanced CBCT image set is performed systemically for each catheter tip position during angiography workup since 2013.
  (c) since November 2017, a quantitative ^{90}Y TOF-PET image is systemically acquired after the treatment.
- **assessing pre- and post-treatment imaging:** the therapeutic and imaging procedures have been reviewed in an attempt to reduce the mismatches between [^{99m}Tc]Tc-MAA and the ^{90}Y-microspheres distributions; *e.g.* [^{99m}Tc]Tc-MAA administration technique (*e.g.* volume, rate, ...), and [^{99m}Tc]Tc-MAA-SPECT imaging time.
- **activity planning:** the activity prescription method has evolved from the BSA method to a dosimetric and patient-tailored procedure.
- **activity cross-calibration:** a cross-calibration between the imaging device and the activity meters was performed for both [^{99m}Tc]Tc-MAA and yttrium-90 activities to investigate the accuracy of the activity measurements and the qualitative and quantitative accuracy of emission tomography.
- **predictive and measured absorbed dose comparison:** a retrospective voxel-level dose prediction (based on [^{99m}Tc]Tc-MAA-SPECT/CT) and dosimetry (based on ^{90}Y-PET) was conducted. It proves the feasibility of a more detailed dosimetric activity prescription and dose verification.
- **prospective dose estimation report:** because of the results obtained in the analysis of the retrospective voxel-level dose prediction and dosimetry, our physician refers, difficult cases to employ advanced multi-modal sophisticated analysis, prospectively, to either (i) verify the IA prescribed within the routine UZ Leuven clinical workflow, or (ii) extract more information from different pre-treatment images to include more clinical relevant information (*e.g.* liver functionality, separating tumor and necrosis, CBCT-based LPT segmentation) in activity planning.

– **prospective dosimetry:** a post-treatment prospective report of delivered absorbed dose within different VOIs (*e.g.* TV and NTV in each LPT) is performed using voxel-level dosimetry based on ^{90}Y-PET to verify the output of the clinical procedures.

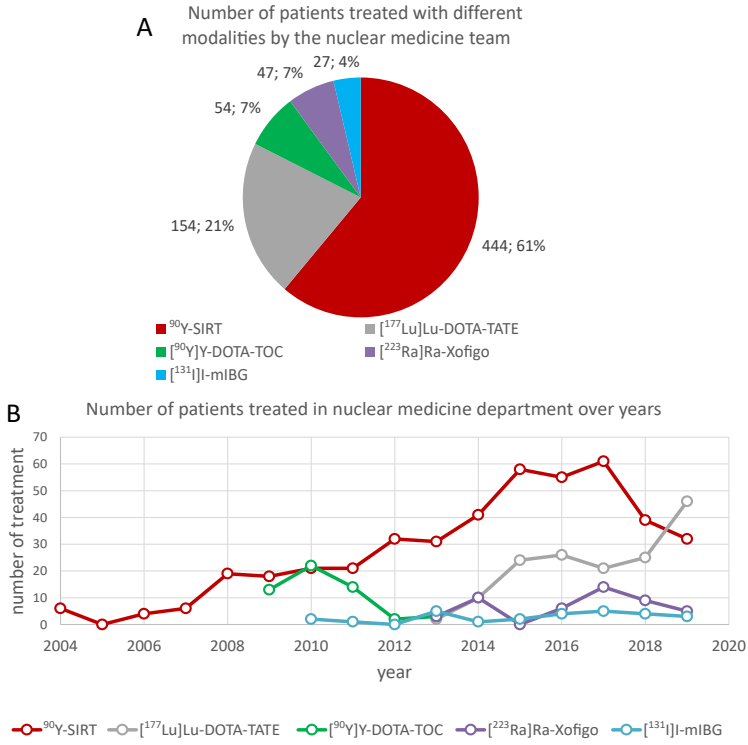

*Figure 2.1: **[A]** Since 2004, in total, 444 patients have been treated with SIRT in UZ Leuven, which corresponds to 61% of the total patients treated in this period; each of the ^{90}Y-DOTA-TOC and [^{177}Lu]Lu-DOTA-TATE treatments are typically made-up of four cycles. **[B]** The number of SIRT sessions has risen over the years, and SIRT is one of the main radionuclide treatments in UZ Leuven.*

In line with SIRT procedures described in section 1.7, the current SIRT workflow is described in figure 2.2:

1. **evaluation:** in UZ Leuven, a MDT assigns eligible patients to the SIRT based on patient, liver, and tumor characteristics extracted from some recent diagnostic images.
   In the angiography workup, a [^{99m}Tc]Tc-MAA-SPECT/CT, together with planar gamma camera, provides information about intra- and extrahepatic (*e.g.* LSF) activity distribution. During this workup, an early and late arterial phase contrast-enhanced CBCT are also performed for each catheter tip position to assess **(a)** extrahepatic activity accumulation, **(b)** define LPTs, and **(c)** track the vascularity of the tumors.
2. **planning:** based on the images described above, the final decision for proceeding with SIRT is taken and treatment parameters such as the type of microsphere to be used, the catheter positions to be used and their resulting LPT are decided.

Then, a nuclear medicine physician prescribes the IA based on one of the methods detailed in the guidelines. By using multi-modal image processing, it is also possible to perform a voxel-level dose estimation for each proposed IA.

3. **treatment:** after administering the prescribed activity, post-treatment imaging using either TOF-PET/CT or TOF-PET/MR can be performed the same day or the day(s) after (*cfr.* ^{166}Ho-QuiremSpheres for which the post-treatment evaluation could be performed many days later).
   A report of pre- and post-treatment voxel-level dosimetry could be offered to give an overview of the delivered dose to the different LPTs and tumors.

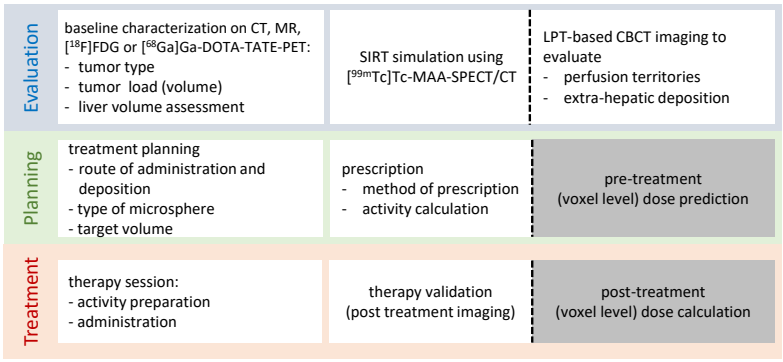

Figure 2.2: The current SIRT workflow in UZ Leuven consists of three phases: patient and tumor evaluation, treatment planning, and treatment. The gray boxes represent the steps that are still in the research phase.

In this chapter, a review on the current status of the SIRT in UZ Leuven, together with the achievements in practicing dosimetry and/or multi-modal image processing, is described. R software version 3.6.1 (R Foundation for statistical computing, Vienna, Austria) was used for all statistical analysis. An example of the pre- and post-treatment dose assessment report is also provided at the end of this chapter (section 2.3). More results are provided in the following chapters.

2.1 SIRT in UZ Leuven: facts and figures

Some aspects of the SIRT workflow are variable and can be different from one patient to another depending on the patient status, liver condition (normal liver parenchyma volume, cirrhotic liver,...), previous treatments (*e.g.* multiple chemotherapy lines, prior SIRT), tumor characteristics (*e.g.* type of the tumor, tumor load, regional spread (segmental, lobar, bilobar)), and the aim of the treatment (tumor control, curative approach,...). Designing a dedicated tool to aid the treatment team for a universal patient-tailored and smooth workflow is not straightforward and needs a sharp eye on details provided by clinical reports and images.

2.1.1 Diagnostic (baseline) images

Diagnostic images are essential for treatment planning (see section 1.7.1). Mainly, these images are utilized for tumor characterization. Depending on tumor type, different imaging techniques are preferred for screening, staging, and tumor and liver assessment. So, as mentioned before, any treatment planning workflow in SIRT should support registration and VOI segmentation for different image modalities, *e.g.* [^{18}F]FDG-PET/CT, [^{68}Ga]Ga-DOTA-TATE PET/CT, MR and ceCT imaging. As illustrated in figure 2.3, both FDG-avid and non-FDG-avid tumors are treated frequently in UZ Leuven.

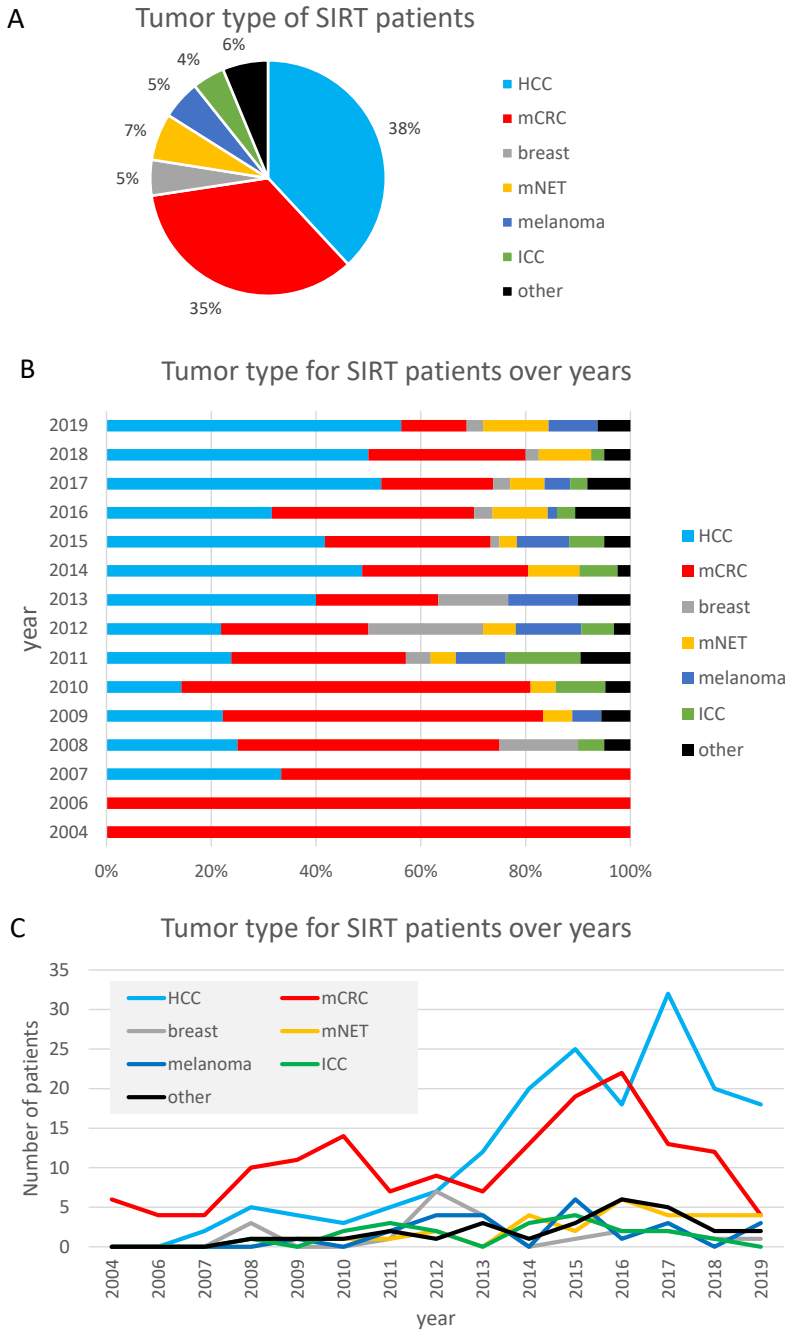

*Figure 2.3: **[A]** From 444 patients treated with SIRT, HCC, and mCRC are the most frequent tumor types, which demonstrates the importance of both MR and CT based tumor definition. **[B]** and **[C]** Over years, HCC has superseded mCRC as most frequent indication.*

2.1.2 SIRT simulation using MAA workup and CBCT imaging

2.1.2.1 MAA workup

From 412 SIRT procedures, for which the data was available, pre-treatment simulation with [^{99m}Tc]Tc-MAA was carried out on average 24.3±0.8 days before treatment (first interquartile range, median, and third interquartile range of days difference are 16, 22 and 29 days, respectively). It is hypothesized that this time difference is small enough to limit liver or tumor volume change and more importantly change in the tumor vasculature [200].

As mentioned in section 1.7.3, some authors briefly stated the number of administered particles/microspheres as a potential factor for activity homogeneity. The specific activity of the calibrated resin microsphere is 50 Bq/microsphere, which corresponds to around 20 million microspheres for each GBq of fresh activity. On the contrary, this number is widely variable for [^{99m}Tc]Tc-MAA particles due to its short half-life (6.01 hours) compared to the shelf-time (as a result a highly variable specific activity), potentially high residual activity, etc. The number of administered [^{99m}Tc]Tc-MAA particles is typically 100 to 300 times less than the resin microspheres. So, the [^{99m}Tc]Tc-MAA residual activity, which reduces this number linearly, is one of the factors for optimizing this step.

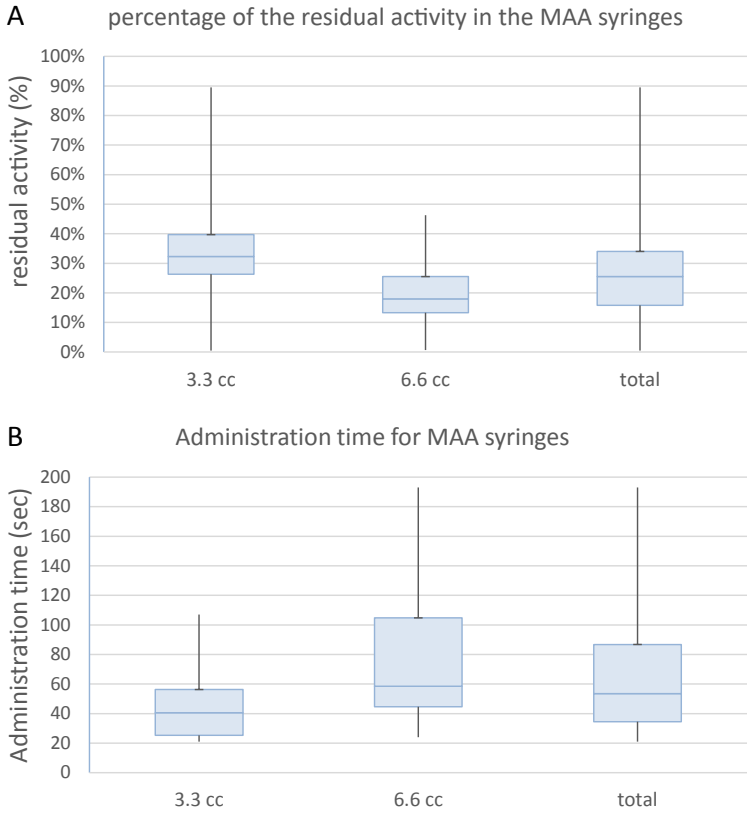

*Figure 2.4: **[A]** The percentage of the residual activity in the syringes for MAA study is lower in big syringes (6.6 cc). This amount could be up to near 90% of the prepared activity. **[B]** Manual administration of the MAA is performed as slow as possible.*

To improve the [^{99m}Tc]Tc-MAA procedure, some actions and routine clinical modifications were applied in UZ Leuven to the workup since the second quarter of 2015:

- **volume of injected solution:** to compensate the volume difference between the left and right lobe (anthropometrically, the right lobe is twice the volume of the left lobe), for the small LPTs, big LPTs, and whole liver evaluation, around 50 MBq in 3.3 cc, 100 MBq in 6.6 cc and 150 MBq in 6.6 cc are prepared.
- **activity documentation:** the prepared activity, residual activity after administration, and actual time of activity injection are documented to measure the netto injected activity.
- **slow injection:** the responsible expert is asked to administer the activity as slow as possible. After this consideration, the injection time is increased from around 10 seconds to an average of 41 and 59 seconds for a syringe with 3.3 cc and 6.6 cc, respectively. From July 2016, the duration of the administration is also documented.

From 132 pre-treatment sessions, this information has been documented for 99 left lobe, 123 right lobe, 6 whole liver, and 14 segmental administrations. The percentage of the residual activity (normalized by prepared activity) is reflected in figure 2.4. The result indicated that even after slow administration (about a minute), the residual activity in the syringes was not negligible. No correlation between the residual activity (neither in Bq nor in the percentage of the prepared activity) and LPT volume, tumor volume, tumor involvement, administration duration, or administration time (to check the effect of the [^{99m}Tc]Tc-MAA shelf-time) was found.

These results suggest that the number of administered [^{99m}Tc]Tc-MAA particles could even be lower than what is expected. This, potentially, has two important effects on dosimetry, which need to be further investigated:

- A smaller number of administered particles in [^{99m}Tc]Tc-MAA compared to the treatment session could influence the predictive power of [^{99m}Tc]Tc-MAA.
- In bilobar treatment, partitioning the total liver into different LPTs is a crucial step in finding the fractional uptake (in voxel-level dosimetry) and T/N ratio (in the PM). Usually, in the [^{99m}Tc]Tc-MAA workup, the syringes containing 100 MBq and 50 MBq for big and small lobe are prepared to administer the activity proportional to their volume (generally volume of the right lobe is assumed to be twice the volume of the left lobe). In case of accurate LPT segmentation, theoretically, this (im)balance does not affect the administered activity accuracy (because of the normalization of the voxel activity by the total activity in each lobe). Still, any error in separating the LPTs could potentially increase the dosimetry error, especially when there is a high uptake or interesting VOI (*e.g.* TV or high uptake within NTV) in the region which is wrongly segmented. Our results showed that the residual activity is sometimes too high to keep the balance between ratio of the administered activity in different LPTs and their volumes (see section 3.4.4). We believe that CBCT-based LPT segmentation is an effective tool to improve the lobe segmentation and follow the perfused volume (or territory) of each [^{99m}Tc]Tc-MAA administration.

Analysis revealed a good correlation between the activity in the prepared syringe and the netto administered activity ($r^2 = 0.918$) with some small bias. The results are provided in figure 2.5, which recommends that if one needs to provide a netto injected activity of 50, 100, and 150 MBq, the correspondent prepared activity in the syringes should be around 70, 120, and 175 MBq, respectively.

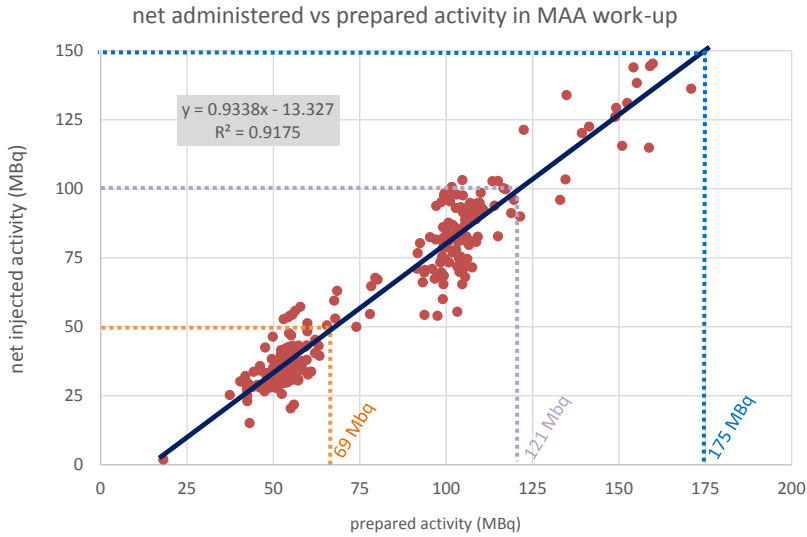

Figure 2.5: Correlation of the netto administered [^{99m}Tc]Tc-MAA with the prepared activity. According to these results, it would be recommended to prepare an additional amount of 19, 21 and 25 MBq if the target net activities equal 50, 100 and 150 MBq, respectively.

2.1.2.2 CBCT imaging

As mentioned above CBCT imaging can be used as a complement to the [^{99m}Tc]Tc-MAA scan to provide more accurate dose estimations, especially for treatment with more than one administration. Since November 2013, CBCT imaging has been implemented in the pre-treatment angiography evaluation (see section 1.2.1.3). As mentioned before, this modality is used as an indication of the intra- and extrahepatic activity uptake. In pre-treatment workup, CBCT images are acquired for each planned branch of the HA. So, this imaging technique could provide some information about perfusion territories of the different branches of the HA. This information could be beneficial, especially when SIRT is performed by administering activity(ies) within sub-branch(es) of the common HA (*e.g.* left and/or right HA). Figure 2.6 gives an illustration about the frequency of different SIRT scenarios in UZ Leuven.

2.1.3 Treatment planning

The treatment planning, which is described in section 1.7.4, is a crucial step in the SIRT workflow to spare NTV from a high absorbed dose and provide sufficient dose to the TV to avoid disease progression or kill the tumor. On the other hand, there is currently not a standard guideline or recommendation for the calculation of the activity that needs to be administered, given the therapy approach. In this section, we report our evolution in the area of treatment planning (*e.g.* overall survival analysis of different SIRT patient groups) to gain insight into the impact of activity planning on patient outcomes. These preliminary analyses are only for informational use since not all (clinical) covariates were taken into account and further investigation should improve methodological and reporting quality. All survival analysis (Kaplan-Meier) were performed using R software version 3.6.1 (R Foundation for statistical computing, Vienna, Austria). Cox's proportional hazards model was used for data analysis. The pairwise log-rank test was used for comparison.

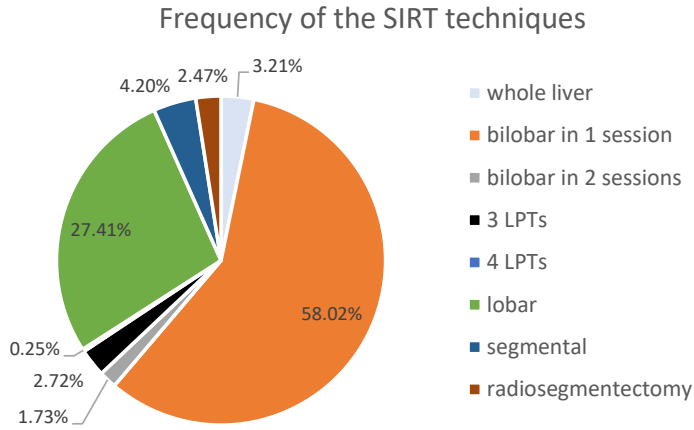

Figure 2.6: Targeting the entire liver by placing the catheter tip in the common hepatic artery is applied in only 3% of the SIRT sessions in UZ Leuven. This shows the importance of the LPT definition in SIRT treatment planning.

A treatment plan depends on several factors, including the type of the tumor. When applying SIRT, the mNET and HCC tumors are known to show a better survival compared to the other tumor types (see sections 1.1.4.1 and 1.1.5.2). Figure 2.7 represents a Kaplan-Meier survival analysis of all patients treated with resin microsphere in our database. Patients with mNET do not reach the median yet and the median survival for patients with HCC, mCRC, and other tumors are 13.5, 8.5, and 8.6 months, respectively.

Depending on the type of microsphere, a number of methods for calculating the IA can be found in the literature, recommendations, and package inserts (see section 1.7.4). The resin microsphere is used almost for all SIRT sessions in UZ Leuven (6 SIRT sessions with glass microspheres and one with ^{166}Ho-QuiremSpheres have been used in total until the end of 2019). Among all methods, the BSA is the most frequently used prescription method as this was used historically and in multi-center clinical trials according to protocol, but it has been replaced by the MIRD and PM since 2018. There is a tendency to use more personalized dosimetry with the PM. In 2019, this method is used in 72% of the prescriptions (see figure 2.8). In 2017 and 2018, the treatment planning was initiated with the BSA as a mere starting point. If the calculated activity based on the BSA was close to the activity calculation based on the MIRD method (*e.g.* 40 to 50 Gy to the total liver), no modification was made and the BSA is documented as the prescription method.

As described in sections 1.6.3 and 1.7.4, several aspects could be mentioned to support the advice of replacing the BSA method by more scientific and internal dosimetry based methods:

- SIRT is not a systemic treatment and should not be addressed by the patient weight and height. This is explicitly stated in the new European regulations [201].
- Despite a known moderate to weak correlation between the BSA and liver volume, the BSA activity planning method is based upon an estimation of the size of the liver from the body surface area [167,202]. We observed only a very poor correlation (r^2=0.085) between the BSA and the total liver volume (see figure 2.9).
- In many centers, still, the BSA method is applied when the PM is not suitable, *e.g.* ill-defined or/and diffuse tumors, when VOI definition is technically or practically challenging, or when the [^{99m}Tc]Tc-MAA is suspected to be a poor predictor for the treatment. Even in these circumstances, instead of the BSA method, the MIRD method (which can be interpreted as the fixed activity concentration per unit of

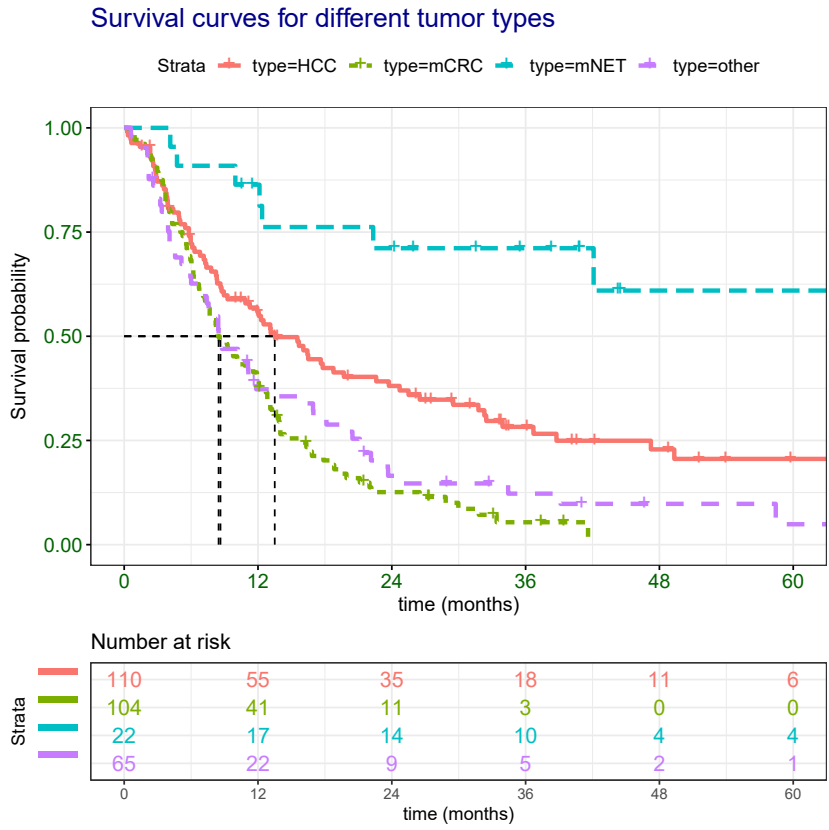

Figure 2.7: mNET and HCC patients showed a better OS than other tumor types, the p-values for pairwise comparisons were (HCC versus mCRC): 0.0001, (HCC, mNET): 0.001, (HCC, other tumor types): 0.01, (mCRC, mNET) < 0.0001,(mCRC, other tumor type): 0.33, and (mNET, other tumor type) < 0.0001. The difference between mCRC and HCC overall survival (HR= 1.86, 95% CI: 1.37-2.53; p-value< 0.001) was more pronounced in a longer period of follow up (e.g. two or three years); the fraction of patients alive (mCRC versus HCC) patients after 12, 24 and 36 months are (39% versus 50%), (11% versus 32%), and (3% versus 16%), respectively.

volume/mass, *e.g.* 0.8 MBq/ml for 40 Gy to the total liver) could be easily applied which does not rely upon the tumor segmentation and the predictive power of the [^{99m}Tc]Tc-MAA simulation.

- Historically, the BSA is considered as a safe (conservative) treatment planning. Our evaluation (see figure 2.9) showed that by calculating the IA based on the BSA method, only half of the patients received a total liver dose below 50 Gy, and one quarter of the patients would receive a total liver dose of above 58 Gy, which could be potentially toxic. So, the BSA method could be considered to deliver a total liver dose of between 43 Gy (Q1) and 58 Gy (Q3) to half of the patients. Still, it could be detrimental to deliver a possibly toxic dose to one quarter of the patients and could lead to under-dosing another quarter of the patients, which could be avoided by using the patient-tailored treatment planning concept.

- Some evidence shows that using dosimetric methods could potentially improve the tumor response and OS (section 1.6.2). Figure 2.10-A shows an OS analysis of all patients (with a mix of tumor type) treated with resin microsphere for whom

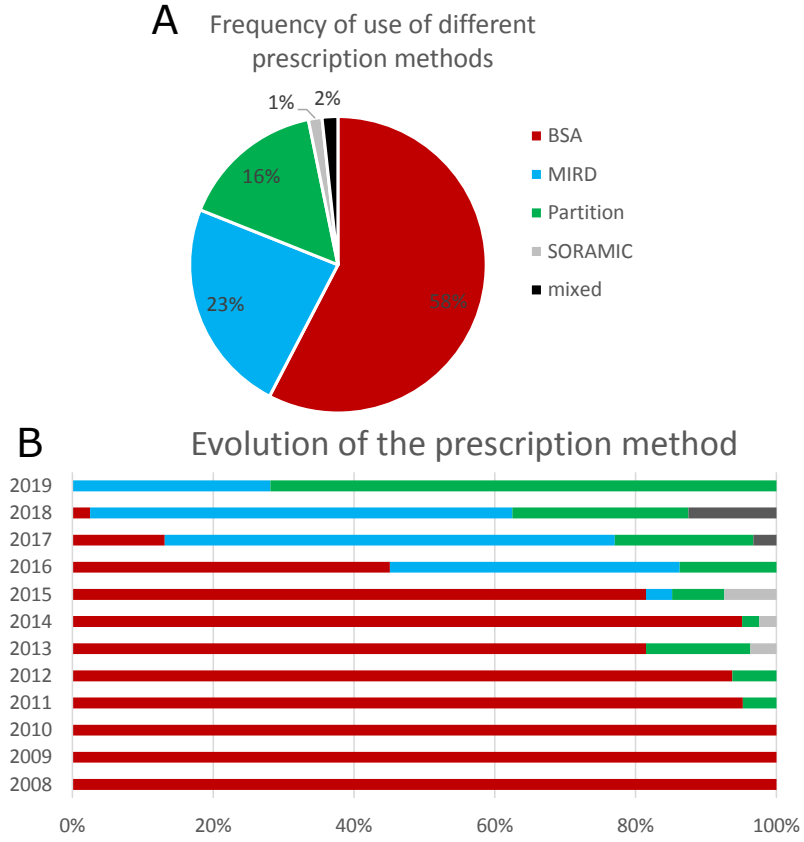

*Figure 2.8: **[A]** In total, for 39% of the patients, the prescription has been made based on dose estimation to the liver (MIRD method) or TV and NTV compartments (PM). **[B]** Since 2017, dosimetric methods were used for more than 80% of the patients; in 2019, most of the prescriptions take into account the absorbed dose to the TV and NTV.*

the data were accessible. Here, the treatments were stratified by the prescription method (SIRFLOX look-up table and mixed strategies have been excluded due to their limited use). The median survival for patients treated with the BSA-, MIRD- and PM-based prescription were 9.2, 13.5, 19.7 months, respectively. These results show a significantly better median survival when the prescription was made using the MIRD method compared to the BSA method (p-value=0.018), with a HR of 0.64 (95% CI, 0.46-0.88; p-value=0.006). The differences between median survival of the patients prescribed by the PM compared to either the BSA (p-value=0.059) or MIRD (p-value=0.848) method were not significant. When comparing PM and BSA prescription, a HR of 0.59 (95% CI, 0.37-0.99; p-value=0.04) was calculated. HR for PM and MIRD prescription was 0.95 (95% CI, 0.54-1.65; p-value=0.85). On the other hand, a pair-wise Fisher's exact test showed a dependency between prescription method and the tumor type, *i.e.* the prescription of the patients with HCC and mNET tumor (which had the best median survival over other types of liver malignancies) were more based on the PM compared to the other tumor types (p-value<0.01). There are two important sources of bias in this comparison: **(a)** Usually, PM is used in prescription when a good targeting is observed with a high T/N ratio. Typically, HCC and mNET have a high tumor uptake, also they have a better prognosis than mCRC which is chemorefractory. **(b)** Another potential

bias is the tumor burden. PM is usually used for patients with one single lesion. For patients with diffuse tumor burden, other methods could have been used.
When comparing the non-dosimetric prescription (BSA method) and dosimetric prescriptions (pooled PM and MIRD) outcome, a pairwise Fisher's exact test showed that the proportions depended on the tumor type (HCC patients are more treated with dosimetric methods compared to other tumor types; p-value<0.01). The result of the median survival comparison was in favor of dosimetric prescriptions (13.9 versus 9.2 months; p-value=0.001) and showed some evidence of improvement in overall survival (HR of 0.63; 95% CI, 0.47-0.84; p-value=0.002). The survival analysis is provided in figure 2.10-B.
Figure 2.11 provides an OS analysis of the patients with HCC treated with SIRT with two different types of strata (a potential bias is that the BSA was the most frequent prescription method till 2016 and then it was replaced with dosimetric methods (PM and MIRD method)):

(a) Figure 2.11-A shows a median survival of 19.7, 16.4, and 9.3 months when the treatment was planned by the PM, MIRD method and BSA method, respectively. But these differences were not statistically significant (all pairwise p-values were more than 0.60).

(b) As illustrated in Figure 2.11-B, when dosimetric prescriptions (MIRD and PM) are pooled, a median survival of 16.4 months was observed, which was higher (not significantly) than BSA-based prescription (9.3 months; p-value=0.19). No significant effect of dosimetric prescription for HCC on survival was noted (overall survival HR of 0.73; 95% CI, 0.46-1.16; p-value=0.19).

For patients with mCRC, when the IA was calculated using dosimetric methods, a better median survival was observed compared to the non-dosimetric methods (12.7 versus 8.4 months; p-value=0.007). Dosimetric prescription for mCRC patients were positive predictor of survival (HR of 0.51; 95% CI, 0.31-0.84; p-value=0.008). The survival analysis is illustrated in figure 2.12.

- Another reason to abandon the MIRD method is that one needs to specify the target dose to the entire section of the liver treated, but the optimal dose value is unknown (see section 1.7.4.3). To investigate the feasibility of defining an optimal liver dose, a survival analysis of all patients treated with resin microspheres has been performed (see figure 2.16). Lobar and segmental treatments were excluded. The treatment was categorized by the total liver delivered dose: low liver absorbed dose (less than 40 Gy), medium liver dose (between 40 and 50 Gy), and high liver dose (more than 50 Gy). A pairwise Fisher's exact test showed that this dose thresholding was independent of the tumor type (figure 2.13 illustrates the box plot of the absorbed dose for each tumor type).
The median survival (see figure 2.16) for patients treated with low, medium, and high liver absorbed dose groups were analyzed: **(1)** treating patients with a low absorbed dose showed a lower median survival compared to patients received a medium absorbed dose (6.5 versus 11.9 months; 0.001) and was associated with worse overall survival (HR of 2.06; 95% CI, 1.41-3.01; p-value < 0.001); and **(2)** patients treated with high absorbed dose showed a lower median survival compared to patients received a medium absorbed dose (9.1 versus 11.9; p-value= 0.048) with a HR of 1.39 (95% CI, 1.00-1.94; p-value= 0.051).
Figure 2.14 shows the overall survival analysis based on the same total liver dose threshold for the patients with HCC and mCRC malignancies:

(a) **HCC patients:** compared to median survival for medium liver absorbed dose (median survival of 31.8 months), no significant effect on survival was noted for **(1)** low liver absorbed dose (median survival of 7.1 months; p-value = 0.17) with a HR 1.89 of (95% CI, 0.93-3.86; p-value= 0.08), or **(2)** high liver absorbed dose (median survival of 8.3 months; p-value = 0.19) with a HR of 1.79 (95% CI, 0.86-3.73; p-value= 0.12).

(b) **mCRC patients:** compared to median survival for medium liver absorbed dose (median survival of 10.1 months): **(1)** a significant lower median survival was observed for patients who received low liver dose (4.7 month, p-value = 0.006) with a HR of 2.5 (95% CI, 1.38-4.52; p-value= 0.002), and **(2)** for patients with high liver absorbed dose, no significant effect on median survival (8.6 month; p-value= 0.57) and overall survival (HR of 1.16; 95% CI, 0.71-1.89; p-value= 0.56) was found.

We also investigated the effect of receiving a so-called optimum liver dose (between 40 and 50 Gy for HCC patients and more than 40 Gy for mCRC patients) on OS. These strata were defined based on the obtained results in survival analysis for different liver absorbed dose thresholds in figure 2.14. One of the possible reasons for excluding HCC patients with liver absorbed dose of more than 50 Gy from the optimum dose group is the fact that NTV of the patient (compared to mCRC patients) are more sensitive to the absorbed dose. As illustrated in figure 2.15:

(a) For HCC patients, receiving a non-optimum liver dose was associated with worse median OS (31.8 versus 7.4 months; p-value=0.056), with a HR of 1.84 (95% CI, 0.98-3.48; p-value=0.059).

(b) For mCRC patients, receiving a non-optimum liver absorbed dose was associated with poor median survival (7.2 versus 10.1 months; p-value=0.001) and overall survival (HR of 2.31; 95% CI, 1.36-3.93; p-value=0.002).

These results supports the notion that replacing BSA by dosimetric methods in activity planning may improve the treatment outcome. One limitation of this analysis is the lack of information about patient condition in each group. We found a relation between survival and activity planning method, but still we do not know if the treatment planning method is the cause of increased survival. Some potential biases are:

- the prescription method depends on tumor targeting. For patients with high tumor uptake and/or high tumor burden based on [^{99m}Tc]Tc-MAA study, PM is usually used for prescription.
- it is known that different tumor types have different tumor uptake and burden. HCC and mNET typically have high T/N ratio and also they show better OS compared to other tumor types (*e.g.* mCRC).

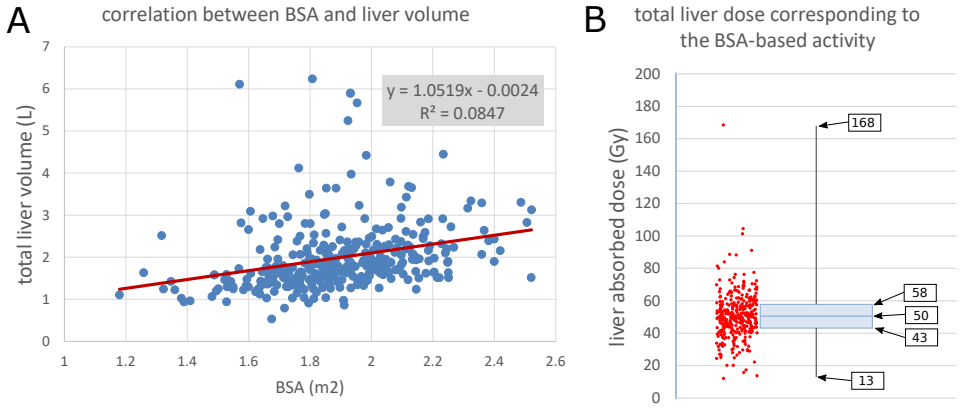

*Figure 2.9: [**A**] Body surface area of the patient had a weak correlation with the total liver volume (n=333). [**B**] BSA-based IA corresponded to a considerable variation of the total liver absorbed dose which could be as high as 160 Gy; the individual points are also provided (red dots).*

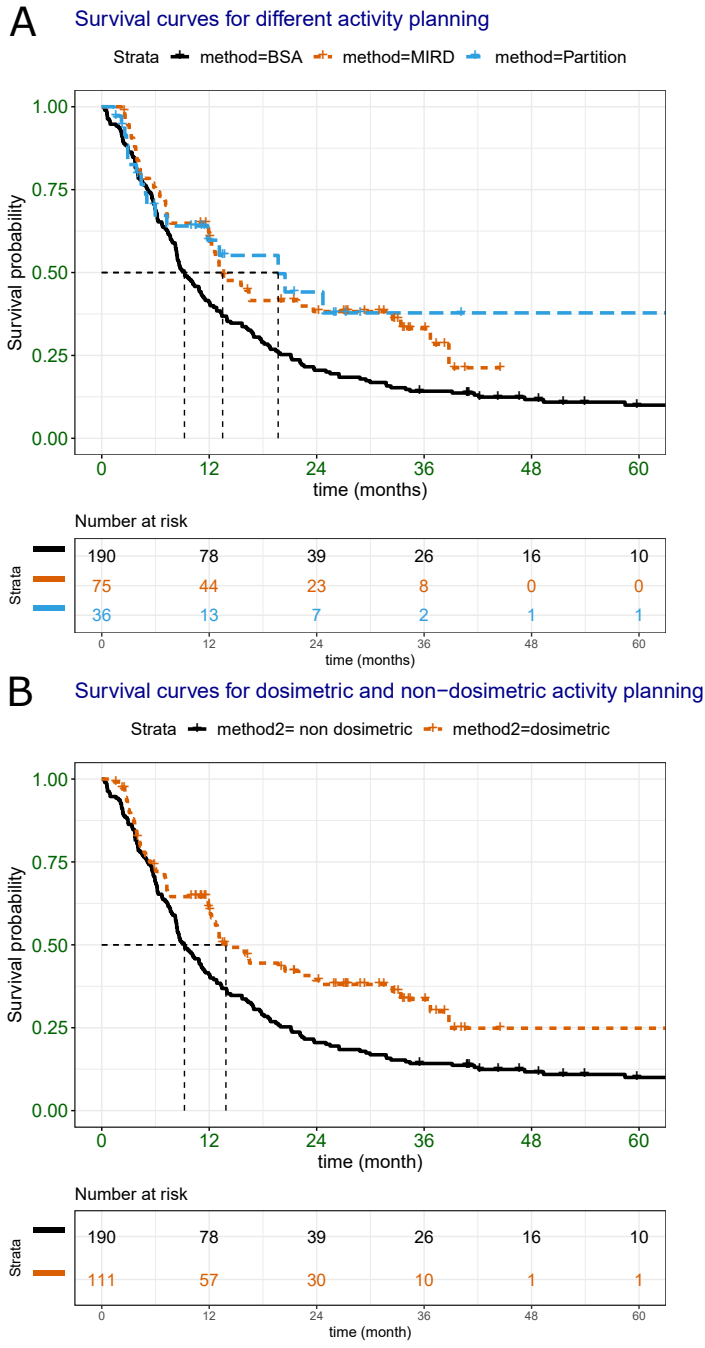

*Figure 2.10: **[A]** Patients treated with the MIRD method had better median survival than patients treated with the BSA method (13.5 versus 9.2 months; p-value=0.02) with a HR of 0.64 (95% CI, 0.46-0.88; p-value=0.006). The median survival of the patients treated with the PM was 19.7 months. The pairwise Fisher's exact test showed that there was a statistically significant association between the prescription method and tumor type; SIRT for HCC patients were prescribed more by PM compared to BSA (p-value < 0.001) and MIRD (p-value $= 0.004$). **[B]** Patients treated with dosimetric prescription had a better median survival (13.9 versus 9.2 months; p-value=0.001) with some evidence of improvement in overall survival (HR of 0.63; 95% CI, 0.47-0.84; p-value=0.002).*

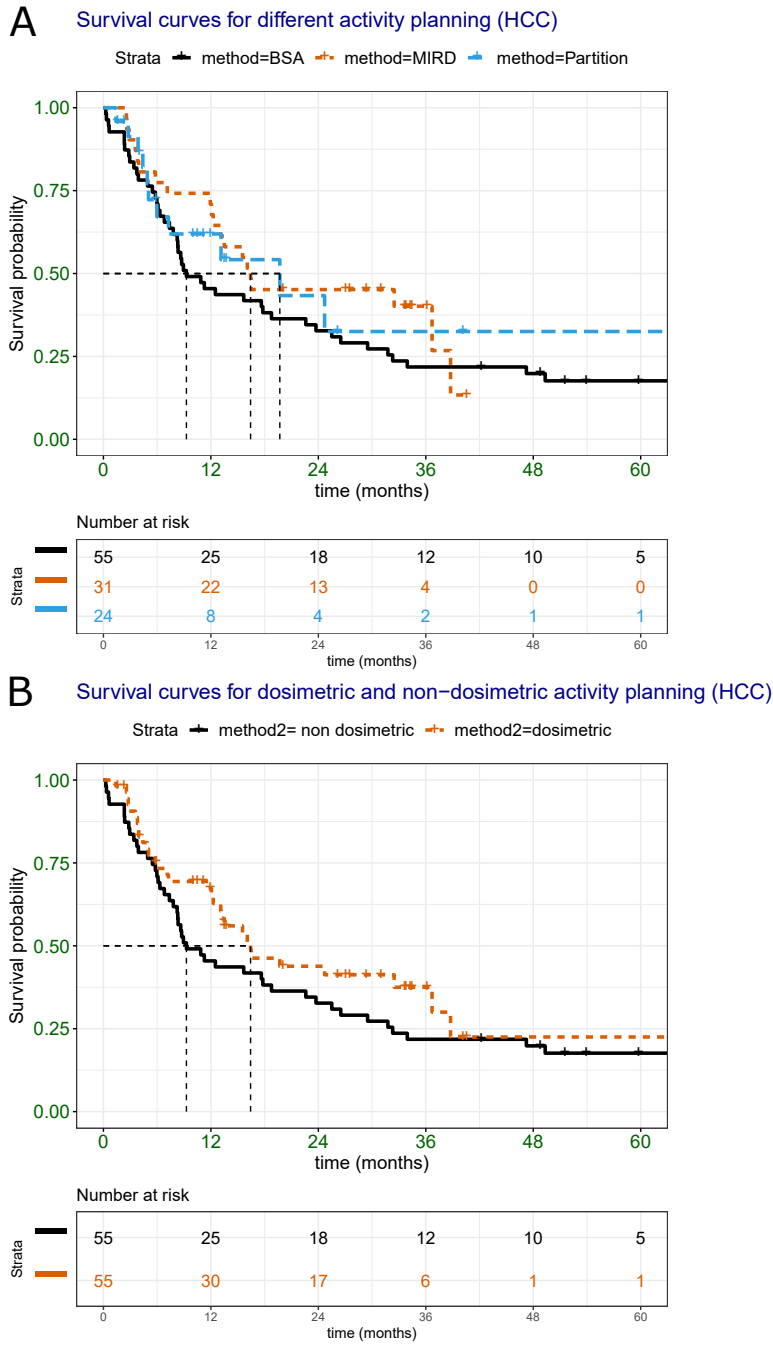

*Figure 2.11: For patients with HCC: [**A**] The median survival of the patients with HCC tumors receiving SIRT by applying the BSA was 9.3 months which was lower (not significantly) than MIRD (16.4 months; p-value= 0.61) with HR 0.71 (95% CI, 0.42-1.22; p-value=0.22) and PM (19.7 months; p-value= 0.61) with a HR of 0.77 (95% CI, 0.39-1.49; p-value=0.43) [**B**] The group with dosimetric prescription has a better median survival compared to the group with non-dosimetric prescription (16.4 versus 9.3 months; p-value=0.19) with a HR of 0.73 (95% CI, 0.46-1.16; p-value=0.19).*

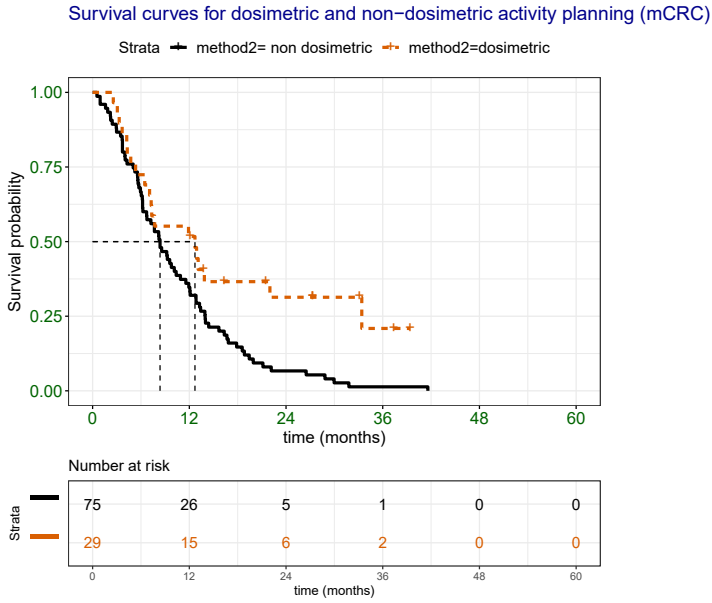

Figure 2.12: Patients with mCRC showed a better survival when the treatment was planned by using dosimetric methods compared to the BSA method. The median survival for dosimetric and non-dosimetric sessions were 12.7 and 8.4 months, respectively (p-value=0.007). Also, dosimetric prescription was positive predictor of survival (HR of 0.51; 95% CI, 0.31-0.84; p-value=0.008). Because the PM was applied only for two mCRC patients, survival analysis for these patients was not performed separately.

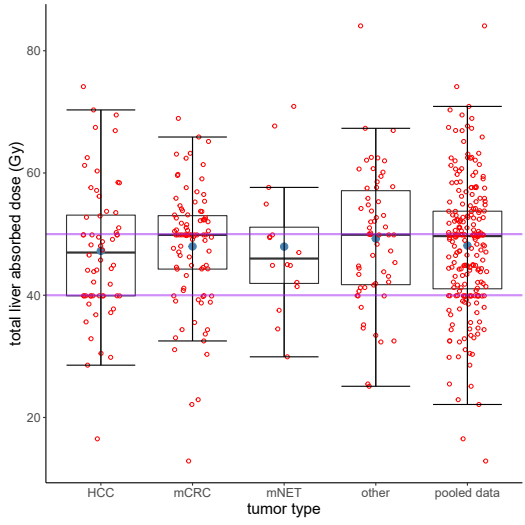

Figure 2.13: The box plot of total liver absorbed dose (normal liver and tumor) for different tumor types.The purple lines indicate absorbed doses of 40 and 50 Gy to the total liver (tumor and non-tumor tissue together) which are mentioned in several studies for activity planning [171, 203] but is considered less reliable for safety consideration compared to PM which considers the NTV absorbed dose [204].

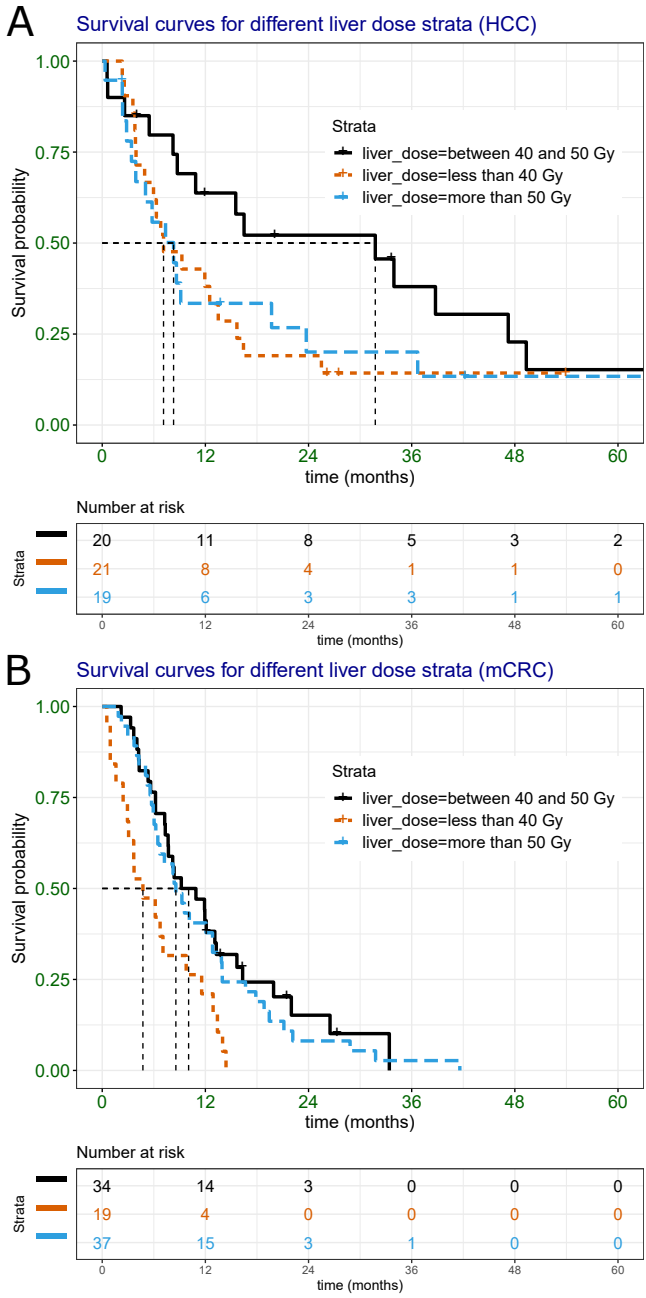

*Figure 2.14: [**A**] The median survival of the patients with HCC tumors receiving medium liver absorbed was 31.8 months compared to **(1)** low liver absorbed dose (7.1 months; p-value = 0.17) with a HR of 1.89 (95% CI, 0.93-3.86; p-value= 0.08), and **(2)** high liver absorbed dose (8.3 months; p-value = 0.19) with a HR of 1.79 (95% CI, 0.86-3.73; p-value= 0.12). [**B**] When comparing mCRC patients receiving medium liver absorbed dose (median survival of 10.1 months), a worse median survival (4.7 month, p-value = 0.006) and overall survival (HR of 2.5; 95% CI, 1.38-4.52; p-value= 0.002) was observed when the liver dose was lower. This association was not significant for patients receiving higher liver absorbed dose doses (8.6 month; p-value= 0.57) with a HR of 1.16 (95% CI, 0.71-1.89; p-value= 0.56).*

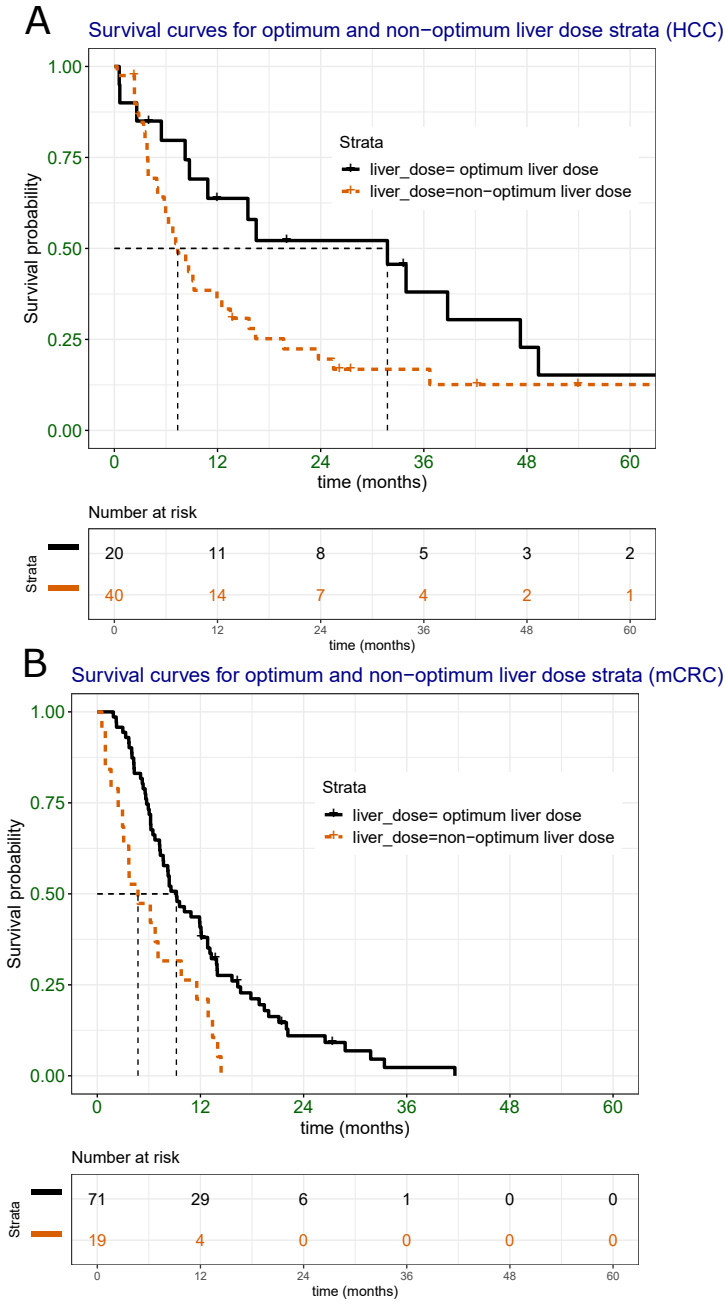

*Figure 2.15: [**A**] The median survival of the patients with HCC tumors receiving a liver absorbed dose either less than 40 Gy or more than 50 Gy (non-optimum dose) was 7.4 months compared to other patients receiving a liver absorbed dose of between 40 to 50 Gy (31.8 months; p-value= 0.056) with a HR of 1.84 (95% CI, 0.98-3.48; p-value= 0.059). [**B**] mCRC patients with non-optimum liver absorbed dose (less than 40 Gy) had a statistically significant decrease in median survival (7.2 versus 10.1 months; p-value= 0.001) and overall survival (HR of 2.31; 95% CI, 1.36-3.93; p-value= 0.002).*

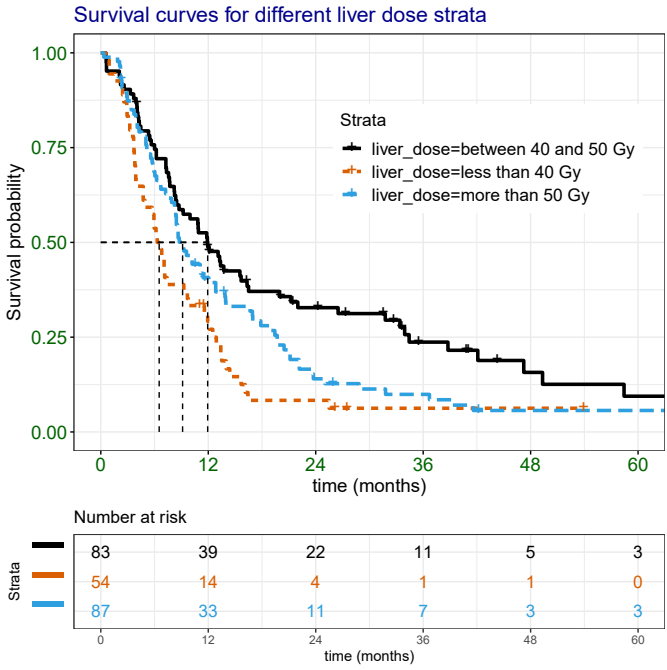

*Figure 2.16: Compared to Patients treated with medium total liver dose (median survival of 11.9 months) **(1)** patients treated with low liver dose showed a worse median survival (6.5 months; p-value= 0.001) and overall survival (HR of 2.06; 95% CI, 1.41-3.01; p-value < 0.001), and **(2)** patients treated with higher liver dose showed a trend to a worse median survival (9.1 months; p-value= 0.048), with a HR of 1.39 (95% CI, 1.00-1.94; p-value= 0.051).*

2.1.4 Yttrium-90 imaging and activity quantification

On the day of treatment, a nuclear medicine technologist prepares the prescribed activity for each LPT using a radionuclide calibrator (see section 1.7.5). Since November 2017, a day after administering the prepared activity (or in some cases on the day of the treatment), a TOF-PET image is performed to assess the distribution of the microspheres inside the body. As described in section 1.7.6, these images are used to perform a post-treatment evaluation/dosimetry. In total, the quantitative imaging has been performed for 61 patients from November 2017 to the end of 2019. A PET/CT camera (Discovery MI, GE Healthcare, Waukesha, MI, USA) was used for 12 patients (ten patients treated with resin microspheres and two patients with glass microspheres) and a PET/MR camera (Signa, GE Healthcare, Waukesha, MI, USA) was used for post-treatment imaging of 49 patients treated with resin microspheres.

Before using these modern cameras with an excellent time resolution for PET in the SIRT workflow, two procedures have been performed, first cross-calibration with the clinical radionuclide calibrators in UZ Leuven and a determination of the precision of the PET/MR in recovering the activity.

2.1.4.1 NEMA phantom filled with yttrium-90

In the first study, a NEMA phantom (PET Phantom - NEMA NU 2-2007) has been filled with yttrium-90 (^{90}Y-chloride) provided by BTG. The chelating agent EDTA was added to the solution to prevent adhesion of the activity to the wall of the phantom. The spheres and background of the NEMA phantom were filled with a solution with activity concentration of 0.704 and 0.093 MBq/ml as determined by the radionuclide

calibrator in our radiopharmacy room (IBC-Lite with a VIK-202 ionization chamber; Comecer, Joure, The Netherlands). The reported activity by the supplier was taken as the true activity but there might be an error there due to limited accuracy of the supplier value; for resin microspheres, the activity of the source vial is claimed by the manufacturer as 3.0 GBq ± 10% and some studies showed even a higher deviation (*e.g.* 26% higher than the activity labelled by the vendor) [205]. A PET/MR imaging was performed during 11 hours. The data were reconstructed with attenuation, scatter, and decay correction (as detailed in [206]). To validate the concentration ratio between the spheres and background activity, samples from spheres and background were measured using a gamma counter (1480 Wizard 3-inch gamma counter, Wallac / Perkin Elmer; Turku, Finland), which is referred to as wellcounter. Figure 2.17 shows the activity concentration ratio of the biggest sphere and background as determined by the different methods.

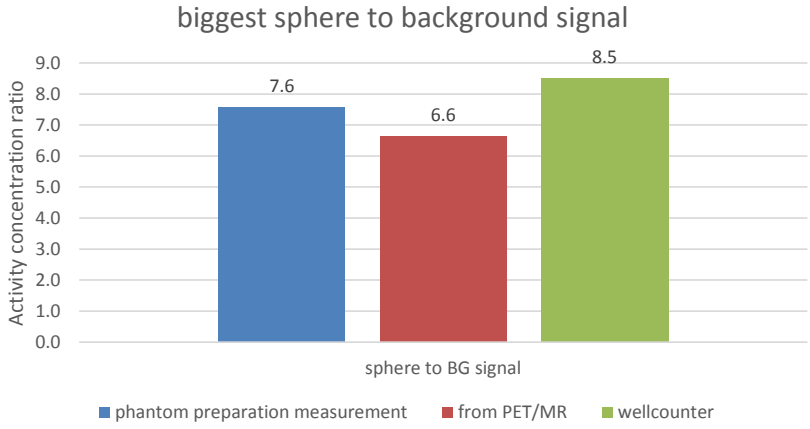

Figure 2.17: The ratio between the activity in the biggest hot sphere and background in the NEMA phantom; comparing the calibrated activity in the phantom preparation (using VIK-202 radionuclide calibrator), PET measurement and measured count on the well counter

The total recovered activity in PET was 20% lower than documented activity in the NEMA phantom (measured by the VIK-202 radionuclide calibrator); the total recovered activity in the PET reconstruction was 926 MBq at the time of imaging, while the total time corrected calibrated activity in the NEMA phantom was 1168 MBq.

2.1.4.2 Cross calibration with a Sirtex Vial

On November 16th 2017, a SIRT session was canceled at the last minute, and the vial was used for cross-calibration purposes. This vial has been imaged on the PET/MR camera on November 20th 2017. Two days later, the activity of this vial has been measured by two activity calibrators in the nuclear medicine department. The activity measurement by UZ Leuven equipment was within 10% for the declared activity by the supplier, which is a regulatory requirement, Federal Agency for Nuclear Control; Belgian radiological protection competent authority (FANC).

The result is provided in figure 2.18, which shows a better correspondence between the vendor (SIRTEX) provided activity (1.203 GBq) and the activity measured by activity calibrators- radiopharmacy room (IBC-Lite with a VIK-202 ionization chamber; Comecer, Joure, The Netherlands): 1.272 GBq and injection room calibrator (Capintec CRC®-55tR;Capintec, Ramsey, NJ, USA):1.269 GBq- than the total recovered activity on the PET/MR (1.434 GBq).

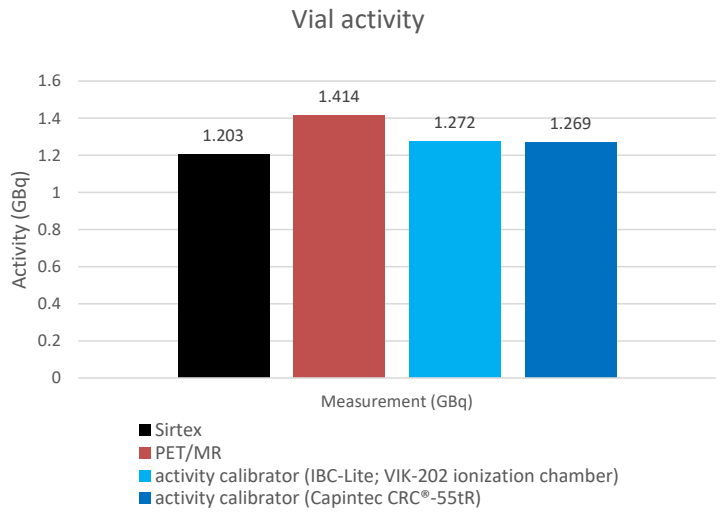

Figure 2.18: The activity of a SIRTEX vial was measured by two activity calibrators and PET/MR camera, the result of the activity calibrators were within 10% (legal aspect; FANC) of the vendor provided activity.

2.1.4.3 Total activity of the PET images for the patients

These initial simple studies provide some insight into the precision of the activity measurement using PET imaging for capturing the yttrium-90 distribution. For the NEMA phantom, the ratio between total activity in the PET image and calibrated activity was 0.79, and for the SIRTEX vial study this ratio was 1.11.

To investigate this more, we compare the measured activity on PET images and what has been documented as the prepared (calibrated) activity in the prescription sheets (see figure 2.19). For the patients imaged on the PET/CT camera (n=10), the ratio between the total activity in the reconstructed PET and calibrated activity has a median (first and third interquartile range) of 1.31 ([1.25,1.45]), the minimum and maximum of this ratio were 1.15 and 1.79.

For 49 patients imaged by PET/MR after treatment, the median (first and third interquartile range) was 0.95 ([0.86,1.01]) with minimum and maximum ratio of 0.63 and 1.25.

Any deviation from unity for this ratio could be explained by:

- **residual activity in the vial, catheter,...:** we believe that this would not explain substantial differences or an overestimation of the activity in the PET images (*e.g.* ratio above 1 which was the case for all PET/CT studies).
- **calibration error:** as it is mentioned in the vial study, the calibrators have shown a better correspondence with the vendor, but still the volume, geometry, and the positioning of the vial in the activity calibrator could affect the precision of the measurement. Because the same highly skilled expert who was aware of this phenomena performed the vial measurement in clinical routine very carefully, we believe it could theoretically produce only a systemic error and not such a wide deviation, which has been observed.
- **reconstruction error:** this result suggests that the PET reconstruction on two cameras from the same vendor behaves differently (the preparation of the activity is the same and performed by the same expert). Therefore, the acquisition and reconstruction parameters were examined, which revealed that the problem may have

been caused by a different parameter selection in the scatter correction procedure. This will be investigated.

Despite the source of this discrepancy, two options are available for using ^{90}Y-PET imaging for post-treatment dose calculation: **(1)** using the reconstructed PET image as a quantitative representation of the activity distribution; **(2)** by assuming that the PET image is relatively quantitative and the calibrated activity is deposited completely within the PET field of view (*i.e.* no activity outside the imaging area and no residual activity in the administration set). Hence, scaling of the PET image would allow us to recover the total administered activity. In this manuscript, we used the second method. For further investigation, we believe that examining the residual activity, and cross-calibration of the different PET cameras together with the activity calibrators using phantoms and syringes (to investigate the effect of the geometry, position, and volume) are beneficial to understand the source of this error. Some studies investigated on methods on end-user activity calibration and the US national institute of standards and technology (NIST) traceable activity calibration standards for resin microspheres [205, 207].

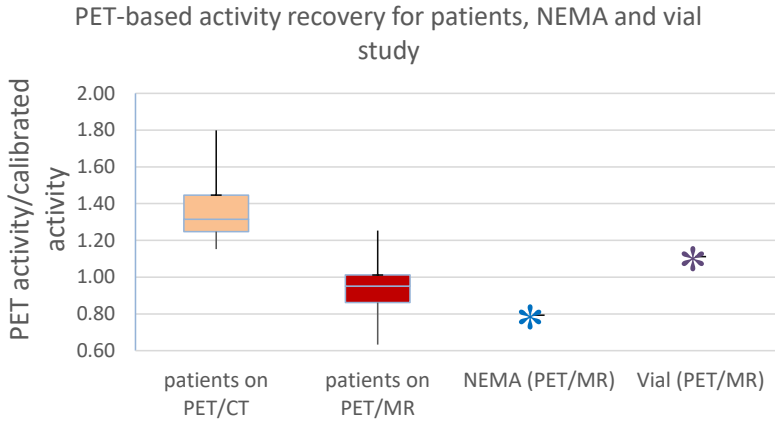

Figure 2.19: When comparing the total administered activity measured using radionuclide calibrators and reconstructed activity in the different PET systems, a significant deviation has been observed. Importantly, our PET/CT camera always measures an activity significantly higher than what has been reported in the clinical documents due to quantification inaccuracies.

2.2 In house software for multi-modal image analysis in SIRT workflow

The objective of our in-house software, developed as part of this research project, is to **(1)** implement an image registration tool to align all pre- and post-treatment relevant images to a common space, **(2)** employ advanced and multi-modal segmentation methods to improve VOI (*e.g.* TV, liver, LPT, ...) delineation, and **(3)** convert predictive and therapeutic activity uptake information into the relevant dosimetric reports. This workflow should support a number of medical imaging modalities which are part of the SIRT routine according to the guidelines, vendor manuals, and the clinical protocol in UZ Leuven [153]:

- Diagnostic images either [^{18}F]FDG-PET/CT for FDG-avid tumors or MR or ceCT for non-FDG-avid tumors (or [^{68}Ga]Ga-DOTA-TATE PET/CT for mNET tumors): for patient selection, tumor definition and volumetric analysis (liver volume, lobe volumes, and tumor burden), as detailed in 1.7.1.

- CBCT images: for identifying the liver arterial anatomy, evaluating tumoral feeders, defining LPT, precise arterial mapping and identifying extrahepatic feeders, which is described in section 1.7.3.
- [^{99m}Tc]Tc-MAA SPECT/CT: for simulating the therapy session: to provide a prediction of extrahepatic shunts (lung, stomach, ...) and spatial distribution of the treatment activity within the liver (see section 1.7.3).
- ^{90}Y TOF-PET imaging after the administration of the ^{90}Y-microspheres: to verify the accumulation of the microspheres within the TV and NTV (section 1.7.6).

In current clinical routine, in absence of an image registration algorithm, these images are usually analyzed side by side and often with manual segmentation and visual assessment. Some studies are promoting advanced image processing techniques, such as image registration and (semi-) automatic VOI delineation to amend patient selection, IA calculation, definition of treatment strategy, treatment verification, and analysis of the follow-up studies [73].

Based on the new EU directive [201], treatment prescription and therapy verification need to be patient-specific. This reflects the emerging need for image acquisition and processing efforts in this field [208]. This procedure can be used both treatment planning and treatment verification with more accuracy (see section 1.5.5). For example:

- **combined VOI segmentation:** without a decent image registration technique, all volumes should be derived from a single image (CT or MR). Using our proposed approach, each VOI is delineated by employing the most relevant available modality; defining semi-automatically:

  1. tumors on MR, [^{68}Ga]Ga-DOTA-TATE PET, and [^{18}F]FDGPET, the gold standards for primary tumors, mNET and other metastatic liver tumors, respectively,
  2. total liver on multiple CT or MR, and
  3. perfusion territories on CBCTs instead of using anatomical landmarks on CTs.

  This multi-modal VOI segmentation could be used as an alternative or quality control step for the current clinical VOI segmentation workflow. Any difference in VOI volumes could influence the clinical decision making process.

- **dosimetry/administered activity report:** matching between an observed and circumscribed tumor location (based on [^{68}Ga]Ga-DOTA-TATE or [^{18}F]FDG uptake or MR images) and [^{99m}Tc]Tc-MAA uptake is a crucial factor for treatment planning before treatment. Also, after treatment a good correspondence between tumor location and ^{90}Y-microspheres (*i.e.* from ^{90}Y-PET) uptake can be used for predicting treatment outcome. These mappings are currently checked visually on different studies side by side. An accurate multi-modal image registration will enable a voxel- or tissue-level analysis of the TV and NTV activity uptake and absorbed dose. These results cover clinically valuable information in:

  1. **patient selection:** to evaluate if SIRT is a suitable option for a particular patient,
  2. **therapy planning:** to check if the selected catheter tip position is optimal or treatment re-planning should be considered,
  3. **activity prescription:** based on predictive doses in different levels, *e.g.* organ-level (total liver absorbed dose), tissue-level (dose to the normal and non-normal liver), or at voxel-level dosimetry,
  4. **comparing treatment predicted dose and actual absorbed dose:** to check whether the treatment reaches its goal.

A multi-modal image analysis procedure is offered for processing and analyzing all pre-treatment and post-treatment images (see chapter 3). Figure 2.20 describes the software

design. First, this involves aligning all images to an identical space. Then a semi-automatic and multi-modal delineation of the desired tissues (*e.g.* entire liver, tumors, and LPT) using information from all relevant studies are performed. The final outcome is the pre- and post- treatment dosimetry in different levels, calculating prescribed IA using various proposed methods, post-treatment verification and possible analysis of follow-up images.

In this project, we also investigated the role of CBCT in VOI definition and its impact on dosimetry. To our knowledge, this had not yet been done before. In addition, there is no other study investigating the accuracy of multi-modal image registration involving non-contrast, low-dose CT ([^{99m}Tc]Tc-MAA study). Because our analysis showed that registration accuracy was adversely affected by the noise of these CTs, the CT tube current has been increased in our clinical [^{99m}Tc]Tc-MAA-SPECT/CT studies (higher than a low dose CT, which is typical for a non-contrast enhanced hybrid CT but still lower than a high dose diagnostic CT protocol).

2.2.1 Image registration algorithms

The CT from the [^{99m}Tc]Tc-MAA study is selected as the reference image because the SPECT image in the same session is the core of the predictive dosimetry, and this study is performed for all patients undergoing SIRT. Therefore, all anatomical (CT, MR, and CBCT) images are registered to this image non-rigidly. Using position information extracted from the digital imaging and communications in medicine (DICOM) header, the functional images (*i.e.* PET and SPECT) are registered using the deformations obtained from their anatomical counterpart (*i.e.* MR or CT).

Developed algorithms (described in section 3.3.4.1) for image alignment include:

- **Rigid registration:** A multi-resolution, rigid registration is always performed before non-rigid registration to accelerate the final registration and make it more robust. For CT-to-CT registration, the sum of the squared differences (SSD), and for inter-modality registration, mutual information (MI) is used as the cost function. For cases with a disparate liver shape between floating and reference images, the liver voxels, segmented out by employing a CNN developed in our group, are given a higher weight in the computation of the cost function. In cases for which the rigid registration is not good enough as the initial step for non-rigid registration, a manual guidance tool is provided. In this tool, the user is free to match a set of points in the reference and floating image to guide the registration.

- **Non-rigid registration:** A multi-resolution, non-rigid registration algorithm, developed at our institution, was the basis for our further research. The non-rigid registration is based on the spring algorithm, that is detailed in [209]. In this algorithm, the deformation is expressed with a displacement vector for each voxel. In our algorithm, it is assumed that each pair of neighboring voxels are interconnected via a non-linear spring. Voxels are assigned to tissue classes with uniform intra-class, and different inter-class spring characteristics like stiffness and maximum allowed deformation. These classes include air, liver, non-liver tissue and bone, and these are defined by thresholding the floating image. The liver class could also be determined by the convolutional neural network (CNN) liver segmentation algorithm described in the next subsection. A lower rigidity is applied to the non-liver voxels compared to a high stiffness to the liver. This encourages realistic deformations and discourages extreme deformations in (almost) uniform regions (*e.g.* intra-organ regions) where there are not many features to guide the image registration. It also helps to minimize the effect of aligning other structures adjacent to the liver on the alignment of the liver. MI or SSD is used as the cost function for inter- and intra-modality registration, respectively. For cases where the registration fails due to an extensive non-rigid liver shape deformation or real liver volume change between floating and reference images, the operator has the option to guide the registration. This is done by defining pairs of corresponding points

in both images. During the registration, a high cost is assigned to the distance between these points to ensure that they will be aligned as intended.

As a quality assurance (QA) step for the non-rigid registration, a local Jacobian determinant was provided to assess the degree of compression or expansion in each proposed VOI (especially within the liver). To evaluate the local non-rigidity of the registration visually, the deformation is applied to a grid of parallel planes. In the next chapters (3), the result of registration evaluation is presented.

2.2.2 Liver segmentation

A multi-modal joint region growing method has been designed to outline the liver using information from the CT component of the [^{99m}Tc]Tc-MAA workup and other pretreatment images (*e.g.* ceCT and PET from [^{18}F]FDG study). The initial step of region growing is manual segmentation of the liver in every 15$^{\text{th}}$ transverse slice on the CT component from the [^{99m}Tc]Tc-MAA study. In each step of the subsequent iterative region growing, the mean and standard deviation of the segmented voxels in all selected images in the previous step is employed to re-label some of neighboring voxels as the liver. Finally, the resulting VOI is adjusted manually and closing and opening operations are applied. This method is described in detail in the next chapter (3). It is also possible to import the delineations from clinical/commercial softwares in DICOM standard format (*e.g.* RTstruct).

Currently, a faster alternative and automated method is the CNN that is developed in-house as part of another research project supporting radionuclide therapy (see chapter 4) to delineate the liver on CT images (*i.e.* CT image from the [^{99m}Tc]Tc-MAA study). The CNN model is a revised version of a dual pathway, 11-layer deep, three-dimensional structure (named DeepMedic) that is initially designed for brain lesion segmentation [210]. The modified model contains three pathways, each consisting of ten layers, which are connected via $3 \times 3 \times 3$ convolutional kernels followed by two common pathways based on $1 \times 1 \times 1$ convolutional kernels. It was trained with 139 datasets from different liver segmentation challenges and SIRT patient datasets from UZ Leuven [211].

2.2.3 Perfusion territory (lobe) segmentation

In the current clinical workflow, a diagnostic baseline CT or MR image is used to split the liver into liver lobes (or segments) based on anatomical landmarks, predominately based on venous structures. Here, an alternative approach is provided, where the liver was partitioned using contrast-enhanced CBCT images. Contrast enhancement in the early or late arterial phase of the CBCT study is used to separate different parts of the liver, which are called liver perfusion territories instead of liver lobe or segments (see chapter 3). A graphical user interface was developed to cut the liver on CBCT (or CT) by drawing just a few separation lines on different transverse slices. It usually takes less than a minute for the expert for each case. The next chapter describes the result of the LPT segmentation using CBCT images.

2.2.4 Tumor segmentation

As mentioned before, depending on the tumor type, different image modalities are favored to delineate the tumors. As mentioned in section 1.7.1, the gold standard modality for segmenting FDG-avid and mNET tumors are [^{18}F]FDG-PET and [^{68}Ga]Ga-DOTA-TATE-PET. For other tumor types, MR image is routinely preferred. In some circumstances, other modalities ([^{99m}Tc]Tc-MAA-SPECT, ^{90}Y-PET, ceCT, and CBCT) are used for tumor definition.

For thresholding the functional images (PET or SPECT), an adaptive thresholding scheme (tumor-specific thresholding) is used to delineate tumors on the uptake image [212]. Initial segmentation (so-called tumor core) is set to $\mu + 2.802 \times \sigma$, where μ and

σ are mean and standard deviation of the liver activity uptake. Then, for each tumor core, a specific threshold is calculated using individual core and background uptake. This method is described in detail in the chapter 3.

For anatomical images, either a manual tool or region growing from manually provided seed points in each slice of the median filtered image is provided. But, it appeared over time that our tools are inferior (*i.e.* more time consuming) than available commercial softwares (*e.g.* MIM software). It is also possible to import the resulting contours from other softwares in a standard DICOM format.

2.2.5 Dosimetry

In this step, [^{99m}Tc]Tc-MAA-SPECT or ^{90}Y-PET is utilized to report dose prediction and dose calculation, respectively, within each VOI that has been segmented (*i.e.* liver, LPT, and TVs). The dosimetry is performed at the tissue level (PM) or voxel-level (see section 1.5.5). For the tissue level, the MIRD method is applied by assuming the radiation is homogeneously distributed within each of the compartments. For the voxel-level dosimetry, the calculations can be done according to the local deposition method or by making use of pre-defined dose-point kernels based on Monte Carlo simulation. Both methods have been implemented (see section 1.5.5.3). Voxel-level dosimetry provides cumulative dose-volume histograms (cDVHs) that present the heterogeneity of the absorbed dose distribution in the different compartments. The dose prescription and dosimetry results are detailed in chapter 4, some examples also provided in section 2.3 and chapter 5.

2.2.5.1 Injected activity calculation and pre-treatment report

A software was developed that generates LaTeX -based pre-treatment reports (see the subsection 2.3). This report consists of:

1. **validation of segmentation results:** a comparison between semi-automatic segmentation and manual segmentation volumes performed by an expert
2. **IA calculation:** the software computes the IA based on different methods mentioned in the microsphere package insert and guidelines, including the empirical method, BSA, SIRFLOX look-up table, MIRD and PM method, and voxel-level dosimetry.
3. **absorbed dose report:** a detailed voxel-level dosimetry analysis is also provided for each of above mentioned activity and the prescribed activity.

2.2.5.2 Post-treatment report and pre- and post-treatment comparison

An automatic routine has been designed to generate a LaTeX -based post-treatment report (one example is provided in the next subsection, 2.3). This report includes the voxel-level dose verification using the ^{90}Y-PET image.

Moreover, a comparison between [^{99m}Tc]Tc-MAA based dose prediction and actual dose calculation is reported using different measures to indicate if the therapeutic goal was reached:

1. comparing absorbed doses in different VOIs (*e.g.* TV and NTV) is the most straightforward way to compare predictive and measured absorbed dose,
2. the difference between the cDVH and DVH curves provides information about a possible deviation in absorbed dose distribution,
3. a voxel-by-voxel dose difference analysis evaluates the predictive power of the [^{99m}Tc]Tc-MAA study (see 2.3.8.1),
4. In clinical routine, the desired absorbed dose to the TV and NTV compartments are derived from TCP and NTCP curves, respectively. These models usually have a sigmoid shape. This means that the probability of tumor control and non-tumor complication changes dramatically around a critical absorbed dose. So, for each of

these compartments, an absorbed dose change below and above certain thresholds has a smaller effect on the cells. In other words, in the area of extensive tumor over-dosing or under-dosing, the tumor cell dose difference does not change probability of the tumor control a lot. For the non-tumoral liver cells, also absorbed dose difference below or above the safety threshold does not alter the likelihood of complications a lot.
By considering this idea, one could compare predictive and measured absorbed dose by employing these dose-levels in the tumor and non-tumor compartments to investigate if the predictive dosimetry could estimate ideal/non-ideal absorbed doses in each compartment (see 2.3.8.2). For example, if it is desired to know to what extent [^{99m}Tc]Tc-MAA-based dosimetry predicts tumor under-dosing, by choosing a sufficient tumor dose level (*e.g.* 100 Gy), a joint histogram is introduced to report the percentage of the voxels within the TV that received more than 100 Gy in both predictive and measured absorbed doses. It can, also, report the volume percentage for which the [^{99m}Tc]Tc-MAA predicted correctly or wrongly an under-dosing within the tumor, and wrongly sufficient tumor coverage. The same concept is also provided to validate the predictive value of the [^{99m}Tc]Tc-MAA-based dosimetry for NTV over-dosing or substantial lower irradiation.

5. a routine is also provided to extract the γ-index to verify the match between [^{99m}Tc]Tc-MAA dose distribution and actual dose distribution (see 2.3.8.3).
The γ-index evaluation method [213], which is also used in radiotherapy [214, 215], quantifies the dose differences between pre- and post-treatment dosimetry by combining information about the dose values and about their spatial distribution [216, 217]:
   - In low dose gradient regions, the doses are compared directly, based on a dose-difference (DD) acceptance tolerance, *e.g.* 3% of the maximum of the measured dose (global γ-index) or 3% percentage of measured dose in each voxel (local γ-index).
   - In high dose gradient regions, where a small spatial deviation between two dose distributions results in a large dose difference, a distance-to-agreement (DTA) acceptance tolerance (*e.g.* 3 mm or 3 voxels) is used.

   Analytically, the γ-index at a point r_t is defined by comparing this point with each point r_r in a distance range:

$$\gamma(r_t) = \min_{\forall r_r} \Gamma(r_t, r_r) \tag{2.1}$$

   Where,

$$\Gamma(r_r, r_c) = \sqrt{\frac{|r_r - r_t|^2}{\mathrm{DTA}^2} + \frac{|D_r - D_t|^2}{\mathrm{DD}^2}} \tag{2.2}$$

   Here, D_t and D_r are the target dose value at r_t and the reference dose value at r_r, respectively. The pass—fail criterion is then defined. If the γ-index is equal to or less than 1, the dose at the spatial target point is considered to pass the test. Conversely, if the γ-index is greater than 1, the test fails.

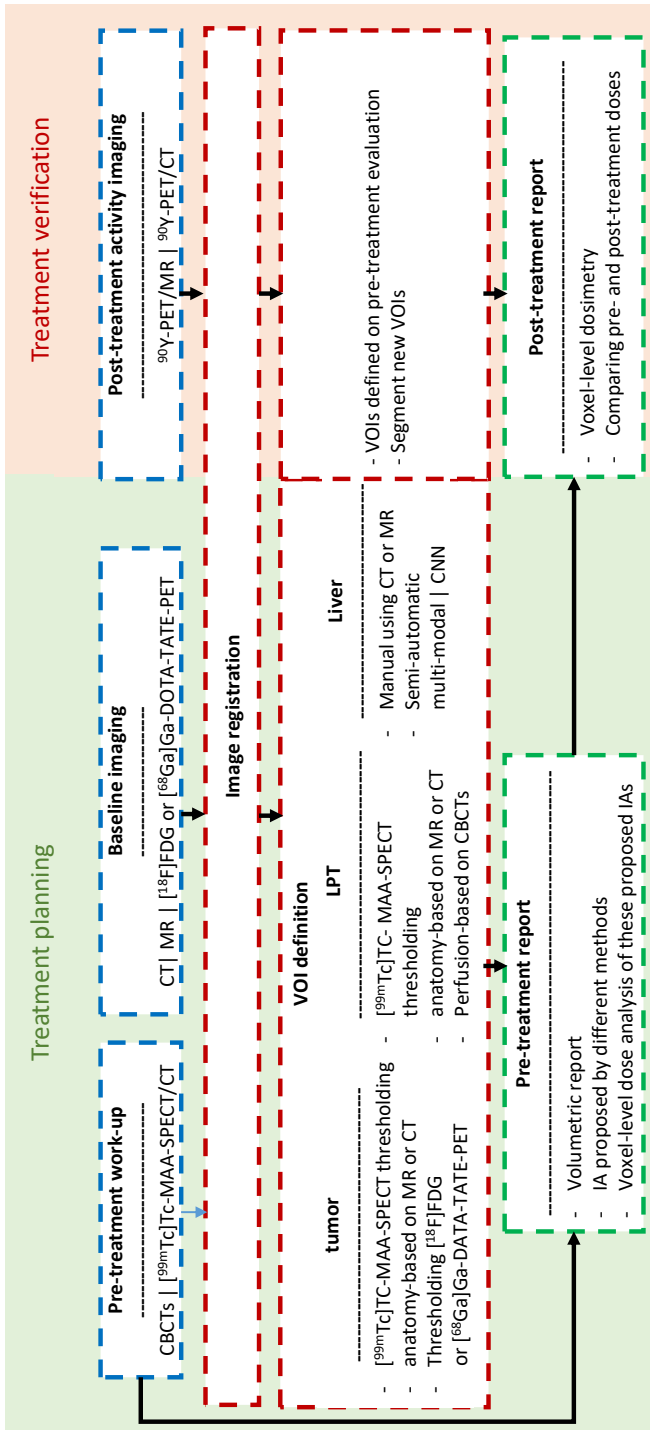

Figure 2.20: The workflow of proposed software for multi-modal image analysis in the SIRT dosimetry

2.3 A clinical case of a pre- and post-treatment dosimetry

Here, one example of a prospective predictive dosimetry and dose verification is reviewed.

2.3.1 Patient information

Here in tables 2.1 and 2.2, relevant information about the patient is given. This patient suffers from bilobar mNET.

SIRT code	Gender	Weight (kg)	Height(m)	BSA (m2)	BMI(kg/m2)
YPT043	OTHER	74	1.58	**1.76**	29.6

Table 2.1: Patient information

preSIRT date	SIRT date	Tumor type	SIRT type	LSF(%)
dd/mm/yyyy	dd/mm/yyyy	**mNET**	**bilobar**	5.8

Table 2.2: Therapy information

Relevant clinical information from tumor board report:

- Known rectal neuroendocrine tumor.
- Multifocal liver metastasis in the left and right liver lobe with an increase in volume and number. The most massive liver injury was in the left liver lobe.

Relevant clinical information from pre-treatment workup:

- Heterogeneous activity distribution observed. It was mostly pronounced in the right liver lobe. An intense localization in segments I, VIII, and IV was reported.
- LSF of 5.8% has been estimated based on planar imaging.

2.3.2 Activity prescription

For this patient, the PM was employed for activity planning. In this setting, an absorbed dose of 25 Gy to the NTV, and 150 Gy to the TV has been projected:

- **left lobe IA**: 1.833 GBq
- **right lobe IA**: 1.560 GBq

The volumes have been determined on a diagnostic CT image (see table 2.3), and a T/N ratio of 12.3 has been estimated using some ROIs over [^{99m}Tc]Tc-MAA-SPECT/CT. An inconsistency in the T/N ratio, volumes, and absorbed doses may be perceived when a different segmentation and dosimetry method is practiced (*e.g.* our voxel-level dosimetry, see table 2.3). More details are provided in section 1.5.5.2. All the activities and absorbed doses in this report were calibrated to the planned treatment time.

2.3.3 Proposed multi-modal image analysis and dosimetry method

Figure 2.38 provides one slice of the registered images and VOI segmentation.

segmentation (see section 2.2):

- [^{99m}Tc]Tc-MAA-CT from [^{99m}Tc]Tc-MAA study was utilized for liver segmentation. The segmentation was performed by an in-house CNN model trained for liver segmentation on CT images. Then, the output of the CNN was manually adjusted.

– [^{68}Ga]Ga-DOTA-TATE-PET was used for tumor definition (threshold at 15% of SUV_{max} of the tumor); the tumor definition was confirmed by our physician.
– CBCTs were employed for lobe separation.

Dosimetry (see section 2.2):

– Voxelized fractional uptake was estimated from [^{99m}Tc]Tc-MAA-SPECT and ^{90}Y-PET/CT for predictive and measured dosimetry, respectively.
– Activity maps were masked by the segmented liver. It was assumed that all the IA would be retained inside the liver perfusion territories.
– To convert activity maps (Bq) to the absorbed dose distribution (Gy), a local energy deposition method was used.

2.3.4 Overview of segmentation

As described in table 2.3, there is a good agreement between the total liver volume reported in the prescription sheet and CNN result (Δ = 41 ml).

Also, volumes of the left and right liver lobe based on contrast-enhancement in the CBCTs and volumes that have been summarized in the prescription sheet (CT-based separation using anatomical landmarks) were comparable. The difference between the left to the entire liver volume ratios had a difference of less than 1%.

The situation for tumor segmentation was somewhat different. The volume of the anatomical tumor segmentation on CT (prescription sheet) was around twice the [^{68}Ga]Ga-DOTA-TATE-PET-thresholding volume (our proposed method). In the entire liver, CT suggested a tumor involvement of 58%, but our software reported a tumor involvement of 33% (see table 2.3).

One transaxial slice of the segmentation is provided in figure 2.38.

parameter	method	left lobe	right lobe	entire liver
TV (cc)	clinical routine	759	622	1381
	new software	471	325	796
	Δ	-288	-297	-585
NTV (cc)	clinical routine	131	872	1003
	new software	440	1189	1629
	Δ	309	317	626
entire VOI vol (cc)	clinical routine	890	1494	**2384**
	new software	911	1514	**2425**
	Δ	21	20	41
tumor involvement (%)	clinical routine	**85.28**	**41.63**	**57.93**
	new software	**51.74**	**21.46**	**32.83**
left to entire (%)	clinical routine	-	-	**37.33**
	new software	-	-	**37.56**

Table 2.3: segmentation analysis, comparing our segmentation results and clinical records

2.3.5 Calculated activity based on different models

In the previous chapter (see 1.7.4), various activity planning methods are described in detail. The SIRFLOX-lookup table (noted as SFX) is a modified version of the BSA method, which was used in the SIRFLOX trial [169]. Some acronyms are used in the tables of this subsection:

– **TI:** tumor involvement
– **LSM:** lung shunt modifier for reducing IA based on empirical method when LSF is higher than 10% (see section 1.7.4.1)

- **LPM:** liver part modifier to split the IA in the right and left lobe injection when using empirical method (see section 1.7.4.1) or BSA method (see section 1.7.4.2)
- **FU_{VOI}:** fractional uptake of the VOI, *e.g.* TV or NTV
- **IA*:** initial total IA before splitting in the left and right perfusion territory (sum of IAs for all the LPTs)
- **$MIA_{org/VOI}$:** maximum activity based on the organ or VOI dose tolerance
- **$mIA_{org/VOI}$:** minimum activity based on the organ or VOI dose lower criterion
- **IA_{method}:** lobe IA based on the mentioned method
- **D_{VOI}:** mean dose to the VOI, *e.g.* TV or NTV
- **Vx_{VOI}:** volume percentage of the VOI that receive at least x Gy, *e.g.* $V90_{TV}$ is volume percentage of the tumor volume that receive at least 90 Gy
- **Dx_{VOI}:** the minimum absorbed dose that x% of the VOI received, *e.g.* $D50_{NTV}$ is volume percentage of the NTV that receive at least 50 Gy

Injected activity by empirical method

lobe	TI	LSM^+	IA* (GBq)	LPM	IA_{emp}
left	0.33	1.0	2.5	0.38	0.939
right				0.62	1.561

$^+$: LSF of 5.8% was used (table 2.2).

Table 2.4: Empirical method's parameters [153]; activities are reported in GBq

Injected activity by BSA method

lobe	BSA(m^2)	TI	LPM	IA*	$IA*_{tot}$	MIA^+_{lung}	IA_{BSA}
left	1.757	0.52	0.38	0.779	1.885	10.372	0.779
right		0.21	0.62	1.106			1.106

$^+$: LSF of 5.8% was used, and 30 Gy was set as the lung absorbed dose tolerance.

Table 2.5: BSA method's parameters [153]; activities are reported in GBq

Injected activity by SIRFLOX look-up table

lobe	BSA(m^2)	TI	LSF(%)	IA*	LPM	IA_{SFX}
left	1.757	0.33	5.8	1.900	0.38	0.714
right					0.62	1.186

Table 2.6: SIRFLOX method's parameters [169]; activities are reported in GBq

Injected activity by MIRD method (MIRD50 or 50 Gy to the entire lobe)

For the total liver (TV and NTV compartments together) a dose criterion of $D_{\text{entire liver}} < 50$ Gy is set, which corresponds to an activity concentration of 1.0 GBq per litre [203].

lobe	Vol_{liv}	IA*	MIA_{lung+}	LPM	IA_{MIRD}
left	2.425	2.425	10.372	0.38	0.911
right				0.62	1.514

$^+$: LSF of 5.8% was used, and 30 Gy was set as the lung absorbed dose tolerance.

Table 2.7: MIRD method's parameters; activities are reported in GBq

Injected activity by compartmental partition model

IA_{PM-low} and $IA_{PM-high}$ methods denote the lowest and highest acceptable IA (minimum and maximum of the therapeutic window, if there is any). So, IA_{PM-low} is more conservative and aims to calculate an IA, which leads to a sufficient dose to the TV while keeping the NTV dose below the safety threshold. On the other hand, $IA_{PM-high}$ increases the IA up to reaching NTV tolerance dose.

VOI	D_{NTV} (Gy)	D_{TV} (Gy)	D_{lung} (Gy)
Lobes or entire liver	< 50	> 150	< 30

Table 2.8: Criteria [87, 159, 218] used for the compartmental PM

lobe	T/N	FU_{TV}	FU_{NTV}	mIA_{TV}	MIA_{NTV}	MIA_{lung}	$IA_{PM\text{-}low}$	$IA_{PM\text{-}high}$
left	1.30	0.58	0.42	2.436	1.054	10.372	1.054	1.054
right	4.36	0.54	0.46	1.798	2.611		1.798	2.611

Table 2.9: Compartmental Partition method's parameters; activities are reported in GBq

As one can see in table 2.9, there is a therapeutic window in the right lobe, as the maximum activity (based on NTV mean absorbed dose) is higher than the minimum activity (based on TV mean dose). On the contrary, the calculations for the left lobe did not demonstrate a range of acceptable activities; which means that for the left lobe, the T/N ratio is not sufficient to spare the NTV from maximum tolerance mean dose when deciding to achieve an acceptable TV mean dose.

Injected activity by voxel-level dosimetry

Similar to PM, $IA_{vox-low}$ and $IA_{vox-high}$ denote the lowest and highest acceptable IA.

VOI	D_{NTV} (Gy)	$V50_{NTV}$ (%)	D_{lung} (Gy)	D_{TV} (Gy)	$V80_{TV}$ (%)
Lobes or liver	< 50	< 50	< 30	> 150	> 70

Table 2.10: Criteria for voxel-level activity planning [87, 159, 218–220]

lobe	$mIA(D_{TV})$	$mIA(V80_{TV})$	$MIA(D_{NTV})$	$MIA(V50_{NTV})$	MIA_{lung}	$IA_{vox-low}$	$IA_{vox-high}$
left	2.532	12.277	1.096	1.526	10.372	1.096	1.096
right	1.869	1.632	2.715	4.431		1.869	2.715

IA(criterion) denotes the IA based on a defined criterion.

Table 2.11: Voxel-level dosimetry method's parameters; activities are reported in GBq

As illustrated in table 2.11, there was a therapeutic window for the right lobe ([1.869, 2.715] GBq). On the other hand, in the left lobe there was no activity that met all the criteria; an injected activity of 1.096 GBq was the boundary of the safety threshold, but to fulfill the TV mean and volumetric dose criteria, the IAs of 2.532 and 12.277 GBq would be needed, respectively. The reason behind such high IA to satisfy the volumetric tumor criterion was the presence of a low [^{99m}Tc]Tc-MAA uptake area in the tumor in this lobe (see figure 2.38-B). As illustrated in figure 2.38-D, based on [^{68}Ga]Ga-DOTA-TATE-PET, this area was not suspected to be necrotic. Fortunately, post-treatment imaging showed a better uptake within this area (see figure 2.38-F), which is discussed in the next section.

Figures 2.22 to 2.25 represent the mean dose and some cDVH parameters within the TV and NTV compartments in different VOIs as a function of the administered activity. The mean dose increased linearly with IA. The percentages of the compartment that received at least critical amounts of absorbed dose are also provided.

Figure 2.22 describes the change of some dosimetric parameters in the NTV in the right lobe by increasing the IA. As can be seen in this figure, all the curves were increasing slowly. This means that a wide range of acceptable IA was predicted based on NTV irradiation. This is mostly due to a large volume of the NTV which received negligible [^{99m}Tc]Tc-MAA uptake, as can be seen in figure 2.21 (this can be seen as a very early drop in figure 2.28-B, *i.e.* very low doses). The opposite situation could be observed in the left lobe (see figure 2.24), where the dosimetric parameters increased with a higher steepness below 1.5 GBq and became close to their convergence to a high volume percentage around 2.5 GBq. This means that NTV was more at risk of over-irradiation for this lobe compared to the right lobe, due to a considerable uptake all over the NTV (this can be seen as a relatively late drop, *i.e.* median high doses, in the cDVH of the NTV, see figure 2.29-B).

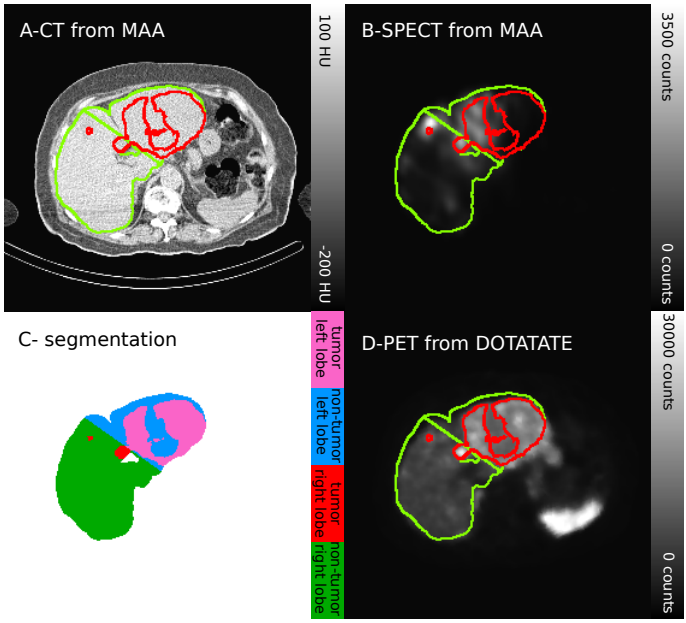

*Figure 2.21: A transaxial slice of the images illustrates a large volume of the NTV within the right lobe which received very low [^{99m}Tc]Tc-MAA uptake; **[A,B]** CT and SPECT images from pre-treatment workup, **[C]** segmentation map, in other images, the green and red contours represent the liver and tumor segmentation illustrated here, **[D]** CT and PET from baseline image ([^{68}Ga]Ga-DOTA-TATE study).*

On the other hand, TV dose parameters within the right lobe, which were presented in figure 2.23, showed a good dose coverage in the range of 1 to 3 GBq of the activity; the curves grow very fast and reach a convergence of more than 90% coverage (which could be seen as a so-called shoulder or flat line at the beginning of the cDVH for TV, *i.e.* very low doses, see figure 2.29-C).

Also, figure 2.25, which reflects the effect of administered activity on the dose parameters of the TV in the left lobe, shows that while the mean dose to the TV increased well by the increase in the administered activity, the tumor coverage in terms of cDVH parameters were not adequate; an early convergence was observed for the curves, but

they converged to only around half of the TV. Even a very high IA (2 to 6 GBq) was not enough to cover more than 65% of the TV with a sufficient dose because of the presence of a relatively big low uptake area within the TV. This kind of result could only be obtained with voxel-level dosimetry, and the mean dose to the TV (PM) could easily fail to show insufficient TV absorbed dose coverage because the mean dose increased linearly with the IA (which can be seen as a very fast early drop, *i.e.* very low doses, and an late shoulder in the cDVH of TV, *i.e.* medium high doses, see figure 2.28-C). The post-treatment dosimetry is discussed in section 2.3.8.

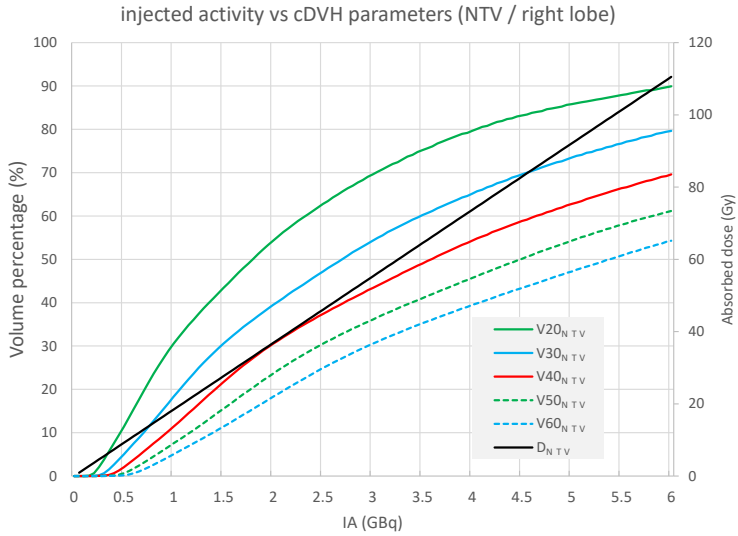

Figure 2.22: Mean dose and cDVH parameters in the right lobe as a function of IA

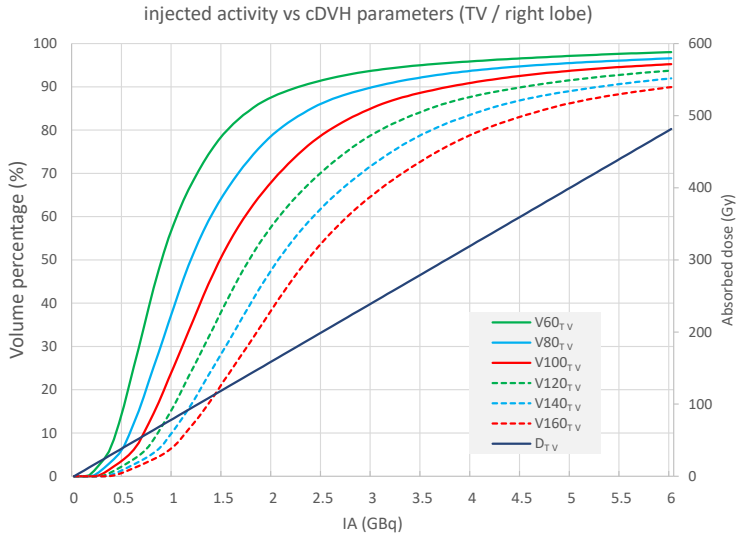

Figure 2.23: Mean dose and cDVH parameters in the right lobe as a function of IA

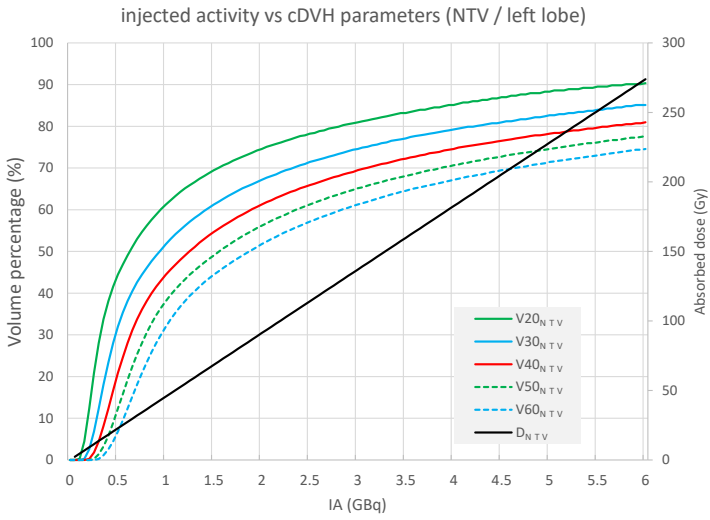

Figure 2.24: Mean dose and cDVH parameters in the left lobe as a function of IA

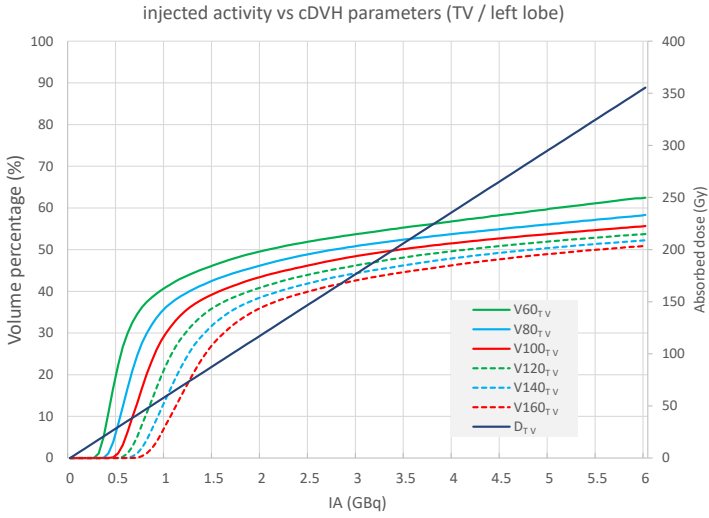

Figure 2.25: Mean dose and cDVH parameters in the left lobe as a function of IA

2.3.6 Dosimetry report for injected activity calculated based on different methods

Figure 2.26-A shows an overview of the total IA and IA for each lobe calculated based on different methods defined in the previous chapter (section 1.7.4). The black bars in the following figures correspond to the actual prescribed activity in the clinical routine. As it is stated before (in section 2.3.2), this activity was prescribed based on the PM (150 Gy to the TV and 25 Gy to the NTV compartment). The comparison between our dosimetry result and this projected dose for prescribed activity is not straightforward due to different approach in (see section 1.5.5.2):

– VOI segmentation: defining lobes based on CT instead of CBCT, tumors on CT instead of [^{68}Ga]Ga-DOTA-TATE-PET (see table 2.3).
– T/N ratio estimation: deriving from some ROIs on the [^{99m}Tc]Tc-MAA-SPECT rather than the entire TV and NTV VOI.

These variations in dosimetry methodology should be taken into account when comparing these projected doses and our calculated dose parameters.

Figure 2.26-A demonstrates that IA based on the empirical method was comparable with the MIRD for both lobes, which corresponded to a higher activity (and doses) compared to the BSA and SIRFLOX-lookup table.

For the left lobe, the voxel-level dosimetry and PM proposed a very similar activity, without any therapeutic window. This indicated a non-optimum tumor coverage in the left lobe.

For the right lobe, the PM and voxel-level dosimetry proposed a wide therapeutic window, which means that the treatment team had a variety of choices for administered activity, which was a higher maximum IA than proposed by the other methods.

In terms of the mean dose to the NTV compartment (see figure 2.26-C), all the methods were safe and did not reach the 50 Gy dose level. But, analyzing the dose to the TV in figure 2.26-D, we see that all methods failed to reach the TV dose of 150 Gy in the left lobe. For the right lobe, all methods except PM and voxel-level dosimetry failed to meet mean tumor dose criterion (150 Gy). Therefore, by considering only the mean dose criteria in this lobe, administered activity calculated by empirical, BSA, SIRFLOX, and MIRD were not within therapeutic window and cannot considered to be effective based on meeting the TV mean dose criterion.

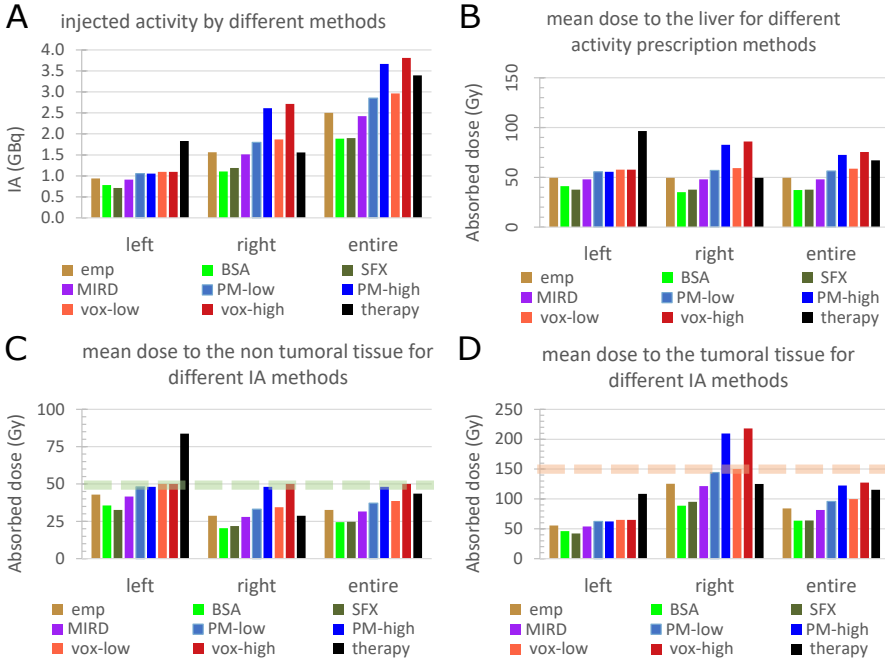

Figure 2.26: IA and mean dose report for activities reported by different methods; empirical (emp), BSA, SIRFLOX (SFX), MIRD, partition method (PM-low and PM-high), voxel-level dosimetry (vox-low and vox-high), and therapeutic administered activity. When analyzing these graphs, one should consider that the left lobe is mostly tumoral (85% tumor involvement).

The cDVH report in figure 2.27-D revealed that for the right lobe, only the activity based on PM-high and voxel-level dosimetry was high enough to cover more than 70% of the TV with at least 80 Gy (activities calculated based on the empirical and MIRD method were also very close to meet this criterion). For the left lobe, none of the estimated activities were sufficient to ensure this coverage. The cDVH parameters for NTV also showed that all the methods were safe for this compartment, and less than half of the NTV compartment received more than 50 Gy.

Cumulative dose-volume histogram of the TV, NTV, and whole (both TV and NTV) of the left, right, and entire liver are provided in figures 2.28 to 2.30.

As you can see in figure 2.28, the irradiation of the NTV for none of the methods exceeded the safety threshold (bold green dashed lines), and depending on the activity prescription method, half of the NTV in this lobe received more than 24 to 36 Gy. These numbers were even lower for the right lobe, and for all the methods, half of the NTV in this lobe received around 14 to 31 Gy or more (see figure 2.29).

As the liver is a parallel organ, for the NTV, the dose distribution to the entire liver is more critical than the lobar assessment. Figure 2.30 shows that in the entire liver for voxel-level ($IA_{vox-high}$) method, half of the NTV compartment received at least 32 Gy, and for all the other methods, this number did not exceed 31 Gy.

Figure 2.28 also implies that the TV dose distribution of the left lobe was not sufficient; for example, 70% of the tumor volume for all the methods received at least a dose of less than 8 Gy. This number for the right lobe (see figure 2.29) varied for different methods, and ranged from 55 Gy for the BSA and 132 Gy for the voxel-level dosimetry ($IA_{vox-high}$).

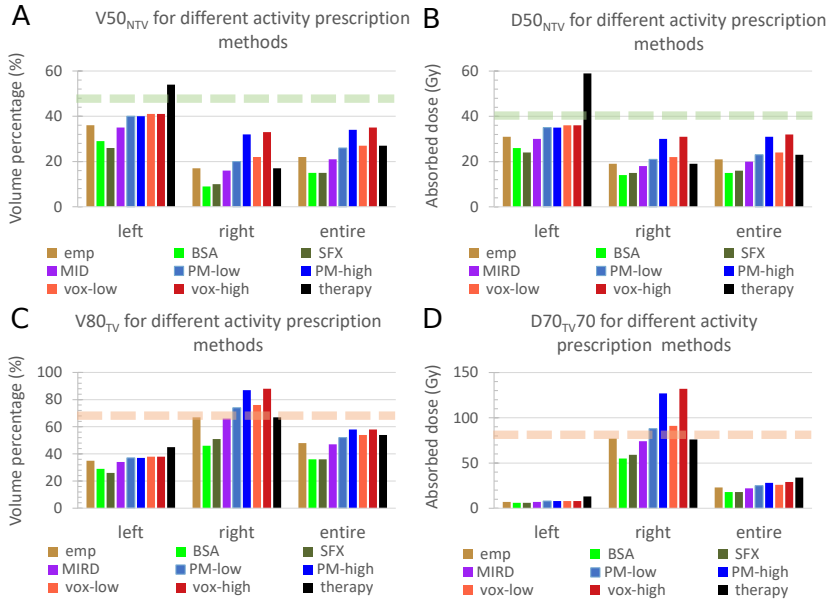

Figure 2.27: Volumetric (cDVH) report for activities reported by different methods; empirical (emp), BSA, SIRFLOX (SFX), MIRD, partition method (PM-low and PM-high), voxel-level dosimetry (vox-low and vox-high), and therapeutic administered activity. When analyzing these graphs, one should consider that the left lobe is mostly tumoral (85% tumor involvement).

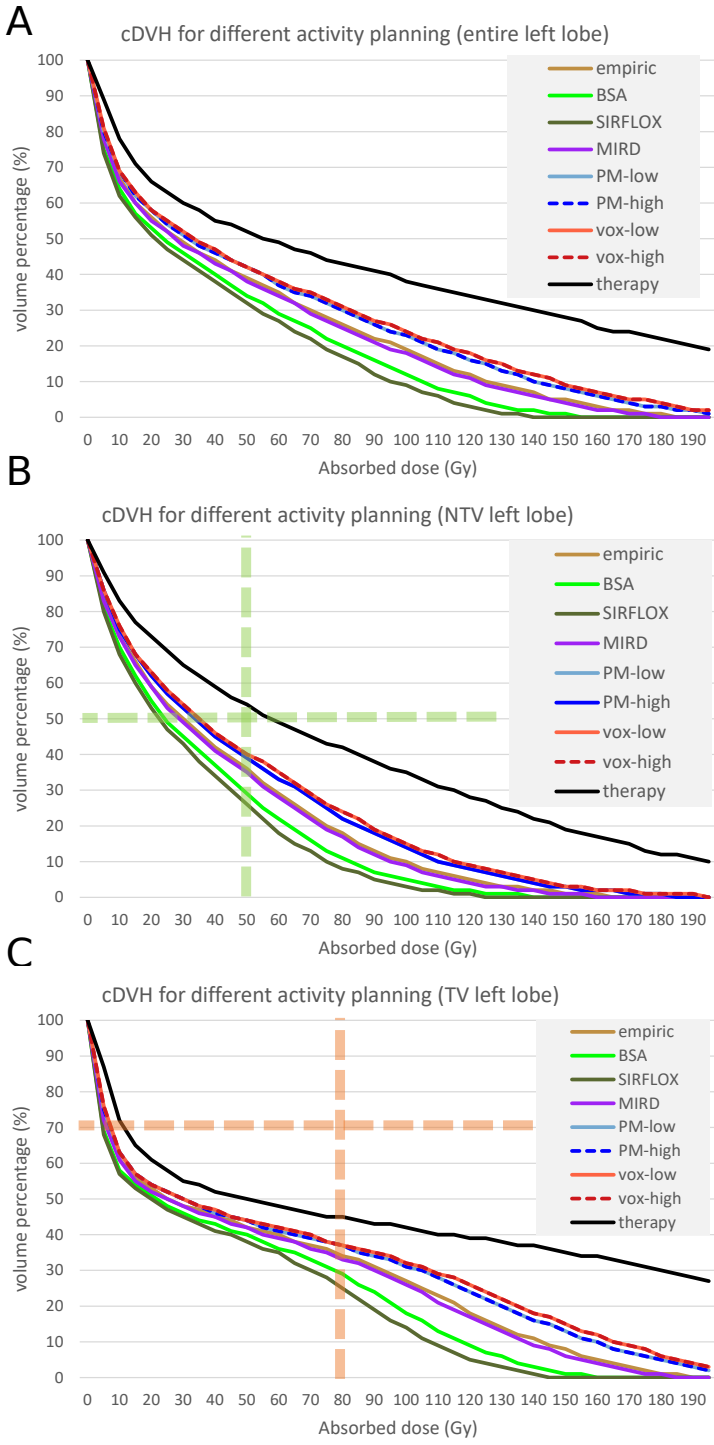

Figure 2.28: cDVH obtained from different activity prescription methods for the left lobe; empirical (emp), BSA, SIRFLOX (SFX), non-compartmental partition model (NCP), partition modal (IA_{PM-low} and $IA_{PM-high}$), voxel-level dosimetry ($IA_{vox-low}$ and $IA_{vox-high}$), and therapeutic administered activity.

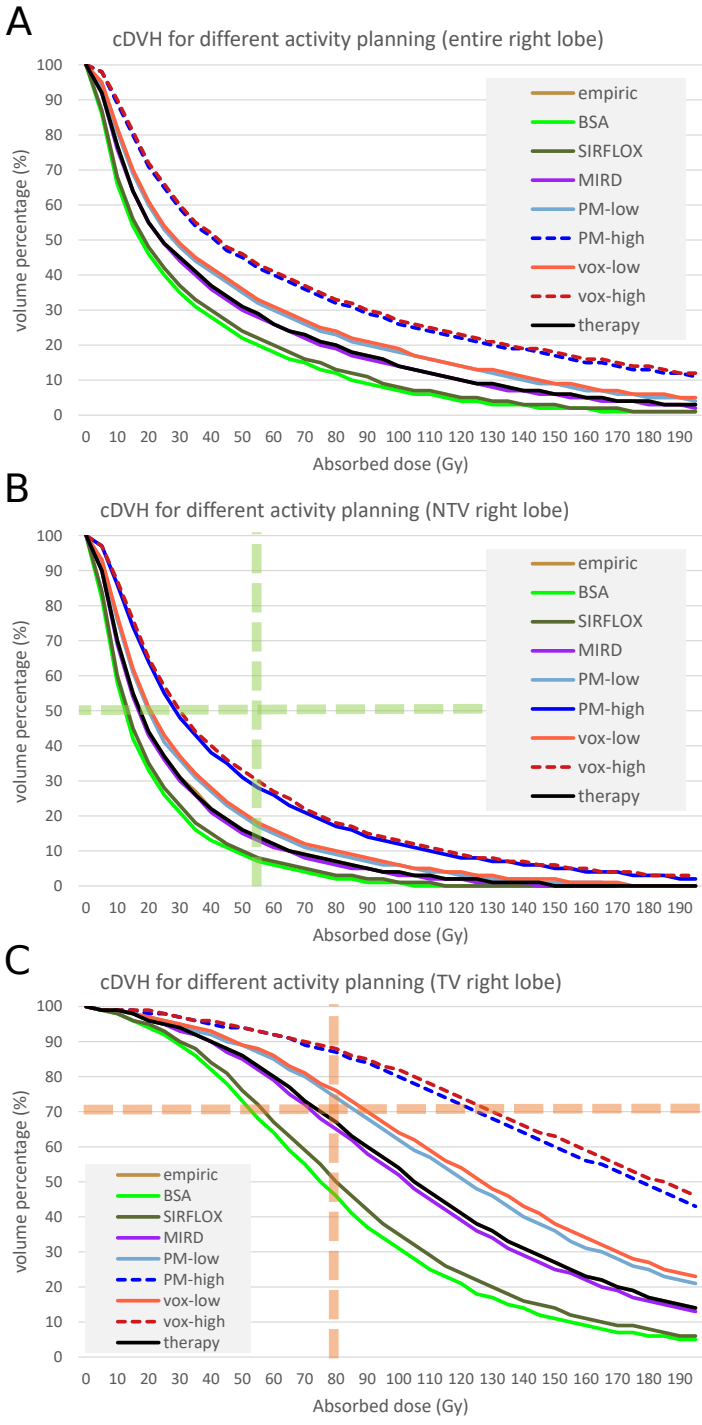

Figure 2.29: cDVH obtained from different activity prescription methods for the right lobe; empirical (emp), BSA, SIRFLOX (SFX), non-compartmental partition model (NCP), partition modal (IA_{PM-low} and $IA_{PM-high}$), voxel-level dosimetry ($IA_{vox-low}$ and $IA_{vox-high}$), and therapeutic administered activity.

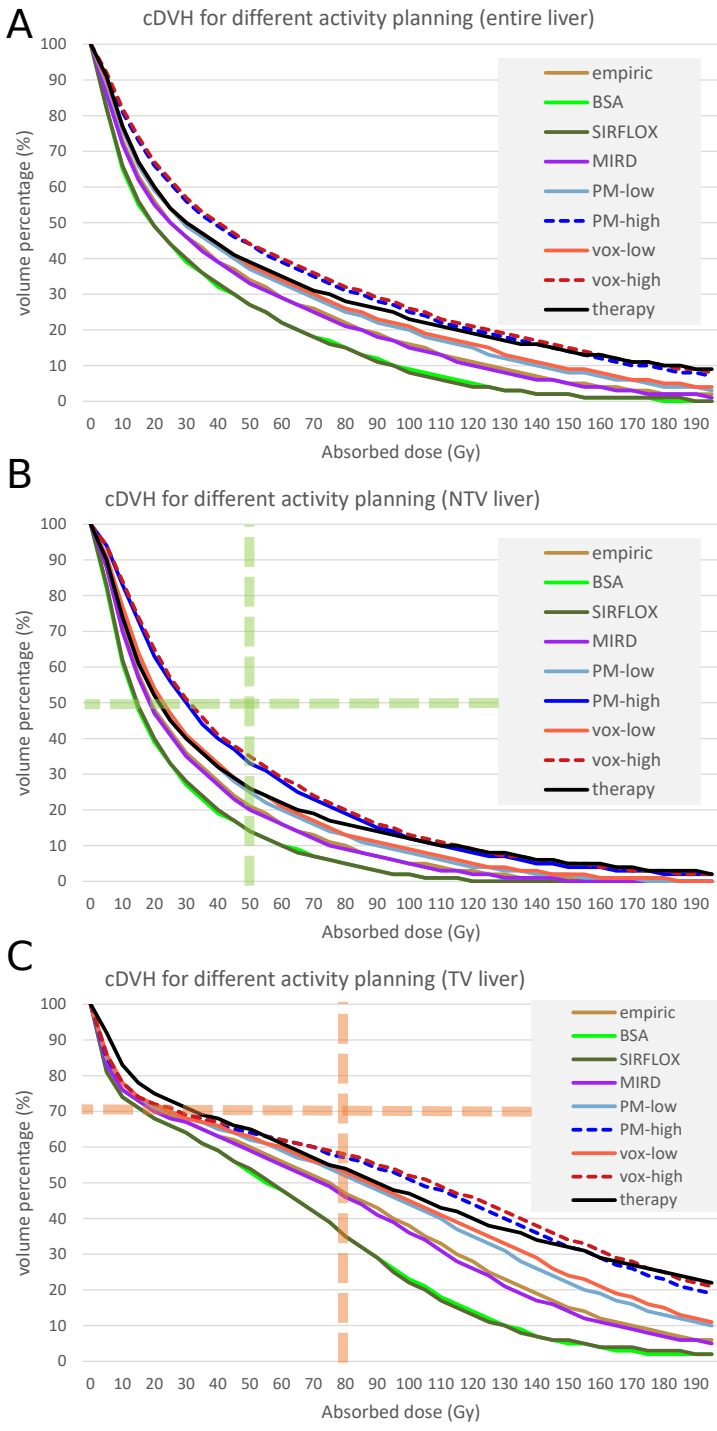

Figure 2.30: cDVH obtained from different activity prescription methods for the entire liver; empirical (emp), BSA, SIRFLOX (SFX), non-compartmental partition model (NCP), partition modal (IA_{PM-low} and $IA_{PM-high}$), voxel-level dosimetry ($IA_{vox-low}$ and $IA_{vox-high}$), and therapeutic administered activity.

2.3.7 Predicted and measured dosimetry for the prescribed activity

2.3.7.1 Dosimetry/Activity overview

Here, the pre-treatment dose estimation and post-treatment dose verification using the actual prescribed activity are described in detail. One transaxial slice is shown for all pre- and post-treatment images in figure 2.38.

For the total NTV compartment in the entire liver, [^{99m}Tc]Tc-MAA based dose prediction is very close to the measured dose. Based on the dose verification (and predictive dose), this IA resulted in 37 Gy (predictive: 44 Gy) to the NTV in the entire liver; around 76% (predictive: 73%) of this compartment (measured: 1237 cc, predictive: 1194 cc) received less than 50 Gy, and half of the NTV received less than 20 Gy (predictive: 22 Gy). When comparing the predictive and measured mean dose to the NTV tissue in each lobe, predictive dosimetry overestimated the mean dose (84 versus 68 Gy) for the left lobe, and underestimated for the right lobe (29 versus 25 Gy).

Measured (and predictive) mean TV dose for the left and right lobe and entire liver were 112 Gy (predictive: 109 Gy), 167 Gy (predictive: 126 Gy), and 134 Gy (predictive: 116 Gy), respectively. More than 45% (absolute volume of 213 cc), 67% (absolute volume of 219 cc), and 54% (absolute volume of 432 cc) of the TV in the left and right lobe and entire liver were predicted to receive at least 80 Gy, respectively. But post-treatment dose verification corresponded to approximately 70% of the tumor receiving more than 80 Gy for both lobes and entire liver, which were equivalent to an absolute volume of 333, 227, and 560 cc for the left lobe, the right lobe, and entire liver, respectively. This means that in both lobes, predictive dosimetry underestimated the tumor coverage of 80 Gy. In other words, dose measurement suggests that 70% of the tumor in both lobes and entire liver received at least around 80 Gy, while predictive dosimetry underestimated this parameter; a predictive $D70_{TV}$ of 12, 76, and 35 Gy were estimated for the left lobe, right lobe and entire liver based on [^{99m}Tc]Tc-MAA-SPECT.

These results are discussed in more detail in the next subsections. Three months follow-up [^{68}Ga]Ga-DOTA-TATE-PET/CT (see figure 2.38-U and V) showed a development of central necrosis in the treated liver metastasis in both lobes. Unfortunately, new liver and bone metastases were detected. The patient was treated with PRRT after SIRT.

2.3.7.2 Cumulative dose-volume histograms

Predictive cDVHs, using actual prescribed activity, are given in figure 2.31. The difference between the predictive and measured cDVH is also given in figure 2.34.

Figure 2.32 also provides the dose-volume histogram (DVH), not the cDVH, for different VOIs. The use of DVHs is limited in the SIRT workflow, and dose distributions are usually reported in cDVHs. But in the case of examining the predictive value of [^{99m}Tc]Tc-MAA particles, one may want to look at the difference between predictive and measured volume percentage in different dose bins. This information is provided in figure 2.34.

As shown in figure 2.31-B, predicted dose-volume histograms for TV and NTV in the left lobe were very close to each other (green and red dashed lines), which indicates that [^{99m}Tc]Tc-MAA-based dose did predict a poor differential dose distribution between TV and NTV.

Post-treatment dose verification shows that the DVH for the left lobe TV and NTV compartment (solid green and red line) were less close to each other compared to the predictive lines (dashed lines), which means that therapeutic microspheres showed a better distribution within the TV compared to the prediction. The difference between predictive and measured cDVH curves (subtracting predicted cDVH from measured curve) for this lobe is illustrated in figure 2.33 (light red and green lines). As you can see for NTV, the difference was always in the range of [-20, 40] % of the tumor volume. For the doses less than 120 Gy, prediction underestimates the TV dose, but in high doses, there is

Table 2.12: Activity/dosimetry overview

criterion *	left lobe			right lobe			entire liver		
	pre	post	Δ	pre	post	Δ	pre	post	Δ
FOV fractional uptake(%)	-	-	-	-	-	-	**108.12%**	**127.71%**	**19.60%**
VOI activity (MBq/cc)*	2.013	1.891	-0.122	1.033	1.156	0.123	1.401	1.432	0.031
VOI activity(MBq)*	1833.0	1721.7	-111.3	1564.0	1749.6	185.6	3397.0	3471.3	74.3
TV activity (MBq/cc)*	2.263	2.328	0.064	2.616	3.475	0.859	2.407	2.796	0.389
TV activity (MBq)*	1066.4	1096.8	30.3	849.9	1129.0	279.1	1916.4	2225.7	309.4
NTV activity (MBq/cc)*	1.744	1.422	-0.322	0.601	0.522	-0.079	0.909	0.765	-0.144
NTV activity (MBq)*	766.6	624.9	-141.6	714.1	620.6	-93.5	1480.6	1245.5	-235.1
T/N ratio	**1.3**	**1.6**	**0.3**	**4.4**	**6.7**	**2.3**	**2.6**	**3.7**	**1.0**
VOI dose(Gy)	96.6	90.7	-5.9	49.6	55.4	5.9	**67.2**	**68.7**	**1.5**
D_{NTV} $(Gy)^{+}$	83.7	68.2	-15.5	28.8	25.0	-3.8	**43.6**	**36.7**	**-6.9**
D_{TV} $(Gy)^{++}$	**108.6**	**111.7**	**3.1**	**125.5**	**166.7**	**41.2**	**115.5**	**134.2**	**18.6**
$V50_{NTV}, \%$**	54.2%	56.4%	2.2%	16.6%	12.1%	-4.5%	**26.7%**	**24.0%**	**-2.7%**
$V80_{TV}, \%$***	**45.2%**	**70.7%**	**25.5%**	**67.3%**	**69.9%**	**2.6%**	**54.2%**	**70.4%**	**16.1%**
$V50_{NTV}, cc$	238	248	10	197	144	-53	435	391	-44
$V80_{TV}, cc$	213	333	120	219	227	8	432	560	128
$D50_{NTV}$	59	59	0	17	16	-1	22	20	-2
$D70_{TV}$	12	81	69	76	80	4	35	81	46

* All activities were decay corrected for (planned) administration time and were calibrated by IA
** $V50_{NTV} \leq 50\%$ [219]
*** $V80_{TV} \geq 70\%$ [220]
\+ [$D_{NTV} \leq 50$ Gy] [87]
++ [$D_{TV} \geq 70$ Gy] [159]

an overestimation of the TV dose. For the NTV compartment, the range of difference between predictive and measured dose was less ([-13, 8] Gy). In the area of the decisive dose to the NTV liver (between 40-60 Gy), the underestimation was limited. Figure 2.34 gives a better insight into where the discrepancy is more pronounced; in this figure the DVH differences for different VOIs (*e.g.* TV dose in light red line) are shown with dose bins of 10 Gy. This figure indicates a volume percentage difference of 5% for the doses between 65 Gy to 135 Gy, which was the most interesting dose interval for this compartment. For the NTV compartment (light green line), by comparing dose differences with a dose bin of 10 Gy, most of the disagreement happened around 55 to 105 Gy, which is also an interesting dose interval.

Figure 2.31-C shows that in the right liver lobe, there was an excellent difference between TV and NTV irradiation for both predictive (dashed red and green lines) and measured dose (solid red and green line). Also, predictive (dashed lines) and measured (solid lines) doses for both TV (red) and NTV (green) were very close, which means that [^{99m}Tc]Tc-MAA was a good surrogate in this lobe. This is also provided in figure 2.33-C (orange and blue lines). The difference between cDVH of the TV and NTV never exceeded 10 and 7%, respectively. Figure 2.34 shows that a small discrepancy (less than 2.5%) is reported in the volume of the TV that received doses of around 55 to 95 Gy. For the NTV compartment in this lobe, predictive, and measured dose above 140 Gy were identical. The most pronounced differences (figure 2.34) were recorded as a mild overestimation in the range of [0, 35] Gy and a mild underestimation between 35 and 65 Gy.

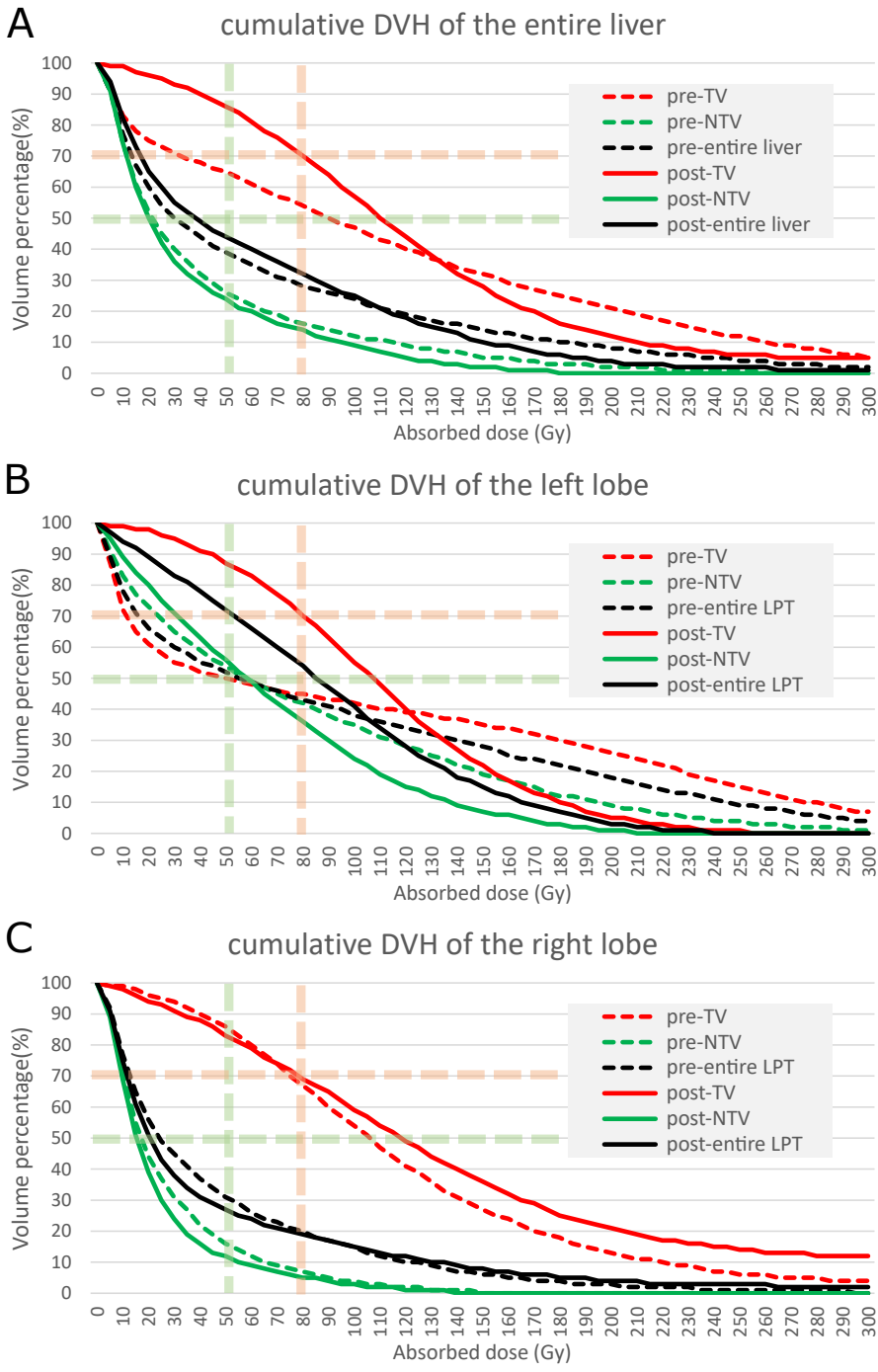

Figure 2.31: cDVH of different VOIs

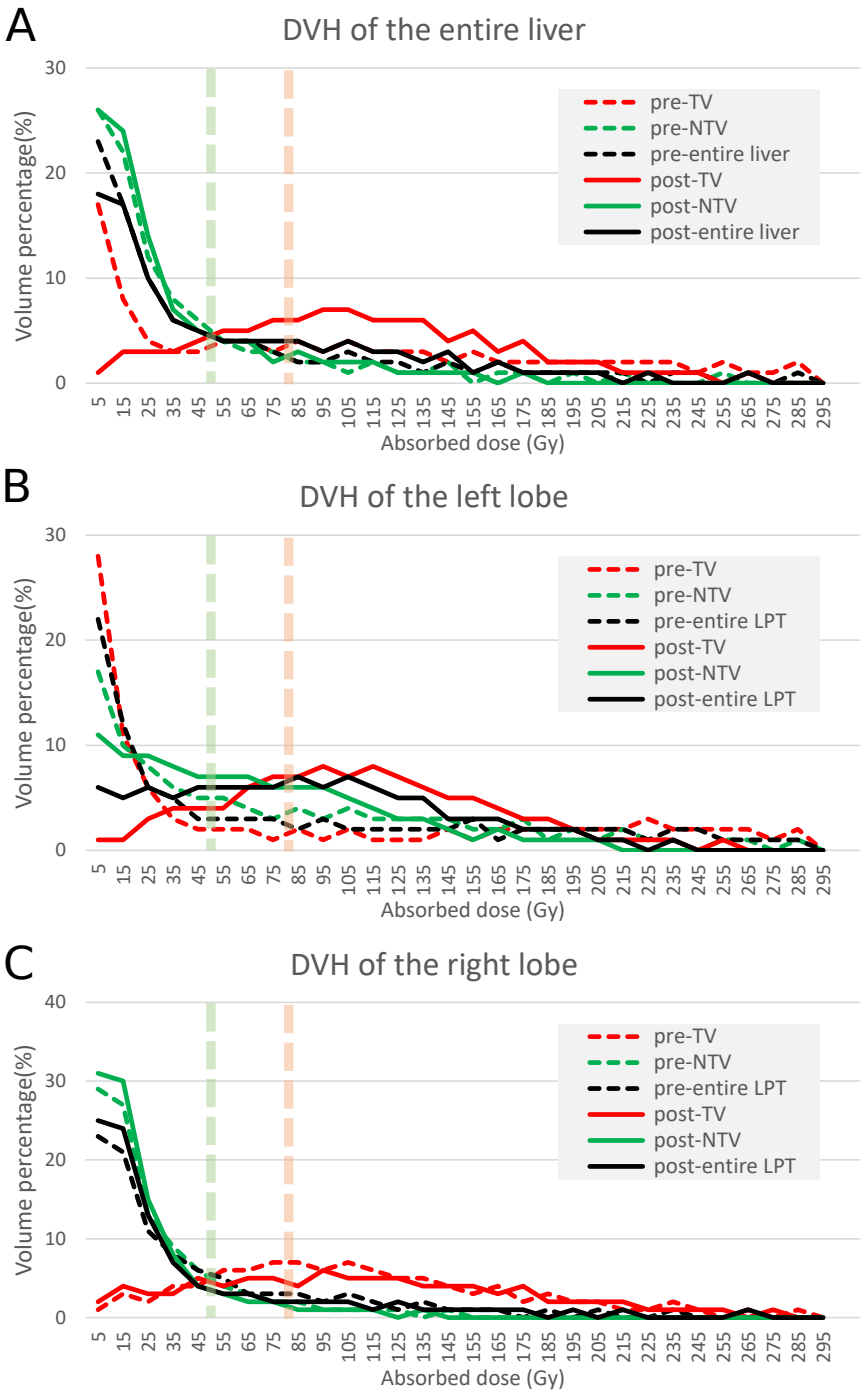

Figure 2.32: DVH of different VOIs

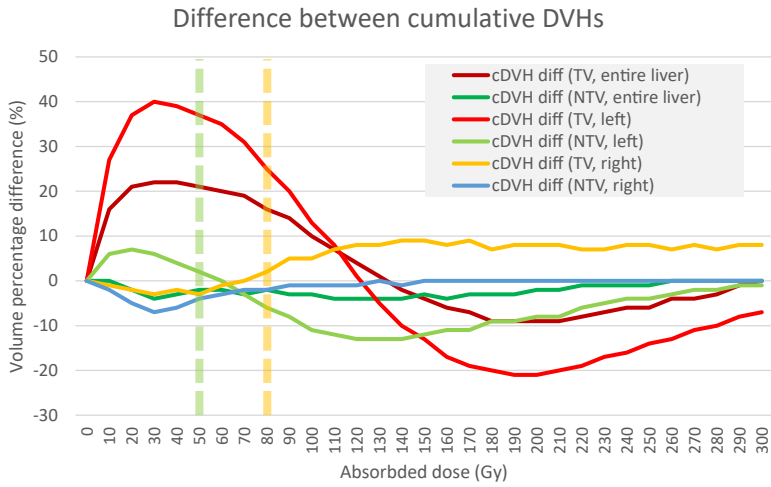

Figure 2.33: Difference between measured and predicted cDVH of different VOIs, positive values associated with higher post treatment measured cDVH compared to pre-treatment predicted cDVH

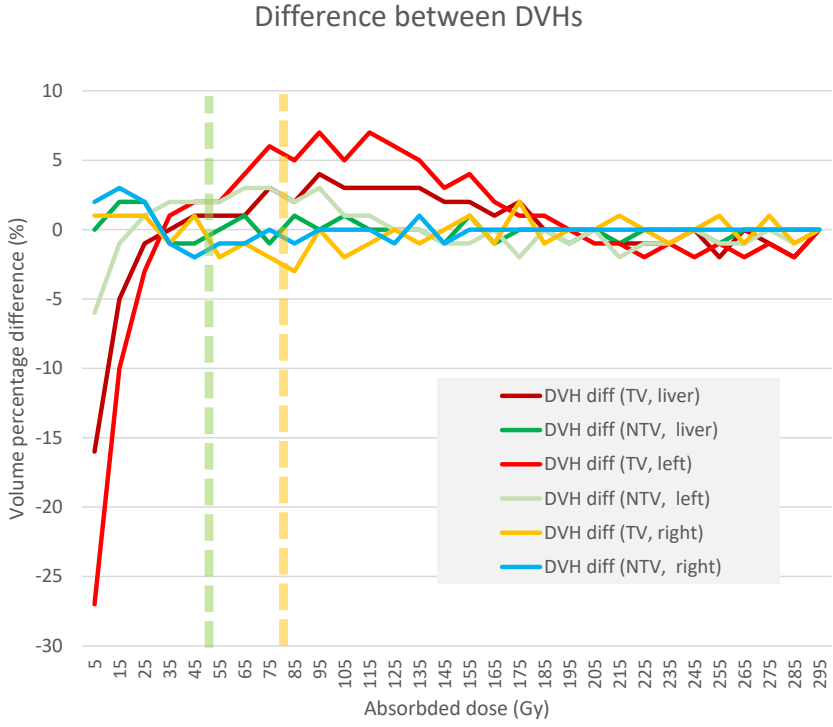

Figure 2.34: Difference between measured and predicted DVH of different VOIs with absorbed dose bins of 10 Gy (positive values meaning higher measured DVH)

2.3.8 Voxel-by-voxel comparison between predicted and measured dose

2.3.8.1 Dose difference analysis

The most naive way to analyze voxel-by-voxel dose difference between predictive and measured absorbed dose is reporting the distribution of the difference (see figure 2.38).

The interquartile ranges of the dose differences in different VOIs are provided in the following figures. Figure 2.35-A illustrates the interquartile ranges of the voxelized absolute dose difference, and 2.35-B shows the interquartile ranges of the absorbed dose differences normalized by the measured absorbed dose in each voxel.

As can be seen in figure 2.35-B, the median absolute difference between the measured and predicted dose for TV and NTV voxels in the left lobe were 34 and -4 Gy, respectively. Moreover, the first and third interquartile range of the TV and NTV voxels showed a significant deviation between predicted and measured dose. For TV, this range was [-99, 92] Gy and for NTV voxels, this range equaled to [-77, 48] Gy. In the entire left lobe, the median dose difference was 12 Gy. When analyzing the normalized difference (figure 2.35-B), the TV and NTV voxels had a median of absorbed dose difference of 50% and -10% of their measured dose. Also, for one quarter of the TV and NTV voxels, the predicted dose overestimated the absorbed dose by 80 and 180% of the measured dose or more. On the other hand, for one-quarter of the TV and NTV voxels, the underestimation of the absorbed dose based on the predicted dose was more than 90 and 70% of the measured dose.

The inconsistency between measured and predicted dose was lower for the right lobe. The median of the absolute dose difference between measured and predicted dose for TV, NTV, and entire lobe voxels were 10, -1, and -1 Gy. The first and third-interquartile range for absolute dose difference between measured and predicted dose for TV and NTV voxels in this lobe were [-35, 62] and [-12.7] Gy. The first-interquartile range of the dose differences normalized by the voxel measured dose for TV and NTV compartment were -0.4 and -0.9. Also, the third-interquartile range of the normalized dose difference showed that only one-quarter of the predicted dose for both TV and NTV voxels in this lobe underestimated the measured dose by 40%.

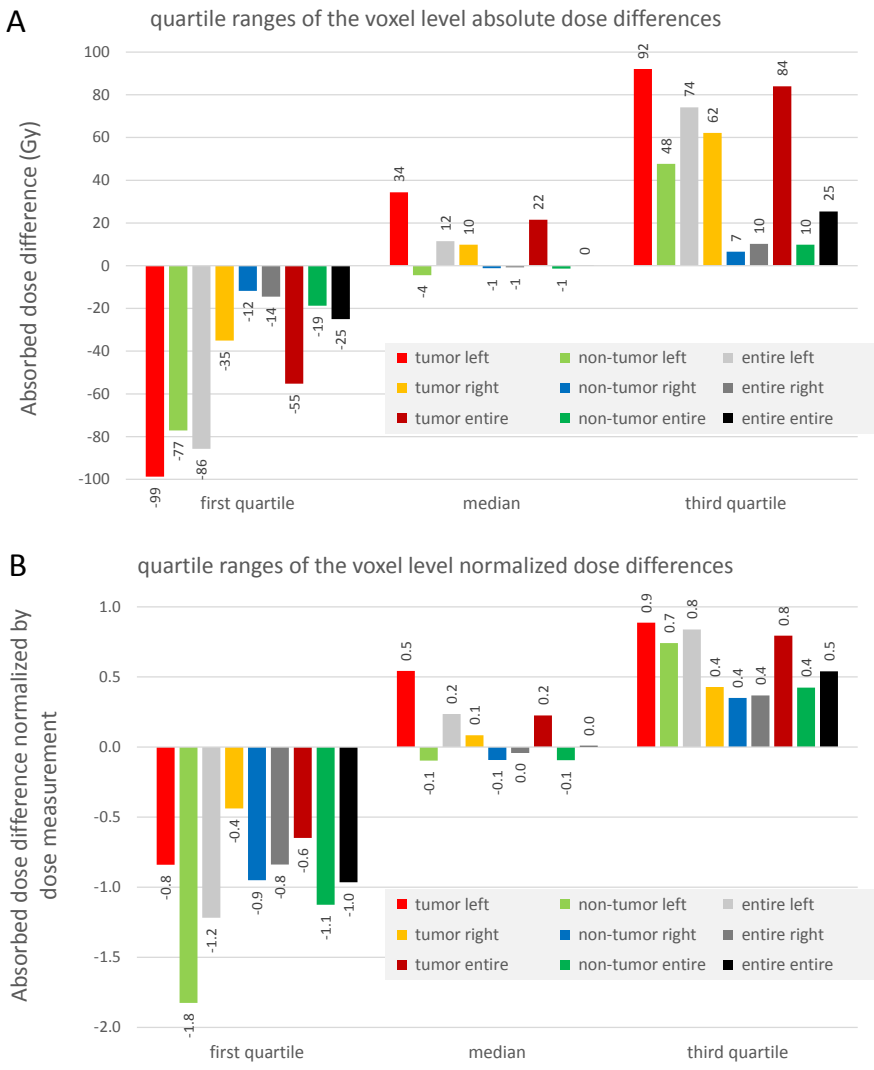

*Figure 2.35: Interquartile ranges of the **[A]** absolute and **[B]** normalized dose difference between measured and predictive dosimetry (positive values are associated with higher post-treatment measured doses)*

2.3.8.2 Tissue level joint histograms

By using TCP curve for mNET [218], a minimum threshold of 150 Gy is accepted as a dose with a high tumor response probability (see section 5.2.4). Also, an absorbed dose of 80 Gy is considered to be the cut-off for predicting nonresponse. By using NTCP curve, a dose of 50 Gy is considered as a safety threshold, an absorbed dose of 40 Gy is also used to illustrate the lowest dose recommended (*e.g.* for cirrhotic NTV or for patients that were treated heavily with chemotherapy) [71, 73].

Taking these values into account, a comparison between dose-levels in NTV and TV in each lobe is provided (see figure 2.38). Absorbed doses are binned using 40 and 50 Gy for NTV and 80 and 150 Gy for TV.

NTV, left	pre $\in [0,40]Gy$	pre $\in [40,50]Gy$	pre $\in [50,+\infty]Gy$	total
post $\in [0,40]Gy$	**15.8%**	1.9%	18.8%	34.2%
post $\in [40,50]Gy$	3.0%	**0.4%**	3.8%	9.5%
post $\in [50,+\infty]Gy$	21.9%	2.9%	**31.6%**	56.4%
total	38.4%	5.2%	54.2%	100%

Table 2.13: Joint histogram of the NTV (left lobe) dose in pre- and post-treatment dosimetry

NTV, right	pre $\in [0,40]Gy$	pre $\in [40,50]Gy$	pre $\in [50,+\infty]Gy$	total
post $\in [0,40]Gy$	**71.8%**	4.6%	7.2%	83.6%
post $\in [40,50]Gy$	2.2%	**0.6%**	1.6%	4.4%
post $\in [50,+\infty]Gy$	3.1%	1.2%	**7.8%**	12.1%
total	77.1%	6.4%	16.6%	100%

Table 2.14: Joint histogram of the NTV (right lobe) dose in pre- and post-treatment dosimetry

NTV, liver	pre $\in [0,40]Gy$	pre $\in [40,50]Gy$	pre $\in [50,+\infty]Gy$	total
post $\in [0,40]Gy$	**56.7%**	3.8%	10.3%	70.8%
post $\in [40,50]Gy$	2.4%	**0.5%**	2.2%	5.1%
post $\in [50,+\infty]Gy$	8.1%	1.7%	**14.2%**	24.0%
total	67.2%	6.0%	26.7%	100%

Table 2.15: Joint histogram of the NTV (whole liver) dose in pre- and post-treatment dosimetry

TV, left	pre $\in [0,80]Gy$	pre $\in [80,150]Gy$	pre $\in [150,+\infty]Gy$	total
post $\in [0,80]Gy$	**20.2%**	1.5%	7.6%	29.3%
post $\in [80,150]Gy$	23.4%	**4.5%**	20.6%	48.5%
post $\in [150,+\infty]Gy$	11.2%	3.5%	**7.5%**	22.2%
total	54.8%	9.5%	35.7%	100%

Table 2.16: Joint histogram of the TV (left lobe) dose in pre- and post-treatment dosimetry

TV, right	pre $\in [0,80]Gy$	pre $\in [80,150]Gy$	pre $\in [150,+\infty]Gy$	total
post $\in [0,80]Gy$	**16.0%**	10.7%	3.5%	30.2%
post $\in [80,150]Gy$	10.1%	**17.4%**	6.0%	33.5%
post $\in [150,+\infty]Gy$	6.6%	11.6%	**18.1%**	36.3%
total	32.7%	39.7%	27.6%	100%

Table 2.17: Joint histogram of the TV (right lobe) dose in pre- and post-treatment dosimetry

TV, liver	pre $\in [0,80]Gy$	pre $\in [80,150]Gy$	pre $\in [150,+\infty]Gy$	total
post $\in [0,80]Gy$	**18.5%**	5.3%	5.9%	29.7%
post $\in [80,150]Gy$	18.0%	**9.8%**	14.6%	42.4%
post $\in [150,+\infty]Gy$	9.3%	6.8%	**11.8%**	27.9%
total	45.8%	21.9%	32.3%	100%

Table 2.18: Joint histogram of the TV (whole liver) dose in pre- and post-treatment dosimetry

Agreement levels:

We could also categorize these dose bins into the following levels:

- **Good agreement:** when the pre- and post-treatment doses belong to the same dose interval; combining the green blocks in tables 2.13 to 2.18 (*e.g.* predictive and measure NTV dosimetry both report a dose of between 40 and 50 Gy).
- **Moderate agreement:** when the pre- and post-treatment doses belong to the neighboring dose intervals; combining the blue blocks in tables 2.13 to 2.18 (*e.g.* TV, predictive TV dose is less than 80 Gy and post-dose TV dose verification is between 80 and 120 Gy).
- **Poor agreement(better in treatment):** when the pre- and post-treatment doses are very different, i.e. one belongs to the first and the other to the third dose interval, but the actual dose to the tumor was higher and the actual dose to the NTV was lower than predicted; the yellow blocks in tables 2.13 to 2.18 (*e.g.* predictive dose to the NTV is more than 50 Gy while the measured dose in this volume is less than 40 Gy).
- **Poor agreement(worse in treatment):** when the pre- and post-treatment doses are very different, i.e. one belongs to the first and the other to the third dose interval, but the actual dose to the tumor was lower and the actual dose to the NTV was higher than predicted; the red blocks in tables 2.13 to 2.18 (*e.g.* predictive dose to the TV is more than 150 Gy while the measured dose in this volume is less than 80 Gy).

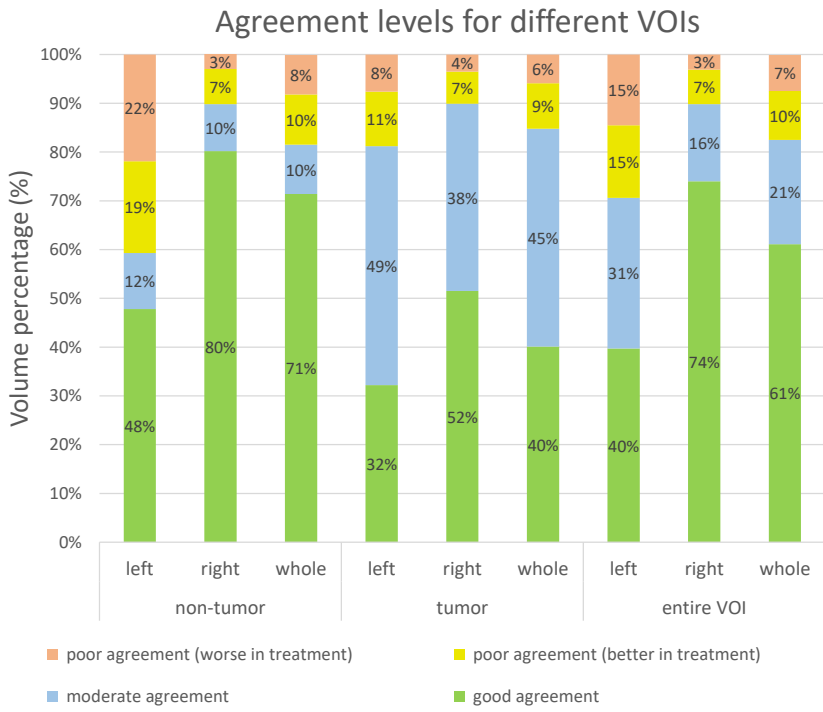

Figure 2.36: Agreement levels of predictive and measured doses

2.3.8.3 γ-index

Here you can find the volume percentage of different VOIs which passes this local γ-index criteria (see section 2.2.5.2):

- DD= 3 % of the post-treatment dose for each voxel
- DTA= 3 times MAA-SPECT voxel size (14.4 mm)

Here, both DD and DTA can be chosen arbitrarily. In our evaluation, the most common passing criteria (3% of the post-treatment dose and 3 voxel size) is used which was originally proposed by Low *et al.* [213]. By employing other values than proposed, one can achieve a different value of γ-value, and new pass-fail criteria would be defined.

Figure 2.37 provides the percentage of the passed voxels in different VOIs, figure 2.38 shows one transaxial slice of this test. So, in the entire liver, 69% of the voxels (60% of the TV and 74% of the NTV voxels) passed the γ-index criteria. The passed voxels in the TV, NTV and entire lobe were higher for the right lobe; γ-index suggests that around 80% all the voxels of the NTV voxels of the right lobe received similar absorbed dose based on predictive and measured dose, but around half of the NTV in the left lobe did not pass the criteria.

Around 85% of the TV voxels in the right lobe showed a good agreement between predictive and measured dose based on their γ-index; this number was only around 44% of the TV voxels in the left lobe.

In total, 82% and 49% of the voxels within the right and left lobe passed the γ-index criteria.

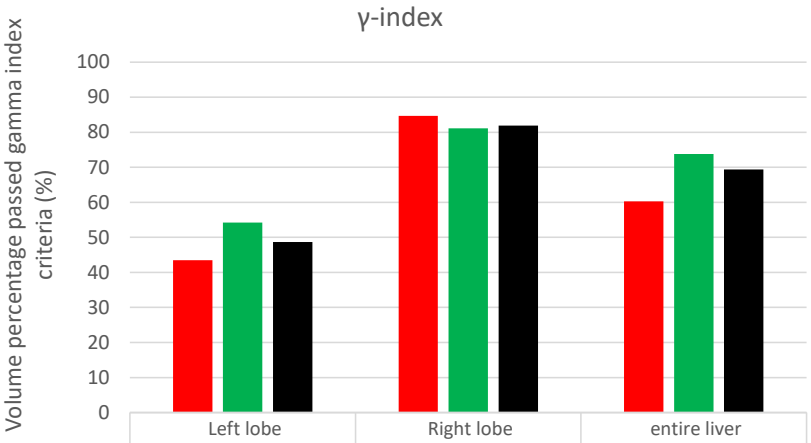

	Left lobe	Right lobe	entire liver
TV	43.5	84.7	60.3
NTV	54.2	81.1	73.8
entire VOI	48.7	81.9	69.4

Figure 2.37: Volume percentage of different VOIs which passes the local γ-index criteria

2.3.8.4 Conclusion

In this section, several methods were presented to clarify different ways which can be used to analyze differences between the predicted and measured doses in clinical routine. These approaches give insights about possible match or mismatch between estimated and measured doses from different angle. For this case, in the left lobe there were two interesting results: (1) there is a large part of the tumor without any [^{99m}Tc]Tc-MAA

uptake. Fortunately, that part received ^{90}Y-microsphere. So, the treatment was much better than the prediction. This mismatch happened mostly in two dose intervals: low dose (between 0 to 25 Gy) and medium-high absorbed doses (between 75 to 135 Gy). Both of these dose intervals were important in treatment planning. (2) in the part of the tumor where there was [^{99m}Tc]Tc-MAA uptake, the correlation between [^{99m}Tc]Tc-MAA intensity and yttrium-90 intensity was only moderate.

2.3.9 A transaxial slice of the images and dosimetry results

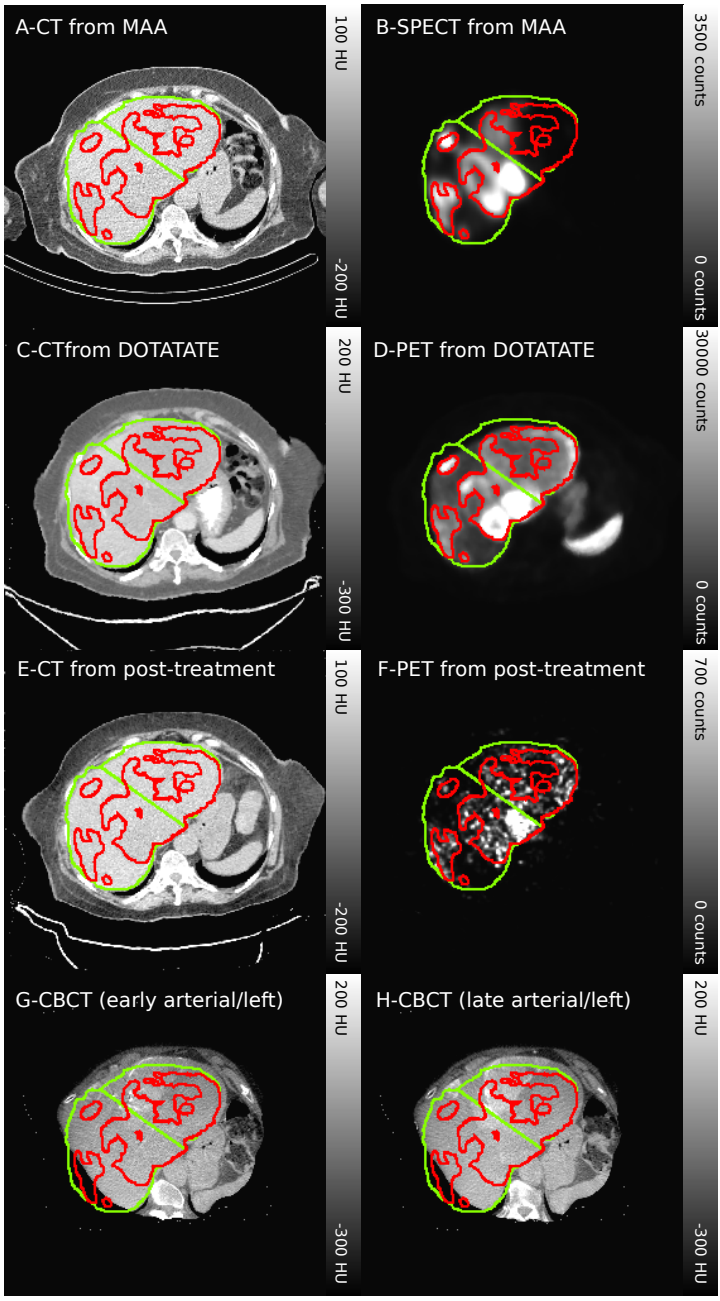

Figure 2.38: A transaxial slice of the images and dosimetry results ***[A,B]*** *CT and SPECT images from pre-treatment workup,* ***[C,D]*** *CT and PET from baseline image ([*^{68}*Ga]Ga-DOTA-TATE study),* ***[E,F]*** *CT and* ^{90}*Y-PET images from post-treatment imaging,* ***[G,H]*** *early and late arterial phase CBCTs for the left lobe*

continued on the next page ...

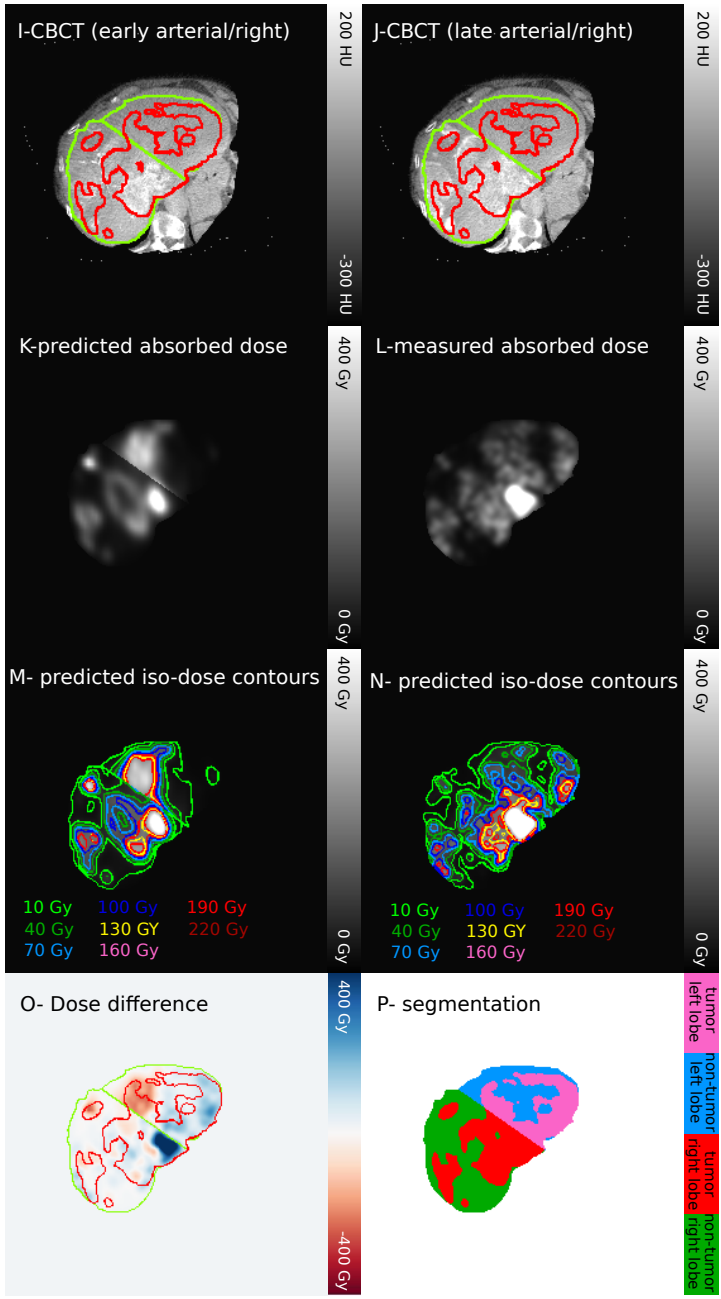

Figure 2.38: ***... continued from the previous page***
A transaxial slice of the images and dosimetry results ***[I,J]*** *early and late arterial phase CBCTs for the right lobe* ***[K,L]*** *predictive and measured dose maps converted from images* ***B*** *and* ***J****, respectively,* ***[M,N]*** *the same images as* ***K*** *and* ***L*** *with iso-dose contours,* ***[O]*** *the difference between measured dose and predictive dose (image* ***K*** *subtracted from image* ***L****),* ***[P]*** *segmentation map, green and blue are partitioned liver (from image* ***A****) into left and right lobe (by using images* ***E*** *to* ***H****); the green and red contours in the images* ***A*** *to* ***J*** *represent the liver and tumor segmentation illustrated here,*
continued on the next page ...

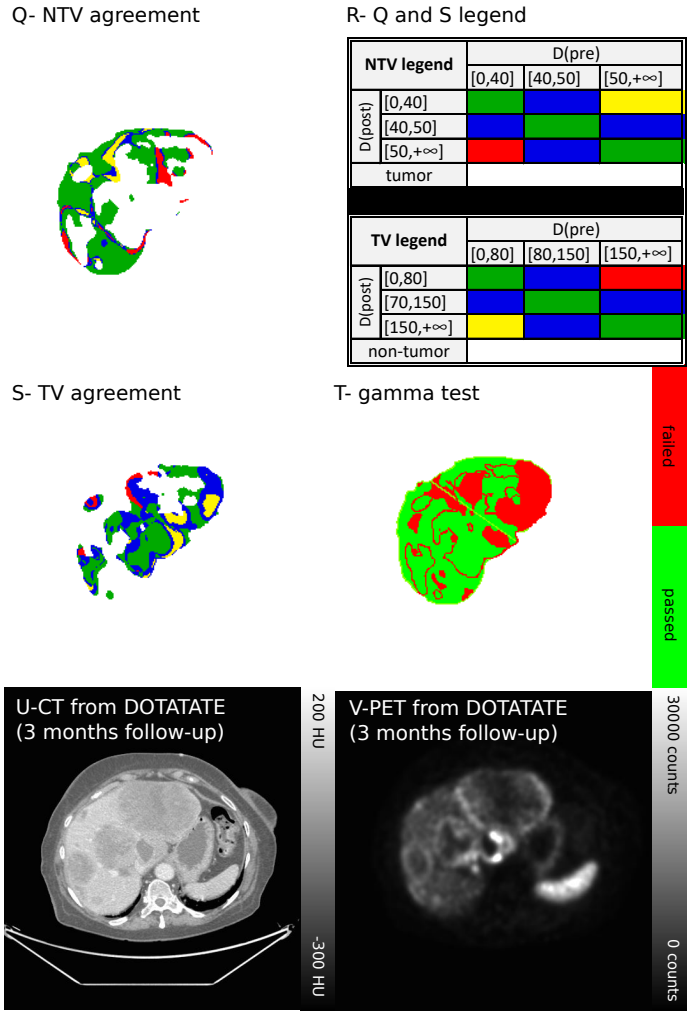

Figure 2.38: ***... continued from the previous page***
A transaxial slice of the images and dosimetry results ***[Q,S]*** *agreement level which corresponds to the joint-histogram of the predictive and measured dose* ***[T]*** *passed and failed pixels using local γ-index,* ***[U,V]*** *CT and PET from 3 months follow-up image ([^{68}Ga]Ga-DOTA-TATE study).*

Chapter 3

Multi-modal image analysis for semi-automatic segmentation of the total liver and liver arterial perfusion territories for radioembolization

This chapter has been published as:
Rangraz EJ, Coudyzer W, Maleux G, Baete K, Deroose CM, Nuyts J. "Multi-modal image analysis for semi-automatic segmentation of the total liver and liver arterial perfusion territories for radioembolization." EJNMMI research. 2019 Dec 1;9(1):19.
Appendix 2 is not included in the published paper.

3.1 Abstract

Purpose: We have developed a multi-modal imaging approach for SIRT, combining [^{99m}Tc]Tc-MAA-SPECT/CT and/or ^{90}Y-PET, contrast-enhanced CBCT, and [^{18}F]FDG-PET/CT for voxel-based dosimetry, as a tool for treatment planning and verification. For absorbed dose prediction, a segmentation of the total liver volume and of the liver perfusion territories is required.

Method: In this paper we proposed a procedure for multi-modal image analysis to assist SIRT treatment planning. The pre-treatment [^{18}F]FDG-PET/CT, [^{99m}Tc]Tc-MAA-SPECT/CT and contrast-enhanced CBCT images were registered to a common space using an initial rigid, followed by a deformable registration. The registration was scored by an expert using Likert scores. The total liver was segmented semi-automatically based on the [^{18}F]FDG-PET/CT and [^{99m}Tc]Tc-MAA-SPECT/CT images, the liver perfusion territories were determined based on the CBCT images. The segmentations of liver and liver lobes were compared to the manual segmentations by an expert on a CT image.

Result: Our methodology showed that multi-modal image analysis can be used for determination of liver and perfusion territories using CBCT in SIRT using all pre-treatment studies. The results for image registration showed acceptable alignment with limited impact on dosimetry. The image registration performs well according to the expert reviewer (scored as perfect or with little misalignment in 94% of the cases). The semi-automatic liver segmentation agreed well with manual liver segmentation (dice coefficient of 0.92 and an average Hausdorff distance of 3.04 mm). The results showed disagreement between lobe segmentation using CBCT images compared to lobe segmentation based on CT images (average Hausdorff distance of 14.18 mm), with a high impact on the dosimetry (differences up to 9 Gy for right and 21 Gy for left liver lobe).

Conclusion: This methodology can be used for pre-treatment dosimetry and for SIRT planning including the determination of the activity that should be administered

to achieve the therapeutical goal. The inclusion of perfusion CBCT enables perfusion-based definition of the liver lobes, which was shown to be markedly different from the anatomical definition in some of the patients.

Keywords: Radioembolization, Selective internal radiation therapy (SIRT), Transarterial radioembolization (TARE), Liver segmentation, Liver lobe segmentation, Liver perfusion territory segmentation, CBCT

3.2 Introduction

Radioembolization (RE), also known as selective internal radiation therapy (SIRT) or transarterial radioembolization (TARE), is a promising therapy in both safety and efficacy aspects for non-resectable primary and metastatic liver malignancies [33,45,221–223] which is recommended in guidelines in the salvage setting in mCRC and HCC when other therapies are contraindicated or have failed, and for small tumors in patients waiting for liver transplantation [32, 133]. Several large RTCs have investigated SIRT in HCC and mCRC and did not meet their primary endpoint, highlighting the need for optimization of the technique and patient selection [33, 73, 221, 224–226].

In SIRT, millions of implantable microspheres containing yttrium-90 are administrated into the HA during a femoral arterial catheterization [153, 227] which results in higher concentration in the tumors located within that liver perfusion territory than within the normal liver parenchyma [228].

Before injecting the ^{90}Y-microspheres, a simulation is performed in which the patient specific vascular anatomy is determined and specific arteries are coiled to prevent extrahepatic dissemination [229]. Then, MAA particles labeled with technetium-99m are injected and within the hour after injection a scintigraphic planar imaging and SPECT with X-ray CT (SPECT/CT) are performed [148]. These images are used to quantify a possible pulmonary shunt and determine extrahepatic uptake. These SPECT/CT images can be used to predict the intrahepatic distribution of the ^{90}Y-microspheres as well, enabling a pre-therapeutic dosimetric analysis. Subsequently, the patient undergoes a second procedure in which a prescribed amount of ^{90}Y-microspheres are injected. Yttrium-90 is a β emitter. In soft tissue, 2.23% of the electrons produce a bremsstrahlung photon with an energy of 50 keV or more. Its decay also has a very small positron branching ratio (32 per million decays) [230, 231]. Therefore the actual distribution of the spheres can be determined by bremsstrahlung emission computed tomography (BECT) or ^{90}Y-TOF-PET [232–234].

Because of the high kinetic energy of the emitted electrons (mean energy of 0.934 MeV, mean and maximum tissue penetration of 2.5 and 11 mm, respectively), treatment with ^{90}Y-resin microspheres can achieve an absorbed dose (the energy that will be absorbed per unit of tissue mass) of about 100 to 1000 Gy to the tumor which is sufficient for complete tumor ablation, while keeping the healthy tissue irradiation below the safety threshold (typically in the order of 30-50 Gy) [235, 236]. Estimating the absorbed dose to the TVs and NTV has a key role in radionuclide therapy for predicting the tumor response and healthy liver toxicity [237].

The so-called partition method is a tissue level dosimetry method that is used widely as a tool to predict mean absorbed dose in the TV and NTV. This method assumes uniform activity in TV and NTV compartments [238]. However, there are some concerns about using the mean absorbed dose in SIRT because of the inherent activity heterogeneity. For this reason, using a more detailed dosimetry is vital for treatment optimization [73, 239]. The role of [^{99m}Tc]Tc-MAA-based dose estimation for a safe NTV absorbed dose and efficient TV absorbed dose has been investigated in several studies [175, 240, 241]. Post-treatment dosimetry has also been studied to verify the treatment planning [107,242–244].

Recent arguments over choosing between an activity prescription based on BSA and dosimetry based prescription in the treatment planning procedure [245, 246] accentuate the relevance of quality control, dosimetry process verification and standardization in the field of SIRT. In addition to the activity distribution estimation uncertainties (*e.g.*

simulating power of MAA, partial volume effect, breathing motion, ...), some errors are introduced by image processing techniques *e.g.* image registration and segmentation, which need to be avoided [73]. To date, activity calculation based on BSA is used for SIRT with resin microspheres in one-third of European hospitals regardless of availability of numerous commercial softwares designed for dosimetry [247,248]. This is possibly due to lack of image processing validation, error estimation or complexity of the process and regulation.

Image registration accuracy has been investigated for CT to CT liver registration for contrast-enhanced diagnostic CTs [249]. Over the past decade, numerous semi-automatic and automatic approaches for liver segmentation [250,251] on CT that rely on histogram based methods [252, 253], graph cut [254–256], region growing [256–258], geometric deformable model and level set [259–261], probabilistic atlas [262, 263], statistical shape models [264–266], and recently neural network [267–270] have been proposed. Despite these efforts, image registration and segmentation remains a challenging task for SIRT application for several reasons:

1. liver is a soft tissue and liver shape is heavily dependent on patient positioning (*e.g.* the position of the arms);
2. the liver shape in SIRT patients differs from the normal shape, because of preceding treatments (liver resection, liver ablation, chemotherapy) and tumor growth which makes it challenging to use liver segmentation techniques which are dependent on the liver shape for these patients;
3. liver is a soft tissue and its Hounsfield units are similar to those of adjacent organs like the heart, spleen, stomach and kidney, which makes liver segmentation on non contrast-enhanced CTs (*e.g.* CT from [^{99m}Tc]Tc-MAA study) hard, even for experts.
4. CT from [^{99m}Tc]Tc-MAA study is not a dedicated diagnostic CT, this low-dose CT usually suffers from streak artefacts; and
5. the interval between the [^{99m}Tc]Tc-MAA and the diagnostic high-dose, contrast-enhanced CT from [^{18}F]FDG study can be up to weeks to even one or two months and the liver can deform dramatically over time for several reasons *e.g.* tumor change.

Although liver segmentation techniques offer highly accurate results for healthy liver on contrast-enhanced CTs, few studies applied volumetric methods to the baseline and/or non-contrast-enhanced, low-dose CTs for radiation therapy planning. Monsky *et al.* propose a method based on iterative watershed segmentation to semi-automatic volumetric segmentation of the liver, tumor and necrosis using multi-phase CTs in 14 patients. They compare their results with manual liver segmentation and report a good inter- and intra-observer reproducibility [271]. Goryawala *et al.* present a framework for extracting 3D liver segmentation based on coupling a k-mean algorithm with a localized contouring method. They applied their method to 5 patients aiming at minimizing human intervention [272]. In [273], they improved their method by decreasing the human intervention time and applying their workflow to 34 patients with liver metastatic.

To overcome the inaccuracy of liver segmentation due to the similar Hounsfield values of the liver and its surrounding organs in non-contrast-enhanced CTs, some studies use co-segmentation algorithm, using information from different co-registered modalities (*e.g.* [^{18}F]FDG-PET and CT) to guide the liver segmentation. Wang *et al.* use FDG uptake difference between the liver and adjacent organs to separate them for 12 patients [274]. Later, they apply their method to more patients [275] and using probabilistic atlas [276]. Mendes *et al.* present a framework for outlining liver using CT alone, PET alone and a hybrid modality liver segmentation using information from PET and CT together [277].

The main aim of this study is to develop a multi-modal image analysis approach that can be used for voxel-level and partition model dosimetry, using pre-treatment simulation based on the [^{99m}Tc]Tc-MAA study. This methodology is generic and can be extended for post-treatment dose verification images. For this purpose, we developed and evaluated

a new methodology for image registration, for liver segmentation using all pre-therapy image data, for tumor segmentation using [^{18}F]FDG-PET/CT, and for LPT segmentation using the CBCT.

To our best knowledge, this is the first attempt to investigate the role of lobe segmentation based on contrast-enhanced CBCT for dosimetry and activity prescription. LPTs are usually segmented using the anatomical landmarks on CT, which reflect the standard anatomical venous lobe segmentation [278]. In our hospital, contrast-enhanced CBCT are acquired in the early and late arterial phase during the angiographic workup to outline the different LPTs [279, 280].

To our knowledge there are no reported studies investigating the registration accuracy for SIRT therapy planning; CBCT and low-dose, non-contrast-enhanced CT registration. We are also implementing a multi-model liver segmentation approach which uses the [^{18}F]FDG-PET/CT aligned to the CT from the [^{99m}Tc]Tc-MAA-SPECT/CT study. The current version is still semi-automatic and its preliminary evaluation shows that it produces a segmentation similar to that produced by an expert operator on the contrast-enhanced CT using commercial software. Nevertheless, we present the method already here because we believe that such a multi-modal segmentation approach has the potential to improve the segmentation of the liver and the tumors. Details about the method are provided as supplementary material.

The paper is organized as follows: In section 3.3, the multi-modal image analysis algorithm is described: first all images are registered to the same space, then the liver, the LPTs and the tumors are delineated. Then, the results of the proposed algorithm are shown and compared to a manual segmentation by an expert in section 3.4. Finally, in section 3.5, our results are discussed. In section 3.7 some conclusions are presented and some future directions are discussed.

3.3 Methods and materials

3.3.1 Patient selection

Between May 2014 and December 2017, 22 consecutive patients underwent bilobar SIRT in the University Hospitals Leuven (UZ Leuven) with early and late arterial phase CBCT imaging for both lobes before treatment (for delineating different LPTs) and with [^{18}F]FDG-PET/CT imaging (for delineating FDG-avid malignancies). Of these, 5 patients were excluded from the study due to artefacts or low image quality in the [^{99m}Tc]Tc-MAA-SPECT/CT study (n=3), CBCT images (n=1) and [^{18}F]FDG-PET/CT study (n=1). Pre- and post- treatment images were collected and analyzed retrospectively. From these patients, a set of 7 patients with a HCC, 2 breast, 2 melanoma, a colorectal and an esophageal cancer was arbitrarily selected to optimize the parameters of the algorithm (so called "training set") and 10 patients, 6 colorectal cancer, an esophageal cancer, a neuroendocrine tumor, a colon cancer and a cholangiocellular cancer were used for an independent evaluation (so called "test set"). A list of the optimized parameters is provided in appendix 1 (section 3.8). Detailed patient characteristics are provided in the appendix 2 (section 3.9).

3.3.2 Pre-treatment studies

Pre-treatment studies were performed for SIRT (see figure 3.1) based on the European Association of Nuclear Medicine (EANM) guideline [154], the recommendations of the American Association of Physics in Medicine (AAPM) [153] and the SIRTEX manual [281].

For a SIRT simulation, about 150 MBq of [^{99m}Tc]Tc-MAA was infused into the HA at the position where the therapeutic activity was expected to be administered (about 100 MBq and 50 MBq to the vessels that feed right and left LPTs respectively). A SPECT/CT was performed as soon as possible [148], typically within 1 hour on a Symbia T16 camera (Siemens Healthineers, Erlangen, Germany).

SPECT, using a dual-head gamma camera, was performed with rotation over 180 °, 60 views per detector and 21 sec per view in a 128×128 matrix with 15% energy window centered at the photopeak of technetium-99m (140 kev) using low-energy high-resolution collimators. The reconstruction was done using the ordered subset expectation maximization (OSEM) algorithm accounting for attenuation, position dependent collimator blurring and a scatter contribution, which was estimated using a dual-energy scatter window. Phantom experiments were done to determine the calibration factor (producing a system sensitivity of 11.7 $^{\mathrm{cpm}}/_{\mathrm{kBq}}$), which absolutely quantifies the reconstruction of the images, these results are in line with results provided by Zeintl *et al.* [282]. This image was reconstructed with an isotropic voxel size of 4.8 mm. The CT scan (120 mAs, 110 kV) was acquired with 0.9 mm in plane voxel size and 1.0 mm slice thickness.

During the angiographic workup, contrast-enhanced CBCTs were acquired in the early and late arterial phase, outlining the LPTs of the hepatic artery branches. CBCTs were performed using XtraVision (Philips Healthcare, Amsterdam, Netherlands). These images are not mentioned in the guidelines and there are not many centers that acquire these images as part of the SIRT procedure.

For some patients (*e.g.* patients with FDG-avid tumors), a whole body [^{18}F]FDG-PET/CT with a Biograph 40 TruePoint TrueV system (Siemens Healthineers, Erlangen, Germany) was performed up to two months before treatment to provide the tumor metabolic data. CT imaging was done mostly with intravenous contrast-enhancement for outlining the total liver and the liver tumor burden (85mAs, 120kV, plane voxel size of 0.98 mm, slice thickness of 1.5 mm). The PET images were reconstructed using resolution recovery, attenuating and scatter correction. Voxel size and slice thickness are 2.9 mm and 5 mm, respectively.

3.3.3 SIRT procedure

SIR-Spheres (SIRTEX Medical Ltd, Sidney, Australia) were used in all patients. According to the resin microspheres' manufacturer guideline (SIRTEX Medical Ltd, Australia, North Sydney NSW), determination of therapeutic activity was based on the BSA method [281] or a 1-compartment partition method (MIRD method) aiming at keeping the dose to each lobe below 40 to 50 Gy [203]. The activity was adjusted to have a lung absorbed dose below 30 Gy. The calculated activity was administered according to the manufacturer recommendation [281].

3.3.4 Image processing

We proposed a multi-modal image analysis approach for registering all pre-treatment images to an identical space. These aligned images were used for semi-automatic total liver, tumor and LPT delineation. All codes were written in house using IDL 8.4 (Harris Geospatial Solution, Boulder, CO, USA).

Before registering all images to an identical space, a box was defined manually for each image which contains the entire liver; this makes the whole procedure faster and also gives a data reduction for the image registration and segmentation. To define the box for each image, the first and the last plane that contain liver were selected in each of the three orthogonal views (6 planes). Then, the images were cropped by these boxes and the cropped images were used in the entire workflow (see figure 3.2).

To suppress the noise and increase the voxel intensity homogeneity within the liver, which is helpful for image registration and segmentation, the CT and CBCT images were filtered by three consecutive 2D median filtering with a width of 3 by 3 voxels; first plane-by-plane filtering in the xy-direction, then zx-direction, and finally the yz-direction. This filter better preserves the organ's edges than Gaussian filtering (see figure 3.2). The smoothed images were used as intermediate for segmentation and registration and the unsmoothed images were also processed in each step.

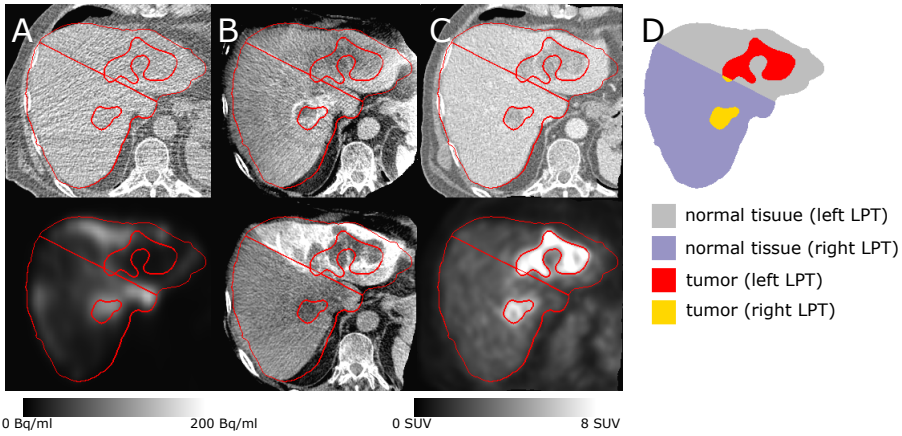

*Figure 3.1: Single transaxial slice of SIRT pre-treatment studies and segmentation result (patient ID BI01 from training set in our database): **[A]** the CT and activity image of the [^{99m}Tc]Tc-MAA-SPECT/CT scan. Correction for scatter and attenuation is applied and a phantom-based calibration factor is used to obtain images of absolute technetium-99m concentration [kBq/cc]. **[B]** CBCT images with contrast-enhancement facilitating delineation of the right and left liver lobe **[C]** the CT and PET of the [^{18}F]FDG-PET/CT study. **[D]** the segmented liver, tumor and LPTs*

3.3.4.1 Image registration

The aim is to have all images in an identical space, we refer to the resulting set of aligned images as the meta-image. Image registration was done in two steps:

First, early and late CBCTs for each LPT were aligned by a rigid registration. This multi-resolution registration used the sum of square differences as the cost function. After registration, averaging over all CBCTs creates an image which covers a larger field of view than the individual CBCTs, because each image is typically focused on a single liver lobe. We refer to this image as meta-CBCT. In addition, the contrast-enhancement is suppressed due to averaging which helps further registration.

Then, the meta-CBCT and CT from the [^{18}F]FDG study (CT_{FDG}) images were registered to the CT from the [^{99m}Tc]Tc-MAA study (CT_{MAA}) non-rigidly (starting from a initial rigid registration) and the PET image was deformed with the deformation obtained for the corresponding CT image. CBCT images were acquired in breath hold. [^{18}F]FDG-PET/CT, and [^{99m}Tc]Tc-MAA-SPECT/CT imaging allowed shallow breathing. Consequently, breathing impact is unavoidable [283]. These images were acquired in clinical routine and were not gated for respiratory movement. So, in this study breathing motion is part of the uncertainties.

The multi-resolution non-rigid registration was done with the algorithm described in [209]. Mutual information was used as the cost function. This algorithm represented the deformation with a displacement vector in every voxel. The deformation was constrained by assuming that neighboring voxels are connected by non-linear springs, which can have different rigidity for voxels belonging to different classes. The image was segmented by thresholding into air, liver, other soft tissues and bone. The rigidity of the liver was set to a relatively high value, while that of all other tissues was set to a low value. This was done to ensure that the liver registration is good and as rigid as possible, and that it is not hindered by alignment of the other structures surrounding the liver. Moreover, the registration is mostly driven by the high intensity gradients near the liver boundaries. By favoring rigidity, a useful alignment for structures inside the liver can be obtained. Indeed, the perfusion and [^{18}F]FDG uptake will not always be matched, and identifying mismatches is highly relevant for treatment planning/verification (see image 3.1). The

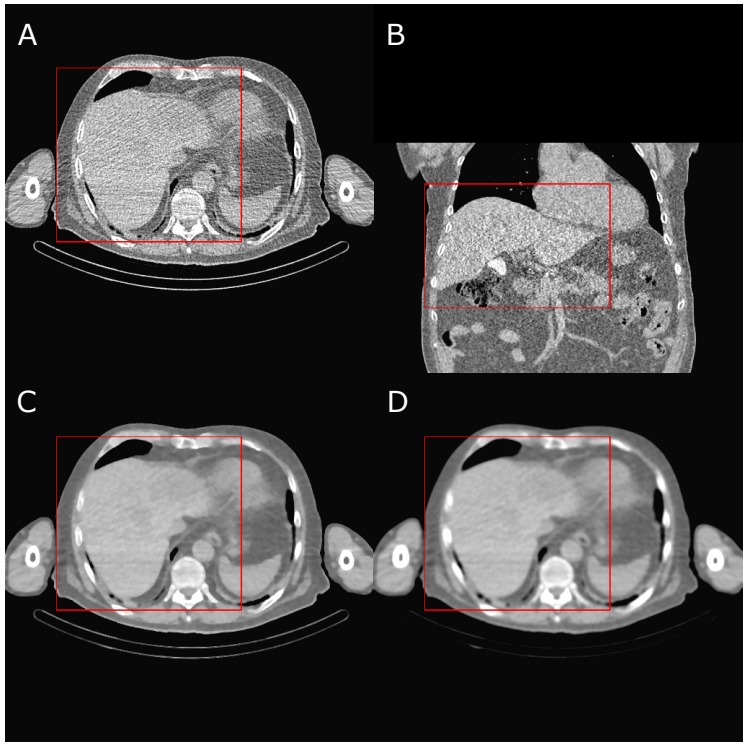

*Figure 3.2: Patient ID BI01 from training set in our database; **[A and B]** transaxial and coronal view of a CT_{MAA}, **[C and D]** median filter and Gaussian filter (FWHM=4) of the same slide in transaxial slice (image **C** is sharper and voxels within the liver are more homogeneous; red contours shows the boxes that are defined for data cropping)*

CBCTs and CT_{MAA} acquisitions were within hours from each other with minimal organ change in between.

3.3.4.2 Evaluation of registration methodology

Expert evaluation: To evaluate CT_{FDG} to CT_{MAA} non-rigid registration, an expert (CMD) scored the results by using a 5-point Likert method. The co-registered datasets were displayed in an orthogonal viewer with transverse, coronal and sagittal sections and were scored by using these predefined categories:

1. **major misalignment;** major impact on dosimetry, dosimetry results not reliable
2. **pronounced misalignment;** substantial impact on dosimetry is expected
3. **moderate misalignment;** little impact on dosimetry is expected
4. **little misalignment;** no significant impact on dosimetry is expected
5. **near perfect alignment;** no intervention warranted and dosimetry deemed reliable

The following positions were inspected using a cursor point consisting of intersecting orthogonal lines:

- cranial, caudal, lateral and medial most extreme positions of the liver contour
- the hilar fat at the portal bifurcation

- the ligamentum falciforme
- the gallbladder bed
- inlying calcifications in the liver (most often due to calcified liver metastasis), if present
- liver metastasis if visible on the non-contrast-enhanced CT
- biliary cysts, if present
- coils in hilar vascular structures from pre-SIRT workup, if present

Local volume change: The liver is assumed to be a non-compressible organ. One can consider the non-tumor tissue/tumor volume changes over time owing to the time difference between the [^{18}F]FDG and [^{99m}Tc]Tc-MAA study, but still we assumed that local volume changes should be small and could be used as a metric in the evaluation of the registration results.

We used the Jacobian determinant [284, 285] to evaluate to which extent $\mathrm{CT_{FDG}}$ to $\mathrm{CT_{MAA}}$ registration was locally volume preserving in three different VOIs for each patient: the entire liver, excluded liver and eroded liver. For the entire liver, the Jacobian of the voxels belonging to the manual liver segmentation was analyzed. For eroded liver, the manual liver segmentation eroded by a 10 mm kernel was used and excluded liver was defined as the entire liver subtracted by the eroded liver.

The most obvious feature of the liver used by the registration algorithm is its boundary, in particular for non contrast-enhanced CT images. The Jacobian is computed in a region near the liver boundary to evaluate the balance between rigidity and similarity ("excluded liver"). In non contrast-enhanced CT images, the center of the liver contains very few features, the deformation in the center is mostly driven by the deformation of the boundaries and the rigidity constraint. To evaluate the propagation of the deformation to the center of the liver, the Jacobian is also computed in the central part ("eroded liver").

3.3.4.3 Image segmentation

To define all the VOIs needed for the dosimetry report, one needs to delineate the entire liver, the tumors and the different liver perfusion territories. All the variables which were used for liver, tumor and LPT segmentation and validation are listed in table 3.1.

step	variable	description
tumor segmentation	THR(init)	initial threshold of FDG uptake for tumor core definition
tumor segmentation	BG(T_i)	measured background of tumor i
tumor segmentation	max(T_i)	measured maximum FDG uptake of tumor i
tumor segmentation	THR(T_i)	final threshold for tumor i
liver evaluation	DICE	dice coefficient
liver evaluation	TPR	true positive ratio (sensitivity)
liver evaluation	PPV	positive prediciton value
liver evaluation	RV	relative volume
liver/LPT evaluation	aHD	average Hausdorff distance
liver/LPT evaluation	mHD	maximum Hausdorff distance
LPT evaluation	Vdiff	volume difference
LPT evaluation	Rratio,Lratio	right and left volume ratio

Table 3.1: List of variables that are used in VOI segmentation and validation

Liver segmentation: The entire liver was segmented by a joint region growing by using information from three co-registered images at the same time (CT_{MAA}, CT_{FDG} and the [^{18}F]FDG-PET). This procedure benefits from co-segmentation; the liver is segmented based on the low-dose and low-quality CT from [^{99m}Tc]Tc-MAA study which is the most important pre-treatment study, but information from [^{18}F]FDG study also helps the algorithm to have better initial liver segmentation and smoother manual modification by the expert. Details about liver segmentation are provided as supplementary material (see section 3.10 and figure 3.14).

Tumor segmentation: An adaptive thresholding method was used for tumor segmentation. This method is very similar to the fixed threshold level, but the threshold level is calculated from the tumor specific background and tumor max SUV [141,212]. First, the [^{18}F]FDG-PET image was converted to SUV values. Then, a mean (μ) and standard deviation (σ) were computed within the liver. To find the tumor cores, an initial threshold (THR(init)) was set to (confidence interval of 99.5% corresponding to 2.802 sigmas):

$$\mathrm{THR(init)} = \mu + 2.802 \times \sigma \tag{3.1}$$

Then, each of the detected tumor cores was independently processed to yield a final tumor volume. A mask was generated for each tumor core (T_i) after dilation with a uniform sphere of radius 25 mm. The background for T_i ($\mathrm{BG}(T_i)$) was defined as the mean value of all voxels in the mask that had an SUV of less than 2.5, the tumor specific threshold ($\mathrm{THR}(T_i)$) was defined as [212] (see figure 3.3):

$$\mathrm{THR}(T_i) = \mathrm{BG}(T_i) + 0.41 \times (max(T_i) - \mathrm{BG}(T_i)) \tag{3.2}$$

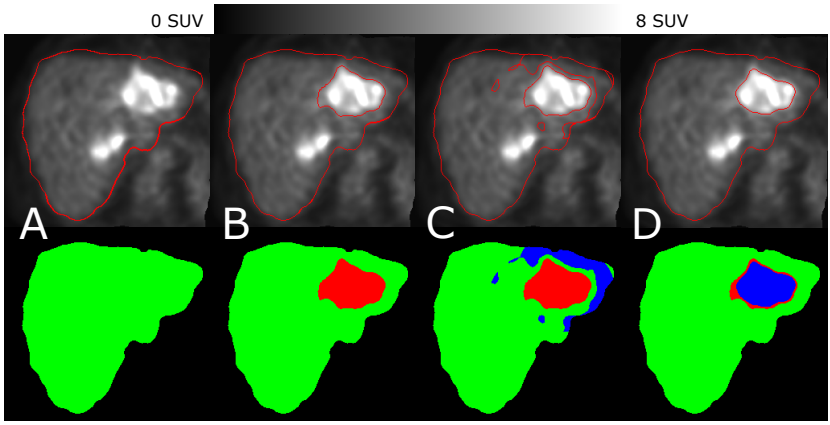

*Figure 3.3: Tumor segmentation steps for one of the tumors (patient ID BI01 from training set in our database) that is visible in the slice by using the method proposed in [212], for the other tumor(s) the same algorithm was used **[A]** initial [^{18}F]FDG-PET and (liver segmentation: green), **[B]** [^{18}F]FDG initial threshold and finding initial tumor burden (liver segmentation: green , tumor cores: red), **[C]** finding specific background for each tumor (liver segmentation: green; tumor cores: red; background: blue), and **[D]** final tumor thresholding (liver segmentation: green; initial tumor volume which is not included in the final tumor segmentation: red; final tumor segmentation: blue)*

Perfusion territories segmentation: The task is to separate the left and right LPT based on the contrast-enhancement in the early or late arterial phase of the CBCT. The early arterial phase aimed at capturing the arterial vessels (how arcuate they are? how do they bifurcate? do they go to the tumor?). On the other hand, the late arterial phase aimed at depicting the perfused parenchyma (what is the treatment volume?). To segment the liver in two lobes, an expert drew lines in at least 3 different transverse slices on one or more aligned CBCT(s) that shows a higher contrast signal in the perfused volume (most often the late arterial phase). Then a plane was fit to these lines by using the least square method. The plane was reviewed by the same expert in all 4 sets of CBCTs and revised when needed (see figure 3.4).

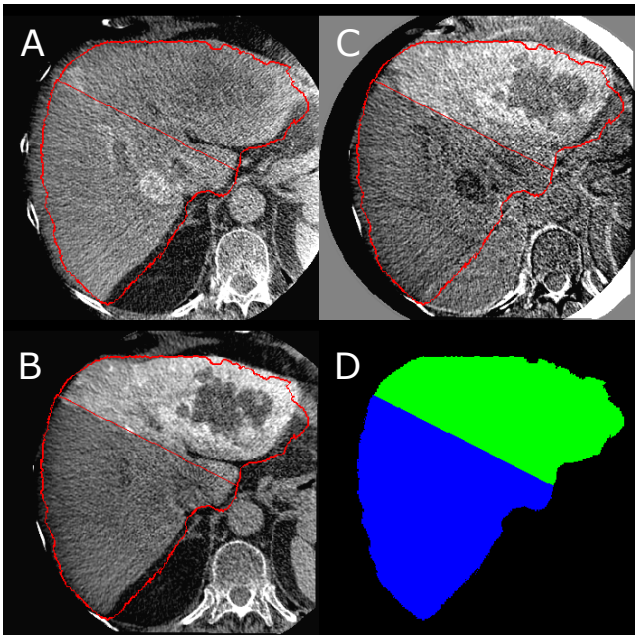

*Figure 3.4: Perfusion territory segmentation (patient ID BI01 from training set in our database); **[A and B]** CBCTs with late contrast-enhancement for the right and left liver perfusion territory respectively, **[C]** difference between two CBCTs, **[D]** LPT segmentation result (right lobe: blue; left lobe: green)*

3.3.4.4 Liver Segmentation comparison and validation

A second segmentation of the liver by an expert (WC) on a single contrast-enhanced CT was used to validate our segmentation methodology. This manual segmentation was done using Siemens Syngo MMWP Volume software [286].

Our segmentation results were compared to those obtained by manual segmentation using dice coefficient, true positive ratio (TPR) or sensitivity, positive predictive value (PPV), relative volume (RV), average Hausdorff distance (aHD) and maximum Hausdorff distance (mHD). Dice coefficient is the most used method to evaluate volume overlapping, TPR shows the ratio of the gold standard that is covered by our segmentation, PPV shows the fraction of our segmentation that is covered by the gold standard, RV reports the volume ratios and mHD and aHD are based on distances between the boundaries of the two segmentations [287, 288].

Dice index, TPR, PPV, RV, aHD and mHD between a volume A and the gold standard segmentation B are given by:

$$\begin{cases} \text{DICE} = \dfrac{2 \times |A \bigcap B|}{|A| + |B|} \\ \text{TPR} = \dfrac{\text{number of true positives}}{\text{volume of the gold standard}} = \dfrac{|A \bigcap B|}{|B|} \\ \text{PPV} = \dfrac{\text{number of true positives}}{\text{volume of the test}} = \dfrac{|A \bigcap B|}{|A|} \\ \text{RV} = \dfrac{\text{volume of the test}}{\text{volume of the gold standard}} = \dfrac{|A|}{|B|} \\ \text{aHD[mm]} = \dfrac{1}{|S(A)| + |S(B)|} \times \Big(\sum\limits_{s_a \in S(A)} \min\limits_{s_b \in S(B)} \|b - a\| + \sum\limits_{s_b \in s(B)} \min\limits_{s_a \in S(a)} \|a - b\| \Big) \\ \text{mHD[mm]} = \max \Big[\max\limits_{s_a \in S(A)} \min\limits_{s_b \in S(B)} \|b - a\|, \max\limits_{s_b \in S(B)} \min\limits_{s_a \in S(A)} \|a - b\| \Big] \end{cases} \tag{3.3}$$

Here, S(X) denotes the set of surface voxels of X and $\|.\|$ is the Euclidean distance in mm.

3.3.4.5 Impact of using the CBCT images instead of the CT image for defining LPT

To evaluate our methodology to delineate LPTs of different branches of the hepatic artery (left and right hepatic artery in our patient selection), a second segmentation was done on a single CT by defining a plane to cut the CT for segmenting two different LPTs by using the anatomical landmarks. To manually segment the liver in two lobes, the expert (WC; who performed lobe segmentation on CBCT) segmented the LPTs on the CT images with the same tool that has been used to segment them on the CBCT images. To avoid bias, the expert segmented the LPTs on CT two weeks after CBCT-based LPT segmentation. Then, this separation plane was used to define different LPTs by using the transformed liver segmentation.

The VOI for the left and right LPT were compared by using volume difference (Vdiff), left LPT volume ratio (Lratio), right LPT volume ratio (Rratio), aHD and mHD.

Left/right volume ratio was used to compare the left/right volumes derived from these two LPT segmentations; these parameters can be re-formulated as the ratio of RtoW and LtoW, which calculate right and left LPT to entire liver volume. LtoW and RtoW are two key parameters in dosimetry and therapy planning in SIRT. They are used in most of the activity calculation methods (BSA, partition method,...) to split total activity into the right and left lobe activity:

$$\begin{cases} RtoW = \dfrac{\text{volume of the right LPT}}{\text{volume of the entire liver}} \\ LtoW = \dfrac{\text{volume of the left LPT}}{\text{volume of the entire liver}} \end{cases} \tag{3.4}$$

Volume difference is the liver volume which is assigned to different lobes by CBCT and standard venous anatomical lobe segmentation, normalized by total liver volume. Similar to the liver segmentation evaluation, aHD and mHD are based on distances between the (operator defined) planes that are used to separate the LPTs.

$$\begin{cases} \text{Vdiff} = \dfrac{|L_A \bigcap R_B| + |L_B \bigcap R_A|}{|L_B \bigcup R_B|} \\ Rratio = \dfrac{|R_B|}{|R_A|} = \dfrac{\text{RtoW of the CT based lobe segmentation}}{\text{RtoW of the CBCT based lobe segmentation}} \\ Lratio = \dfrac{|L_B|}{|L_A|} = \dfrac{\text{LtoW of the CT based lobe segmentation}}{\text{LtoW of the CBCT based lobe segmentation}} \\ \text{aHD[mm]} = \dfrac{1}{|S(A)| + |S(B)|} \times \Big(\sum\limits_{s_a \in S(A)} \min\limits_{s_b \in S(B)} \|b - a\| + \sum\limits_{s_b \in s(B)} \min\limits_{s_a \in S(a)} \|a - b\| \Big) \\ \text{mHD[mm]} = \max \Big[\max\limits_{s_a \in S(A)} \min\limits_{s_b \in S(B)} \|b - a\|, \max\limits_{s_b \in S(B)} \min\limits_{s_a \in S(A)} \|a - b\| \Big] \end{cases} \tag{3.5}$$

where L_A and R_A are the left and right LPT volumes defined by the expert on CBCT images respectively and L_B and R_B are the left and right LPT volumes defined on the CT images. S(A) denotes the set of voxels in the segmented liver which lie on the plane which separates the left and right LPTs. The LPT segmentation in S(A) was derived from the the contrast-enhanced CBCT based segmentation. S(B) is defined in the same way for lobe segmentation based on anatomy (on CT).

3.3.4.6 Role of perfusion territory segmentation in dosimetry

In the SIRT workflow, the volumes of the right and left LPTs are used to compute the activities that should be administered to each of the lobes [153,154,281]. Our hypothesis is that CBCT contains more accurate information about perfusion territories than CT which only contains anatomical landmarks to distinguish the left and right liver lobes and is based on the venous anatomy (which sometimes is different from the arterial perfusion territories). To estimate the impact of using standard venous anatomical lobe segmentation on CT instead of LPT segmentation on CBCT, a simulation was performed:

First, the IA for each LPT was calculated by using the non-compartmental partition method [164] and lobe segmentations based on anatomical landmarks (current clinical workflow):

$$\text{IA}_{\text{partition}}(\text{LPT})[\text{GBq}] = \frac{D_{\text{liver}}[\text{Gy}] \times \text{CT based lobe mass [kg]}}{49.380[^{\text{Gykg}}/_{\text{GBq}}]} \tag{3.6}$$

Where D_{liver} is the desired mean dose to the total liver and 40 Gy was used based on the algorithm by the Gil-Alzugaray *et al.* study [203]. In our calculation lobe volume was converted to lobe mass by using $1.03^{gr}/_{cm^3}$ as the liver density [164].

Then, a second partition dosimetry was performed to evaluate the absorbed dose for the corresponding IA in each LPT by using CBCT-based lobe segmentation results to calculate actual mean absorbed dose (unit: Gy) in each lobe by assuming CBCT-based lobe segmentation as the ground truth:

$$D_{\text{LPT}}[Gy] = \frac{49.380[^{\text{Gykg}}/_{\text{GBq}}] \times \text{IA}_{\text{partition}}(\text{LPT})[\text{GBq}]}{\text{CBCT-based lobe mass [kg]}} \tag{3.7}$$

The impact of using CBCT instead of anatomical LPT segmentations is then assessed by computing the difference of D_{LPT} of equation 3.7 from the intended dose of 40 Gy.

3.4 Results

3.4.1 Evaluation of registration methodology

3.4.1.1 Expert evaluation:

The registration of CT_{FDG} to CT_{MAA} was reviewed by the nuclear medicine expert (CMD). The results for the registration evaluation are shown in figure 3.5 and demonstrate that the proposed method for registering CT_{FDG} to CT_{MAA} was near perfect for 5 patients (29%) and with little misalignment for 11 patients (65%), with moderate misalignment for one patient (6%) and none of the cases were scored as "pronounced misalignment" or "major misalignment". Figure 3.6 shows an example of little misalignment for CBCT and CT_{FDG} to [^{99m}Tc]Tc-MAA non-rigid registration.

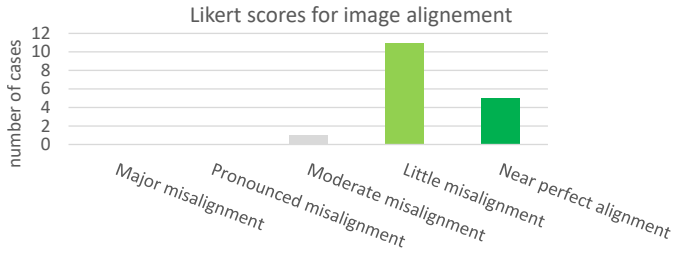

Figure 3.5: Expert Likert score for CT_{FDG} to CT_{MAA} registration

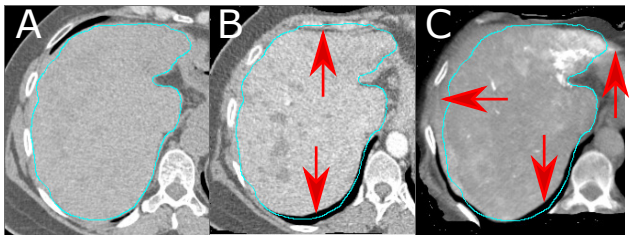

*Figure 3.6: An example (patient ID BI02 from training set in our database) of mis-registration for CT_{FDG} and CBCT to CT_{MAA} non-rigid registration (Likert score for this patient is "little misalignment", contours come from automatic liver segmentation and red arrows point to mis-registration area. **[A]** reference image (CT_{MAA}) **[B]** deformed CT_{FDG} **[C]** deformed meta-CBCTs*

3.4.1.2 Local volume change:

The Jacobian determinant for non-rigid registration deformation is a parameter which shows the local volume change. A Jacobian determinant equal to 1 corresponds to no volume change, greater than 1 corresponds to a local dilation and less than 1 corresponds to a local contraction. Negative Jacobian shows up where the deformation is locally non-revertible. Figure 3.7 shows a transaxial and coronal slice of the non-rigid registration with Jacobian determinant distribution for a patient.

Figure 3.8 shows the statistics of the Jacobian determinant. The median of the Jacobian determinant of liver voxels ranged from 0.81 to 1.05 for all cases, while the median range for eroded liver and exclude liver voxels were very similar ([0.79,1.07] and [0.83,1.05] respectively). But higher local contraction occurred in excluded liver (minimum of Jacobian ranged from 0.36 to 0.67) compare to eroded liver by minimum Jacobian range of [0.45,0.69]. Also, excluded liver had higher local dilation (maximum of Jacobian ranged from 1.47 to 1.78) compare to eroded liver which had maximum Jacobian range of [1.25,1.59].

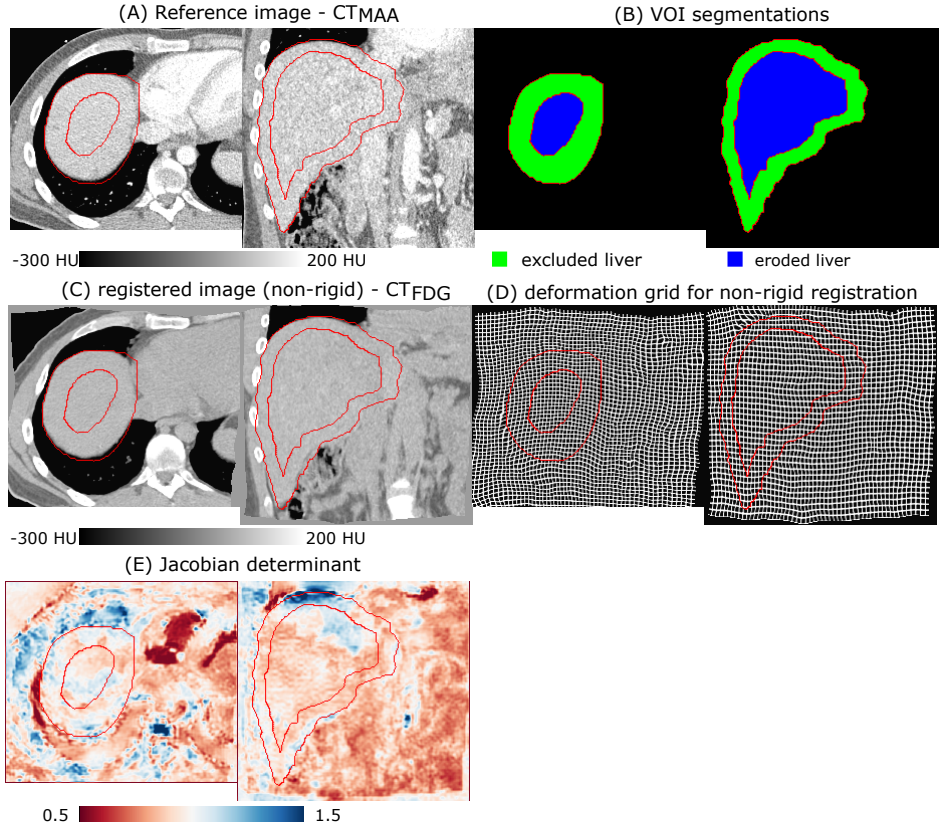

*Figure 3.7: An example (patient ID BI04 from training set in our database) of transaxial and coronal view of non-rigid registration evaluation for a patient with Likert score of "little misalignment", the statistics [min, Q1, median, Q3, maximum] of the Jacobian over all liver voxels, eroded liver and excluded liver for this patient are [0.42, 0.82, 0.89, 0.97, 1.74], [0.58, 0.83, 0.88, 0.96, 1.45] and [0.42, 0.82, 0.90, 0.99, 1.74] respectively (red contours are from excluded liver and eroded liver-see **B**); [**A**] reference image CT_{MAA} [**B**] excluded and eroded liver: eroded liver is manual liver segmentation eroded by 10 mm and excluded liver is the subtraction of excluded liver from liver [**C**] and [**D**] results of non-rigid registration (CT_{FDG} to CT_{MAA}) and the deformation grid and [**E**] Jacobian determinant of the non-rigid registration, blue: local dilation, red: local contraction and white: no local volume change*

3.4.2 Liver Segmentation comparison and validation

Our semi-automatic liver segmentation used joint region growing by using information from CT_{MAA}, CT_{FDG} and [^{18}F]FDG-PET. The results of the joint region growing were manually adjusted for all the patients. The initial liver segmentation (seed for region growing) took up to 4 minutes (median=3 min) and final adjustment took up to 6 minutes (median = 4 min). Figure 3.9 illustrates the performance of the total liver segmentation by 4 volumetric accuracy metrics (dice, TPR, PPV and RV) for all training and test cases. Statistics of these metrics for all patients (test cases and training set) are summarized in table 3.2. Median and mean of the dice coefficient were both 0.92 showing very similar liver segmentation by both methods with very narrow interquartile range. TPR and PPV had a median of 0.94 and 0.92 which means on average 94% of the liver, which was segmented with manual segmentation, was also segmented with automatic segmentation; and 92% of automatic segmented liver volume was also segmented by

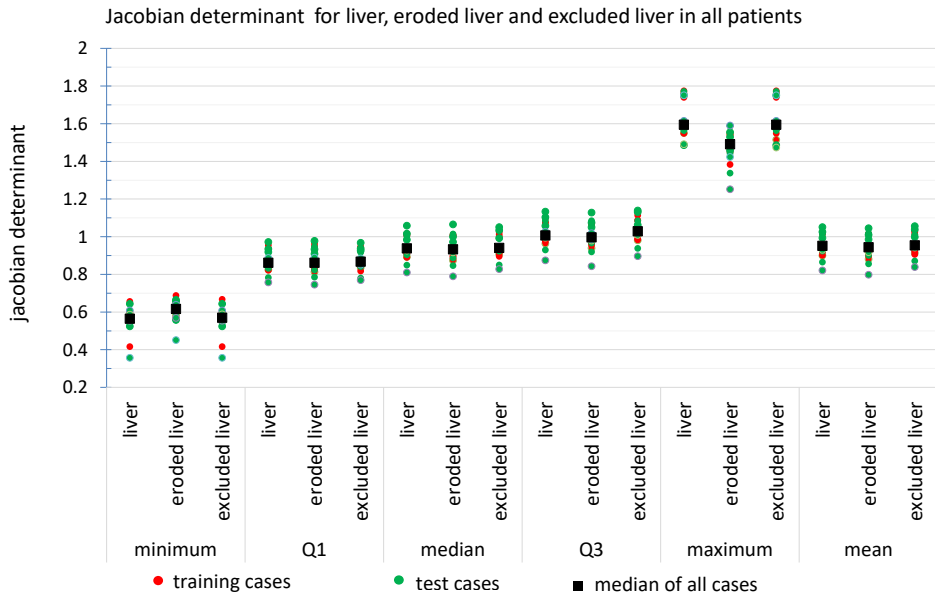

Figure 3.8: First, second and third interquartile range, minimum, maximum and mean of for Jacobian determinant for liver, eroded liver (liver eroded with 10mm) and liver excluded (subtraction of eroded liver of liver), this measure shows the local dilation (Jacobian greater than 1), local contraction (Jacobian less than 1) and no local volume change (Jacobian 1) for each voxel for liver voxels, core of the liver and border of the liver

the manual segmentation. RV is a very important parameter for IA planning. If the partition method or BSA method is used for calculating IA, the volume of the liver plays an important role. So, the ratio between the volumes is a key parameter in liver segmentation for SIRT. Our analysis shows that the median (*i.e.* 1.03) was very close to 1. The accuracy of the segmentation is important if one wishes to use small scale dosimetry (*e.g.* voxel level dosimetry). The average (aHD) and maximum (mHD) distance between the liver surfaces obtained with the semi-automated method and by the expert were 3 mm and 22 mm respectively.

	Dice	TPR	PPV	RV	mHD(mm)	aHD(mm)
minimum	0.87	0.85	0.84	0.88	16.93	2.09
Q1	0.91	0.91	0.89	0.98	20.54	2.51
median (Q2)	0.92	0.94	0.92	1.03	22.39	3.04
Q3	0.93	0.96	0.94	1.08	30.62	3.16
maximum	0.94	0.99	0.96	1.17	47.26	4.23
average	0.92	0.94	0.92	1.03	22.39	3.04

Table 3.2: Evaluation of total liver segmentation for all cases (test set and training set were pooled together); dice coefficient, true positive ratio, positive protective value , relative volume and maximum and average of Hausdorff distances for manual and automatic liver segmentation

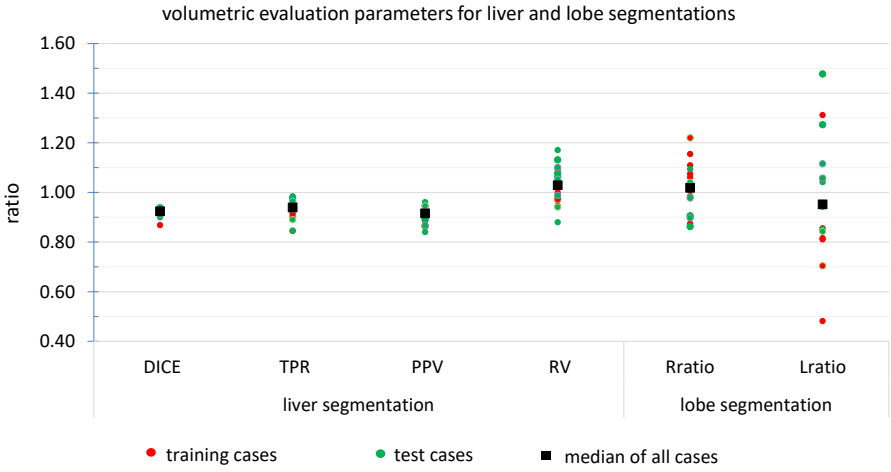

Figure 3.9: Volumetric evaluation of liver and lobe segmentation for training and test cases; Dice coefficient, true positive ratio, positive protective value and relative volume for liver manual and automatic segmentation and ratio between right/left lobe volumes for two different lobe segmentation procedures (anatomical lobe segmentation on CT and LPT segmentation on CBCT)

3.4.3 Impact of using the CBCT images instead of the CT image for defining LPT

Results for the volumetric comparison of the two different lobe segmentation procedures for the test and training sets are illustrated in figures 3.9, 3.10 and 3.12 ; more detailed results for all 17 cases (10 test and 7 training cases) can be found in table 3.3. Figure 3.11 shows an example with a large area of disagreement between CBCT and CT-based LPT segmentation. In this particular case, a tumor was segmented in different LPTs by each of the two LPT segmentation methods.

Surface distances are also provided in table 3.3 and figure 3.10.

	Vdiff	Rratio	Lratio	mHD(mm)	aHD(mm)
minimum	0.02	0.86	0.48	18.01	4.69
Q1	0.05	0.98	0.84	30.13	10.31
median (Q2)	0.08	1.02	0.95	45.80	14.18
Q3	0.11	1.08	1.06	56.91	16.97
maximum	0.14	1.22	1.48	138.16	40.08
average	0.08	1.02	0.97	48.00	15.10

Table 3.3: Evaluation of lobe segmentation for all cases (test set and training set); volume difference, right lobe volume ratio, left lobe volume ratio and maximum and average of Hausdorff distance for CT and CBCT based lobe segmentation

Median of Vdiff (area of disagreement for lobe segmentation) was 8% of the liver volume and in some cases it was as high as 14%. This is an important source of error for high level dosimetry (*e.g.* compartmental partition model and voxel-level dosimetry) when there is a tumor in this disagreement area (see figure 3.11).

The median of the ratio between left/right lobe ratio index, that has a direct effect on splitting the total prescribed IA in all prescription methods, was near 1 (1.02 and 0.95 for Rratio and Lratio respectively) but the deviation from 1 was very high and for some cases this deviation was up to 48% (see section 3.4.4).

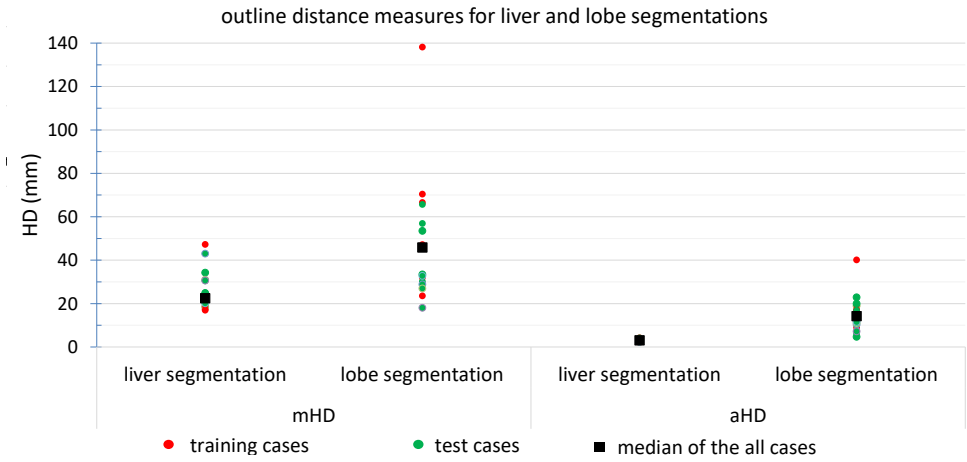

Figure 3.10: Outline maximum and average Hausdorff distance measures (mHD and aHD) between manual and automatic liver segmentation and two different lobe separation planes (on CT and on CBCT) for training and test cases

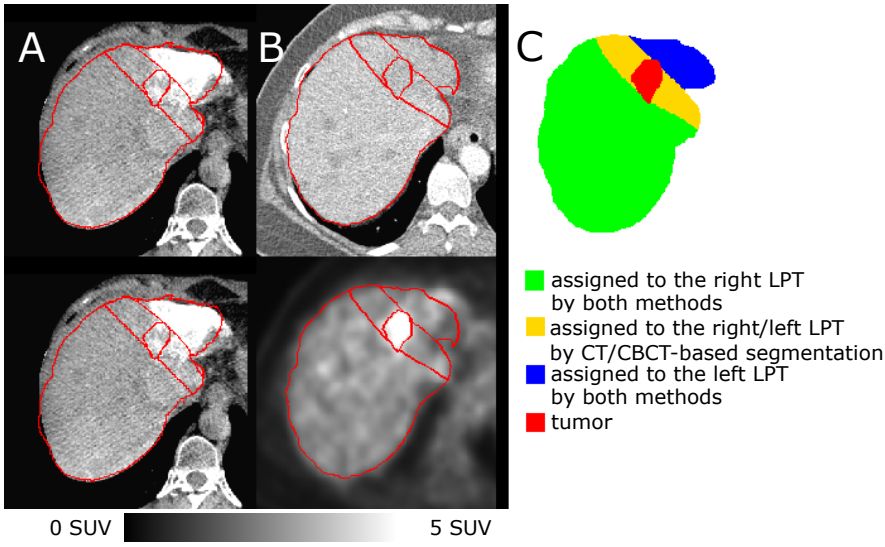

*Figure 3.11: An example (patient ID BI02 from training set in our database) of [**A**] transaxial view of early and late CBCTs, [**B**] the [^{18}F]FDG-PET/CT images, as well as, **(C)** CBCT/CT-based LPT segmentation and tumor segmentation (from [^{18}F]FDG-PET). In this slice, the tumor was segmented in different lobes by the two methods. Comparing the CBCT and CT-based lobe segmentation for this patient showed that 10% of the liver volume was assigned to different lobes (Vdiff), the ratio of "right lobe to entire liver volume ratio" for these two methods (Rratio) was 1.08 and the same parameter for the left lobe (Lratio) was 0.82. Furthermore, the average and maximum distance between lobe separation planes by these two methods (aHD and mHD) were 2.74 and 16.94mm. Dosimetry simulation showed that a mean absorbed dose to the left and right lobe when using CBCT-based lobe segmentation were 19 and 46 Gy respectively, when we aimed at delivering 40 Gy to each lobe using the CT-based LPT segmentation*

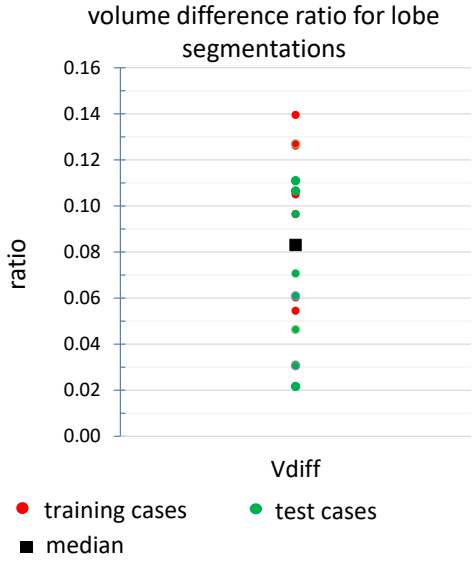

Figure 3.12: Volume difference parameter; the liver volume which was assigned to different lobes by standard venous anatomical (using CT) and perfusion (on CBCT) lobe segmentation for both training and test cases

The median of aHD and mHD between the two separating planes for the all patients were 3.04 and 22.39 mm respectively. This shows a possible error for compartmental partition model and voxel-level dosimetry because the same tumor can be assigned to a different liver perfusion territory, depending on the procedure used to segment the liver lobes. This would be very problematic for using the dosimetric result either for finding IA or post-treatment verification (see figure 3.11).

3.4.4 Role of perfusion territory segmentation in dosimetry

For analyzing the effect of using the standard venous anatomical lobe definitions instead of the perfusion territories, a simulation was designed to calculate the absorbed dose in each CBCT-based LPT. Our dosimetry calculations showed that when we aim at delivering 40 Gy to the total liver a median absorbed dose to the right CBCT-based LPT (using the standard venous anatomical lobe segmentation) was 40.8 with a [min, max] deviation of [-5.9, 8.8] Gy from 40 Gy. For the left lobe the deviation was wider, the median absorbed dose was 38.1 Gy, however, the range of deviation was [-20.7, 19.1] Gy. Figure 3.13 shows the results of the absorbed dose in the left and right LPTs (figure 3.11 shows a transaxial view slice of a LPT segmentations).

3.5 Discussion

Our aim was the development of a semi-automatic procedure for registration and segmentation of all the images acquired in the planning of and during SIRT. The tool aligns all available images and provides semi-automatic delineation of the total liver, the liver perfusion territories and the tumors. The total liver is delineated on [^{18}F]FDGPET/CT, the perfusion territories on CBCT and the tumors on [^{18}F]FDG-PET/CT. Since no ground truth is available, we have evaluated the semi-automated segmentation by comparison to manual expert segmentations and the registrations were evaluated visually by an expert.

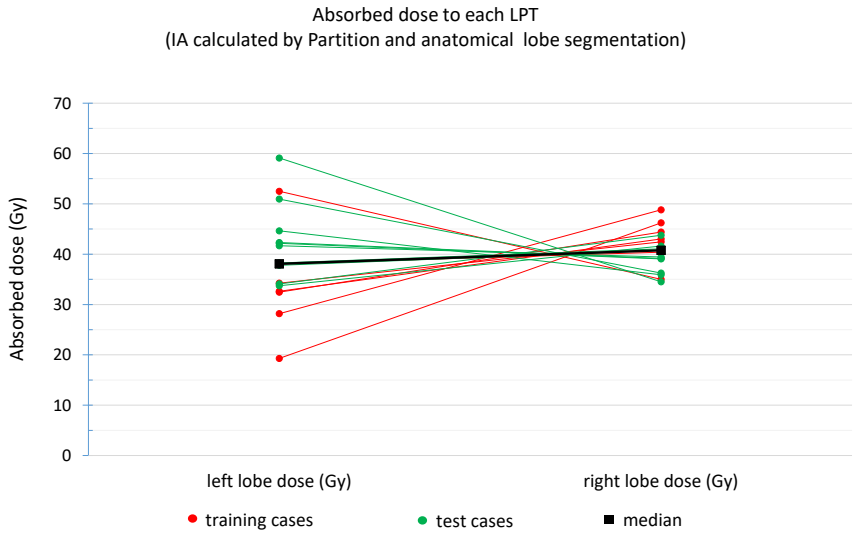

Figure 3.13: Dosimetry simulation result in each lobe when we aimed at 40 Gy based on standard venous anatomy delineation and using CBCT-based LPT segmentation and IA calculated by the partition method

This routine is generic and could be implemented (with minimal modification) in clinical routine for different tumor types and in different scenarios. For example, defining tumor lesions by thresholding the [^{18}F]FDG-PET data (for FDG-avid tumors) and/or contrast-enhanced CT or MR potentially could be used for producing more detailed dosimetric reports, by separating necrotic tissues from viable tumor. Also, our workflow allows for the delineation of liver perfusion territories on the CBCT datasets. This lobe segmentation can be used as an alternative for the current clinical approach, which segments the lobe on a CT image based on anatomical landmarks, predominantly venous structures. The effect of tumor type (*e.g.* different hypervascularity and FDG-avidity) on our proposed method for tumor and LPT segmentation could should be evaluated in further studies.

3.5.1 Validation of registration

Because in our method, we used information from all images to segment different VOIs, the accuracy of registration plays an important role. Also the alignment between the [^{99m}Tc]Tc-MAA-SPECT/CT images and the final segmentation highly affect the dose volume histograms and dosimetry analysis.

The assumption is that in our registration algorithm the deformations inside the liver were more driven by the liver boundary registration than by correct alignment of inner liver structures. For that reason, we maximized the rigidity inside the liver, in the hypothesis that this better approximates the true deformation.

Maximizing the rigidity of non-rigid registration, also, favors local volume preservation in liver voxels. A Jacobian determinant was used to estimate this local volume change due to non-rigid registration. The result of Jacobian determinant analysis showed relatively small volume change for central liver voxels. Bigger volume changes (either contraction or dilation) were observed near the border of the liver.

Sometimes these assumptions (high rigidity of liver movement and lack of local volume change of the liver) are questionable because of some small nonrigid deformation of the

liver and because of anatomical liver changes over time but still it seems reasonable to limit the non-rigidity of liver registration. In those cases, our parameter selection may contribute to mis-registration errors. Another possible source of error in registration could be the artifacts in the CT images (*e.g.* streak artefacts or photon starvation due to elbows inside field-of-view) and non-rigid liver deformation due to patient position. Likert scoring results for registration accuracy showed that this mis-registration was not crucial in most of the cases of CT_{FDG} to CT_{MAA} registration.

In clinical routine, the Jacobian can be used as a quality control step to warn physicians about possible registration problems. Our visual investigation showed that the upper and lower part of the liver were the areas with deviation from Jacobian determinant of 1 for most of the cases. In general, the results suggest that the registration error was low compared to other sources of error in SIRT dosimetry but in areas with mismatch between [^{18}F]FDG-PET and [^{99m}Tc]Tc-MAA-SPECT, we suggest to look more carefully into registration deformation to avoid underestimation of tumor dose/activity and overestimation of NTV dose/activity.

One of the limitations of this study is that during [^{99m}Tc]Tc-MAA-SPECT/CT and [^{18}F]FDG-PET/CT shallow breathing was allowed and breathing motion is not corrected. It has been shown that respiratory motion can impose a large error into final dosimetry results. Bastiaannet *et al.* report 90% to 66% decrease in activity recovery and T/N ratio because of respiratory motion in a series of SPECT/CT Monte Carlo simulation using digital XCAT phantoms. [283].

3.5.2 Validation of liver segmentation

Liver segmentation is very important for dosimetry based prescription of activity. Dice, TPR and PPV parameters showed a high similarity between our semi-automatic segmentation results and manual liver segmentation by an expert, which is used in clinical routine. A comparison between our liver segmentation results and the accurate methods on liver segmentation reviewed by Moghbel *et al.* [251] shows that our Dice metric (mean=0.92) is similar to what is reported in previous published liver segmentation algorithms ($[0.91, 0.94]$), and our relative volume metric (mean=1.03) is comparable with the result of the most accurate algorithms ($[0.943, 0.983] \bigcup [1.003, 1.075]$).

These results show that our semi-automatic liver segmentation was comparable with manual liver segmentation by an expert. Because this segmentation method is applied to a multi-modal image ([^{18}F]FDG-PET and CT) it uses more information and therefore its segmentations could even be slightly superior. This will be further investigated in the future.

3.5.3 Validation of the lobe segmentation

In standard clinical routine, the lobe segmentation is done on a CT image based on anatomical landmarks, predominately based on venous structures. Here, we studied an alternative approach, where the lobes were segmented on contrast-enhanced CBCT images. A graphical user interface was developed to cut the liver on CBCT and CT by drawing just a few separation lines on different transverse slices, it usually takes less than a minute for the expert for each case.

In several cases, the expert separated the liver differently into lobes, depending on whether anatomical CT images or perfusion CBCT images were being used. Evaluation of these two different lobe segmentation procedures suggested that there was a relatively large area in the center of the liver where the standard venous anatomical lobe segmentation on CT differed from the perfusion based segmentation on CBCT. This can cause a large error for total administered activity distribution in bilobar treatment and in dosimetry. If there is a tumor in this disagreement area, there is a risk of assigning the tumor to the wrong perfusion territory, which could lead to serious underdosing of the tumor (see figure 3.11).

3.5.4 Contribution of lobe segmentation methodology in dosimetry uncertainty

LtoW and RtoW - ratio between left/right to entire liver volume- (which is very important for dividing the total IA for left and right lobe) had a median of 0.95 (range:[0.48, 1.48]) and 1.02 (range[0.86, 1.22]) respectively. The volume ratio of the left LPT to the entire liver had a wider range than right to entire because the left lobe is generally smaller than the right lobe and is more sensitive to mis-segmentation. It showed that the left lobe suffered more from under/over-treatment or under/over-irradiation by using the standard venous anatomical lobe segmentation as an estimate of the LPT. In our dosimetric setting, this under-treatment could be up to 21 Gy for the left lobe and 5 Gy for the right lobe. On the other hand over-irradiation of the left lobe was up to 19 and 9 Gy for the left and right lobe respectively.

3.6 Tumor segmentation

In this study, we have focused on FDG-avid tumors that can be delineated by thresholding the [^{18}F]FDG-PET images. In this study an adaptive threshold method was used for tumor segmentation which uses a tumor specific threshold level by considering the SUV_{max} and background SUV for each tumor separately. Because thresholding the [^{18}F]FDG-images is straightforward and the same as the method used by experts to delineate the lesions, we have not attempted to further evaluate the tumor delineation.

3.7 Conclusion

A multi-modal image analysis approach was developed to obtain a personalized liver map (liver, perfusion territories and tumor segmentation) from the pre-treatment [^{99m}Tc]Tc-MAA-SPECT/CT, [^{18}F]FDG-PET/CT and CBCT images. The analysis showed that liver segmentation was comparable with manual segmentation by an expert. Liver perfusion territory segmentation by using CBCT instead of using CT and anatomical features showed to improve segmentation; the results showed a relatively high difference in volumetric parameters that are very important for SIRT in clinical routine.

Our results were based on 7 cases for optimizing and 10 test cases. Extending the number of patients can help us to evaluate our routine in clinical practice.

This procedure can be used in the future to provide semi-automatic voxel-level fractional uptake predictions based on the [^{99m}Tc]Tc-MAA-SPECT/CT. By using this workflow, various dosimetry reports can be computed which can be used to evaluate and improve the safety and effectiveness of SIRT. This method can be used in the future for finding the IA more accurately by using either dosimetric methods (partition, voxel-level dosimetry, ...) or non-dosimetric methods (BSA, SIRFLOX look-up table [169],...).

This procedure was designed for patients with [^{18}F]FDG-avid tumors but in the future it can be extended to using magnetic resonance (MR) images instead of [^{18}F]FDG-PET/CT images in patients with non-FDG-avid tumors such as hepatocellular carcinoma.

3.8 Appendix 1: Optimized parameters

As discussed in section 3.3.4, for optimizing employed image processing techniques (*e.g.* pre-processing, image registration, and VOI segmentation), a set of 7 patients was used to tune the parameters. In table 3.4, a description of the optimized parameters is presented.

section	aim	possible choices and/or parameter values	optimized parameter
3.3.4	noise reduction	2D median filter (neighborhood of 3×3 or 5×5) and Gaussian smoothing (FWHM= 3 and 4 mm)	2D median filter (5×5)
3.3.4.1	CBCTs registration	cost: MI, normalized MI, SSD, and absolute differences	SSD
		optimization: Greedy and Powell	Greedy (faster)
3.3.4.1	initial rigid registration	cost: MI, normalized MI, SSD, and absolute differences	MI for CBCT2CT and SSD for CT2CT
		optimization: greedy and Powell	Greedy
3.3.4.1	non-rigid registration	cost: MI and SSD	MI for CBCT2CT and SSD for CT2CT
		HU intervals for each tissue class (voxels within each class have identical spring characteristics)	**CBCT2CT classes:** outside the FOV [-∞,-1000], air [-1000,-200], liver [100,300], bone [300,+∞], and other tissues[-200,100]. **CT2CT classes:** air [-2000,-250], liver [-250,0], bone [200,+∞], and other tissues [0,200]
		Spring cost function (see formula 6 in [209]), Spring stiffness (ω), spring maximum deformation (B), resolutions, and number of iteration and maximum deformation for each resolution.	Spring cost function's parameters were optimized separately for CBCT2CT and CT2CT registration
3.9	initial liver segmentation	number of slices between two manual segmentations	every 15^{th} slice
		radius of erosion (for core) and dilation (for mask)	dilation and erosion by 20 voxels (18 mm)
		coefficient of the μ in formula 3.8	coefficient of 2
3.9	second region growing	dilation radius when defining a mask	r=20 voxels (18 mm)
		(k_1, k_2) in formula 3.9	$\text{CT}_{\text{MAA}} : (-2.5, 2)$, $\text{CT}_{\text{FDG}} : (-2.5, 2)$ and $\text{PET} : (-2, +\infty)$
3.3.4.3	tumor segmentation	tumor core: multiplication factor for σ in formula 3.1 (3.291, 2.802, 1.960, and 1.645)	factor for $\sigma = 2.802$
		tumor threshold methods based on [141, 212]: $k \times \text{MAX}$ and $\text{BG} + 0.50 \times (\text{MAX} - \text{BG})$ with k= 0.41, 0.50, and 70	$\text{BG} + 0.41 \times (\text{MAX} - \text{BG})$ (formula 3.2)

Table 3.4: List of optimized parameters

3.9 Appendix 2: Patient information

characteristics	all cases	training set	test set
patient information, median [range]			
sex (female/male)	6/11	3/4	3/7
age in years	60.5 [32.9, 72.3]	60.6 [32.9, 72.3]	58.2 [36.2, 69.5]
height in meter	175 [160, 193]	174 [163, 186]	178 [160, 193]
weight in kg	81 [61, 123]	79 [71, 100]	84 [61,123]
tumor cell type, n (%)			
mCRC	7 (41%)	1 (14%)	6 (60%)
breast cancer	2 (12%)	2 (29%)	0 (0%)
melanoma cancer	2 (12%)	2 (29%)	0 (0%)
esophageal cancer	2 (12%)	1 (14%)	1 (10%)
HCC	1 (6%)	1 (14%)	0 (0%)
mNET	1 (6%)	0 (0%)	1 (10%)
colon cancer	1 (6%)	0 (0%)	1 (10%)
cholangiocellular	1 (6%)	0 (0%)	1 (10%)
volumes from prescription sheet (cc), median [range]			
total liver (WL)	1892 [1268, 3127]	1878 [1663, 2721]	1907 [1268, 3127]
total liver (L-LPT)	448 [215, 1197]	390 [251, 1050]	514 [215, 1197]
total liver (R-LPT)	1496 [677, 1930]	1330 [1223, 1839]	1533 [677, 1930]
NTV(WL)	1700 [1218, 2988]	1700 [1513, 2528]	1694 [1218, 2988]
NTV (L-LPT)	390 [135, 1115]	390 [201, 1041]	395 [135, 1115]
NTV (R-LPT)	1319 [700, 1873]	1241 [1184, 1612]	1344 [700, 1873]
tumor (WL)	150 [7, 643]	150 [28, 494]	153 [7, 643]
tumor (L-LPT)	36 [0, 312]	18 [0, 109]	51 [0, 312]
tumor (R-LPT)	130 [7, 479]	146 [10, 479]	93 [7, 331]
clinical information from prescription sheet (%), median [range]			
TI (WL)	7.1 [0.4, 27.8]	8.5 [1.5, 24.2]	5.7 [0.4, 27.8]
TI (L-LPT)	6.9 [0.0, 47.3]	4.8 [0.0, 28.7]	8.7 [0.0, 47.3]
TI (R-LPT)	8.6 [0.8, 27.7]	11.0 [0.8, 27.7]	6.5 [1.1, 20.0]
LtoW ratio	25 [11, 60]	23 [12, 39]	27 [11, 60]
LSF	6.4 [3.8, 8.5]	7.4 [3.8, 8.2]	5.8 [3.9, 8.5]
day differences between different studies and SIRT (days), median [range]			
FDG and SIRT	20 [3, 58]	35 [3, 58]	16 [6, 40]
MAA and SIRT	21 [15, 41]	21 [15, 32]	21 [15, 41]
prescription			
IA calculation method, n (%)			
BSA	14 (82%)	7 (100%)	7 (70%)
PM	3 (18%)	0 (0%)	3 (30%)
IA in GBq, median [range]			
WL	1.850 [1.268, 2.502]	1.837 [1.746, 2.063]	1.882 [1.268, 2.502]
L-LPT	0.457 [0.228, 1.089]	0.457 [0.228, 0.724]	0.469 [0.248, 1.089]
R-LPT	1.339 [0.733, 1.783]	1.339 [1.113, 1.640]	1.414 [1.113, 1.640]

WL:whole liver ; L-LPT:left liver perfusion territory; R-LPT:right liver perfusion territory; LtoW ratio:L-LPT to WL volume; TI: tumor involvement

Table 3.5: Patient characteristics

3.10 Supplementary material: Joint region growing for liver segmentation

A joint region growing method has been designed to delineate the liver using CT from [^{99m}Tc]Tc-MAA-SPECT/CT, and CT and PET from [^{18}F]FDG-PET/CT study. The algorithm consisted of the following three steps:

- **Initial liver segmentation:** first, we manually segmented the liver in every 15$^{\text{th}}$ slice corresponding to 15 mm in the axial direction. The final liver segmentation was done independently in each of these volumes (of 15 slices) by the joint region growing algorithm. The eroded version (r=20 voxels) of the intersection of two neighboring segmentations defined the seed for the joint region growing algorithm, and the dilated (r=20 voxels) union determined the mask of the joint region growing algorithm. In the joint region growing algorithm, a voxel (μ_j) within the selected mask was considered as liver if its intensity satisfies:

$$\forall i : |\mu_j - \mu^i| \leq 2 \times \sigma^i, i = \text{CT}_{\text{MAA}}, \text{CT}_{\text{FDG}}, \text{PET} \tag{3.8}$$

where μ^i and σ^i are the mean and standard deviation of the segmented voxels in image i in the previous step of region growing (see figure 3.14).

- **Second region growing:** the segmentation from the previous step was used as the seed for the second region growing. In this step, the dilated version of the resulting VOI by radius 20 voxels was used as the mask. In the second joint region growing algorithm, a voxel (μ_j) within the selected mask was considered as liver if its intensity satisfies:

$$\forall i : k_1^i \times \sigma^i \leq \mu_j - \mu^i \leq k_2^i \times \sigma^i, i = \text{CT}_{\text{MAA}}, \text{CT}_{\text{FDG}}, \text{PET} \tag{3.9}$$

where μ^i and σ^i are the mean and standard deviation of the segmented voxels in image i in the previous step of region growing. (k_1^i, k_2^i) was set to $(-2.5, 2)$, $(-2.5, 2)$ and $(-2, \infty)$ for $i = \text{CT}_{\text{MAA}}, \text{CT}_{\text{FDG}}, \text{PET}$ respectively, also μ_j was restricted to be below 2.5 Standardized Uptake Value (SUV) for $i = \text{PET}$.

- **Adjustment:** finally, the resulting VOIs were adjusted manually and closing and opening with 3 mm were applied.

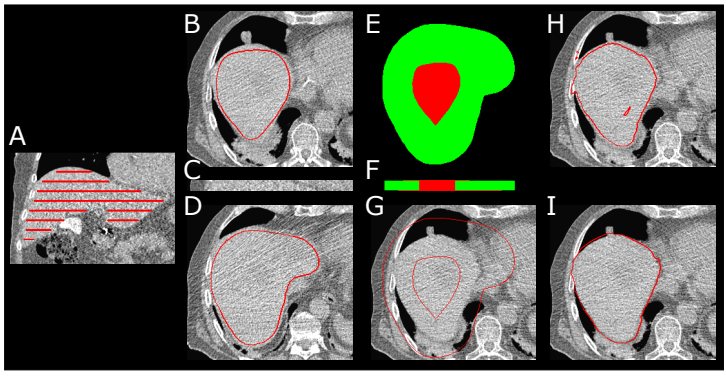

*Figure 3.14: Semi-automatic liver segmentation steps (patient ID BI01 from training set in our database), **[A]** manual liver segmentation in every 15th slices, **[C]** a layer and **[B]** and **[D]** transverse slice of the upper and the lower plane of a sample layer and their manual segmentation, **[E]** and **[F]**the layer region growing seed (red) and mask (green), **[G]** a slice in the middle of the layer and its seed and mask, **[H]** initial region growing result and **[I]** final segmentation*

Chapter 4

Quantitative comparison of pre-treatment predictive and post-treatment measured dosimetry for selective internal radiation therapy using cone-beam CT for tumor and liver perfusion territory definition

This chapter has been accepted as:
Rangraz EJ, Tang X, Van Laeken C, Maleux G, Dekervel J, Van Cutsem E, Verslype E, Baete K, Nuyts J, Deroose CM. "Quantitative comparison of pre-treatment predictive and post-treatment measured dosimetry for selective internal radiation therapy using cone-beam CT for tumor and liver perfusion territory definition." EJNMMI research, 10(1), 1-20.
Appendixes are not included in the published paper.

4.1 Abstract

Background: Selective internal radiation therapy (SIRT) is a promising treatment for unresectable hepatic malignancies. Predictive dose calculation based on a simulation using technetium-99m macro-aggregated albumin ([^{99m}Tc]Tc-MAA) before the treatment is considered as a potential tool for patient-specific treatment planning. Post-treatment dose measurement is mainly performed to confirm the planned absorbed dose to the tumor and non-tumor liver volumes. This study compared the predicted and measured absorbed dose distributions.

Methods: Thirty-one patients (67 tumors) treated by SIRT with resin microspheres were analyzed. Predicted and delivered absorbed dose was calculated using [^{99m}Tc]Tc-MAA-SPECT and ^{90}Y-TOF-PET imaging. The voxel-level dose distribution was derived using the local deposition model. Liver perfusion territories and tumors have been delineated on contrast-enhanced CBCT images, which have been acquired during the [^{99m}Tc]Tc-MAA workup. Several dose-volume histogram (DVH) parameters together with the mean dose for liver perfusion territories, non-tumoral and tumoral compartments were evaluated.

Results: A strong correlation between the predicted and measured mean dose for non-tumoral volume was observed (r=0.937). The ratio of measured and predicted mean dose to this volume has a first, second, and third interquartile range of 0.83, 1.05, and 1.25. The difference between the measured and predicted mean dose did not exceed 11 Gy. The correlation between predicted and measured mean dose to the tumor was moderate (r=0.623) with a mean difference of -9.3 Gy. The ratio of measured and predicted tumor

mean dose had a median of 1.01 with the first and third interquartile ranges of 0.58 and 1.59, respectively. Our results suggest that [^{99m}Tc]Tc-MAA-based dosimetry could predict under- or over-dosing of the non-tumoral liver parenchyma for almost all cases. For more than two-thirds of the tumors, a predictive absorbed dose correctly indicated either good tumor dose coverage or under-dosing of the tumor.

Conclusion: Our results highlight the predictive value of [^{99m}Tc]Tc-MAA-based dose estimation to predict non-tumor liver irradiation, which can be applied to prescribe an optimized activity aiming at avoiding liver toxicity. Predictive dosimetry is also moderately reliable to estimate the tumor absorbed dose.

Keywords radioembolization, selective internal radiation therapy (SIRT), trans arterial radioembolization (TARE), dose estimation, dosimetry, liver perfusion territory segmentation, CBCT, dose validation, dose comparison

4.2 Introduction

Selective internal radiation therapy (SIRT) is an increasingly applied palliative treatment option for unresectable primary and secondary hepatic malignancies. This treatment modality consists of infusing microspheres labeled with either yttrium-90 or holmium-166 within a selected branch of the hepatic artery. Choosing a proper branch of the hepatic artery is usually performed in the course of an angiography session, which aims at finding the tumor-feeding vessel(s) [227]. By infusing hundred-thousands/millions of microspheres through the tumor-feeding microvessels, they will get trapped within the liver, and the concentration of the lodged beads will be superior within the tumor compared to the non-tumoral liver parenchyma. The high energy and low tissue penetration of the used β-emitter (yttrium-90 or holmium-166) lead to higher energy deposited within the tumor compared to the non-tumoral hepatic tissue [228].

Recent studies showed a relation between tumor absorbed dose and tumor control probability, as well as non-tumoral liver absorbed dose and normal tissue complication probability. These insights serve as the basis of precision SIRT, where the prescribed injected activity is determined based on accurate knowledge of the biodistribution of the microspheres. The role of predictive dosimetry is becoming important in SIRT, and many recent studies have indicated to use a multi-compartment or voxel-level predictive dosimetry for this treatment. Ideally, dosimetric assessment should be performed in two steps: **(1)** absorbed dose prediction before treatment for each liver perfusion territory (LPT) which can be applied in an individual treatment planning to prescribe a tailored injected activity using patient-specific dosimetric criteria for liver perfusion territory (LPT), tumor volume (TV), and/or non-tumor volume (NTV); **(2)** absorbed dose evaluation after treatment for each LPT to determine the actual doses that have been given.

By definition, the absorbed dose is the amount of energy per mass (in Gy or $\frac{\mathrm{J}}{\mathrm{kg}}$) delivered to a defined VOI, *e.g.* total liver, LPTs, NTVs, and TVs. To estimate the absorbed dose before treatment, a simulation is performed using [^{99m}Tc]Tc-MAA particles that mimic the intra- and extrahepatic biodistribution of the therapeutic microspheres, which are usually derived from a SPECT/CT image performed shortly after administration. Besides, after administrating the ^{90}Y-microspheres, a BECT/CT and/or PET/CT or PET/MR image is performed which represents the actual activity distribution within the liver which again can be translated to an absorbed dose in each defined volume [73,98].

Several studies showed a good correlation between pre-treatment dose estimation (using SPECT images from a [^{99m}Tc]Tc-MAA study) and post-treatment dose calculation (using ^{90}Y-PET images after treatment). On the other hand, some authors suggest that in certain circumstances, [^{99m}Tc]Tc-MAA based dosimetry poorly predicts the actual absorbed dose. Cremonesi *et al.* provide some useful insight into the variations of existing SIRT dosimetry [71]. Several factors can describe this discrepancy: **(a)** the fundamental

difference between [^{99m}Tc]Tc-MAA and microspheres characteristics (*e.g.* size, morphology, density), **(b)** the difference between administration during the workup and treatment session (*e.g.* catheter tip position, arterial vasospasm, and physiologic variances in hepatic blood flow), and **(c)** different VOI definition for predictive and post-therapy measured dosimetry.

One of the main contributors to over- or underestimation of the predicted and measured doses, is the method used for VOI definition. In many studies, fixed or tumor-specific [^{99m}Tc]Tc-MAA thresholding is used for TV definition [243, 289]. By thresholding the activity map, one considers that tumors correspond to high uptake regions, while the low-activity areas correspond to the non-tumoral liver compartment, which can be questionable if some fraction of the tumor has low uptake (which results in an overestimation of the tumor dose) or if some part of the non-tumoral tissue has a high activity accumulation (underestimation of non-tumoral liver dose) in pre- and/or post-treatment session. Also, this approach might reinforce the correlation between predicted and measured doses. Besides, the LPT definition plays an essential role in the VOI definition for extracting relevant dose reports, especially T/N ratio, tumor to non-tumoral volume ratio within the LPT, and accurate NTV definition for reporting doses. Typically, LPTs are segmented on anatomical images (CT or MR) using anatomical landmarks, which do not necessarily represent the volume that is irrigated by the branch of the hepatic artery tree that will be injected. Our previous study identified this discrepancy as a significant source of uncertainty while reporting the mean predicted dose for each LPT [49].

This study aims to evaluate the use of specific VOI definition (based on catheterization during pre-treatment angiographic workup) for comparing predictive dosimetry and post-treatment dose measurement. In this study, contrast-enhanced CBCT images, which are obtained with the catheter in different positions of the hepatic arterial tree, are used to define LPTs and tumors. After aligning these VOIs to the [^{99m}Tc]Tc-MAA-SPECT and ^{90}Y-PET space, the predicted and measured dose distribution within the tumor and non-tumoral liver parenchyma are reported. To our knowledge, this is the first study applying the CBCT-based VOI segmentation (most importantly for LPT segmentation) to validate [^{99m}Tc]Tc-MAA based dose estimation. Evaluating the correlation between predicted and measured dose is an important step towards precision SIRT and optimizing the likelihood of tumor response while minimizing the risk of normal liver complications.

4.3 Materials and methods

4.3.1 Patients

This retrospective study analyzed 31 patients out of a total of 49 treated patients with ^{90}Y-labelled resin microspheres (SIR-Spheres, SIRTEX Medical Ltd, Sydney, Australia), between November 2017 and April 2019. This time frame was chosen because post-therapy imaging was performed with ^{90}Y-PET since November 2017 in our center. Exclusion criteria were missing data (*e.g.* missing images), insufficient information (*e.g.* contrast enhancement in CBCT images), and patients without a tumor larger than 5 ml. This study was approved by the local University Hospital Ethics Committee (UZ/KU Leuven).

4.3.2 Treatment workflow

All procedures were performed according to the European Association of Nuclear Medicine (EANM) guideline [245] and the recommendations of the American Association of Physics in Medicine (AAPM) [153].

In short, before treatment, all patients underwent a simulation workup. During this session, an angiography was performed to identify the hepatic arterial anatomy, followed by a pair of contrast-enhanced CBCT focusing on each LPT in the early and late arterial phase. These interventional X-ray images were obtained using XtraVision (Philips Healthcare, Amsterdam, Netherlands). The CBCTs were performed by acquiring 60

frames per second while rotating the C-arm around the patient in around 5 to 8 seconds, using 120 kV tube voltage, 188 mA tube current, and tube current and voltage modulation. For early arterial phase scan, a delay of 6 seconds after initiation of the contrast medium injection was used. Then, the late arterial phase scan performed with an 8 second delay after the end of the early arterial scan. The 2D projection images were reconstructed using standard vendor software with 0.66 mm isotropic resolution and matrix size of 384×384×297 pixels. Thereafter, [^{99m}Tc]Tc-MAA particles were administered as slow as possible while taking care to place the catheter at the exact same position as where it will be placed for treatment. During work-up, fluoroscopy techniques were used to assess the catheter tip position. As soon as possible after the administration, a planar gamma camera imaging and a SPECT/CT on a Symbia T16 dual-head gamma camera (Siemens Healthineers, Erlangen, Germany) were acquired to evaluate the possible LSF [148] and activity distribution within the liver. SPECT images were acquired with low-energy, high-resolution collimators with rotation over 180 °, 60 views per detector, and 21 seconds per view at an energy window of 140 keV with a 15% energy window. These projections were reconstructed on a 128×128 matrix in an isotropic voxel size of 4.8 mm using ordered subset expectation maximization algorithm accounting for attenuation, position-dependent collimator blurring, a scatter contribution, which was estimated using a dual-energy scatter window, and a Gaussian post-reconstruction filter of 7.5 mm in full width at half maximum.

Before the treatment, baseline contrast-enhanced CT and/or MR imaging was performed for volumetric assessment (NTV and TV in each perfusion territory). By using this volumetric information together with the activity uptake information extracted from the [^{99m}Tc]Tc-MAA study, an injected activity was prescribed for each LPT by applying either the MIRD method (non-compartmental partition model) or compartmental partition model using a conversion factor of 49.87 $\frac{\text{Gy}\times\text{kg}}{\text{GBq}}$ aiming at patient-specific absorbed dose criteria for whole LPT (MIRD approach) or tumor compartment and non-tumoral liver parenchyma compartment. The dose to the lungs was kept below 30Gy, using the calculated LSF on planar images at face value.

On the day of treatment, for each LPT, the catheter tip was in the same position as during the pre-treatment workup. Exactly identical catheter positioning between diagnostic and therapeutic angiography was confirmed with fluoroscopy techniques by comparing with the previous data set from the MAA work-up A day after administering the prescribed activity, the actual distribution of the microspheres was controlled by a TOF-PET examination on either a PET/MR system (Signa, GE Healthcare, Waukesha, MI, USA) or a PET/CT system (Discovery MI, GE Healthcare, Waukesha, MI, USA). The emission data were corrected for randoms, scatter, attenuation, TOF offset, and dead-time, and reconstructed using maximum-likelihood expectation-maximization algorithm using two iterations and 28 subsets. For PET/MR imaging, the standard vendor attenuation correction was used: the attenuation map is estimated from the Dixon MR images (the Dixon sequence is called LAVA-FLEX) and CT image for the Signa and Discovery systems, respectively. For PET/CT system, a Gaussian post-reconstruction filter of 5 mm full-width at half-maximum in the x- and y-direction and a smoothing filter with coefficients [1,2,1] was applied in the z-direction. The reconstruction voxels have a dimension of 2.73×2.73×2.79 mm^3. For PET/MR system, voxels with 3.13×3.13×2.78 mm^3 dimensions were smoothed with a Gaussian filter with 7 mm full-width at half-maximum in the x- and y-direction and a [1,2,1] filter in the z-direction. More information about ^{90}Y-PET imaging for both PET/MR and PET/CT cameras is described in table 4.1.

Representative images of [^{99m}Tc]Tc-MAA-SPECT/CT, CBCTs, and post-treatment images are available in figure 4.1. One more case is provided in the supplementary material.

4.3.3 Image processing

All described images in the previous section were imported into the MIM software 6.8.4 (MIM software Inc, Cleveland, Ohio) for further processing and extracted as DICOM

parameter	PET/MR	PET/CT
coincidence time resolution (ps)	400	400
[transaxial , axial] FOV (mm)	[600, 250]	[700,198]
number of bed positions	1	1
total acquisition time (sec)	1800	900
random correction method	single-based random correction	single-based random correction

Table 4.1: Details of ^{90}Y-PET imaging for PET/MR and PET/CT camera

images to be processed in IDL 8.4 (Harris Geospatial Solution, Boulder, CO, USA). All manual VOI correction/delineation has been done with MIM software, and image processing was performed using in-house software written in IDL.

4.3.3.1 Image registration

A multi-resolution, non-rigid registration is applied to register CBCT images to the CT from the [^{99m}Tc]Tc-MAA study as well as the CT or MR from the ^{90}Y-PET images. This algorithm is described in detail in our previous publication [49]. In short, this algorithm represents the deformation with a displacement vector in every voxel, assuming non-linear springs connect neighboring voxel pairs. Voxels are assigned to tissue classes (*i.e.* air, liver, non-liver tissue, and bone), and the features of the springs (*i.e.* stiffness, maximum deformation) can have different values for different classes. A lower rigidity is applied to the non-liver voxels compared to a high rigidity to the liver, in order to favor realistic deformations, and discourage excessive deformations in (almost) uniform regions that have hardly any features to guide the registration.

4.3.3.2 Liver segmentation

First, a convolutional neural network model is used to segment the entire liver on the CT image from the [^{99m}Tc]Tc-MAA study. The convolutional neural network model is a modified version of the dual pathway, 11-layer deep, three-dimensional structure (named DeepMedic) designed for the task of brain lesion segmentation [210]. The modified model contains three pathways. Every pathway has 10 layers connected via $3\times3\times3$ convolutional kernels followed by two common pathways based on $1 \times 1 \times 1$ convolutional kernels. It was trained with 139 datasets from three liver segmentation challenges (SLIVER07 [288], LiTS17 [290], and Medical Segmentation Decathlon [291]) and 12 SIRT patient datasets from UZ Leuven [211]. Then, the output of the convolutional neural network (whole liver volume) was reviewed/corrected using MIM.

To segment the liver within post-treatment ^{90}Y-PET space, the deformation derived from the registration algorithm is used to transform the liver segmentation on the [^{99m}Tc]Tc-MAA to the post-treatment space. Then, contours were exported as DICOM RTstruct sets and imported to the MIM software. A slight manual adaptation was performed using MIM software tools to compensate for imperfections as a result of the registration process and volumetric variations between post-treatment MR or CT and CT images from [^{99m}Tc]Tc-MAA study.

4.3.3.3 LPT and tumor segmentation

CBCT images were analyzed by an experienced nuclear medicine physician (*CMD*) using MIM; each LPT was delineated semi-automatically using the corresponding contrast-enhanced CBCT set. To separate different LPTs, an expert drew a few lines in different transverse slices based on the contrast-enhancement in the early or late arterial phase of the CBCT, then a surface was fitted to these lines. Besides, tumors bigger than 5 ml were delineated manually on each CBCT by delineating the contrast-enhancing part of the tumor. Contours were exported as RTstruct sets and imported to the in-house

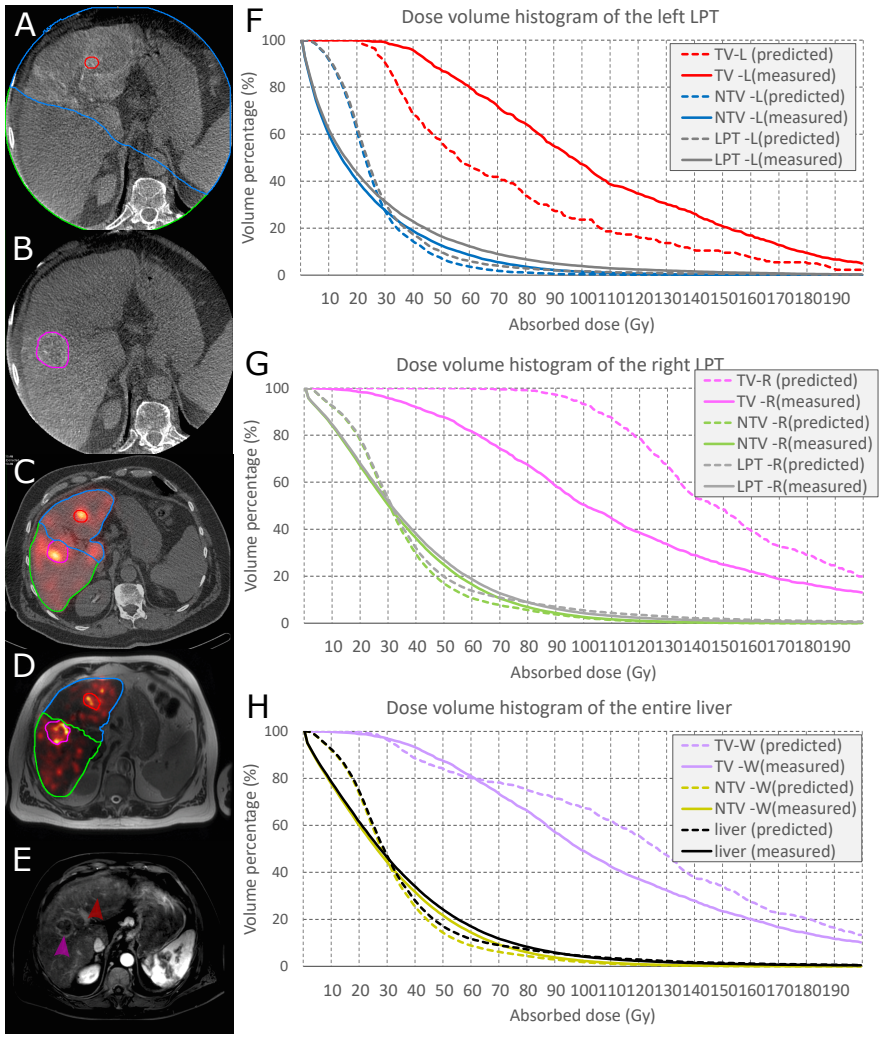

*Figure 4.1: Single transaxial slice of a pre- and post-treatment study and dosimetry results (patient ID 42): **[A and B]** late arterial phase CBCTs focusing on the left and right lobe, the contrast-enhancement is used to segment the right and left LPT (green and blue area) and to segment the tumors (red and pink contours). **[C and D]** a fusion-view of $[^{99m}Tc]$Tc-MAA-SPECT/CT and ^{90}Y-PET/MR images. The contours represent registered VOIs which are delineated on CBCTs masked by the total liver; **[E]** Baseline MR image, with red and pink arrow pointing to the tumors which have been delineated on CBCTs (figures **A** and **B**) **[F and G]** dose-volume histograms of the tumor, non-tumoral liver parenchyma, and total LPT for left and right LPT from predictive(left lobe: tumor, non-tumoral tissue, and total LPT mean dose of 73, 26 and 28 Gy; right lobe: tumor, non-tumoral tissue, and total LPT mean dose of 160, 35 and 39 Gy) and post-treatment (left lobe: tumor, non-tumoral tissue, and total LPT mean dose of 106, 22 and 27 Gy; right lobe: tumor, non-tumoral tissue, and total LPT mean dose of 119, 35 and 38 Gy) dosimetry. **[H]** dose-volume histogram of the tumor, non-tumoral liver parenchyma, and total liver when combining both LPTs from predictive dosimetry (tumor, non-tumoral tissue, and total LPT mean dose of 128, 32 and 36 Gy) and post-treatment dose measurement (tumor, non-tumoral tissue, and total liver mean dose of 115, 32 and 35 Gy).*

software written in IDL. All VOIs (LPTs and tumors) from CBCTs were transferred non-rigidly to the pre- and post-treatment images based on the information provided by the non-rigid registration mentioned above.

For each tumor, additional steps were designed to avoid **(1)** a volumetric discrepancy between the original CBCT tumor segmentation and registered tumors on [^{99m}Tc]Tc-MAA-SPECT and ^{90}Y-PET space, **(2)** small shifts between activity map and tumor due to inaccuracies of the non-rigid registration:

- **step 1, initial alignment:** using the displacement of the tumor mass centers provided by the non-rigid registration, the tumor volume was rigidly propagated on the SPECT and PET from pre- and post-treatment images.
- **step 2, location verification:** the nuclear medicine expert corrected the center of each registered segmented tumor by specifying a different point with a mouse click, if that was necessary.
- **step 3, location optimization:** an algorithm was designed to optimize the tumor location by maximizing the tumor uptake while minimizing the distance from the location obtained in "step 2". For that purpose, the rigid alignment of the tumor was optimized with Powell's algorithm. The cost function penalized large translations and prevented translation that would put the center of shifted VOI outside the boundary of the original VOI. After finding the optimum of the cost function, the final VOI was obtained by thresholding the fuzzy VOI produced by the optimization procedure.

$$cost = \begin{cases} -\frac{\sum_{i\in T_{\text{new}}} A_i - \sum_{i\in T_{\text{init}}} A_i}{\sum_{i\in T_{\text{init}}} A_i} + \beta \times \left(\frac{\|\mathrm{C}_{\text{new}} - \mathrm{C}_{\text{init}}\|}{5\times \mathrm{d}}\right)^3 & , \mathrm{C}_{\text{init}} \in T_{\text{new}} \\ +\infty & , \text{otherwise} \end{cases} \tag{4.1}$$

Here, T_{new} and T_{init} denote the new and initial tumor VOI, A denotes the activity map ([^{99m}Tc]Tc-MAA-SPECT or ^{90}Y-PET), C_{new} and C_{init} indicate the new center point location, and the one obtained in "step 2", and d denotes the diagonal of the voxel in mm (*i.e.* in [^{99m}Tc]Tc-MAA-SPECT or ^{90}Y-PET voxel size).

4.3.4 Absorbed dose calculation

To perform dosimetry, we assumed: **(1)** there was no biological clearance, **(2)** the activity was exclusively injected into the planned LPTs, and **(3)** the energy of the activity within each voxel was fully deposited in the same voxel (local energy deposition model). To recover the total administered activity for post-treatment dose assessment, the relative post-treatment ^{90}Y-PET uptake value was used by assuming that all the administered yttrium-90 activity has ended up in the liver (*i.e.* an LSF of 0% was used). Measuring the residual activity in treatment session is not implemented in our clinical routine. We assume that all the prepared activity is delivered to the patient, unless the interventional radiologist suspects a possible problem with the activity administration. We measured the residual activity in the vial for 10 previous administrations and these only showed a negligible amount.

In the pre-treatment assessment, to calculate the voxel-level fractional uptake, the SPECT image was normalized to the prescribed activity for each LPT to recover the LPT administered activity. This approach was taken because the portion of the administered [^{99m}Tc]Tc-MAA within each branch prior to the pre-treatment workup does not necessarily mimic the administered ^{90}Y-microspheres in the treatment session.

Afterward, a map of absorbed dose in Gy was determined using the local deposition model by employing a conversion factor of:

$$\mathrm{S}_{\mathrm{self-irradiation}}[\mathrm{Gy/Bq}] = \frac{T_{1/2}[sec]}{\ln 2} \times \frac{E_{\mathrm{ave}}[J]}{\rho[kg/m^3] \times \mathrm{vox}_{\mathrm{vol}}[m^3]} \tag{4.2}$$

where $T_{1/2}$ is the physical half-life of yttrium-90 (64.1×60^2 sec), E_{ave} is the average energy released per decay of yttrium-90 (1.498×10^{-13} J), ρ is the liver tissue density ($1.04 \times 10^3 kg/m^3$), and $\mathrm{vox}_{\mathrm{vol}}$ is the volume of the activity voxels in m^3 which results in a conversion factor of 0.4336×10^{-3} [Gy/Bq] for [^{99m}Tc]Tc-MAA-SPECT voxels, and 2.3061×10^{-3} and 1.7607×10^{-3} for ^{90}Y-PET voxels form post-treatment PET/CT and PET/MR studies, respectively [292].

4.3.5 Pre- and post-treatment dosimetry comparison

Dose-volume histograms (DVHs) for all VOIs were obtained, and also the mean dose to each VOI was computed. For each liver compartment, a series of clinically relevant dosimetry parameters were compared for predicted and post-treatment measured dose maps:

- **VOI mean dose**
- **Dn:** n'th percentile dose,*i.e.* n% of the volume received a dose of Dn or more (D50 and D70 for TV and D30 and D50 for NTV and total LPT compartments),
- **Vd:** volume percentage that receives at least d Gy (V40 and V50 for NTV and total liver/LPT and V70 and V100 for TV compartments)

4.3.6 Comparing predicted and measured doses for fixed-dose criteria

In clinical routine, the desired absorbed dose to the tumor is derived from a tumor control probability curve. Using this curve, a minimum threshold of 70 to 100 Gy is widely accepted as a dose with high tumor response probability [71, 73, 293]. So, if the [^{99m}Tc]Tc-MAA simulation underestimates the tumor dose, but yet the tumor dose is more than these dose thresholds, this underestimation could be less critical than the opposite situation where the pre-treatment simulation suggests a mean dose of more than tumor control threshold, while the post-treatment measured dose is less than the threshold. Using this idea, a scatter plot of predicted and measured tumor dose was partitioned into four areas using 70 Gy as a dose with intermediate tumor response probability. An absorbed dose of 100 Gy is also used to illustrate a high tumor control probability:

1. **The derived tumor mean dose for both predictive and post-treatment dose assessments was above 70 Gy:** predictive dosimetry suggested a good tumor coverage, which was verified after treatment.
2. **Both predicted and post-treatment measured tumor mean dose were below 70 Gy:** predictive tumor dosimetry correctly gave an under-treatment warning.
3. **Predicted tumor dose was less than 70 Gy, while the measured tumor mean dose reached the 70 Gy criterion:** the result of the treatment was better than suggested by the dose prediction.
4. **Predicted tumor dose was above 70 Gy while measured tumor mean dose did not reach 70 Gy:** [^{99m}Tc]Tc-MAA dosimetry falsely predicted a good tumor coverage which did not materialize after treatment.

The same approach was applied for non-tumoral tissue mean dose using normal tissue complication probability curves. A dose of 50 Gy is considered as a safety threshold. An absorbed dose of 40 Gy is the maximal recommended dose in case of cirrhotic non-tumoral liver tissue or patient heavily treated with chemotherapy [71, 73]:

1. **The derived NTV mean dose for both predictive dosimetry and dose measurement was below 50 Gy:** predictive dosimetry could predict the safety of the treatment for non-tumoral liver parenchyma.
2. **Both predicted and post-treatment measured NTV mean dose was above 50 Gy:** predictive NTV dosimetry correctly identified a dose range with a non-zero risk for liver complications.
3. **predicted NTV dose was above 50 Gy, while post-treatment measured mean dose to this VOI did not reach 50 Gy:** predictive dosimetry falsely suggested a potential risk for liver toxicity.
4. **Pre-treatment NTV dose was less than 50 Gy, while measured mean dose of NTV exceeded the 50 Gy limit:** pre-treatment dose prediction did underestimate the risk for liver toxicity.

4.3.7 Comparing predicted and measured doses to the planned dose

For patients whose activity planning was done by employing the partition method, the therapy team agreed on a delivered dose to the non-tumoral liver and tumor compartment, which are called "planned dose criteria" in this document. To calculate the injected activity, the total liver and liver perfusion territories have been drawn on baseline images and tumors have been delineated by thresholding the [^{99m}Tc]Tc-MAA uptake.

The planned dose to the NTV and TV was compared to the doses obtained from predictive dosimetry and post-treatment dose measurement using the relative difference between calculated dose and planned dose in percentage. For predictive dosimetry, deviation from zero indicates the effects of the different VOI definition method used in this study (perfusion based LPT and tumor segmentation on CBCTs) compared to activity planning VOI definition (using anatomical landmarks on CT or MR for LPT segmentation and thresholding [^{99m}Tc]Tc-MAA uptake for tumor definition). Considering post-treatment dose measurement, the difference between planned dose and determined mean dose could be caused by a difference in VOI definition or variation between [^{99m}Tc]Tc-MAA and therapeutic microspheres distribution. The differences are calculated in a way that negative values show doses below and above the planned dose for NTV and TV compartments, respectively.

4.3.8 Statistical analysis

R software version 3.6.1 (R Foundation for statistical computing, Vienna, Austria) was used for all statistical analysis. A Passing–Bablok regression scatter plot was used to compare dose parameters from predictive and post-treatment dose assessment by displaying the regression line and confidence intervals. This method is commonly used to compare two measurement methods by plotting them in x- and y-axis. Also, Pearson correlation was used to evaluate the agreements; r-values greater than 0.3, 0.5, and 0.7 were considered as a weak, moderate, and strong positive linear relationship. In Passing-Bablok graphs, the identity line is displayed using a dashed line, and the solid line and shaded area represent the regression line and 95% confidence interval.

A Bland-Altman plot was also used to calculate the agreement between predicted and post-treatment measured dose parameters. In the Bland-Altman plots, the middle dashed line represents the mean difference, and the purple area is the confidence interval; the green and pink area and their dashed lines also showed the difference $\pm$ standard deviation and their confidence intervals to give a visual impression of the precision of these parameters.

Dose parameters for predictive dose and post-treatment dose measurement were also compared using paired Wilcoxon rank-sum test. A p-value of less than 0.05 was set as a significance threshold.

4.4 Results

4.4.1 Patient and treatment characteristics

Of 49 consecutive patients identified, 31 patients were included, and 18 patients were excluded (see figure 4.2): in 4 patients, the post-treatment PET image was not acquired, only BECT images were available; in 5 patients, the quality of CBCT information was not suitable for tumor and/or LPT delineation; in 3 patients, CBCT images were not available; in 2 patients, the treatment team decided to change the therapy strategy and put the catheter in a different position for the therapeutical procedure compared to the [^{99m}Tc]Tc-MAA workup; in 3 patients, all tumors were smaller than 5 ml and were not considered for dose assessment as partial volume effects are too pronounced. Finally, in the last excluded patient, some voxels within the liver received blood from both administrations within different catheter tip positions in pre-treatment workup. So, it was not possible to extract fractional uptake for each administration from the [^{99m}Tc]Tc-MAA-SPECT image.

Of those 31 patients included, 67 tumors (with a volume bigger than 5 ml) in 47 LPTs (from a total of 65 defined LPTs) were included in this retrospective study. The baseline characteristics for the patients and treatment sessions (LPTs) are described in table 4.2.

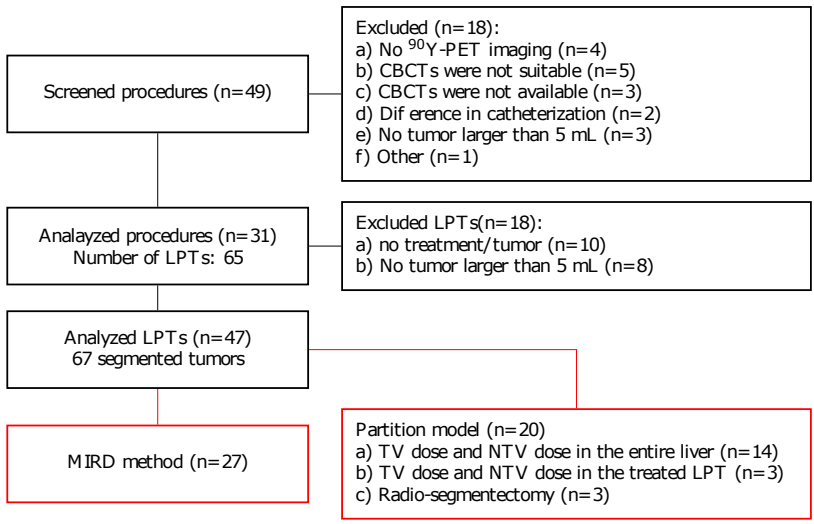

Figure 4.2: Flowchart of patient selection (consort diagram in black blocks), and activity planning in the selected LPTs (red blocks)

Table 4.2: Patient characteristics

patient characteristics	
sex (female/male)	12/19
age in years, median [range]	67 [25-83]
height in meter, median [range]	1.70 [1.52-1.83]
weight in kg, median [range]	74 [48-116]
tumor type, n (%)	
HCC	19 (61.3%)
No cirrhosis	5
Proven cirrhosis	14
NASH	7
ASH	4

HBV	1
HCV	1
Unknown etiology	4
CRC	6 (19.4%)
NET	3 (9.7%)
pancreas	1 (3.2%)
breast	1 (3.2%)
stomach	1 (3.2%)
portal vein embolism, n	
patients with PVE	2
prior treatment, n (median months between last cycle and SIRT [min,max])	
Systemic treatment	13 (1.0 [0.3, 15.2])
anti-angiogenic⋆	6 (9.7 [0.5, 16.6])
anti-angiogenic (directly before SIRT)	3 (0.9 [0.5, 15.2])
anti-angiogenic (not directly before SIRT)	3 (14.1 [5.3, 16.6])
non anti-angiogenic⋆⋆	7 (0.7 [0.3, 13.4])
RFA/MWA	6 (13.8 [3.5, 31.0])
TACE	4 (8.3 [4.1, 48.3])
resection	3 (14.4 [1.3, 41.9])
volumes from prescription sheet (ml), median [range]	
total liver	1741 [789-4122]
non-tumoral liver	1538 [682-2942]
tumor	134 [0-2785]
tumor burden	
median [range], %	8.8 [0.0-67.6]
<5% ,n (%)	10 (32%)
5-10% ,n (%)	8 (26%)
10-25% ,n (%)	8 (26%)
25-50% ,n (%)	3 (10%)
>50% ,n (%)	2 (6%)
MAA workup information	
lung shunt fraction (%)	8.0 [0.0-13.9]
time from treatment in days, median [range]	18 [9-46]
prescription method	
MIRD method, n (%)	16 (52%)
compartmental Partition model, n (%)	14 (45%)
mixture of methods, n (%)	1 (3%)
treatment strategy	
whole liver, n (%)	2 (6%)
bi-lobar, n (%)	15 (48%)
mono-lobar, n (%)	10 (32%)
selective (3 segments), n (%)	3 (10%)
selective (4 segments), n (%)	1 (3%)
prescribed activity	
total administered activity (GBq) [range]	1.527 [0.383-3.700]
number of analyzed tumors (bigger than 5 ml)+	
patients with 1 tumor ,n (%)	16 (52%)
patients with 2-3 tumors ,n (%)	11 (35%)
patients with more than 3 tumors ,n (%)	4 (13%)
analyzed LPTs information from prescription sheet+	
total LPT (cc), median [range]	1001 [57-3172]
non-tumoral liver (cc), median [range]	849 [0-2268]
tumor (cc), median [range]	67 [0, 2785]
LPT to total liver ratio (%), median [range]	54 [3-100]
tumor burden	
median [range], %	9.4 [0.0-100.0]
<5% ,n (%)	16 (34%)

5-10% ,n (%)	9 (19%)
10-25% ,n (%)	11 (23%)
25-50% ,n (%)	8 (17%)
>50% ,n (%)	3 (6%)
post-treatment image modality	
PET/MR - PET/CT, n(%)	28 (90%) - 3 (10%)

⋆ Aflibercept, Regorafenib, Bevacuzimab, or Sorafenib

⋆⋆ Octreotide LAR, FOLFOX, FOLFIRI, Cetuximab, De Gramont, TAS102, Avelumab, Paclitaxel epirubicin + cisplatin + fluorouracil, Exemestane, Gemcitabine + abraxane, Everolimus, Letrozole, Trastuzumab, Pertuzumab, Panitumumab, Lanreotide

4.4.2 Activity planning

As detailed in figure 4.2, of those 47 LPTs, the non-compartmental partition model (MIRD method) was used for 15, 11, and one LPT(s) aiming at 40, 50, and 60 Gy, respectively. For the rest, a compartmental partition model was used with a personalized tumor dose criterion and/or a tissue sparing criterion. In this method a personalized tumor dose criterion (95 Gy, n=1 ; 120 Gy, n=4; 125 Gy, n=1; 135 Gy, n=1; 150 Gy, n=5; 160 Gy, n=1; 240 Gy, n=2; 250 Gy, n=2; 300 Gy, n=3) was used. This method also aimed at sparing liver tissue parenchyma from a certain absorbed dose (non-tumoral liver parenchyma of the entire liver dose of 15 Gy, n=2; 20 Gy, n=1; 25 Gy, n=7, and 30 Gy, n=4, or non-tumoral liver parenchyma of the LPT dose of 20 Gy, 30 Gy, and 40 Gy each for one LPT, and radio-segmentectomy for 3 LPTs).

More details are provided in table 4.2.

4.4.3 VOI segmentation

Considering the 31 patients, there was a high correlation between total liver volumes (Pearson r=0.990) determined on post- and pre-treatment studies; the ratio of the volumes had a median of 1.01 with a first and third interquartile range of 0.99 and 1.04. These volume differences represented either the volume change during the registration or a real biological change.

For 47 analyzed LPTs, the ratio between the volumes defined on post- and pre-treatment images had a median of 1.03 with a first and third interquartile range of 0.98 and 1.07. Again, rather than possible volume change associated with the non-rigid registration, this difference could be explained by a possible biological change.

The LPT to whole-liver volume ratio is a commonly used parameter in SIRT dosimetry. In some prescription methods (*e.g.* BSA and MIRD method), this parameter is used to divide the total prescribed vial to be administrated in different branches of the hepatic artery. When comparing this parameter for LPTs defined on CBCTs with the numbers reported on the prescription sheet, the ratio had a median of 0.99 with a wide interquartile range (first and third interquartile range: 0.90 and 1.09 respectively) which can directly affect the dosimetric analysis.

Two more examples are provided in the supplementary material: (1) figure 4.11 an example of lobar treatment (with bilobar workup) which shows that CBCT-based LPT segmentation nicely followed the activity distribution of the yttrium-90, and (2) figure 4.12, an LPT segmentation example on CBCTs, which could be considered superior to a classical liver lobe/segment delineation because of a specific catheterization.

4.4.4 Predicted and measured doses

Absorbed dose distribution parameters of each LPT derived from pre-treatment [^{99m}Tc]Tc-MAA-SPECT and post-treatment ^{90}Y-PET images were compared for total liver NTV, total LPT, and tumors. Table 4.3 and figure 4.3 summarize the main dosimetric comparison between predictive and post-treatment dosimetry without considering the outliers. The following sections provide more details about this comparison.

Two examples of TV, NTV, and total LPT dosimetry are shown in figures 4.10 and 4.1 (supplementary material).

		predicted		post-treatment		Wilcoxon	Pearson correlation	
VOI	parameter	mean	std	mean	std	p-value	r	p-value
total NTV	mean dose	30.4	11.9	29.5	11.4	0.272	0.937	**<0.001**
	D30	31.4	15.8	32.3	17.0	0.344	0.826	**<0.001**
	D50	18.6	11.2	17.7	12.3	0.355	0.803	**<0.001**
	V40	24.5	11.1	25.1	12.3	0.666	0.805	**<0.001**
	V50	17.6	7.9	18.7	9.8	0.249	0.826	**<0.001**
total LPT	mean dose	63.5	85.6	53.0	52.4	0.135	0.820	**<0.001**
	D30	68.4	95.2	56.8	61.0	0.440	0.755	**<0.001**
	D50	41.8	60.6	31.6	31.7	0.076	0.756	**<0.001**
	V30	48.6	19.9	45.8	17.4	0.286	0.732	**<0.001**
	V50	31.0	19.6	29.6	16.2	0.641	0.772	**<0.001**
tumors	mean dose	152.3	144.7	143.0	137.8	0.918	0.623	**<0.001**
	D50	139.2	129.8	127.8	134.7	0.576	0.597	**<0.001**
	D70	102.8	95.3	87.9	98.6	0.080	0.604	**<0.001**
	V70	64.9	35.4	60.4	30.1	0.275	0.229	0.063
	V100	52.5	36.1	47.4	30.3	0.354	0.381	**0.001**

Table 4.3: Statistical properties of different dosimetric parameters in different VOIs

4.4.4.1 Total liver non-tumor volume

A summary of the tumor dose comparison between [^{99m}Tc]Tc-MAA and yttrium-90 distribution has been shown in table 4.3 and figure 4.3. The Wilcoxon test didn't show any significant difference in any of the dosimetry parameters from the total liver NTV compartment. The mean dose to the total non-tumoral tissue was 30 ± 12 and 30 ± 11 Gy in predictive dosimetry and post-treatment dose measurement; the ratio of measured and predicted mean doses have a median of 1.05 (first and third interquartile range of 0.83 and 1.25). Both predicted and measured dosimetry showed that on average, only around 25% of the non-tumoral tissue parenchyma received more than 40 Gy; the ratio of measured and predicted V40 had a median of 1.00 (first and third interquartile range of 0.86 and 1.29). These volumes were 18% and 19% for predictive dosimetry and post-treatment dose measurement for 50 Gy threshold level; the ratio of measured and predicted V50 had a median of 1.02 (first and third interquartile range of 0.84 and 1.35). The D30 values showed that only 30% of the liver received more than 31 and 32 Gy using predicted and measured doses; the ratio of measured and predicted D30 had a median of 0.95 (first and third interquartile range of 0.66 and 1.36).

A Passing-interquartile regression, which has been shown in figure 4.4, estimated a strong correlation of the mean dose to the non-tumoral liver between predicted and measured doses (r=0.937). Other reported dose parameters for NTV (D30, D50, V40, and V50) also showed a moderate correlation between MAA and ^{90}Y-PET based dosimetry (r bigger than 0.750 for all).

Bland-Altman analysis of NTV gave a mean difference of -0.9 Gy (-9.1, 7.2) for mean dose, 0.9 Gy (-18.2, 19.9) for D30, and -0.6% (-13.9, 15.1) for V40. The difference between predicted and measured mean dose to the total NTV doses did not exceed 11 Gy.

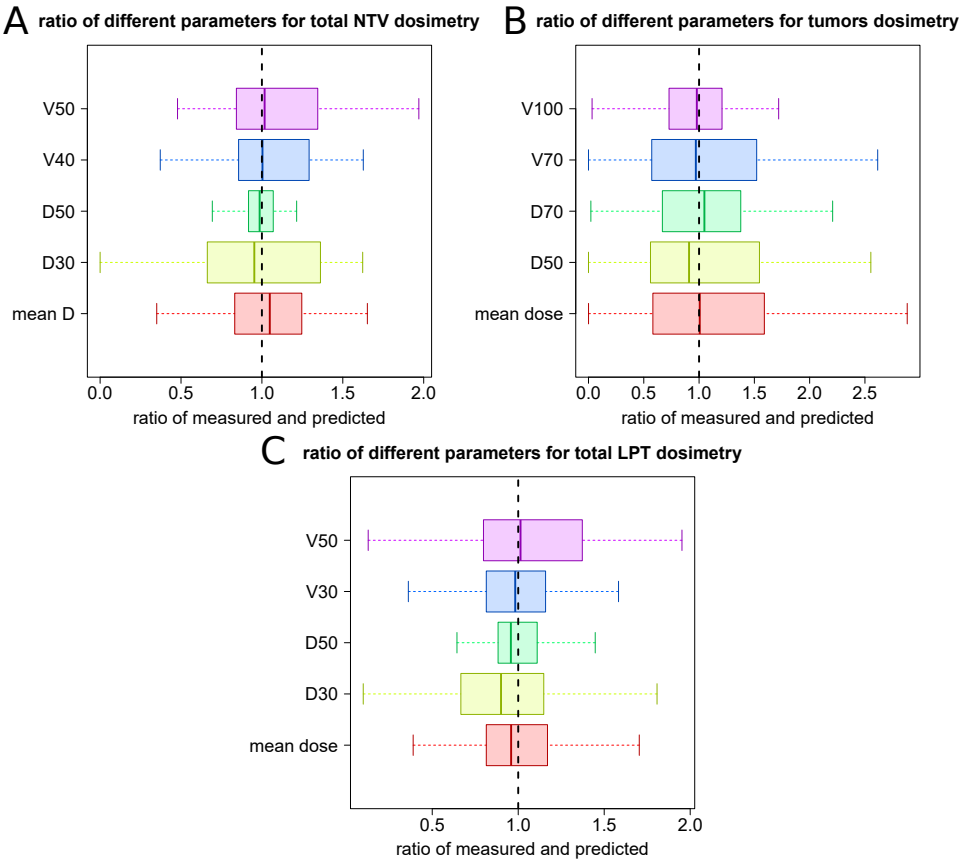

*Figure 4.3: Box-plot of the ratio of different dosimetry parameters derived from **[A]** NTV in the entire liver, **[B]** total LPT (TV and NTV together), **[C]** tumors (the outliers were excluded for visual purposes).*

4.4.4.2 LPT volumes

Table 4.3 and figure 4.3 provide some information about the dose to the total LPT comparison between [^{99m}Tc]Tc-MAA and yttrium-90 distribution. The mean dose of the total LPT estimated on [^{99m}Tc]Tc-MAA and post-treatment dose measurement were 63.5 and 53.0 Gy. The V30 for pre-treatment dose prediction and post-treatment dose calculations were 49 ± 20 and 46 ± 17 %. For other dosimetric parameters, no significant difference was observed.

Bland-Altman analysis of LPT (see figure 4.5) gave a mean difference of -10.5 Gy (-112.7, 91.6) for mean dose, -11.7 Gy (-135.7, 112.4) for D30, and -1.3% (-25.9, 23.2) for V50. The difference between predicted and measured mean dose to the LPT doses did not exceed 25 Gy except for two outliers (*i.e.* radio-segmentectomy strategy).

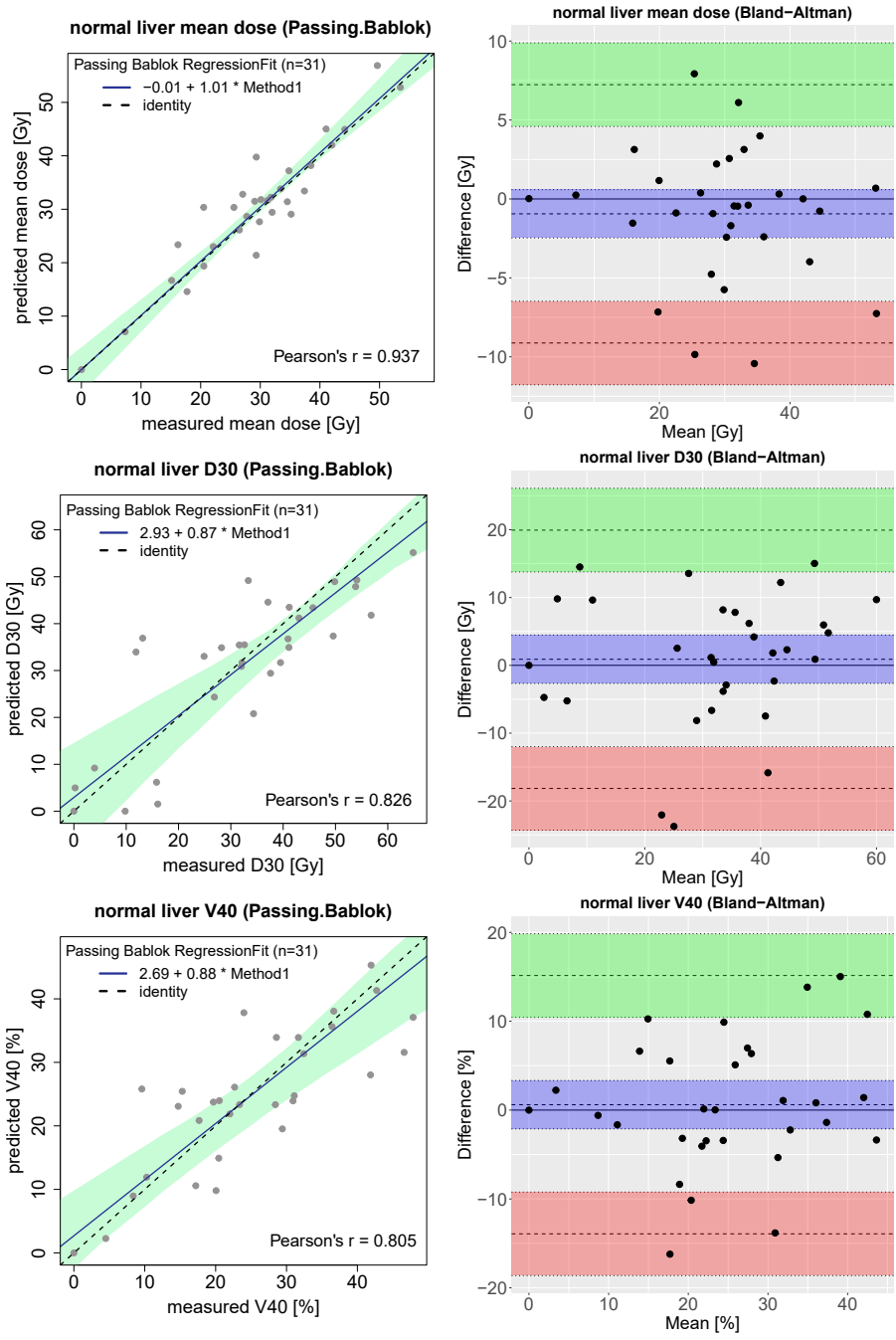

Figure 4.4: Passing–Bablok (left figures) and Bland-Altman (right figures) plots for different dosimetry parameters derived from NTV in the entire liver; mean dose to the non-tumoral liver in the first row, non-tumoral liver D30 in the middle row, and non-tumoral liver V40 in the last row.

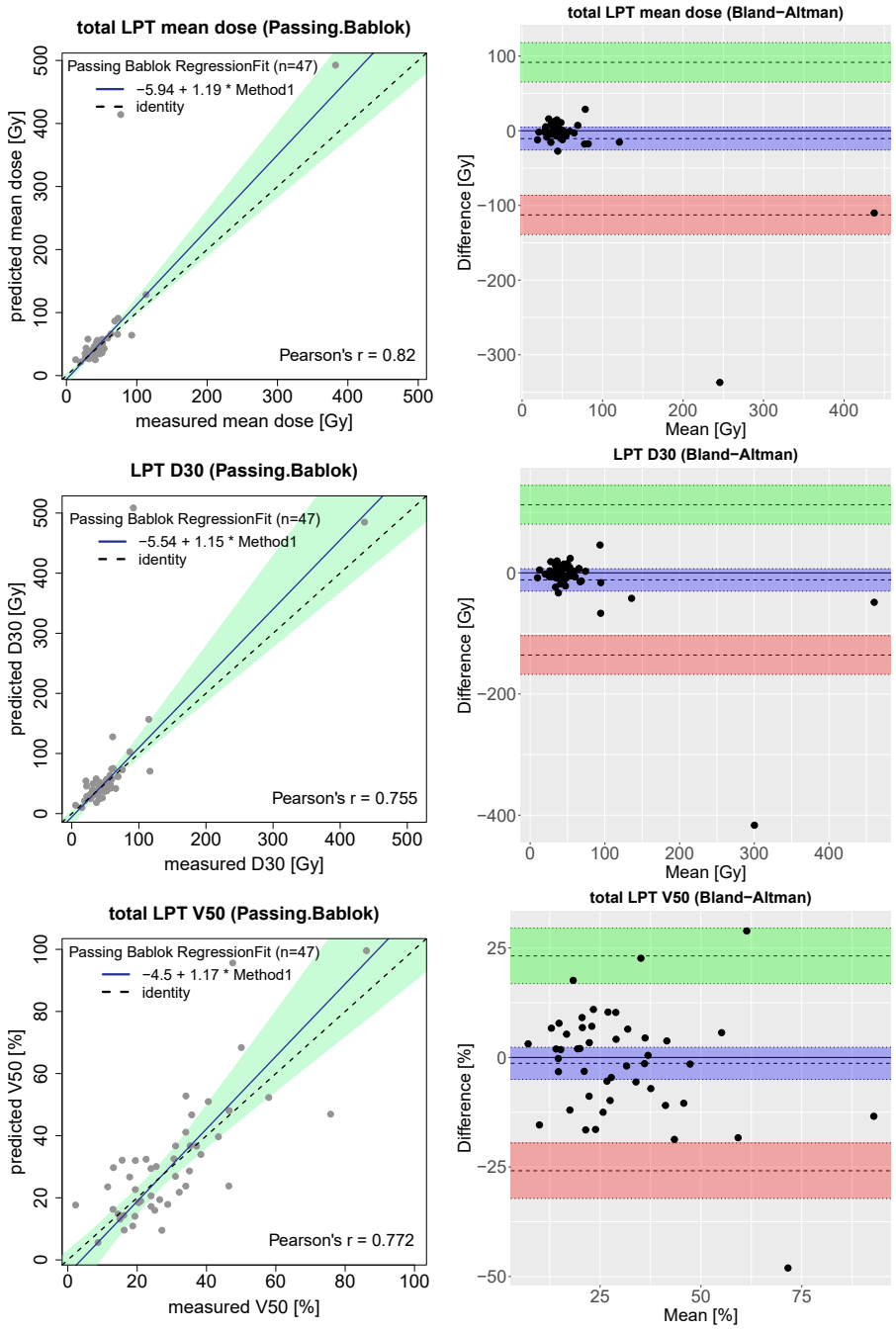

Figure 4.5: Passing–Bablok (left figures) and Bland-Altman (right figures) plots for different dosimetry parameters derived from total LPT (TV and NTV together); mean dose to the total LPTs in the first row, total LPT D30 in the middle row, and total LPT V50 in the last row.

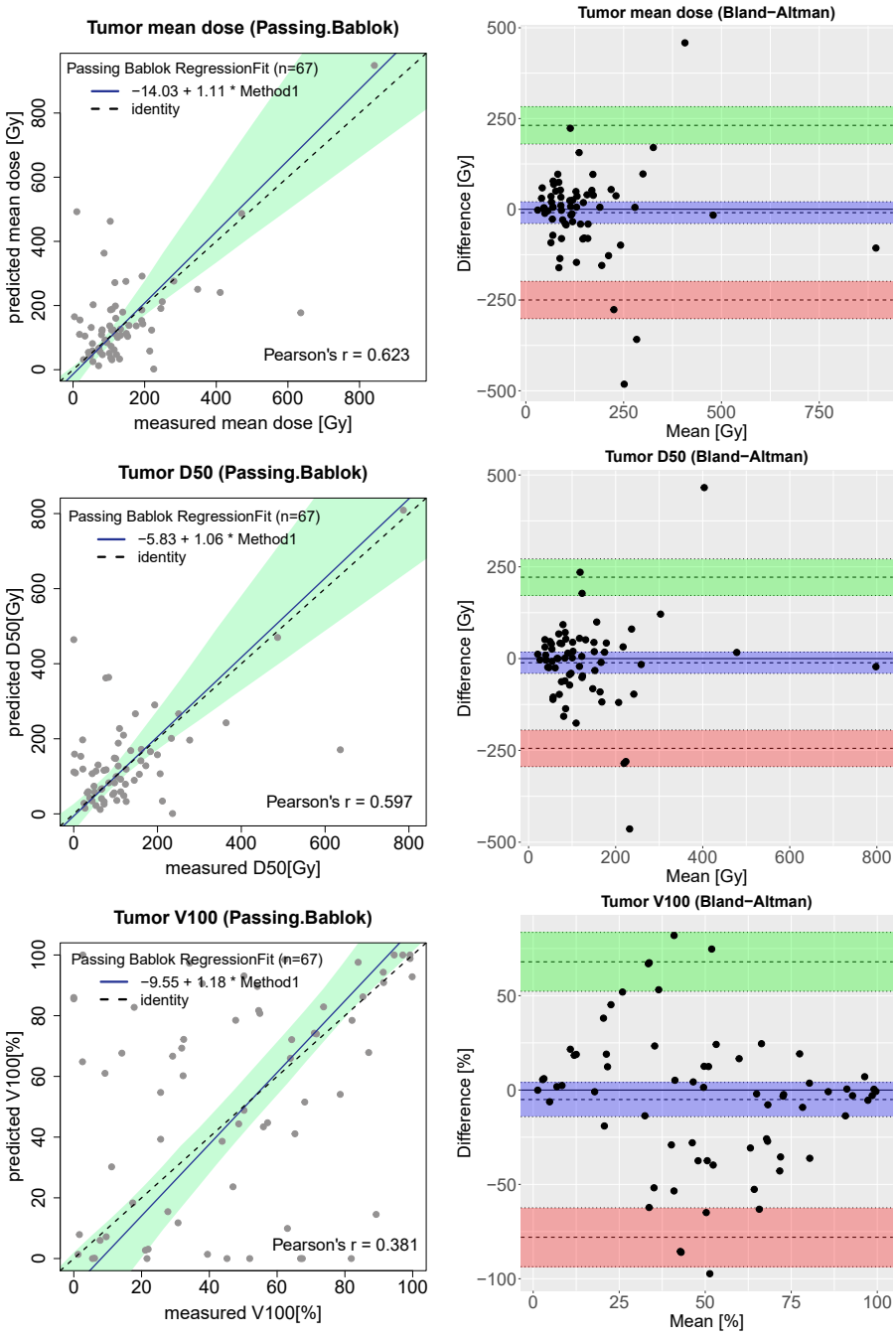

Figure 4.6: Passing–Bablok (left figures) and Bland-Altman (right figures) plots for different dosimetry parameters derived from tumors; mean dose to the tumors in the first row, total tumors D50 in the middle row, and tumors V100 in the last row.

4.4.4.3 Tumor volumes

In table 4.3, a summary of the tumor dose comparison based on the [^{99m}Tc]Tc-MAA-SPECT and ^{90}Y-PET distributions is shown. Predicted and measured dosimetry showed an average of 152 and 143 Gy mean dose to the tumor. As illustrated in figure 4.3, the median of the ratio between measured and predicted tumor mean dose was 1.01, but a larger deviation was reported for predictive and measured dose to the tumors compared to the LPT and NTV. The first and third interquartile range of the ratio of the mean doses were 0.58 and 1.59, which reflected a considerable discrepancy between measured and predicted dose to the tumor volumes.

On average, half of the tumors' volume received an absorbed dose of 139 and 128 Gy or more based on predictive dosimetry and post-treatment dose measurement; the ratio of measured and pre-treatment predicted D50 has a median of 0.91 (first and third interquartile range of 0.56 and 1.55). Based on analyzing V70, around 65% and 60% of the tumor volumes received more than 70 Gy on predictive and measured dosimetry; these volume portions are reported around 53% and 47% for 100 Gy dose threshold level for predictive and post-treatment dose assessments. 70% of tumor volumes received at least 103±95 Gy using predictive dosimetry while post-treatment dose calculation showed that 70% of the tumor volumes received at least 88 ± 99 Gy; the median, first and third interquartile range of the ratio between D70 in post-treatment dose measurement and predictive dosimetry were 1.05, 0.67 and 1.38 respectively.

A Passing-Bablok and Bland-Altman analysis of mean dose to the tumor and D50 and V100 is shown in figure 4.6 that shows remarkable higher variations and relatively limited agreement between predicted and measured dose compared to NTV and LPT. Moderate correlations existed between the mean dose of pre-treatment simulation and post-treatment dose measurement (r=0.623). On the other hand, our data does not show a significant correlation between other tumor parameters derived from DVH. Bland-Altman analysis of tumors gave a mean difference of -9.3 Gy (-249.9, 231.3) for the mean dose.

4.4.5 Comparing predicted and measured doses for fixed dose criteria

In the previous section, pre-treatment dose simulation and post-treatment dose measurement in different VOIs have been compared using mean dose and different DVH parameters.

Figure 4.7 represents a scatter plot that shows predicted versus measured mean dose with four colored areas: the green area is the area in which both predicted and measured doses are either less than 50 Gy or more than 50 Gy (n= 29 and 1 from 31 patients); the blue area represents the patients whose pre-treatment simulation estimates the NTV mean dose of more than 50 Gy, while ^{90}Y-microsphere distribution showed a dose of less than 50 Gy after treatment (n=1); the red area is the risky area where [^{99m}Tc]Tc-MAA simulates a safe treatment, whereas the actual dose to a NTV was more than 50 Gy (n=0). More details are provided in table 4.4.

The same plot is provided in figure 4.7 for TV compartments. For 39 out of all 67 tumors, both predictive and post-treatment dose assessment suggests a tumor mean dose of more than 70 Gy (upper green area); for seven tumors, measured tumor dose was less than 70 Gy, and [^{99m}Tc]Tc-MAA simulation indicated this as well (lower green area); the blue area is the area where predictive dosimetry failed to estimate a dose of more than 70 Gy, while the actual treatment reached that dose limit (n=13); for eight tumors, pre-treatment simulation suggested a sufficient dose (more than 70 Gy) and post-treatment dose measurement revealed that the microsphere treatment did not meet this limit; the prediction was too optimistic here. Figure 4.8 shows an example of this mismatch between predictive dosimetry and post-treatment dose measurement. Table 4.5 provides more details.

		measured TV dose			
		low dose [0, 70] Gy	intermediate dose [70, 100] Gy	high dose [100, +∞] Gy	total
predicted TV dose	high [100, +∞] Gy	7	4	32	43
	intermediate dose [70, 100] Gy	1	2	1	4
	low dose [0, 70] Gy	7	5	8	20
	total	15	11	41	67

Table 4.4: Comparing predicted and measured TV doses and fixed dose criteria; joint- histogram of tumor absorbed dose using bins of 0, 70, 100 Gy that corresponds to no tumor irradiation, intermediate and high tumor control probability, respectively

		measured NTV dose			
		low dose [0, 40] Gy	intermediate dose [40, 50] Gy	high dose [50, +∞] Gy	total
predicted NTV dose	high [50, +∞] Gy	0	1	1	2
	intermediate dose [40, 50] Gy	0	3	0	3
	low dose [0, 40] Gy	26	0	0	26
	total	26	4	1	31

Table 4.5: Comparing predicted and measured NTV doses and fixed dose criteria; joint- histogram of total NTV absorbed dose using bins of 0, 40, and 50 Gy that corresponds to no non-tumoral irradiation, lowest dose recommended to the non-tumoral compartment and safety threshold, respectively

4.4.6 Comparing predicted and measured doses to the planned dose

For 13 patients, the injected activity was prescribed by applying a compartmental partition model by thresholding [^{99m}Tc]Tc-MAA uptake to distinguish between TV and NTV. Figure 4.9 provides the relative difference between calculated absorbed dose derived from predictive and post-treatment analysis of NTV and the planned absorbed dose. So, negative values correspond to a lower dose to the NTV than what has been prescribed, which has happened in 6 patients for both predictive dosimetry and post-treatment dose measurement. The median (first, third interquartile) for this relative difference was 6% (-42, 21%) and 0% Gy (-41, 16%) for predictive dosimetry and post-treatment dose measurement.

For these 13 patients for whom the partition method was used for prescription, measured and predicted absorbed doses of 30 tumors were compared with TV planned dose. Figure 4.9 represents the relative difference between the planned dose to the TV and the calculated dose. The negative values correspond to the cases where the calculated tumor dose is greater than what has been prescribed, which has been reported for 16 and 10 tumors for predictive dosimetry and post-treatment dose measurement, respectively. The median (first, third interquartile) of relative difference for pre-treatment predictive and post-treatment analysis was -3% (-38, 25%) and 22%(-30, 62%) respectively.

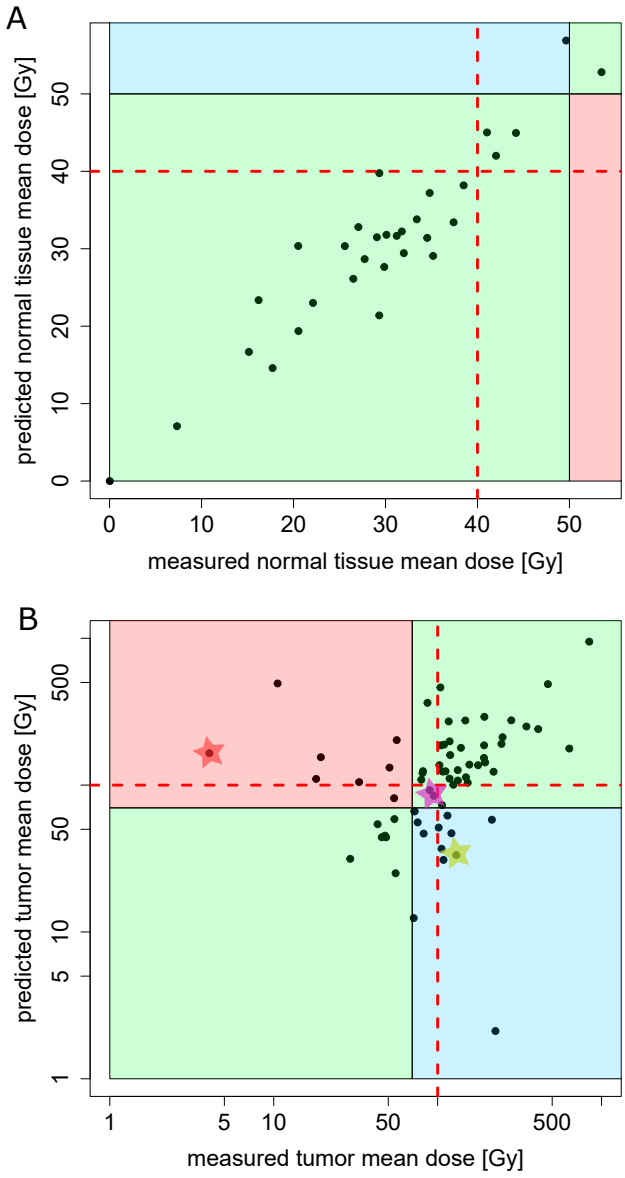

*Figure 4.7: Scatter plot with clinically relevant dose intervals in [**A**] NTV and [**B**] TV VOIs; lower green area: where tumor/non-tumoral liver dose from both predictive and post-treatment dosimetry is less than critical dose; upper green area: where tumor/non-tumoral liver dose from both predictive and post-treatment dose assessment is more than critical dose; blue area: where tumor/non-tumoral liver dose is bigger than critical dose from measured/predictive treatment dosimetry but less than defined dose from predicted/measured doses; red area: where tumor/non-tumoral liver dose is bigger than critical dose from predicted/measured doses but less than defined dose from measured/predicted doses; three red, pink and yellow star correspond to the tumors which have been described in the figure 4.8 (patient ID 20). The red dashed lines correspond to the lowest dose recommended for non-tumor tissue and the high tumor control probability for figures **A** and **B**, respectively.*

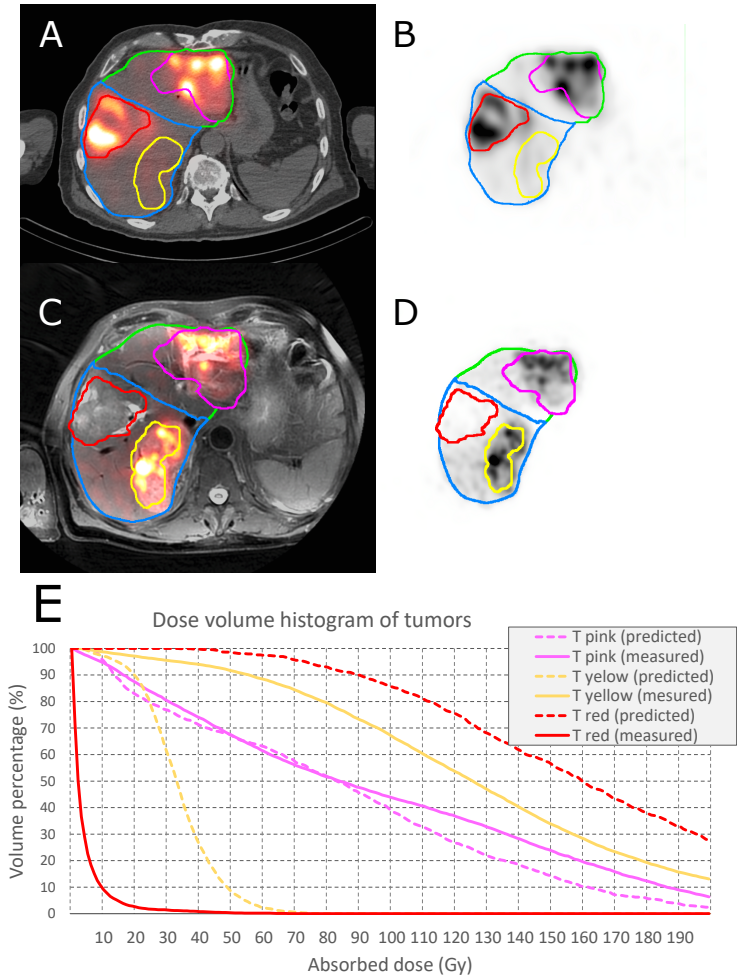

Figure 4.8: An example (patient ID 20) of disagreement between tumor dose between predictive and post-treatment dosimetry. ***[A and B]*** *show pre-treatment image ([^{99m}Tc]Tc-MAA-SPECT/CT) and* ***[C and D]*** *shows post-treatment image (^{90}Y-PET/MR); the tumor contoured in pink: predictive and post-treatment dose assessment were comparable (pre-treatment predicted: mean dose: 84 Gy, D50=83 Gy and V100=39%; post-treatment: mean dose: 95 Gy, D50=84 Gy and V100=44%); the tumor contoured in yellow: predictive dosimetry underestimated the tumor dose (pre-treatment predicted: mean dose: 33 Gy, D50= 33 Gy and V100=0%; post-treatment measurement: mean dose: 130 Gy, D50=125 Gy and V100=67%); and the tumor contoured in red: predictive dosimetry over-estimated the tumor dose (pre-treatment predicted: mean dose: 165 Gy, D50= 159 Gy and V100=86%; post-treatment: mean dose: 4 Gy, D50=2 Gy and V100=0%).* ***[E]*** *dose-volume histogram of the described VOIs based on predictive and post-treatment dose assessments.*
In this case a different catheter positioning between [^{99m}Tc]Tc-MAA workup and treatment resulted in flow variation. A preferential targeting of the tumor in the ventral part of the right liver lobe (red tumor) was observed in the workup. On the other hand, after ^{90}Y-microsphere injection, a preferential targeting of the tumor in the dorsal part of the left liver lobe was obtained. This is one example of a potential pitfall in SIRT in general and a cause of discrepancy between [^{99m}Tc]Tc-MAA-SPECT and ^{90}Y-PET in particular.

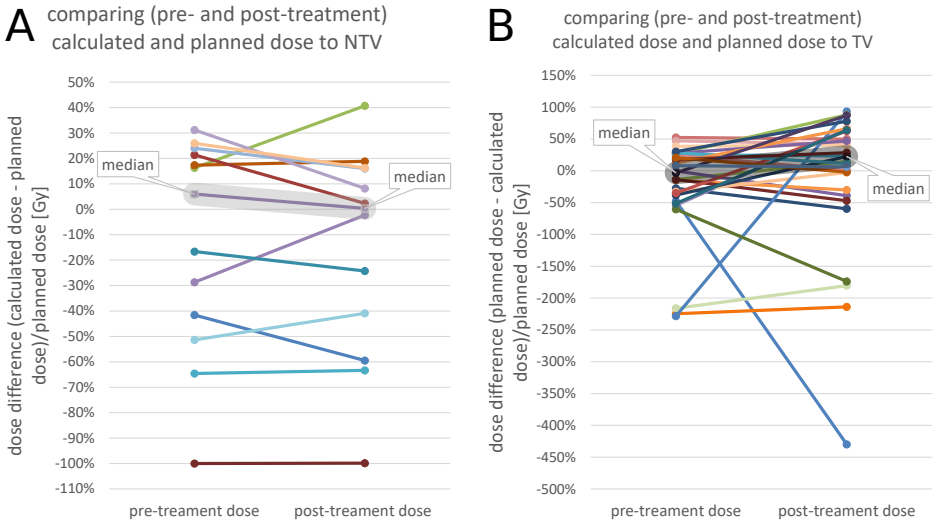

*Figure 4.9: A comparison between calculated doses, and prescribed doses to the **[A]** NTV and **[B]** TV; the difference between obtained dose and prescribed dose is provided in a way that for tumor graph negative values correspond to doses above prescribed dose and for non-tumor tissue graph it is in the opposite way.*

4.5 Discussion

This study presents a framework to compare predicted and measured absorbed doses for SIRT using CBCT-based VOI segmentation. To our knowledge, implementation of the contrast-enhanced CBCT in voxel-level dose comparison has previously not been studied. In other studies, either anatomical landmarks on non-catheter based anatomical imaging modalities (*e.g.* MR or CT) or activity uptake-based imaging modalities (PET or SPECT) were used to define LPTs corresponding to different catheter positions. We demonstrated that activity planning using [^{99m}Tc]Tc-MAA absorbed dose distribution is related to post-treatment microsphere dose distribution in the tumor, non-tumoral, and LPT compartments. The quantitative analysis showed that the correlation between [^{99m}Tc]Tc-MAA absorbed dose distribution is higher in the non-tumoral compartment than in the tumors. The non-tumor mean dose could be used in treatment planning to predict if the normal liver parenchyma receives a safe absorbed dose (*e.g.* less than 50 Gy). In our analysis, we report a correlation between predicted and measured tumor absorbed dose employing a tumor-by-tumor approach instead of the patient averaged tumor dose. Analyzing the averaged predictive and measured tumor dose may lead to artefactual good correlation between pre- and post-therapy imaging. For example, figures 4.1-F and G show large deviations between predictive and measured dose for the left and right sided tumors (under- and overestimation respectively) which balance each other and result in a good correlation when the tumor absorbed doses in the entire liver are averaged (figure 4.1-H). Our results show that for most of the tumors, [^{99m}Tc]Tc-MAA-based dosimetry could correctly predict if the dose to the tumor was sufficient or insufficient (*e.g.* more than 70 Gy).

Predicted absorbed dose estimation is becoming more and more crucial for individual SIRT planning [73]. Bastiaannet *et al.* reviewed the strategies to optimize activity prescription to the current state of radiobiological knowledge regarding SIRT and the current possibilities of performing predictive dosimetry and post-therapy dose measurement [73]. The BSA method is still the most used method for activity prescription. Nevertheless, activity planning using BSA method is driven by patient's body surface area used as a

surrogate of real patient's liver volume [167], which can lead to an overestimation (previous surgery) or underestimation (hepatomegaly caused by the presence of tumor) of the real liver volume [85]. Partition method or voxel-level dosimetry is the potential alternative for prescribing the activity, but applying an accurate partition method is challenging because it relies on VOI segmentation techniques and predictive value of the [^{99m}Tc]Tc-MAA particles.

A disagreement between predicted and measured absorbed dose parameters can occur due to several factors [73,294]; it could reflect the actual discrepancy between [^{99m}Tc]Tc-MAA particles and ^{90}Y-microspheres, as well as the inaccuracy in imaging and/or dose calculation and reporting techniques. Besides the difference in physical characteristics of two used radionuclides for dose prediction and measurement, a different catheter positioning and administration speed, vasospasm during one of the injection session, the embolic effect of the resin microspheres, and change in tumor vascularization between pre-treatment simulation and treatment session can lead to a weak predictive power of [^{99m}Tc]Tc-MAA particles. During the SIRT procedure, attempts were made to use the exact positioning of the catheter during the [^{99m}Tc]Tc-MAA injection and report any mismatching between the catheter tip position. In this study, clinical reports have been reviewed carefully for all screened procedures, and in case of a reported difference in catheterization, the case was excluded from the study.

Calibrated activity in the vial is reported with an error of 20% [186], which can have a direct effect on dosimetry accuracy. Generally, ^{90}Y-TOF-PET imaging is considered to be quantitative with a limited margin of error. To avoid any systematic bias between the total activity (and absorbed dose) in the liver, the activity distribution of the post-treatment ^{90}Y-PET image is rescaled based on the assumption that the total PET activity in the liver should equal the total prepared activity, considering no residual activity in vial nor catheters. On the other hand, the fractional uptake obtained from [^{99m}Tc]Tc-MAA-SPECT is rescaled assuming that the total predicted activity in each LPT should equal the administered activity within the corresponding catheter tip position.

In both predictive and measured dose calculation, the LSF estimation based on planar imaging was not used at face value in the dose calculation as it overestimates the true lung shunt measurement [295]. In our center, the patients with a real lung shunt (planar LSF $>$ 30%; macroscopic vascular connections visible on angiography) are excluded from SIRT. In analyzed patients, the highest LSF was 13.9%. In these circumstances, we believe that the true lung shunting was close to 0%, with a marginal signal coming from the lungs due to the smallest particles in the [^{99m}Tc]Tc-MAA solution, in vivo degradation products moving from the liver to the lungs, and scatter from the liver. This is substantiated by absence of uptake in the lungs according to ^{90}Y-PET in all our patients.

Lastly, any technical aspects of the VOI definition may alter the correspondence between predicted and measured dose parameters. To minimize this inaccuracy, additional control steps have been designed in this study: (a) liver segmentation by CNN in [^{99m}Tc]Tc-MAA-SPECT space and registered liver VOI in ^{90}Y-PET space have been verified and modified by an expert. The ratio between liver volumes has a first, second, and third interquartile range of 0.99, 1.01, and 1.04, respectively. (b) For segmenting the liver perfusion territory corresponding to each catheter tip position, contrast-enhanced CBCT imaging is used. In our previous study, it has been shown that by aiming at delivering 40 Gy to the total liver and prescribing activity based on CT-based liver perfusion territories, absorbed dose to the right and left CBCT-based LPT has a median (range) of 40.8 Gy ([34.1,48.8] Gy) and 38.1 Gy ([19.3, 49.1] Gy) [49]. (c) To optimize the delineation of the tumors, a multi-step hybrid approach (which combines anatomical and physiological information) has been used. Segmented tumors on CBCT images have been projected on activity maps using non-rigid registration. An additional verification step has been designed to avoid wrongfully-assigning the tumor to a nearby non-tumoral high or low uptake area or mislabeling two tumors next to each other. By assuming a high local uptake of the tumor, a cost function was designed to shift the tumor VOI very locally to capture as much activity as possible.

We found a strong correlation between non-tumoral liver mean dose, D30, and V40.

Our results for mean tumor dose confirm the moderate correlation between predicted and measured tumor dose reported by Gnesin *et al.* [243]. They also found a better agreement between NTV compartment than tumors. This possibly reflects the fact that a better overall relation could be achieved in larger volumes (NTVs) than smaller volumes (TVs). Recently, Jadoul *et al.* also reported similar results for HCC tumors [296]. In this study, for LPT segmentation, thresholding the activity uptake by 1% of the maximum activity was used.

Considering the reliability of [^{99m}Tc]Tc-MAA absorbed dose estimation, Chiesa and Maccauro discussed the usefulness of extracting the correlation between predictive and post-therapy dosimetry parameters from a patient population to "optimize treatment on the average" [297]. Indeed, the interpretation of a moderate correlation between predictive and measured dose in a patient-tailored treatment planning is still debatable without considering the confidence intervals. For example, a moderate correlation was established for the tumor dose but figure 4.6 illustrates many tumors with an overestimation or underestimation of the tumor dose using predictive dosimetry. As can be seen in this figure the confidence interval for tumor mean dose in the Bland-Altman figure is about 250 Gy while the confidence interval for non-tumoral mean dose is [-9, 7] Gy (see figure 4.4). So, an accurate tumor dose prediction from the pre-treatment data for a specific patient was not reached.

We adopted 70 Gy as the requirement for tumor response and 50 Gy as the safety threshold for non-tumor irradiation. Our results showed that for 97% of the patients, the [^{99m}Tc]Tc-MAA mean dose could predict either a safe activity planning or over-dosing of the healthy tissue (*e.g.* radio-segmentectomy). Also, for 69% of the tumors, [^{99m}Tc]Tc-MAA based dose estimation could predict if the dose to the tumor was sufficient (more than 70 Gy).

We also compared predicted and measured absorbed doses to the projected (planned) absorbed dose. The planned absorbed dose has been calculated before treatment to prescribe activity based on the partition method. In this dosimetry scheme, activity thresholding is used to calculate T/N ratio. So, any inconsistency between planned absorbed dose and predicted absorbed dose reflects the effect of different applied VOI definition (activity thresholding and anatomical tumor segmentation) solely. Notably, segmenting the tumoral lesion into different compartments (viable tumor and necrosis) is dependent on the imaging modality used. Here, we delineated the contrast-enhancing part of the tumor on CBCT (hypervascular areas) which could be different from tumor segmentation on MR or thresholding the [^{99m}Tc]Tc-MAA-SPECT or [^{18}F]FDG-PET. Taking necrosis into account is more important for tumors with a high percentage of necrosis, typically large tumors. Our analysis suggests a median (first and third interquartile range) difference of 6% ([-42, 21]%) and -3% ([-38, 25]%) between the projected and predicted mean dose for the non-tumoral and tumor compartments, respectively. It confirms that thresholding the [^{99m}Tc]Tc-MAA could result in an overestimation of the tumor dose prediction up to 50%. A more substantial discrepancy has been observed when comparing the planned dose and measured doses.

To control image noise in ^{90}Y-PET images, these are usually smoothed using Gaussian filters. The optimized FWHM of this filter is a matter of debate. Some researchers suggest avoiding over-smoothing of the images to capture the real granularity of the microsphere distribution [298, 299]. On the other hand, some end-users prefer to smooth at a higher level for visual assessment. In this study, we use the reconstructed post-treatment PET images by using protocols developed in different departments for PET/CT and PET/MR camera. Unfortunately, different FWHMs for PET were used when combined with CT or MR, which changes the images' final spatial resolution. In the future, we will modify the PET/CT protocol to match the PET/MR imaging.

Several limitations could be mentioned for this study. First, the study design is retrospective. Also, the number of analyzed cases was limited; further studies, including more patients in homogeneous tumor types, are required to determine a better evaluation of the predictive value of [^{99m}Tc]Tc-MAA. In addition, detailed lesion analysis (*e.g.*

separating necrosis and viable tumor) could be performed in the future to refine tumor dosimetry.

Most importantly, the impact of tumor type (with different degrees of vascularization and tumor load) and clinical scenario (*e.g.* radiation segmentectomy) on the correlation between predictive and measured dose distribution has not been studied much. So, more research is definitely needed to assess the predictive power of [^{99m}Tc]Tc-MAA for microspheres distribution in different types of hepatic malignancies (primary and secondary lesions).

4.6 Conclusion

In this study, we demonstrated that CBCT based dose estimation using a [^{99m}Tc]Tc-MAA study is related to the post-treatment dose measurement. The agreement is stronger for non-tumoral liver parenchyma, or total LPT than for the tumor compartment. Therefore, [^{99m}Tc]Tc-MAA based activity planning using safety threshold could be used for SIRT planning before treatment to increase the tumor dose while avoiding overdosing of the normal liver parenchyma.

Supplementary material

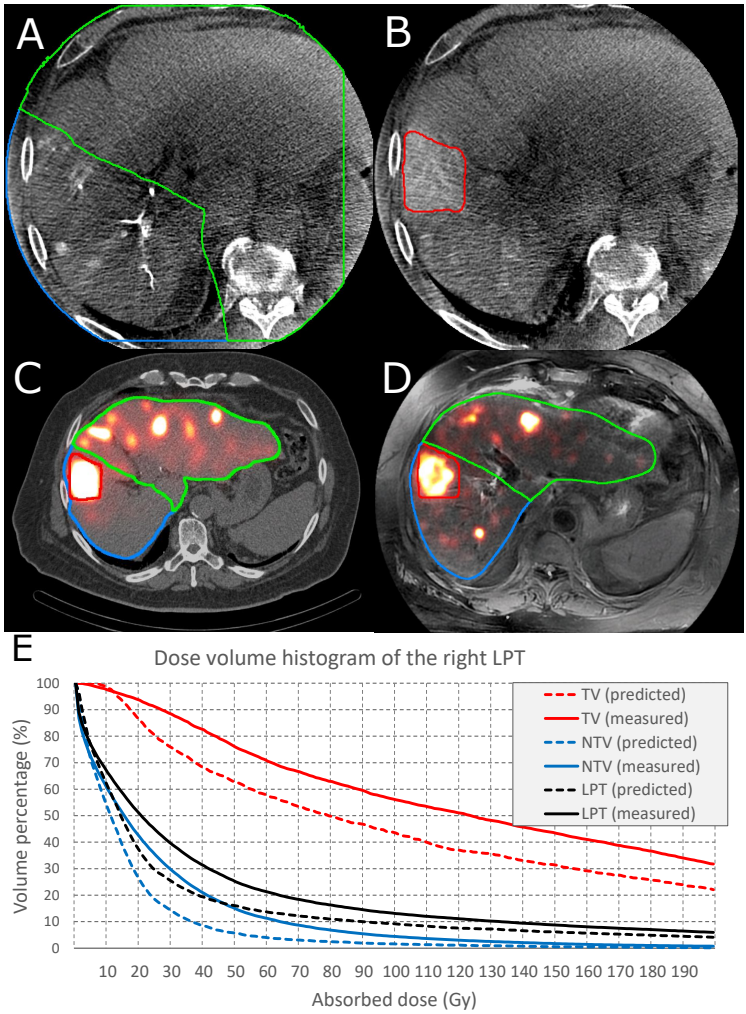

*Figure 4.10: Single transaxial slice of a pre- and post-treatment study and dosimetry results (patient ID 26): **[A and B]** early and late arterial phase CBCTs focusing on the right LPT, the contrast enhancement is used to segment the right LPT (blue line) in the early phase image and to segment the tumor (red contour) on the late phase. **[C and D]** a fusion-view of [^{99m}Tc]Tc-MAA-SPECT/CT and ^{90}Y-PET/MR images. The contours are delineated on CBCT, transferred to CT (non-rigid registration), and masked by the total liver (blue, green, and red contours correspond to the right, left LPTs, and tumor). **[E]** dose-volume histogram of the tumor, non-tumoral liver parenchyma, and total LPT from predictive dosimetry (tumor, non-tumoral tissue, and total LPT mean dose of 113, 17 and 34 Gy) and measured doses (tumor, non-tumoral tissue, and total LPT mean dose of 149, 27 and 47 Gy).*

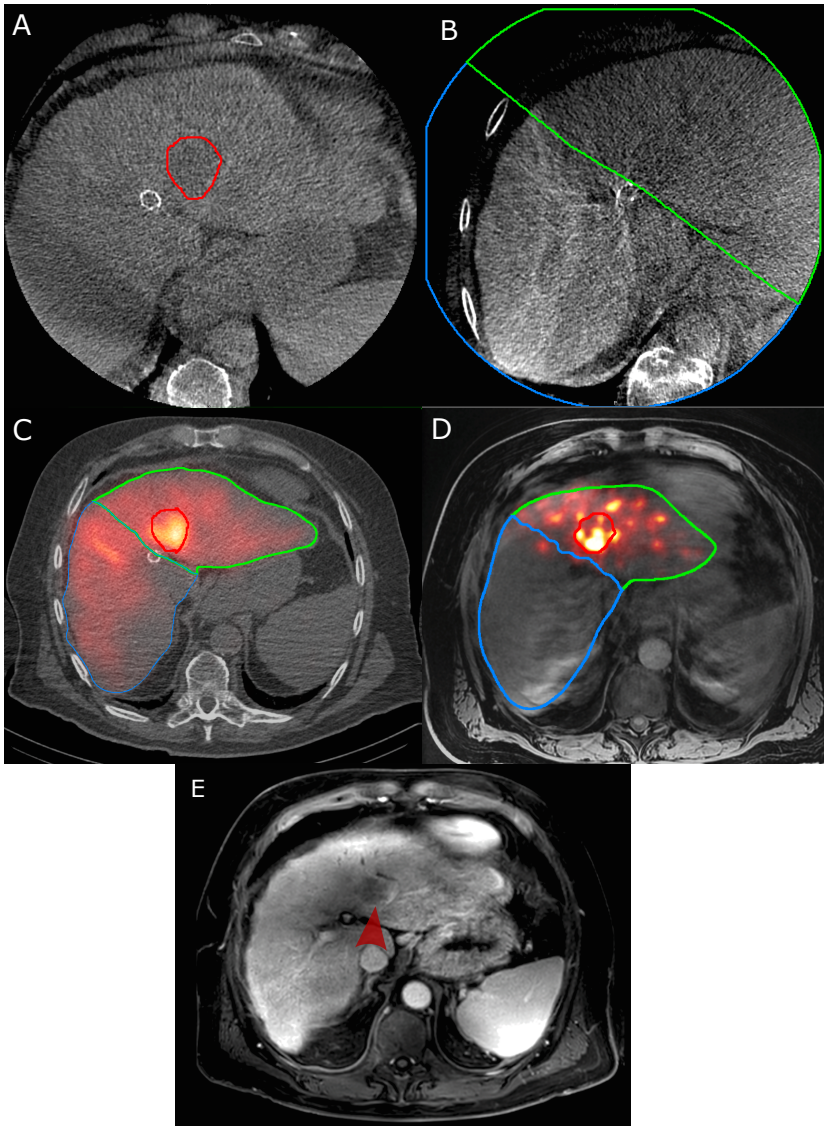

*Figure 4.11: An example of the role of CBCT in VOI segmentation. In this case, CBCT-based LPT segmentation (left lobe) matched with yttrium-90 activity deposition. This confirms that our workflow performed well for this case. Single transaxial slice of a pre- and post-treatment studies (patient ID 16): **[A]** a late arterial phase of CBCT focusing on the left liver LPT, the contrast enhancement is used to segment the tumor (red contour). **[B]** a late arterial phase of CBCT focusing on the right liver LPT, the contrast enhancement is used to segment the right and left LPT (blue and green area). **[C and D]** a fusion-view of [^{99m}Tc]Tc-MAA-SPECT/CT and ^{90}Y-PET/MR images. The contours represent registered VOIs delineated on CBCTs masked by the total liver. During the simulation, [^{99m}Tc]Tc-MAA were injected in both liver lobes, but during the therapy session, microspheres were administered within the left lobe only. One can see the correspondence of CBCT based LPT segmentation and the volume infused with microspheres on the post-treatment ^{90}Y-PET images. **[E]** A baseline MR image, the red arrow point to the tumor which has been delineated on CBCT (figures **A**)*

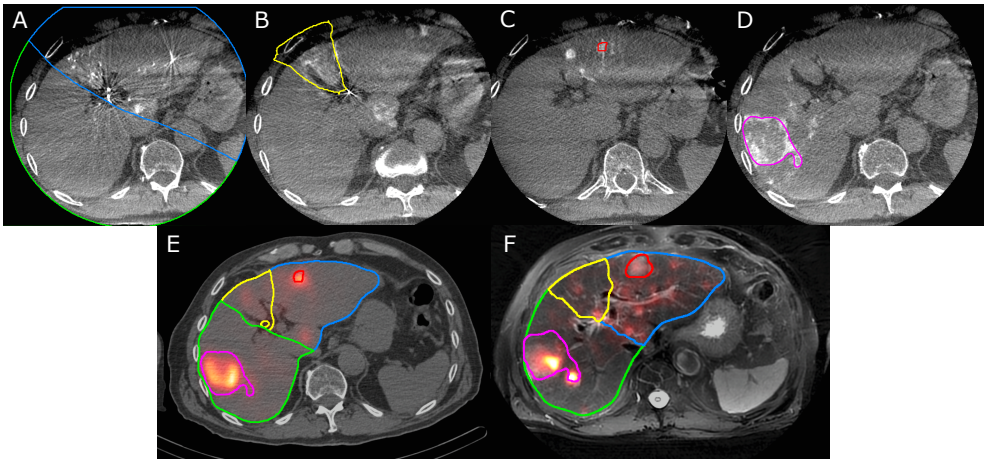

*Figure 4.12: An example of the role of CBCT in VOI segmentation for super-selective LPTs: single transaxial slice of a pre- and post-treatment studies (patient ID 46):**[A and B]** an early arterial phase of CBCT focusing on the right and middle LPT and a late arterial phase of CBCT focusing on the middle LPT, the contrast enhancement is used to segment three compartments. **[C and D]** the late arterial phase of CBCT focusing on the right and left LPT, the contrast enhancement is used to delineate tumors. **[E and F]** a fusion-view of [^{99m}Tc]Tc-MAA-SPECT/CT and ^{90}Y-PET/MR images. The contours represent registered VOIs delineated on CBCTs masked by the total liver.*

4.7 Appendix 1[1]

This section reports on the predicted absorbed doses obtained from the injected activities as computed with the following methods:

1. **empirical method**,
2. **BSA method**,
3. **SIRFLOX:** look-up table introduced in the SIRFLOX trial,
4. **MIRD method:** 50 Gy to the entire LPT (TV and NTV)[2],
5. **Partition method:** this method aims at achieving a TV absorbed dose as close as possible to 90 Gy, while keeping the NTV absorbed dose below 40 Gy. To obtain the partition method, two different IA calculations were performed:
   - **Partition(NTV) method:** partition model aiming at 40 Gy to the NTV, and
   - **Partition(TV) method:** partition model aiming at 90 Gy to the TV.

   Then, the minimum of these two IA is selected as $\mathrm{IA}_{\mathrm{Partition}}$:

$$\mathrm{IA}_{\mathrm{Partition}} = \begin{cases} \mathrm{IA}_{\mathrm{Partition(TV)}} & , \mathrm{IA}_{\mathrm{Partition(TV)}} \leq \mathrm{IA}_{\mathrm{Partition(NTV)}} \\ \mathrm{IA}_{\mathrm{Partition(NTV)}} & , \text{otherwise} \end{cases} \tag{4.3}$$

The results of the mean dose and selected DVH parameters are provided in figures 4.13 to 4.15:

- As illustrated in these figures, the empirical and BSA methods allowed a more favorable tumor mean absorbed dose, $\mathrm{V100}_{TV}$ and $\mathrm{D50}_{TV}$ compared to other methods. Still, it may induce a wide range of NTV irradiation. Based on our results, by using the BSA method, NTV absorbed dose can be as high as 110 Gy; the first and third quartile range of the NTV absorbed dose was around 40 and 75 Gy. Also, for this method, $\mathrm{V40}_{\mathrm{NTV}}$ and $\mathrm{D30}_{\mathrm{NTV}}$ gave a median [minimum, maximum] of 48 [0, 84] % and 61 [0, 121] Gy, respectively.
- Injected activity in the SIRFLOX trial was adapted from BSA, aiming at reducing the activity for patients with high tumor burden. Our results also show that this method was safe for most of the cases. For all cases, the mean dose to the NTV was less than 50 Gy.
- For the MIRD method, the mean absorbed dose was less than 50 Gy for all cases but $\mathrm{V40}_{\mathrm{NTV}}$ could be as high as 61% with first and third quartile range of [0, 60] %.
- On the other hand, as intended, the partition method maximized the tumor absorbed dose while preserving the NTV dose below a certain threshold. For this method, $\mathrm{V40}_{\mathrm{NTV}}$ and $\mathrm{D30}_{\mathrm{NTV}}$ never exceed 45% and 55 Gy, respectively.

[1] This appendix is not included in the published paper

[2] This is the absorbed dose criterion mentioned in literature for SIRT with standard setting. In patients with reduced liver function, a total liver absorbed dose of 40-45 can be set. Also, in case of more selective SIRT, a higher total liver absorbed dose can be used.

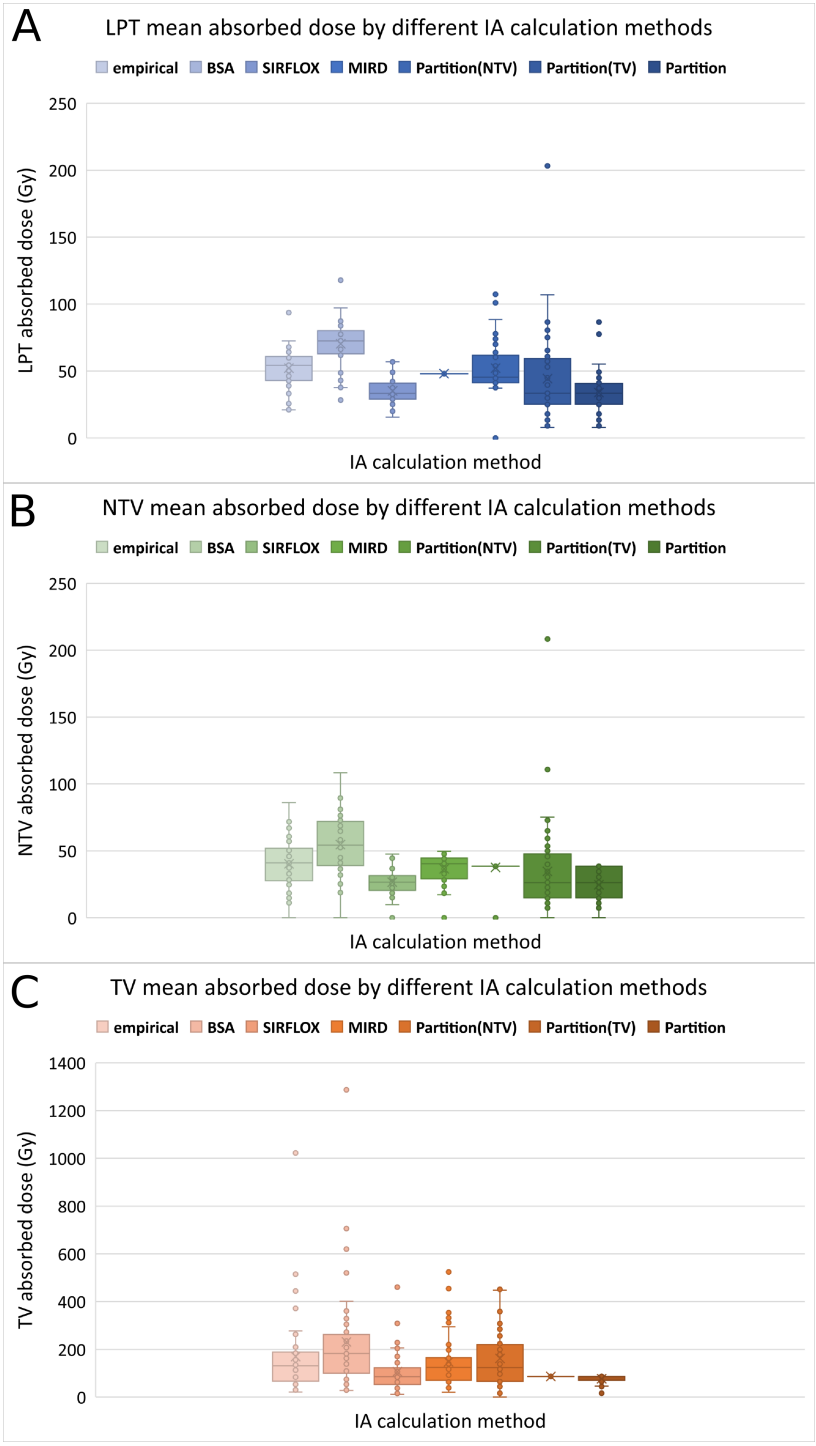

*Figure 4.13: Predicted mean absorbed dose of [**A**] LPT, [**B**] NTV, and [**C**] TV for different IA calculation methods.*

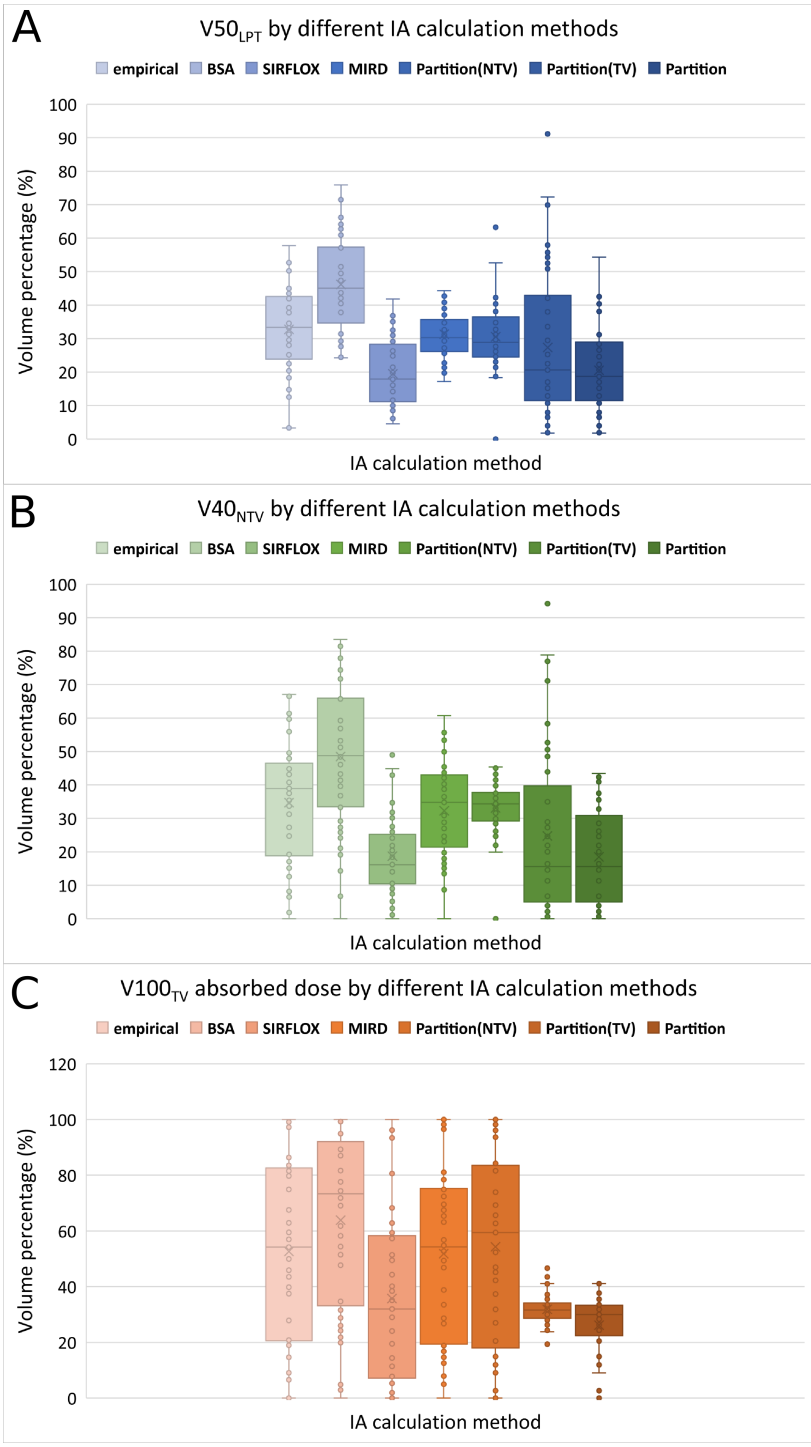

*Figure 4.14: Predicted [**A**] $V50_{LPT}$, [**B**] $V40_{NTV}$, and [**C**] $V100_{TV}$ for different IA calculation methods.*

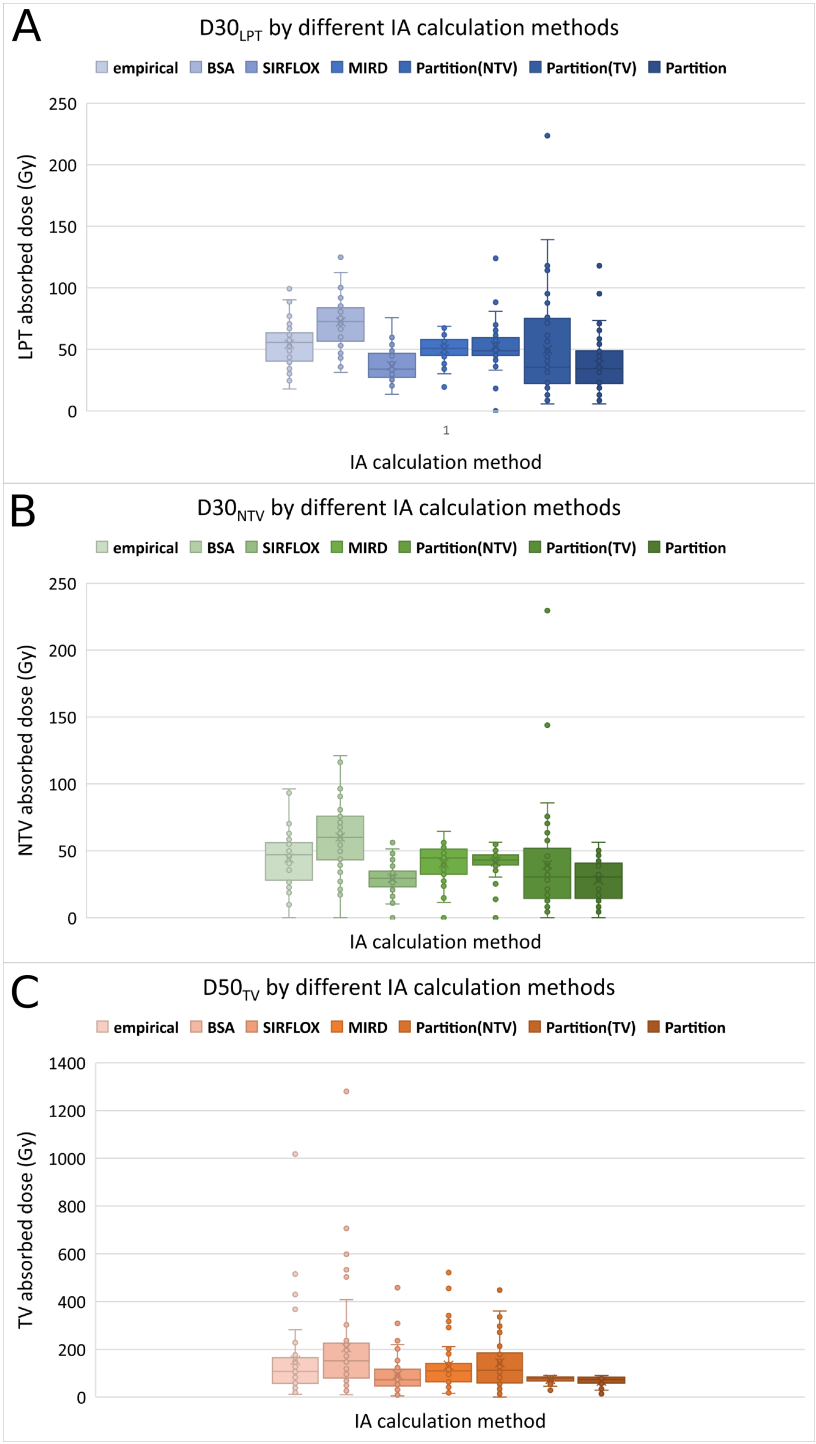

*Figure 4.15: Predicted **[A]** $D30_{LPT}$, **[B]** $D30_{NTV}$, and **[C]** $D50_{TV}$ for different IA calculation methods.*

4.8 Appendix 2[3]

When assessing the TV and NTV absorbed dose, compensating for absorbed dose heterogeneity is a challenge for both EBRT and radioembolization. Absorbed dose distribution is usually evaluated using **(1)** visual 3D dose maps and **(2)** DVHs, which downgrades the distribution to 2D histograms to describe a large amount of data in 3D distributions. The latter assumes that hepatic tumor and liver parenchyma consists of several identical functional sub-units.

In this study, DVH parameters (*e.g.* $V40_{NTV}$ and $V100_{TV}$) are used to compare different dose maps (*e.g.* pre-treatment dose estimation and post-treatment), which only use some of the information of the DVH. An alternative for reducing DVH information to a single value for parallel organs is the equivalent uniform dose (EUD) [300]. EUD considers all dose distribution and calculates a biologically weighted average of the voxel doses within tumor or NTV, which would provide the same radiobiological effect (*e.g.* NTCP and TCP for NTV and TV, respectively) as the actual non-uniform absorbed dose distribution.

EUD is heavily investigated in EBRT [301] and several studies are investigating this parameter in radioembolization [302,303]. In this section, we present preliminary results of implementing Jones-Hoban EUD formalism for comparing predictive and measured dose for NTV [74]:

$$\mathrm{EUD} = -\frac{1}{\alpha}\ln\left(\frac{\sum_i e^{-\alpha D_i}}{N}\right) \tag{4.4}$$

Here, N is the number of voxels, D_i is the dose at the voxel i, and α denotes the radiosensitivity of the cellular population (which depends only on the cell type and the linear energy transfer of the particles). However, the liver parenchyma radiosensitivity in radioembolization are still under investigation. In this section, we used reported $\alpha = 0.0065$ 1/Gy by Dawson for whole liver EBRT. Chiesa *et al.* reported a lower α (0.002 1/Gy) by evaluating in vivo cellular survival fraction by using the relative volume reduction of the perfused parenchyma [302]. In another study, a higher radiosensitivity ($\alpha = 0.0104$ 1/Gy) was derived from TD50=41.6 Gy from results of Jackson *et al.* [304].

As illustrates in figure 4.16, the pair difference of predicted and measured EUD shows a larger deviation ([-35, 70] %) than the mean absorbed dose ([-27, 48] %). This suggests that by employing radiobiological parameters, larger uncertainties might be observed between NTV dose prediction based on [^{99m}Tc]Tc-MAA-SPECT and measured absorbed dose based on ^{90}Y-PET.

[3]This appendix is not included in the published paper

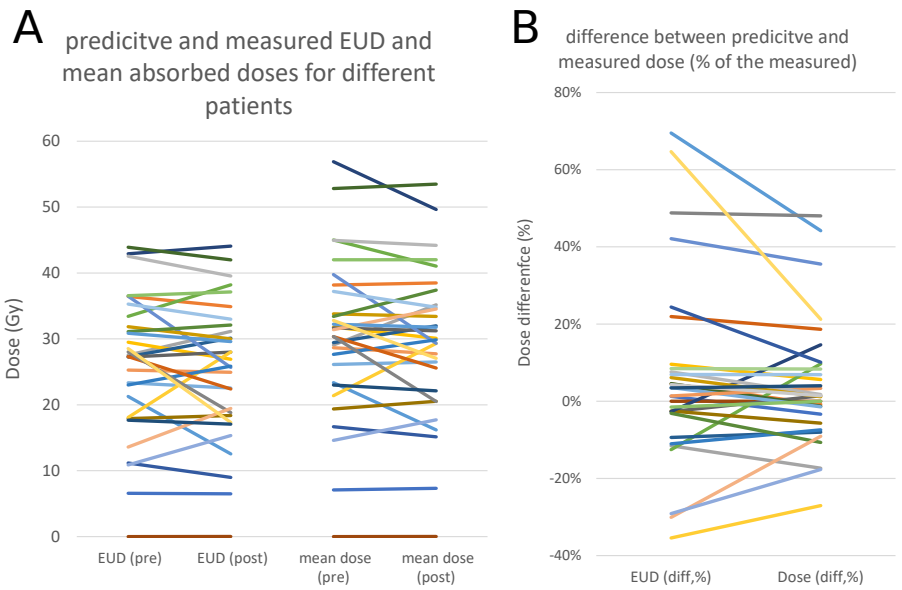

*Figure 4.16: [**A**] Comparing predicted and measured EUD (left-sided pairs) and predicted and measured mean dose (right-sided pairs) [**B**] normalized difference between predicted and measured EUD compared to difference between mean doses.*

Chapter 5

Prospective dosimetry case reports: examples of future research directions

This chapter was written in a form which could be published in Medical dosimetry (journal of the American Association of Medical Dosimetrists) as a case report study with a very limited modification.

Abstract

SIRT is a promising treatment for hepatic malignancies. Several image-based investigations, *e.g.* volumetric report and absorbed dose assessment, are mandatory for SIRT treatment planning and treatment verification based on national and international regulations.

General treatment workflows are described in guidelines, recommendations, and the package inserts of the manufactures. But guidance to tackle particular clinical conditions can be ill-defined and different centers practice their own workflow to analyze the treatment process. Examples include **(i)** high lung shunt, **(ii)** very high tumor to non-tumoral liver activity concentration ratio, **(iii)** inconsistency between treatment simulation and observed treatment result, and **(iv)** management of patients with a limited future liver remnant and functionality. No universally accepted standard procedure is defined in the literature for these settings and more advanced multi-modal image-based analysis may be beneficial.

Here, we present some clinical case reports to describe our latest research in employing advanced image processing techniques to enrich our treatment workflow for special clinical scenarios.

Keywords radioembolization, selective internal radiation therapy (SIRT), dosimetry, liver perfusion territory, cone-beam CT, lung shunt, tumor segmentation, normal tissue complication probability, hepatobiliary imaging, [^{99m}Tc]Tc-mebrofenin

5.1 Introduction

A workflow for the use of resin ^{90}Y-microspheres (SIR Spheres, SIRTEX, Sidney, Australia) is described in the package insert of the manufacturer [281]. Several guidelines provide recommendations on the use of these spheres, such as the European Association of Nuclear Medicine (EANM) guideline [154], and the recommendations of the American Association of Physics in Medicine (AAPM) [153]. These procedures are generic and are useful for a vast majority of the patients. In the preceding chapters, the dosimetry workflow and some patient population studies were presented. Also, an example of a standard pre- and post-treatment dosimetry report was covered in section 2.3.

In the day-to-day clinical practice, each patient has unique clinical features and needs, necessitating a tailored activity planning strategy, based on dosimetry. Here, some examples of patient-tailored prospective use of an advanced activity planning workflow to address clinically relevant questions are provided. The cases are presented to illustrate the gain of the multi-modal image analysis and feature extraction from all available studies. To give some insights into potential future research topics, these cases are covered in this report:

- **case 1:** activity prescription for a case with high estimated lung shunt fraction (eLSF),
- **case 2:** a case that illustrates the usefulness of VOI definition based on cone-beam CT (CBCT) in comparing predicted and measured dose,
- **case 3:** a case report on the role of tumor and liver perfusion territory (LPT) segmentation in dosimetry,
- **case 4:** the first case of utilizing the voxel-level dosimetry as a treatment planning method in our department. In this case, [^{99m}Tc]Tc-mebrofenin (BrIDA) imaging [305] was used to analyze regional liver functionality during the activity prescription process.

5.2 Case descriptions

5.2.1 Case1: Activity prescription for a workup with substantial lung shunt fraction

A 69 year old patient with a complicated condition was referred to our department as a candidate for SIRT. This patient (72 kg, 183 cm) suffered from a large metastatic neuroendocrine tumor (NET), WHO grade 1, with central necrosis. Primary surgery was not offered at the time due to high tumor load and to the close vicinity to hepatic blood vessels. The following two options were reviewed at the MDT:

1. a right-sided SIRT without treating the left lobe, even if there was a tumor involvement in the left liver lobe (segment IV). The intention was to fulfill a right radiation lobectomy to introduce hypertrophy of the future liver remnant in the left lobe, which would allow an extended right hemihepatectomy (including segment IV) subsequently. Segments I, II, and III are free of tumor.

2. a portal vein embolization on the right lobe to induce hypertrophy of the contralateral liver lobe. However, portal vein embolization was considered challenging because percutaneous approach to the portal vein may be complicated due to location (relative to the blood vessels) and size of the tumor.

The patient underwent a pre-treatment workup, consisting of administering [^{99m}Tc]Tc-MAA in the left and right HA. Planar and SPECT/CT imaging were performed around 1 and 1.75 hours after administration, respectively. On the SPECT/CT image, a heterogeneous activity distribution over both liver lobes was observed. Substantial tumor uptake was documented at visual evaluation. There was no evidence of extrahepatic activity deposition (*e.g.* stomach, duodenum, gallbladder, ...) except for a relatively high lung shunting. A eLSF of 28.7% was calculated using planar imaging (see figure 5.1-A). The treatment team decided to consider SIRT on condition that a personalized dosimetry estimates a favorable tumor dose coverage and safe NTV absorbed dose while keeping the lung dose less than 30 Gy. So, after the first pre-SIRT workup and before the second MDT meeting, a dosimetry report was established to predict the TV, lung, and NTV absorbed dose.

The results, which are presented in the following subsection, were the subject of discussion in the second MDT. They concluded that the risk of lung toxicity was too high to perform SIRT in the setting (*i.e.* catheter position) used in the first simulation. It was

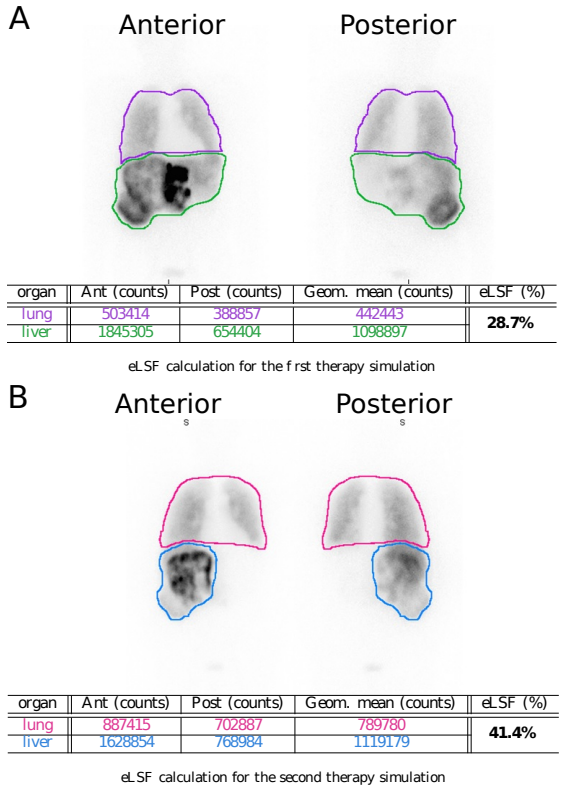

*Figure 5.1: **[A]** An LSF of 28.7% was calculated based on planar imaging for the first pre-SIRT workup. **[B]** The second workup suggested that even a higher amount of lung shunting could be expected by practicing a different catheter tip positioning.*

proposed to repeat the pre-treatment workup with a different catheterization strategy, injecting only the right hepatic artery. In this second right lobe only workup, an even higher eLSF (41%) was observed (see figure 5.1-B), demonstrating that the eLSF was mainly caused by the right lobe, in all likelihood due to intra-tumoral shunting.

Finally, it was decided not to perform SIRT as a too high lung dose would be delivered with activities needed to obtain a substantial anti-tumoral effect in a large mNET (*e.g.* to obtain a tumor dose of 120 Gy, an IA of 1.7 and 11.0 GBq was calculated to be injected to the left and right perfusion territory, respectively. Using these IAs, an absorbed dose of 182 Gy was estimated for 1 kg lung).

Then, right-sided portal vein embolization was performed to obtain hypertrophy of the left liver lobe. Two months later, left liver hypertrophy was observed; the total liver volume (including large right-sided tumor mass) was 5873 ml, and the future residual liver volume was 1370 ml (23% of the total liver volume). Despite this left hypertrophy, surgery still did not seem safe because of limited tumor downstaging. MDT decided to start chemotherapy (combination of capecitabine and temozolomide) for this patient.

Dosimetry report

Several imaging studies were analyzed to perform predictive dosimetry for this patient (see figure 5.2):

– a [^{68}Ga]Ga-DOTA-TATE-PET/CT was performed a month before the first [^{99m}Tc]Tc-

MAA study. By thresholding the [^{68}Ga]Ga-DOTA-TATE-PET image, a viable tumor was located. Thereafter, a necrosis compartment was manually outlined. These VOIs were transferred to the [^{99m}Tc]Tc-MAA-SPECT image, using the image registration algorithm proposed in our previous study [49].

– two LPTs were segmented on the CBCT. The VOIs were transferred to the [^{99m}Tc]Tc-MAA-SPECT space.
– the liver was segmented by applying a CNN-based delineation algorithm [211] on CT from [^{99m}Tc]Tc-MAA study.

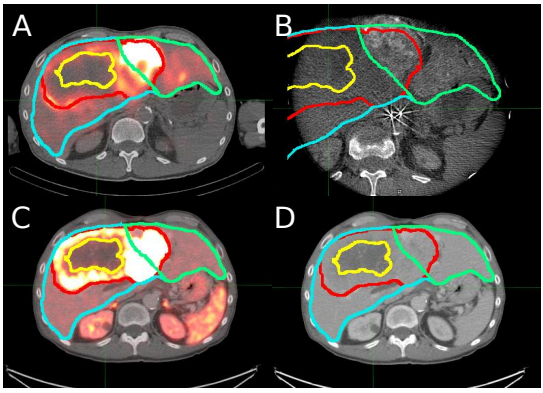

*Figure 5.2: This figure includes one transverse slice of all the images used in the predictive dosimetry. The green, blue, red, and yellow contours represent the left lobe, right lobe, viable tumor, and necrosis. **[A]** The [^{99m}Tc]Tc-MAA-SPECT/CT estimated the microsphere distribution. This study suggested a higher activity concentration within the viable tumor in the left lobe than the viable tumor in the right lobe; the CT from this study was used for liver segmentation. **[B]** The late arterial phase contrast-enhanced CBCT, which highlighted the left liver perfusion territory. It was used to separate the left and right liver perfusion territories (green and blue contours). **[C and D]** These images show the fusion and CT from [^{68}Ga]Ga-DOTA-TATE-PET/CT study, respectively. The viable tumor received a high uptake, while the necrotic part had a very low uptake and was hypodense in the CT. This information was used to separate viable tumor (red) and necrosis (yellow).*

parameter	left lobe	right lobe	entire liver
viable TV (ml)	279	2299	2578
necrotic volume (ml)	0	368	368
NTV (ml)	771	1770	2541
entire VOI volume (ml)	1050	4437	5486
T/N ratio	3.45	2.36	2.30

Table 5.1: Segmentation and activity report

The local deposition model was applied to convert the fractional activity uptake, derived from [^{99m}Tc]Tc-MAA-SPECT, to Gy per unit of IA (in GBq). Then, different dose parameters were obtained for various IAs (see figure 5.3). In the left lobe, which involved a small part of the tumor, an IA of around 1.7 GBq was adequate to deliver a viable tumor dose of 120 Gy with $V100_{TV}$ of 47%; at the same time, a NTV absorbed dose of 34 Gy, and $V50_{NTV}$ of 17% was estimated. The lung dose from this IA within the left HA (using the first [^{99m}Tc]Tc-MAA simulation) was 24 Gy.

Conversely, the predictive dosimetry for the right lobe was not as promising as the left lobe. An IA of around 11.0 GBq was needed to achieve a viable tumor dose of 120 Gy and

$V100_{TV}$ of 54%. For this considerably high activity, NTV and lung dose (using the first [^{99m}Tc]Tc-MAA simulation) of 51 and 154 Gy were estimated, respectively. These results implied that to reach a sufficient TV dose, a very high IA was required, which resulted in a very high lung absorbed dose (a cumulative dose of more than 178 Gy to the lungs). In addition, because of the distribution of the [^{99m}Tc]Tc-MAA particles within the TV, even with this high activity, only less than 40% of the TV would receive 80 Gy or more. These results showed that SIRT with that catheterization strategy was contraindicated.

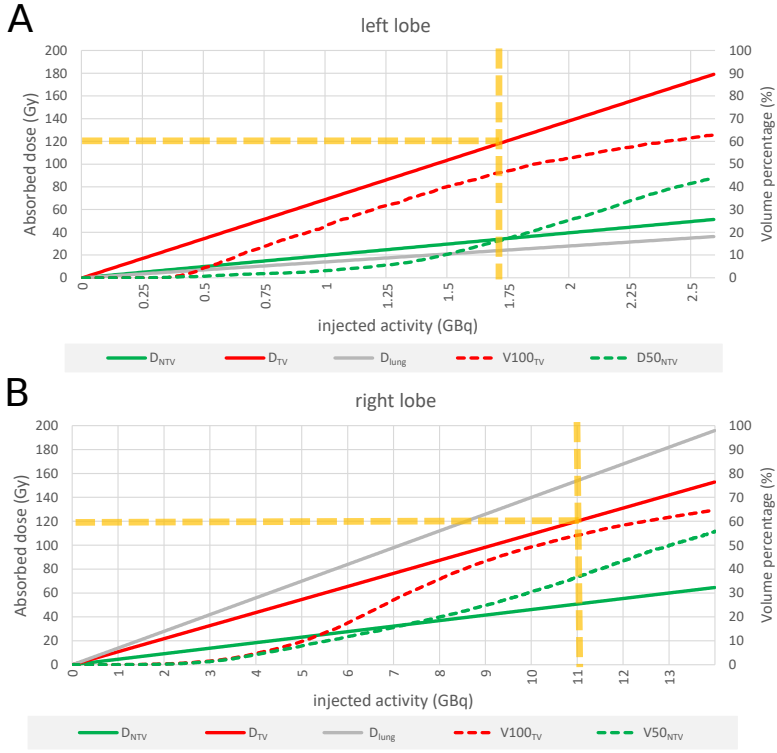

*Figure 5.3: Lung, TV and NTV absorbed dose analysis for different IAs in the **[A]** left lobe and **[B]** right lobe using the first [^{99m}Tc]Tc-MAA simulation. The viable tumor dose coverage was better for the left lobe (279 ml), while the dose to viable tumor in the right lobe (2299 ml) did not reach 120 Gy even for a very high IA (e.g. 11.0 GBq, which gave an unacceptable lung dose of around 155 Gy). The orange dashed lines illustrates the IA which corresponds to 120 Gy to TV.*

Discussion

SIRT is an established treatment option for metastatic neuroendocrine tumor (NET) NET [38, 44, 218]. These tumors demonstrate hypervascularity for two-third of the tumors and iso-vascularity for the rest [306]. In case of hypervascular tumors, SIRT has the advantage of maximizing tumor irradiation while minimizing toxicity to normal parenchyma. High lung shunt fraction in [^{99m}Tc]Tc-MAA workup can occur when a large number of [^{99m}Tc]Tc-MAA particles pass through tumor arteriovenous shunts and accumulate within the lung parenchyma. Substantial eLSF is considered as a contraindication for SIRT, as it could indicate a large lung shunting of yttrium-90 containing microspheres and cause radiation-induced pneumonitis, which can have substantial impact on quality of life and result in death.

For cases with high LSF, two different approaches are recommended in the guidelines:

(i) direct activity reduction based on the extent of eLSF, and (ii) recalculating the prescribed activity by estimating the lung absorbed dose and limit the activity based on estimated lung absorbed dose (*e.g.* 30 Gy). But none of these approaches mention the effect of possible activity reduction on TV and NTV absorbed dose. In this case we consider mean dose and DVH parameters for TV and NTV together with mean dose to the lung during the activity prescription process. In this case, the treatment team decided not to treat the patient, as the maximum injectable activity based on lung absorbed dose was not sufficient to reach a satisfactory tumor irradiation.

5.2.2 Case2: Discrepancy between projected and measured dose

A SIRT session was performed for a 78 year old patient with HCC. Based on diagnostic MR and CT images, a massive central and two satellite tumors, involving segments II and IV, were diagnosed. After a MDT discussion, TACE was deemed contra-indicated because of the extensive tumor load. Hence, SIRT was considered as an alternative aiming at controlling tumor progression.

The treatment was planned based on a pre-SIRT workup. During the workup, a super-selective catheterization of the HA was performed, and perfusion territories of the left and right HA were evaluated. Dual-phase CBCTs indicated the bulky tumor in segment IV and two other smaller tumors. The tumors were irrigated from both the left and right HA. An accessory branch to segment I did not contribute to the blood flow to the tumors. Afterwards, a [^{99m}Tc]Tc-MAA-SPECT/CT was performed, which predicted poor targeting, particularly within the right lobe. In this lobe, almost no difference was found between the ventrally located tumor and dorsal healthy liver. An eLSF of 4.8% was calculated.

The treatment was planned a month after [^{99m}Tc]Tc-MAA workup by using the MIRD method with an entire liver absorbed dose of 50 Gy (equivalent to 1 MBq/ml). The therapeutic microspheres were administered in a comparable manner to the workup, except for one difference; an anti-reflux catheter was used during the treatment session. We hypothesized that the microsphere distribution with the use of an anti-reflux catheter could be different, in an unpredictable manner, compared to a regular micro-catheter. Interestingly, on the day of the treatment, preferential tumor targeting was observed. We performed detailed dosimetry, particularly with respect to predictive versus measured dose comparison. Detailed dosimetry is provided in the following sub-sections.

Three months after treatment, an arterial and venous phase ceCT, and contrast-enhanced MR images were performed. The two satellite lesions showed a prominent response. For the big tumor, no volume increase was observed, and it was evaluated as stable disease or response due to its prominent central necrosis (see figure 5.4).

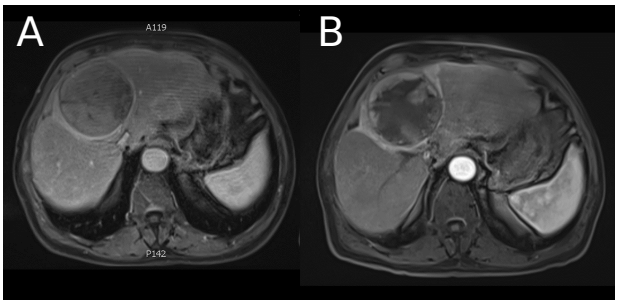

*Figure 5.4: **[A]** Latest MR image before SIRT, performed 1.5 month before treatment session, **[B]** a follow-up MR performed three months after SIRT session. These images demonstrated the appearance of prominent central necrosis*

Dosimetry report

By using a projected absorbed dose of 50 Gy (or 1 MBq per ml) to the entire liver (TV and NTV), 0.522 and 1.027 GBq of resin microspheres were prescribed for the left and right liver lobe, respectively.

Fractional uptakes were derived from the [^{99m}Tc]Tc-MAA-SPECT and ^{90}Y-PET for the predictive and post-treatment dosimetry, respectively. The dosimetry was performed based on the local deposition model utilizing these VOIs:

- **liver:** the liver was delineated by applying the CNN on the CT from the [^{99m}Tc]Tc-MAA workup with some manual adjustment,
- **tumor:** tumors were segmented on CBCTs,
- **LPTs:** two LPTs were segmented on CBCT images.

For post-treatment dosimetry, all the VOIs were aligned to the post-treatment ^{90}Y-PET using non-rigid registration. A comparison between segmented volumes used in pre- and post-treatment dosimetry, together with the manual segmentation (which was used for prescription) are provided in table 5.2; screenshots of three different transverse slices of various studies, as well as defined VOIs are shown in figure 5.5.

parameter	method	left lobe	right lobe	entire liver
TV (cc)	clinical routine	-	-	-
	predictive dosimetry	166	202	368
	post-treatment dosimetry	162	200	366
NTV (cc)	clinical routine	-	-	-
	predictive dosimetry	318	822	1140
	post-treatment dosimetry	345	856	1202
entire VOI vol (cc)	clinical routine	**520**	**1000**	1520
	predictive dosimetry	484	1024	1508
	post-treatment dosimetry	507	1057	1564
tumor involvement (%)	clinical routine	-	-	-
	predictive dosimetry	**34**	**20**	**24**
	post-treatment dosimetry	**32**	**19**	**23**
left to entire (%)	clinical routine	**34**	-	-
	predictive dosimetry	**32**	-	-
	post-treatment dosimetry	**32**	-	-

Table 5.2: Segmentation analysis; comparing our segmentation results and clinical records.

A comparison between predictive dosimetry and measured dose distribution is provided in table 5.3. Cumulative dose-volume histogram are also provided in figure 5.6. The voxel-level dosimetry revealed that:

- TV mean dose in post-treatment is notably higher than pre-treatment evaluation for the right lobe (72 versus 189 Gy). In the left lobe, the underestimation of the TV dose by [^{99m}Tc]Tc-MAA was less notable (82 versus 108 Gy).
- more than 56%, 83%, and 70% of the tumor volume received a dose of 100 Gy or more in left, right draining regions, and entire liver.
- 85% of the NTV received an absorbed dose of less than 30 Gy (with a mean dose of only 17 Gy).

criterion *	left lobe			right lobe			entire liver		
	pre	post	Δ	pre	post	Δ	pre	post	Δ
TV activity (MBq/cc)	1.70	2.25	0.55	1.50	3.94	2.44	1.59	3.14	1.55
NTV activity (MBq/cc)	0.75	0.46	-0.29	0.91	0.31	-0.60	0.87	0.35	-0.52
T/N ratio (ratio)	**2.26**	**4.91**	**2.65**	**1.65**	**12.88**	**11.23**	**1.84**	**9.00**	**7.16**
VOI dose(Gy)	52	49	-3	49	48	-1	**50**	**48**	**-2**
D_{NTV} (Gy)	36	22	-14	44	15	-29	**42**	**17**	**-25**
D_{TV} (Gy)	**82**	**108**	**26**	**72**	**189**	**117**	**76**	**153**	**77**
$V30_{NTV}$ (%)	42	23	-19	74	11	-63	65	15	-50
$V100_{TV}$ (%)	23	56	33	14	83	69	18	70	52

Table 5.3: Overview of the predictive and measured dosimetry comparison.

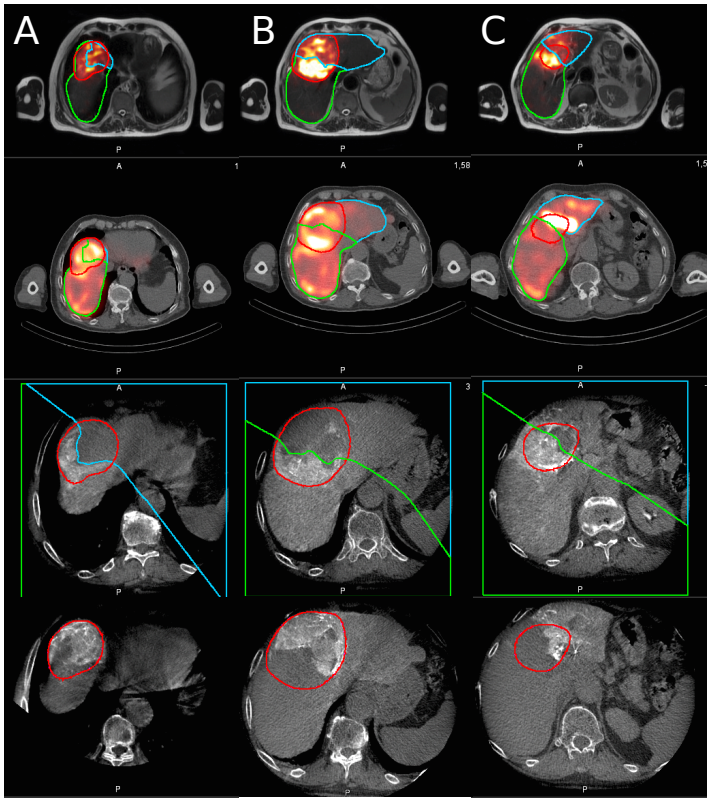

Figure 5.5: Three different slices of the images employed in dosimetry; the green, blue, and red contours outline the right lobe, left lobe, and tumor.
The first row shows the post-treatment ^{90}Y-PET/MR; the second row is the [^{99m}Tc]Tc-MAA-SPECT/CT; the third and fourth rows are late arterial phase CBCTs for the right and left perfusion territories.
This figure represents the importance of the CBCT imaging not only in separating different perfusion territories but also in defining portions of the tumor that receive activity from various branches of the hepatic artery.
A visual comparison between pre-treatment simulation ([^{99m}Tc]Tc-MAA-SPECT/CT) and post-treatment activity measurement (^{90}Y-PET), indicates that the simulation underestimated the tumor uptake.

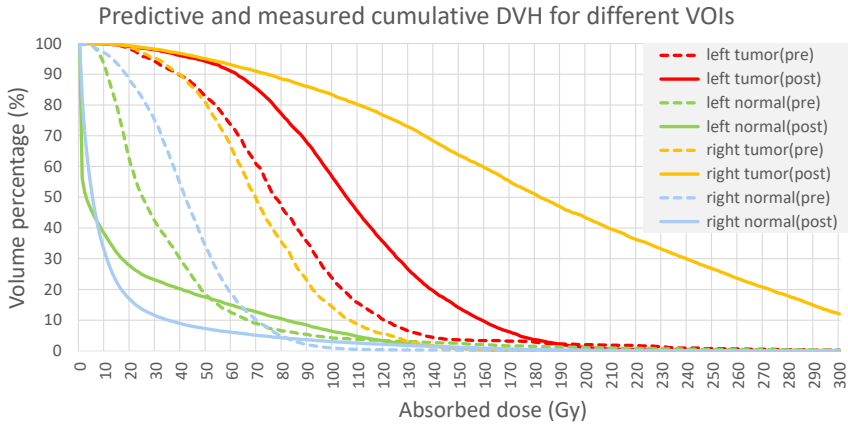

Figure 5.6: Cumulative dose-volume histogram showed that for both lobes, predicted dosimetry underestimated the TV dose and overestimated the NTV dose significantly.

Discussion

As mentioned above, for this patient more extensive tumor uptake with greater TV absorbed dose (by a factor of 2.0) was observed. As a result, decreased activity deposition in areas of NTV was measured compared to the workup. As the catheterization was similar for this patient, we believe that this large mismatch between [^{99m}Tc]Tc-MAA and ^{90}Y-microsphere activity distribution was due to the use of anti-reflux catheter in the therapy session. Pasciak *et al.* also reported a similar effect with the use of an anti-reflux catheter [307].

5.2.3 Case 3: Role of VOI segmentation methods in dosimetry

A HCC (diameter, 65 mm) in liver segments V and VIII associated with cirrhosis was diagnosed in a 73 year old patient using MR imaging. TACE and SIRT were discussed in the MDT. Because of the large size, SIRT was recommended as the first option.

A pre-treatment workup was undertaken one month after MR imaging. Selective catheterization of the right HA, by means of a micro-catheter, revealed normal vessel anatomy and large tumor blush. Lung shunting was not a contraindication for SIRT (eLSF: 2.6%). Visual investigation of the [^{99m}Tc]Tc-MAA-SPECT indicated a good tumor targeting in segments V and VIII. There was no evidence of activity deposition within extrahepatic tissues, *e.g.* stomach, duodenum, or gallbladder.

The prescription was made using the radiation segmentectomy approach for segments V and VIII. The tumor volume was 143.8 ml and the ablation volume was measured to be 330 ml (22.5% of the entire liver). The patient was relatively small patient (height, 1.54 cm; weight, 56 kg). The prescribed activity was 1340 MBq to the right lobe using the partition method (a TV projected dose of 205 Gy, and a NTV projected dose of 120 Gy).

The SIRT session was performed a month after [^{99m}Tc]Tc-MAA workup. Post-treatment imaging (^{90}Y-BECT and ^{90}Y-TOF-PET) revealed a high tumor uptake. A post-treatment visual assessment suggested that the activity distribution broadly agreed with the [^{99m}Tc]Tc-MAA imaging in the workup.

Three, six, and thirteen months after SIRT, MR imaging was performed (see figure 5.7). In all follow-up images, a slight tumor volume reduction with the occurrence of central necrosis was observed. So, it was described as a pronounced partial response.

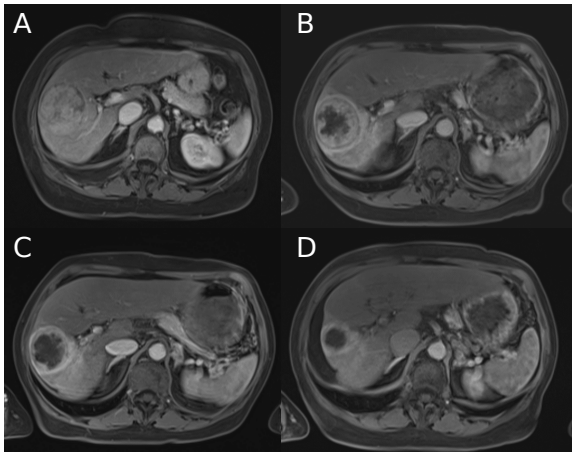

*Figure 5.7: **[A]** latest MR image before SIRT, performed two months before treatment session (lesion diameter: 55.8 mm), **[B]** a follow-up MR performed three months after SIRT session suggested a new central necrosis and some evidence of radiation hepatitis, **[C]** a follow-up MR performed six months after SIRT session showed increased central necrosis, **[D]** a follow-up MR performed thirteen months after SIRT session showed further increased central necrosis, subtotal tumor regression with only very minimal viable component with decrease in size (22.5 mm compared to 55.8 mm in baseline image [A]), with atrophy surrounding irradiated parenchyma and minor ascites.*

This case is selected to highlight the following points (as potential research directions):

1. How personalized dosimetry (*i.e.* PM or voxel-level) can be used to project a higher dose within a small LPT, which is mostly tumoral (radiation segmentectomy).
2. An introductory investigation on the role of tumor segmentation method in the inconsistency between projected dose (based on prescription) and measured dose, which was observed in the previous chapter. By definition, the absorbed dose in each pre-defined VOI depends solely on the deposited energy and mass of the VOI. So, it is evident that different delineation methods could result in different absorbed doses. This case investigates the extent of the effect of the tumor and LPT segmentation on dosimetry as well as calculating an IA by different methods. Not surprisingly, the absorbed dose disagreement within smaller VOIs (*i.e.* TV) was higher than bigger VOIs (*i.e.* NTV compartment). That is why the [^{99m}Tc]Tc-MAA-based dose prediction was considered to be more reliable for the NTV than TV. This result could be investigated among more patients in the future.

The subsequent sub-sections report **(a)** volume differences in various tumor and LPT segmentation methods, **(b)** IAs comparison derived from different methods for these segmentation methods, **(c)** the impact of the segmentation method on different dosimetry parameters (*e.g.* mean dose to the TV and NTV, $V120_{TV}$, and $V60_{NTV}$), and **(d)** the impact of tumor segmentation method on the cDVH before and after the treatment.

Volumetric report

In the following sub-sections, predicted and measured absorbed doses are compared when various strategies were applied for tumor and LPT definition (see figure 5.9):

– **clinic:** these are the volumes that were used for prescribing the activity in the clinical routine: **(a)** the liver was manually delineated on CT, **(b)** the volume of the tumor and LPT, together with T/N ratio were estimated from some VOIs on [^{99m}Tc]Tc-MAA-SPECT.

- **CBCT:** this method was presented in the previous chapter: **(a)** the liver was delineated by implementing CNN on CT from [^{99m}Tc]Tc-MAA study, **(b)** tumor and LPT were segmented manually on CBCT.
- **thresh 20 and 30:** in these methods: **(a)** tumors were segmented by thresholding the [^{99m}Tc]Tc-MAA-SPECT and ^{90}Y-PET images by 20 and 30% of the maximum activity uptake, **(b)** the entire liver (TV and NTV) was delineated by employing CNN, **(c)** as both [^{99m}Tc]Tc-MAA workup and treatment involved only one administration, LPT was also segmented by thresholding the activity images by 3% of the maximum activity uptake. Here, we assume that the activity was deposited solely within the treated LPT.

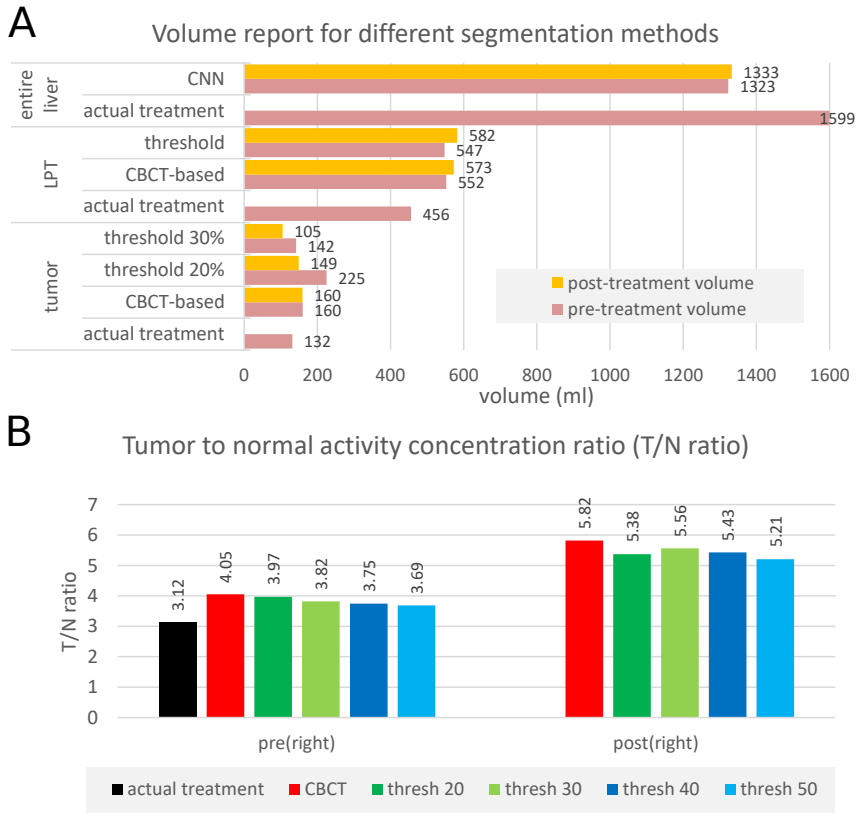

*Figure 5.8: [**A**] The liver, LPT and TV volumes were defined by the detailed methods: CNN-based liver volume was very close to the manually segmented liver on CT. The volume of the LPT segmented on the CBCT was comparable to the thresholding activity by 3% of the maximum uptake and a little bit higher than the CT-based segmentation (used for actual treatment). The TV volume was variable for different approaches; based on the contrast-enhancement on CBCT and CT images, volumes of 160 and 132 ml were segmented, respectively. On the other hand, for activity thresholding methods, the volume was inconsistent between two threshold levels; for example, in the pre-treatment evaluation, thresholding by 20% of the maximum uptake resulted in a volume of around 50% more than the obtained volume from thresholding by 30% of the maximum uptake. [**B**] T/N ratio also depended on the tumor definition. Depending on the effect of the threshold level on the TV and NTV volume, and total activity uptake, utilizing a higher threshold could result in a lower or higher T/N ratio. For all tumor definition methods, T/N ratio measured from the post-treatment imaging was higher than the estimated value based on the pre-treatment workup.*

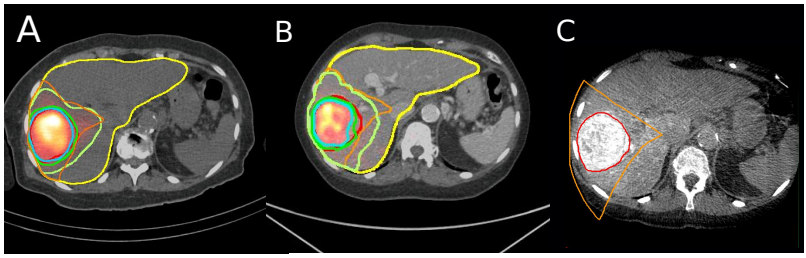

*Figure 5.9: **[A]** Pre-treatment [^{99m}Tc]Tc-MAA-SPECT/CT **[B]** post-treatment ^{90}Y-PET/CT **[C]** late arterial phased CBCT focused on the treated LPT. Several contours are also provided; yellow: liver; light green: LPT by activity thresholding; orange: LPT on CBCT; red: tumor on CBCT; green: thresh 20; and blue: thresh 30.*

Figure 5.8 illustrates the impact of the VOI definition on the volume of the TV and LPT, as well as the T/N ratio. Here, it can be observed that the volume of the LPT was somewhat similar for CBCT- and threshold-based methods, which suggests that the contrast-enhancement in the CBCT image nicely reflected the perfusion territory of the selected branch of HA. Not surprisingly, changing the threshold for tumor segmentation could change the measured volume of the tumor dramatically. Unlike the tumor definition on [^{18}F]FDG-PET, in which the threshold level is documented in the literature, the threshold level for tumor segmentation on [^{99m}Tc]Tc-MAA-SPECT and ^{90}Y-PET images are not standardized. So, the methodology of thresholding is most of the time selected individually for each patient by visual inspection. The threshold-level selection is not an easy task and is user-dependent. For this patient, it has a large impact on the volume of the tumor and T/N ratio. This discrepancy could be considered as one of the causes of the deviation between dosimetry results obtained by different groups.

Prescribed activity by different methods

Tumor definition plays a crucial role in most of the activity planning methods (except the MIRD method). So, an inconsistency in the tumor segmentation could result in a different calculated activity. But the impact of the tumor segmentation could be different for various methods (see figure 5.10). In line with the patient-tailored prescription used in the therapy session, **(a)** for the MIRD method, a mean dose of 160 Gy to the entire LPT (TV and NTV) was set, **(b)** the criteria of 310 and 100 Gy for TV and NTV compartments within the LPT was projected for the PM.

Figure 5.10 suggests that (by design), the MIRD and PM prescribed more activity than the other methods. The influence of the tumor segmentation on empirical, BSA, and MIRD method was more limited compared to other methods. The impact of tumor segmentation was notable in the PM. For example, “thresh 20” suggested 23.7% more administration than “thresh 30”.

Impact of VOI definition on the DVH parameters for different injected activities

Figure 5.11 illustrates the effect of tumor segmentation on the dosimetric parameters for a range of 0 to 3 GBq of administered activity. Based on this figure, the mean absorbed dose to the NTV was less dependent on the segmentation method than the mean TV dose. As shown in figure 5.10, activity prescription based on the MIRD method was similar for all segmentation methods as it only depends on LPT segmentation method (CBCT versus activity thresholding method). Based on this graph, the mean TV and NTV dose within the treated LPT for CBCT-based, “thresh 20”, and “thresh 30” were (333, 277, and 343 Gy) and (82, 70, and 90 Gy), respectively.

A similar situation pertained for VT120 and VH60. For example, to achieve a VT120 of 80%, IA of 1.00, 1.27, and 0.88 GBq were needed by employing tumor VOI based on CBCT, "thresh 20", and "thresh 30", respectively.

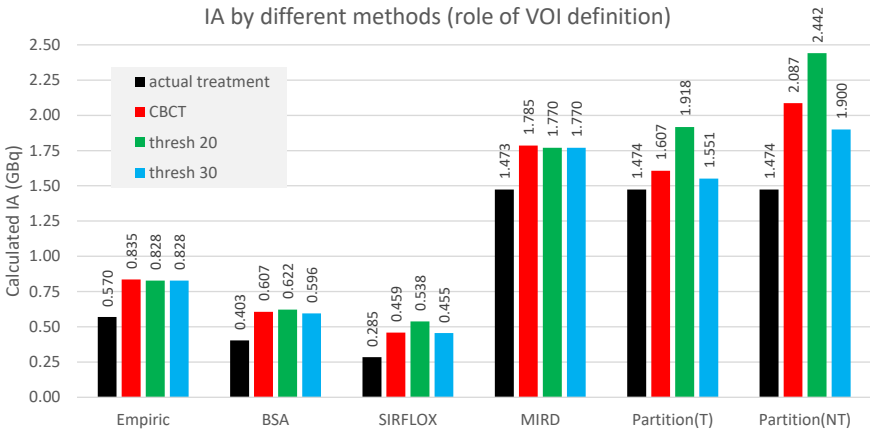

Figure 5.10: Calculated IA by employing different prescription methods using different VOI definitions.

Predicted versus measured dose

As figure 5.8 shows, the post-treatment TV dose measurement was higher than the estimated TV irradiation. Additionally, the cumulative DVH for the measured and predictive dosimetry using several segmentation methods for the actual administered activity (actual treatment) is provided in figure 5.12. The tumor cDVH (figure 5.12-A) shows that the curves were different for different tumor definition methods. The best agreement between the predictive and measured dosimetry was observed for CBCT-based tumor segmentation. A better alignment between the predicted and measured absorbed dose (compared to the TV compartment) was noted in the NTV compartment within the treated LPT (figure 5.12-B). Due to a small target volume and an abundant untouched NTV liver parenchyma, both predicted and measured doses in the entire liver NTV (figure 5.12-C) assert a safe treatment even for such a high administered activity; less than 30% of this compartment received more than 70 Gy.

Mean absorbed doses are also provided in figure 5.13. In line with the results presented in the previous chapter, a better correspondence between predicted and measured mean dose was perceived in the NTV compartment compared to the TV. For example, predicted TV dose was 31, 77, and 85 Gy less than measured mean dose when CBCT, "thresh 20" and "thresh 30" was applied. This figure also suggests that the mean dose to the different compartments was linked to the tumor definition.

Discussion

In this case the impact of segmentation method on dose calculation is explored. Unfortunately, no standard method for tumor and LPT segmentation is described in the literature; several authors, prefer activity thresholding method (*e.g.* on [^{99m}Tc]Tc-MAA-SPECT or ^{90}Y-PET). In a study, a considerable difference between morphological and activity-based tumor segmentation in terms of volume and mean dose were observed [308]. Also, for some patients a high inter-observer variation was reported, when activity-thresholding is used for tumor segmentation [309].

In this case, we compared predictive dosimetry and calculated injected activity by different methods, using CBCT and activity thresholding (by two different activity thresholds) for tumor and LPT definition. We found that SIRFLOX and partition model are highly dependent on delineation method, while empiric, BSA, and MIRD method were consistent between different segmentation methods.

Also, voxel-level dosimetry shows a high variation for both TV and NTV DVH parameters when different segmentation methods are applied. Mean absorbed dose to NTV were more consistent compared to the TV compartment.

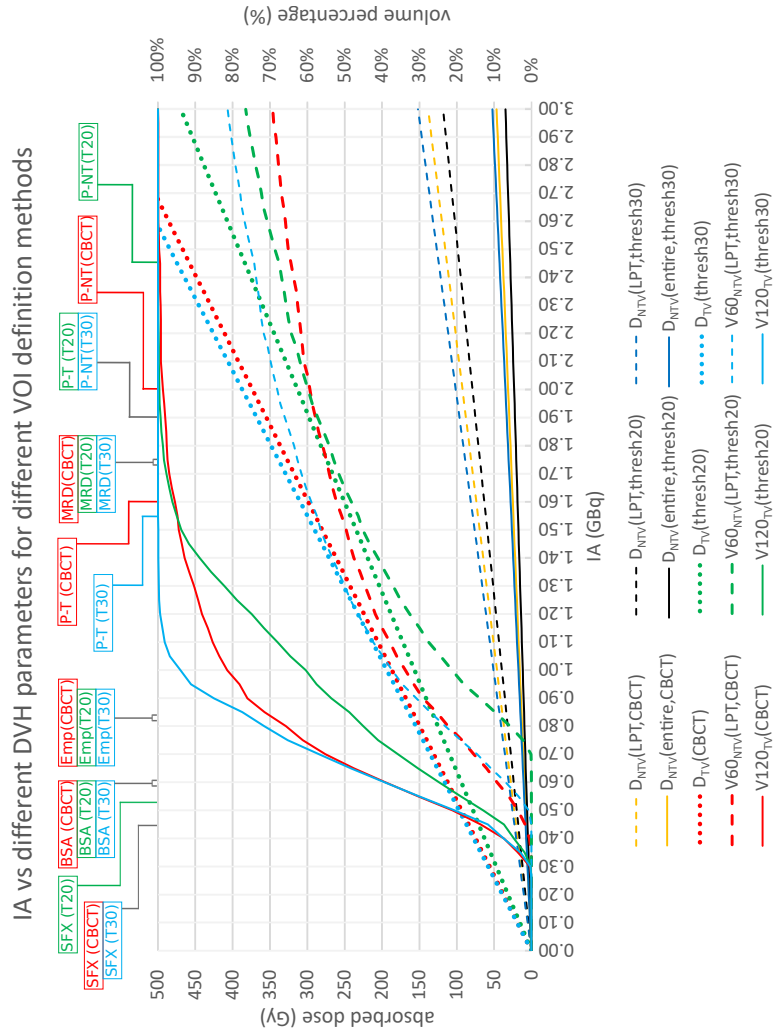

Figure 5.11: Dose parameters ($V120_{TV}$, $V60_{NTV}$, and mean dose to the TV and NTV) as a function of IA for different VOI defining methods. As can be seen, TV dose parameters were highly dependent on the segmentation method. Calculated IAs based on Emp, BSA, SFX, MRD, P-T, and P-NT denote empirical, BSA, SIRFLOX, MIRD, and PM for TV and NTV dose, respectively. For VOI definition methods, CBCT is CBCT-based VOI segmentation, and T20 and T30 are thresholding the tumor by 20 and 30% of the maximum activity uptake.

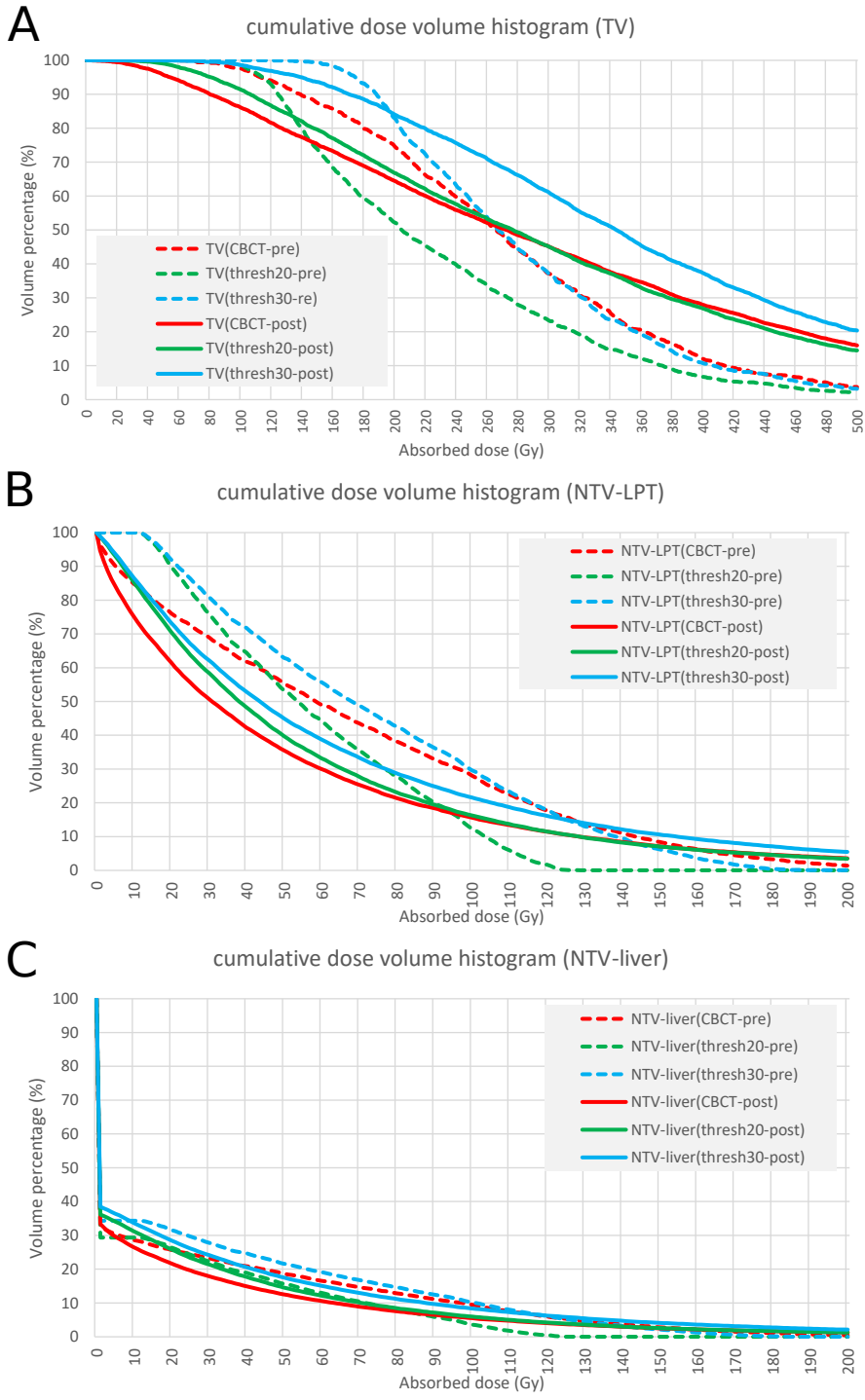

*Figure 5.12: Comparing predicted and measured cumulative DVH using different segmentation methods: **[A]** TV cDVH, **[B]** cDVH of NTV compartments within the LPT, and **[C]** cDVH for entire liver non-liver tissue.*

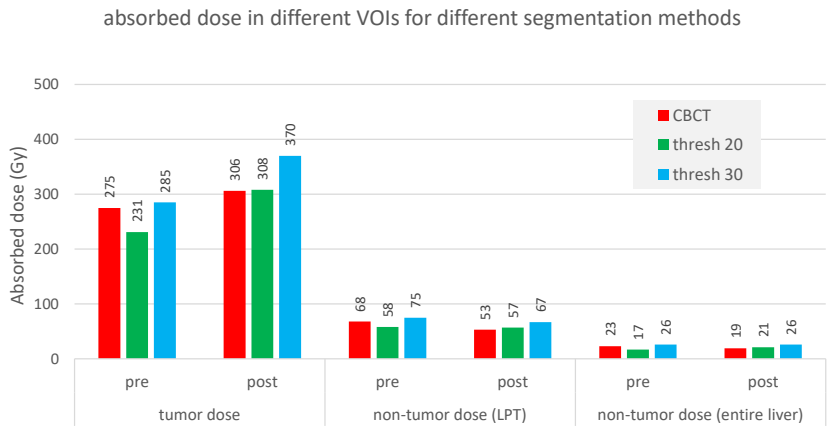

Figure 5.13: Predicted and measured mean absorbed dose to the TV and NTV compartment.

5.2.4 Case 4: Use of voxel-level treatment planning in combination with [^{99m}Tc]Tc-mebrofenin scan

A 49 year old patient with multifocal HCC who was earlier treated with Sorafenib was referred to University Hospitals Leuven (UZ Leuven). An MR imaging was performed two months later and showed a stable tumor (diameters: lateral 15.7 cm, anterior-posterior 12.3 cm, and craniocaudal 16.2 cm) located in segments VIII, V, and IV. Compared to a recent CT examination, the largest tumor was comparable in size, but necrotic and hemorrhagic components had developed within the tumor. The tumor also showed a peripheral arterial hypercaptation.

Hepatomegaly was observed (craniocaudal dimension, 21 cm) with no sign of cirrhosis. A reduction in serum α-fetoprotein (AFP) level showed biochemical response. The MDT discussed the usefulness of SIRT with a main aim of targeting the tumor in the right lobe.

A pre-SIRT workup was performed two months after MR study. Selective catheterizations of the right and left HA were conducted with diagnostic angiography and CBCT. Also, [^{99m}Tc]Tc-MAA was administered in the selected branches of the HA (68 MBq right and 58 MBq left). An eLSF of 5% was determined on the planar image. Based on [^{99m}Tc]Tc-MAA-SPECT, there was no evidence of activity uptake in the extra-hepatic sites. No contraindications were retained and the patient was qualified for SIRT.

Two weeks after pre-SIRT workup, a [^{99m}Tc]Tc-mebrofenin (BrIDA) scan was performed to determine liver functionality [310]. In this study, 150 MBq of ^{99m}Tc-BrIDA was injected intravenously, followed by a dynamic acquisition according to [305]. The SPECT/CT image showed a large photopenic area centrally in the right liver lobe, compatible with an afunctional HCC. A higher functionality was captured in the left liver lobe compared to the non-tumoral right-sided areas. The liver clearance was 12.4% per minute; 11.7% per minute per 1.73 m^2 (patient's body surface area=1.84 m^2).

Two days later, an [^{18}F]FDG-PET/CT scan was performed. The [^{18}F]FDG-PET scan showed a mild uptake (mainly right-sided); the ceCT confirmed prominent central necrosis and several other hypodense liver tumors spread over the liver.

Due to the challenging situation of the patient, we opted for voxel-level dosimetry as the treatment planning method, for the first time in our center. A volumetric assessment showed that the (mostly tumoral) right lobe was larger than the left lobe. The [^{99m}Tc]Tc-mebrofenin scan showed that the NTV on the right side had lower functionality than the smaller left lobe. So, the treatment planning was designed in a conservative setting for the left lobe and a more aggressive setting for the right lobe. In treatment planning, the

voxel-level correspondence of the predicted absorbed dose and the [^{99m}Tc]Tc-mebrofenin scan was also considered.

The SIRT treatment was performed one month after pre-SIRT workup with selective catheterizations of the right and left HA. Visual assessment of the post-treatment ^{90}Y-PET/CT image showed heterogeneous uptake within the liver with a good alignment with the distribution of the [^{99m}Tc]Tc-MAA on the pre-treatment scan and with good tumor targeting (see figure 5.14).

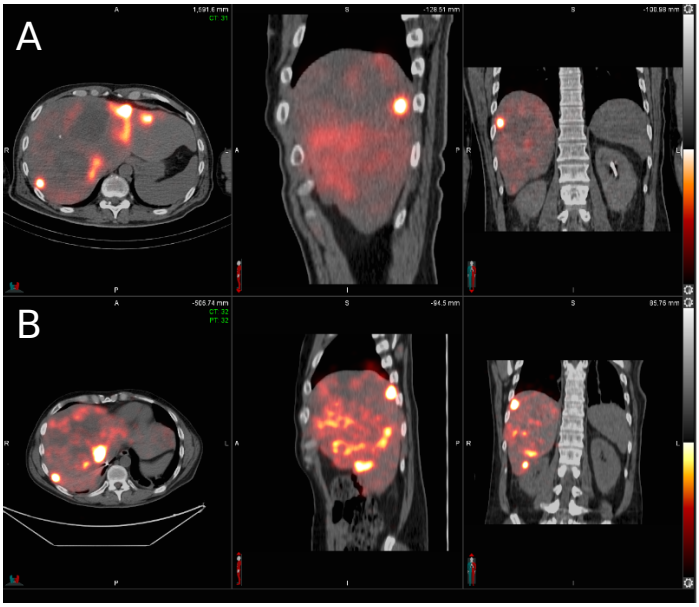

*Figure 5.14: A transaxial, sagittal and coronal view of fusion **[A]** [^{99m}Tc]Tc-MAA-SPECT/CT, and **[B]** post-treatment ^{90}Y-PET/CT.*

VOI segmentation method and activity reports

After registering all images to an identical space, some VOIs were segmented to aid in the activity planning and dose prediction:

- **liver:** the liver was segmented using the CT from the [^{99m}Tc]Tc-MAA study by employing the CNN.
- **tumors:** one big tumor was defined on diagnostic MR (mDixon-arterial), by keeping an eye on the [^{99m}Tc]Tc-MAA-SPECT-CT and BrIDA-SPECT/CT.
  Three more tumors were located on the MR but segmented on [^{99m}Tc]Tc-MAA-SPECT-CT (thresholding by 50% of the maximum uptake).
- **necrosis:** the necrotic portion of the big tumor was segmented out using the CT image from the [^{18}F]FDG study; the necrotic area was photopenic on PET and hypodense on CT.
- **left and right LPT:** two LPTs were separated on the late arterial phase CBCTs.

Table 5.4 provides the volume of the necrosis, viable TV, and NTV in the right and left LPTs. This table indicates that the right LPT represented approximately two-third of this enlarged liver (3699 ml). Around one-third of the left LPT was defined as a viable tumor. In contrast, in the right lobe, both viable tumor and necrosis had a more considerable contribution to the lobe volume (around half and one-third, respectively).

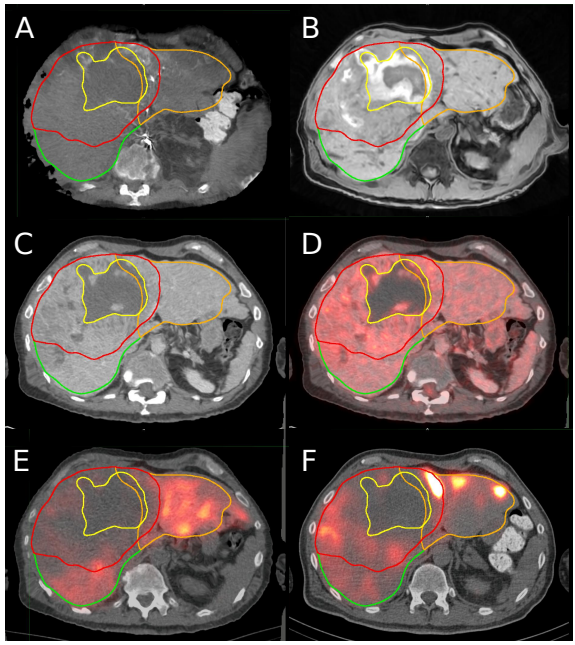

*Figure 5.15: A transverse slice of different studies; red, yellow, orange, and green contours outline the tumor, necrosis, and left and right lobe. **[A]** early arterial phase arterial CBCT for the left HA, **[B]** mDixon sequence from diagnostic abdomen MR imaging, **[C]** and **[D]** CT and fusion image from [^{18}F]FDG-PET/CT study, **[E]** BrIDA-SPECT/CT scan, **[F]** pre-treatment [^{99m}Tc]Tc-MAA-SPECT/CT.*

parameter	left lobe	right lobe	entire liver
viable TV (ml)	408	1116	1524
necrosis volume (ml)	68	508	577
NTV (ml)	838	760	1599
entire VOI volume (ml)	1314	2385	3699
tumoral involvement (%)	31	47	41
Lobe to entire liver (%)	35.5	64.5	

Table 5.4: Segmentation report

Treatment simulation using the [^{99m}Tc]Tc-MAA-SPECT (see table 5.5) confirmed that the estimated activity deposition within the defined necrotic region was negligible. The T/N ratio in both left and right lobes (1.44 and 1.14, respectively) suggest that the mean dose to the TV would be slightly higher than the mean dose to the NTV. So, without considering the heterogeneity of the dose distribution, the treatment may not be considered promising from the perspective of the mean dose, particularly for the right lobe. On the other hand, the [^{99m}Tc]Tc-mebrofenin study (see table 5.6) suggests that only 31.5% of the total liver functionality was located in the larger LPT (right lobe), which encouraged us to go for a more aggressive treatment strategy in that lobe. Conversely, this also validated our conservative approach for the left lobe, as this LPT is the compartment which hosts the vast majority (68.5%) of the liver functionality. This table also verified the necrosis delineation; the counts in the necrotic area on the [^{99m}Tc]Tc-mebrofenin scan were negligible in both lobes (0.07 and 7% of the NTV counts for the left and right liver lobe, respectively).

parameter	left lobe	right lobe	entire liver
viable TV (counts/ml)	658.4	333.3	420.3
necrosis (counts/ml)	74.4	77.8	77.4
NTV (counts/ml)	457.7	292.4	379.1
entire VOI (counts/ml)	500.1	265.8	349.0
T/N ratio	1.44	1.14	1.11

Table 5.5: [^{99m}Tc]Tc-MAA activity report

parameter	left lobe	right lobe	entire liver
viable TV (counts/1e+6)	92	184	275
necrosis (counts/1e+6)	5	29	33
NTV (counts/1e+6)	611	281	892
entire VOI (counts/1e+6)	708	494	1201
normal lobe activity to entire liver normal activity (%)	68.5	31.5	

Table 5.6: BrIDA-SPECT activity report

Dosimetry and normal tissue complication model

Predictive dosimetry was performed by employing the local deposition model, and the defined VOIs described in the previous sub-section.

For modelling the complication of the normal liver in each lobe and entire liver, the NTCP curves from studies by Walrand *et al.* and Strigari *et al.* [74, 75] were utilized. In these studies, the NTCP was modeled as:

$$\mathrm{NTCP(t)} = \varphi(t) = \frac{1}{\sqrt{2\pi}} \int_{-\infty}^{t} e^{-\frac{s^2}{2}} ds, \tag{5.1}$$

where, $\varphi(t)$ denotes the standard normal cumulative distribution function, and t(D[Gy]) is defined as:

$$\mathrm{t(D[Gy])} = \frac{D - \mathrm{TD}_{50}}{m \times \mathrm{TD}_{50}}, \tag{5.2}$$

where, D is the total liver absorbed dose, m is the slope of NTCP versus absorbed dose and TD_{50} is the dose for which 50% complication probability is assumed. here, m=0.28, and TD_{50} = 52 Gy are used [75].

This model obtains a correlation between the NTV mean dose and complication for **a patient population**. So, it could be questioned when using this model for a patient-tailored treatment optimization. Also, this model correlates the liver complication probability and the mean dose of the normal liver parenchyma within the **entire liver**. Thus, exploring a voxel-level interpretation of this model is not confirmed. Regardless of these limitations, here, the NTCP curve for the absorbed dose in each voxel of the normal tissue compartment was applied to have an estimation of the effect of the administered activity on the normal liver functionality and liver clearance:

$$\text{remaining liver function}_{\text{new}} = \frac{\sum_{i \in \mathrm{NTV}} \left[\mathrm{BrIda}_i \times (1 - \mathrm{NTCP}(t(D_i)))\right]}{\sum_{i \in \mathrm{NTV}} \mathrm{BrIda}_i}, \tag{5.3}$$

where, i denotes the voxels within NTV, BrIda_i is the counts of the voxel i in the BrIDA-SPECT image [311], and D_i is the predicted dose of the voxel i.

Then, an estimated clearance ($\text{clearance}_{\text{estimated}}$) is defined using remaining liver $\text{function}_{\text{new}}$ and baseline clearance ($\text{clearance}_{\text{baseline}}$):

$$\text{clearance}_{\text{estimated}} = \text{remaining liver function}_{\text{new}} \times \text{clearance}_{\text{baseline}} \tag{5.4}$$

Activity planning method

Left lobe prescription As discussed, a cautious and conservative strategy was applied to the left lobe. In this setting, an IA was calculated, which corresponded to a fairly low estimated NTV irradiation. This approach was used because the [^{99m}Tc]Tc-mebrofenin scan suggested a very high functionality in this LPT (around two-third of the total liver), while the volume of this LPT was around one-third of the liver. As shown in figure 5.16-A, the IA in the left lobe was calculated from voxel-level dosimetry and projecting the mean dose to the NTV in this lobe (with considering the TV dose, $V40_{NTV}$, remaining liver function, and TV dose). Dosimetric details of this activity planning were:

- left lobe IA = 1.2 GBq;
- mean absorbed dose to the left NTV = 40 Gy;
- $V40_{NTV}$=30%;
- remaining liver function of the lobe = 80%;
- NTCP of the lobe = 21%;
- mean absorbed dose to the TV in the left lobe = 58 Gy;
- $V60_{TV}$ =33%

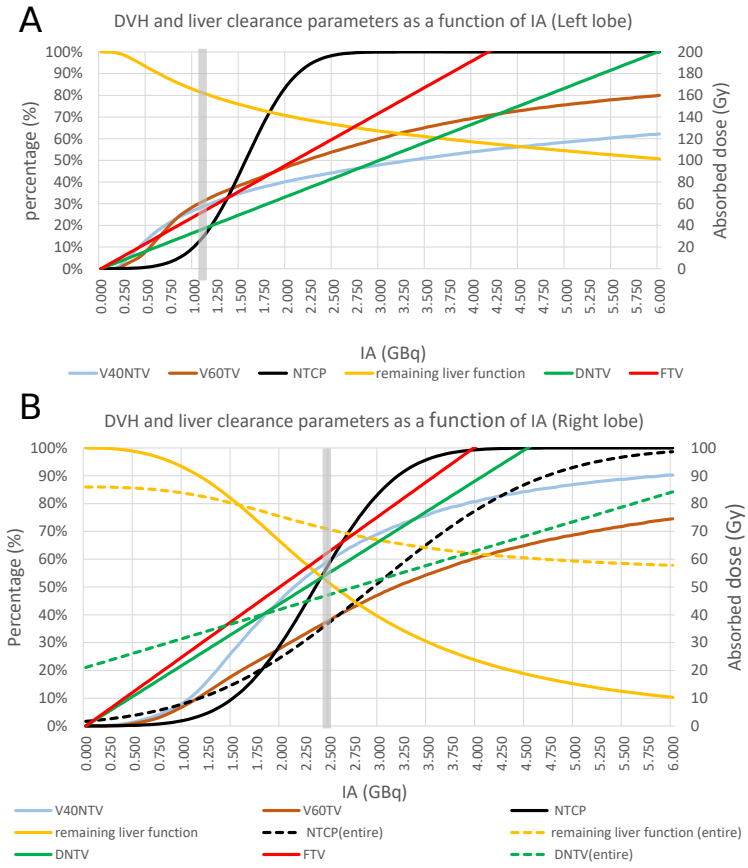

*Figure 5.16: Dose parameters ($V60_{TV}$, $V40_{NTV}$, and mean dose to the TV and NTV) and liver function parameters (NTCP and remaining liver function) as a function of IA for **[A]** left lobe **[B]** right lobe and entire liver. The thick grey line represents the actual prescribed activity in the treatment session.*

Right lobe prescription Then, for the right lobe, a more aggressive treatment planning was used due to its high tumor involvement and lower T/N ratio compared to the collateral lobe (left lobe). So, the IA of the right lobe was calculated by considering TV and NTV absorbed dose, NTCP and estimated new liver clearance of the entire liver as a function of both IA in this lobe and the fixed prescribed IA for the left lobe (1.2 GBq) which has been calculated in the previous step (see figure 5.16-B). The selected IA and the estimated dose parameters were:

- right lobe IA = 2.5 GBq;
- NTCP of the right lobe = 60%;
- mean dose to the right lobe NTV= 55 Gy;
- $V50_{NTV}$ of the right lobe = 45%;
- mean dose to the entire liver NTV = 47 Gy;
- NTCP of the entire liver= 38%;
- remaining function of the entire liver = 70%

parameter	left lobe	right lobe	entire liver
IA (GBq)	1.2	2.5	3.7
T/N ratio	1.438	1.140	1.109
TV mean dose (Gy)	58	63	62
NTV mean dose (Gy)	40	55	47
non-necrosis mean dose (Gy)	46	60	54
$V30_{NTV}$ (%)	36	74	54
$V40_{NTV}$ (%)	30	60	44
$V50_{NTV}$ (%)	26	46	35
$V60_{NTV}$ (%)	23	33	28
$D25_{NTV}$ (Gy)	53	68	64
$D50_{NTV}$ (Gy)	14	47	34
$D75_{NTV}$ (Gy)	4	29	10
$V50_{TV}$ (%)	38	47	45
$V70_{TV}$ (%)	30	31	31
$V90_{TV}$ (%)	23	22	22
$V120_{TV}$(%)	13	12	13
$D25_{TV}$ (Gy)	83	81	81
$D50_{TV}$ (Gy)	32	47	21
NTCP (%)	21	59	38
baseline LPT functional percentage (%)	68.5	31.5	-
remaining function (%)	80	51	71
remaining clearance (%/min)	8.8		
remaining clearance (%/min/1.73 m^2)	7.3		

Table 5.7: Overview of the predictive dosimetry

Dose report for the prescribed activity

Here, cumulative DVHs for the left and right LPT, and the entire liver are presented in figure 5.17. Also, the dosimetry is detailed in table 5.7. The mean TV dose was around 60 Gy, but approximately one-third of the TV received more than 70 Gy for both lobes; about 20% of the TV received more than 80 Gy. Hence, the estimated TV dose coverage was acceptable but not optimal.

For the normal liver parenchyma, the mean dose for the left and right lobe and entire liver were 40, 55, and 47 Gy, respectively. Only 28% of the NTV in the entire liver

received more than 60 Gy. Our model suggested that after the treatment, 71% of the liver function would be preserved (liver clearance, 8.8 % per minute or 8.3 % per minute per 1.73 m^2). So, the treatment was expected to be safe.

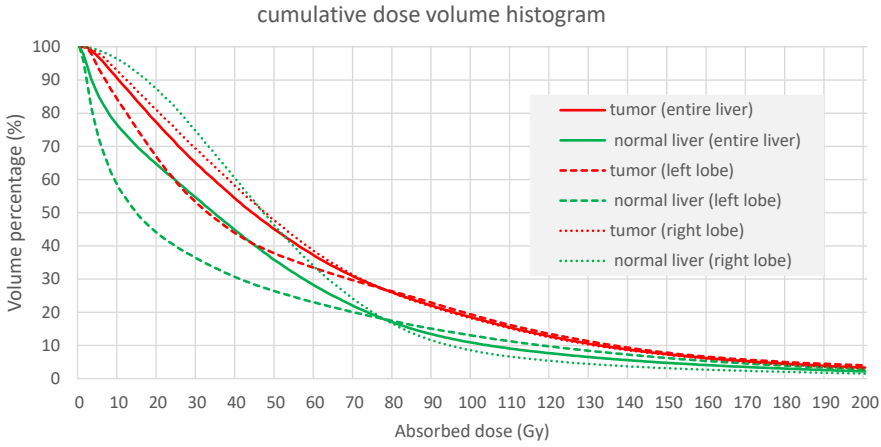

Figure 5.17: Cumulative DVH for the prescribed activity in the TV and NTV in the left and right lobe and entire liver.

Discussion

In SIRT liver, NTV mean absorbed dose is widely used for activity planning. However, in cases with small future liver remnant or patients with limited functional liver parenchyma, NTV (or total liver) absorbed dose may not be the most important factor. For example, in SIRFLOX trial [33], the prescriptions were made based on BSA method but IA was reduced for cases with tumor involvement more than 50%.

Recently, BrIDA-SPECT is discussed as an emerging tool in the assessment of hepatic function. In this case an activity prescription was made using voxel-level dosimetry when combining absorbed dose distribution and voxelized hepatic function. This is a preliminary study and more investigations should be done to standardize the role of hepatobiliary imaging in voxel-level dosimetry based activity planning. In particular, a voxel-level NTCP model relating dose to function reduction could be developed, which would allow to correlate injected activity not only to dose, but to residual function after treatment.

5.3 General conclusion

Today, dosimetry is considered essential in SIRT workflow. Simplified dosimetry using MIRD or partition model by employing only one study (*i.e.* [^{99m}Tc]Tc-MAA-SPECT/CT or ^{90}Y-PET/MR or PET/CT) for calculating both activity uptake and masses of different VOIs is the most used method. This approach is beneficial for most of the patients, but is too simplified for complex situations. In sophisticated circumstances, treatment planning is not straightforward and needs a careful consideration of a multitude of different elements.

Here, we present 4 cases for which a multi-modal image processing facilitated the use of more information from all available images (*e.g.* CBCT and BrIDA-SPECT) to create more detailed reports. These details helped the physician to prescribe an activity based on clinically-relevant information, maximizing both therapy efficacy and safety.

Chapter 6

Discussion, future perspectives, and general conclusion

A complex problem of image-based dosimetry to evaluate the safety and efficacy of intra-arterial SIRT for hepatic tumor management has been approached with by a number of novel designs and image processing procedures. It is not only beneficial for research, but also for clinical practice to assess tumor and non-tumor irradiation before and after treatment and to analyze the biodistribution of the radioactive microspheres within the patient's body. From this perspective, the usefulness of employing all available imaging modalities (especially CBCT) during the SIRT procedure was highlighted in this manuscript.

This chapter summarizes the main contributions of this dissertation and presents the promising directions for future work.

6.1 General summary and discussion

6.1.1 Implementation of dosimetry in SIRT

In SIRT for liver tumors, the estimation of energy deposition (in terms of personalized dosimetry) is crucial at two moments: **(i)** after [^{99m}Tc]Tc-MAA-based therapy simulation and before making the prescription for treatment planning, and **(ii)** after treatment, to verify the delivered and absorbed dose. This is actually what happens in routine radiotherapy (RT), everyday. This approach is somewhat new to nuclear medicine (NM), but it is the level of "radiotherapy" (actually radionuclide therapy or RNT) we need to pursue and implement. However, the absorbed dose prediction and calculation depend upon:

1. **activity distribution:** which is itself associated with the microspheres' characteristics, administration, vessel anatomy, and blood flow. Activity distributions can be measured using quantitative functional imaging. Unlike in many other radionuclide treatments, in SIRT, a single activity imaging is adequate to determine the cumulative activity, as the microspheres lodge into the tissue microvasculature (lesions or normal liver parenchyma) and there is no washout or other pharmacokinetics, except for physical decay.
2. **energy deposition pattern:** which is the amount of energy deposited per unit of mass within a given target organ (or tissue or voxel) for a disintegration occurring in a given source organ (or tissue or voxel). Because of the features of the radionuclides used in SIRT, by using reasonable assumptions, this step could be simplified as a conversion factor. This step could be performed in voxel-level (*e.g.* by employing local energy deposition method) or organ-level (so-called MIRD model) [242].

3. **VOI definition:** which declares the level of dosimetry; liver segmentation is required for all dosimetry methods. For sub-organ level dosimetry, more specific volumes are needed. For example, a liver perfusion territory is necessary for the MIRD model, and tumor segmentation is needed for the partition method and voxel-level dosimetry. Distinguishing necrosis from viable tumor is also crucial when the tumor dose needs to be adequately reported.

Following this dosimetry chain, we focus on absorbed dose data production and reporting, aiming at methodology standardization, and introducing a flexible and reliable framework to report the absorbed dose in well-defined VOIs.

In various fields within medical physics, meticulous treatment planning is an intention to optimize existing treatment workflow and improve outcomes. This requires a broad knowledge of the processes involved in the treatment, as well as inter-patient differences. So, **chapter 1** provides general information about liver, liver cancer and its management, the SIRT concept, its current procedure and challenges, and an overview of the medical imaging techniques used in SIRT. This information is the basis of the other chapters.

6.1.2 Current status of SIRT in UZ Leuven

The first part of **chapter 2** reviews the experience with SIRT in UZ Leuven. Since 2004, more than 450 SIRT sessions were performed in UZ Leuven and this treatment is one of the main radionuclide treatments performed in our hospital. In UZ Leuven, the tendency is to practice advanced imaging and methodology to enhance treatment efficacy and safety. Two important reasons for starting this research project were:

- **usefulness of multi-modal image processing:** UZ Leuven is one of the pioneers in employing modern imaging techniques in SIRT; SPECT/CT is used since 2009 and CBCT is performed within pre-treatment work-up since 2013. ^{90}Y-TOF-PET is applied for treatment evaluation since 2017. Also, depending on the tumor type, MR, [^{18}F]FDG-PET/CT, [^{68}Ga]Ga-DOTA-TATE-PET/CT, and ceCT imaging are performed before and after treatment for tumor and liver assessment. Despite this excellence practice, in clinical workflow, these images were often analyzed independently or visually side-by-side without image registration.
- **dosimetry-based activity planning and treatment evaluation:** for activity prescription, the BSA used to be the most frequently employed method; however, we observed only a very weak correlation between body surface area of the patient and total liver volume (r^2=0.085). We also found that by using the BSA, one-quarter of the patients would receive a total liver absorbed dose of more than 58 Gy, which could be potentially toxic. After using it several years as a mere "starting point" for informative use only, this method has been entirely replaced by the MIRD and PM since 2018. In 2019, the PM was used for around three-quarters of the treatments. Without considering all (clinical) covariates (which could be a limitation), we observed a significantly better survival for patients treated with dosimetry methods in activity planning (*e.g.* partition model). Our findings are in line with other studies that showed a better outcome for dosimetric methods compared to non-dosimetric methods for treating ICC with resin microsphere [29] (multi-center study including UZ Leuven data), HCC with glass [126] and resin microsphere [122].

The potential discrepancy between SIRT simulation using [^{99m}Tc]Tc-MAA particles and actual therapeutic microsphere distribution is one of the concerns in this treatment modality. Several possible reasons for this mismatch have been discussed in the literature (*e.g.* catheter tip positioning, number of administered particles, difference in particle density, flow effect, etc). Generally, the number of microspheres is lower in the [^{99m}Tc]Tc-MAA session. We compensated for the residual activity in [^{99m}Tc]Tc-MAA simulation to ensure that the administered activity agrees with the recommendations [158]. We found that the residual activity in the syringes was not negligible, which could result in even

more imbalance in the number of administered particles. To follow guidelines (administering 50, 100, and 150 MBq for the left, right, and entire liver coverage, respectively), an additional amount of 19, 21, and 25 MBq was added to the standard prescribed activity to compensate for the residual activity in the syringes.

In the MIRD method, an optimized absorbed dose to the entire liver is the defining feature. We investigated this in **chapter 2**, where we found a better survival for patients who received a total liver dose of between 40 and 50 Gy (11.9 months), compared to the patients who received less than 40 Gy (6.5 months, p-value=0.001) and more than 50 Gy (9.1, p-value=0.048). In this initial report, we focus on outlining the impact of total liver absorbed dose on patient outcome but in the current setting, several biases may also arise from clinical covariants. Clearly, the effect of tumor and NTV absorbed dose on patients outcome cannot be addressed in the current study and would need further research to pursue new answers and research directions (by including follow-up images).

Currently, ^{90}Y-PET is used in our center to measure the activity distribution. These images are not used as absolute quantitative images and a patient-specific calibration is applied. We examined the precision of the ^{90}Y-PET imaging in 49 patients, a vial, and a phantom study. The ratio between the total recovered activity in the phantom and vial to the calibrated activity was 0.79 and 1.11 on our PET/MR camera. For the patients imaged on our PET/CT camera (n=10) and PET/MR (n=39), the ratio between the total activity in the reconstructed PET and calibrated activity has a median (first and third interquartile range) of 1.31 ([1.25,1.45]), and 0.95 ([0.86,1.01]), respectively. So, our PET/CT camera regularly measures a significantly higher activity than what has been calibrated; obviously, this cannot be explained by any residual activity that was not injected to the patient. We hypothesize that this discrepancy is due to the difference in scatter correction; on the PET/CT, the so-called "dirty isotope" scatter correction is used which can account for uniform background radiation that is not covered by the scatter and randoms correction. On the other hand, for PET/CT, this feature was not available in the console software release and later not (yet) selected for ^{90}Y-PET imaging. A similar variation was reported by Kafrouni *et al.* [312]. They proposed delay in time of injection and equipment issues, especially systematic bias, as the possible sources of the imprecision.

6.1.3 Software configuration and main contributions of this study

The main contribution of this study was to improve and in particular, to personalize the dosimetry reporting by incorporating relevant imaging information (*e.g.* anatomical and functional information about liver, tumor, necrosis, liver perfusion territory or any other possible details like liver functionality in the future). In this context, a multi-modal image analysis could potentially improve the decision making and treatment planning. Because image segmentation and registration are very challenging, the current standard method in clinical practice is based on approximations, for example:

- patients are described by anthropomorphic models (BSA method), or the tumor and non-tumor volumes are not taken into account and absorbed dose is reported as the mean dose to the entire liver/liver perfusion territory (MIRD model), or sub-tissue heterogeneity of the absorbed dose is neglected (partition model).
- sometimes activity thresholding is utilized to separate tumor and non-tumor compartments. So, it is assumed that the [^{99m}Tc]Tc-MAA-particles or therapeutic ^{90}Y-microspheres are accumulated with **(i)** a higher concentration within the tumor than non-tumor hepatic parenchyma, and **(ii)** an adequate tumor coverage.

The dosimetric tools developed during this thesis are outlined in **chapter 2**. Our image registration workflow provided a rigorous and personalized definition of the selected VOIs; the dosimetric reports were based on the specific anatomical map created from different available images. Some new tools listed below have been added to the list of available tools:

- **image registration:** registering all pre- and post-treatment images to an identical reference space created an excellent opportunity for the treatment group to use all information from all studies which is not the case in the pre-existing clinical workflow.
- **automated liver segmentation:** the entire liver was segmented by a region-growing method, using both CT and [^{18}F]FDG-CT information. The result was comparable to manual liver segmentation on a single CT by an expert. The process was done semi-automatic with minimal user-interaction. Later, this method was replaced by an automatic liver segmentation using CNN and human verification.
- **CBCT-based VOI segmentation was implemented:** currently, in UZ Leuven, only about 3% of patients are treated with a single administration in the proper or common hepatic artery. The vast majority of the patients undergo selective or super-selective administration within a single, two, or more injection sites, most often in a single session. In these circumstances, the prescribed activity needs to be **(i)** divided proportionally to the volume of the LPTs (*e.g.* BSA or MIRD method), or **(ii)** calculated specifically for each LPT based on the distribution of the activity within the tumor and non-tumoral compartments (*e.g.* PM or voxel-level dosimetry).
  There are diverse methods for determining LPT volume like **(1)** simple anthropomorphic models that assume a ratio of 2:1 for the right to left lobe volume, **(2)** manual delineation on CT or MR using the patient's liver vascular map, which is a complicated task due to the variable vascular anatomy of the liver (for example, the origin of the middle hepatic artery which contributes to the segment IV blood flow varies between patients; it can originate from the left or right hepatic artery), and **(3)** artery-specific method by using perfusion territories on CBCT.
  We developed a flexible workflow that makes use of different imaging modalities for LPT definition. Including contrast-enhanced CBCT in SIRT routine is not only valuable in defining the target volume (described in **chapter 3**), but also to ensure sufficient tumor targeting in the hypervascular regions of the tumors (described in **chapter 4**).
- **multi-modal tumor segmentation was included:** thanks to registration techniques, the user has the freedom to delineate tumor, viable tumor, and necrosis on one or multiple preferred imaging modalities e.g. MR, ceCT, CBCT, [^{18}F]FDG-PET, [^{68}Ga]Ga-DOTA-TATE-PET, [^{99m}Tc]Tc-MAA-SPECT, and/or ^{90}Y-PET.
- **tumor VOI alignment:** we also investigated a dedicated tool to align the tumor VOIs to the pre- and post-treatment activity maps, when these VOIs were pre-defined on anatomical images (*e.g.* CBCT). This additional step is designed to improve lesion coincide after registration due to imperfection of combined (hybrid) imaging quality. This automatic and multi-step tool was designed to locally optimize the tumor location in a way that captures as much as possible activity in the tumor volume.

To accomplish the dosimetry task, we proposed a three-step strategy:

1. **preliminary dosimetry report:** to provide preliminary pre-treatment dose estimation for different IA scenarios. This report can be used for treatment planning.
2. **pre-treatment dosimetry report:** when the prescription is made, the pre-treatment dose estimation report is updated to include the dosimetry report (*e.g.* cDVHs) for the prescribed activity.
3. **post-treatment dosimetry report:** by aligning post-treatment ^{90}Y-PET image to the previously registered pre-treatment images, an absorbed dose calculation is reported and compared with the pre-treatment dose prediction by various tools (*e.g.* comparing cDVHs, so-called dose agreements in different dose bins, and γ-index).

This workflow was introduced in **chapter 2**. Also, one clinical example was provided in this chapter including the three steps given above.

6.1.4 Validation of the developed registration and segmentation algorithm

In **chapter 3**, the robustness and restrictions of the proposed image registration and VOI segmentation were investigated with respect to their effect on the estimated doses in general and on the CBCT-based LPT segmentations in particular. The pre-treatment [^{18}F]FDG-PET/CT, [^{99m}Tc]Tc-MAA-SPECT/CT and contrast-enhanced CBCT images were registered to an identical space using an initial rigid registration, followed by a non-rigid registration. An expert scored the registration using Likert scores by assessing the impact of registration errors on dosimetry. After aligning all images together:

1. total liver was segmented semi-automatically by using information from [^{18}F]FDG-PET/CT and SPECT/CT images;
2. different LPTs were determined on the CBCT images;
3. tumors were defined on [^{18}F]FDG-PET using adaptive thresholding, based on the SUV_{max} of the tumor and the SUV_{mean} of the surrounding background.

Then, the segmentations of liver and liver lobes were compared to the manual segmentations by an expert on a CT image. This chapter describes the following validation results:

- **registration scoring:** the results of image registration produced a satisfying alignment, the alignment errors were considered small and with limited impact on dosimetry. The expert Likert score regarding registration results was perfect or with little misalignment in 94% of the cases.
- **registration deformation and volume preservation:** because the liver is more or less homogeneous in the non-contrast-enhanced CT (*i.e.* from the [^{99m}Tc]Tc-MAA study), we hypothesized that the deformation inside the liver was more driven by the liver boundary registration than by correct alignment of inner liver features. So, in the non-rigid registration process, we maximized the rigidity inside the liver, to mimic the true liver deformation better. A Jacobian determinant was applied to compute the local volume change due to the deformable registration. Small volume change was noted in central liver voxels and more significant volume changes (either contraction or dilation) were observed near the liver's border, as intended.
- **validation of liver segmentation:** our liver segmentation results (using our in-house multi-modal region growing algorithm) were compared to the manual liver segmentation by an expert. A dice score of 0.92 was recorded, which was comparable to other published liver segmentation algorithms [251]. The mean ratio of the segmentation volume to the reference volume was 1.03, proving that our algorithm is reliable in terms of liver volumetry. Furthermore, an average Hausdorff distance of 3.04 mm was achieved, which confirmed that liver boundaries between our segmentation and manual segmentation were very close (around three voxels average distance).
- **LPT segmentation:** a more substantial discrepancy was observed between CT and CBCT-based LPT segmentation; an average Hausdorff distance of 14.18 mm was obtained. These variations were present because the liver perfusion territories are not well aligned with the anatomical lobes (*e.g.* tumors in segment IV may receive their blood from the left or right HA or both).
  If a clinically important VOI, such as a tumor or a normal tissue region with high uptake, is located close to the boundary of the LPT, then the accuracy of the LPT segmentation may have a large impact on the dosimetry. That is because assigning such a VOI to the wrong LPT may produce large errors on the dose estimates for that VOI. This is not true only for voxel-level dosimetry; by employing CBCT- and CT-based LPT definition in MIRD method, an average dose difference up to 9 and 21 Gy was observed for the left and right liver lobe, respectively.

In general, we concluded that the registration error was moderate compared to other sources of error in SIRT dosimetry, which motivated us to apply our proposed workflow

to assess the contribution of personalized dosimetry compared to standard dosimetry. In regions with a mismatch between [^{18}F]FDG-PET and [^{99m}Tc]Tc-MAA-SPECT, we recommended looking precisely into registration deformation to avoid underestimation of tumor dose/activity and overestimation of healthy tissue dose/activity.

Additionally, our liver segmentation algorithm was concluded to be accurate enough to be used in clinical routine. Furthermore, we showed the feasibility of using CBCT for LPT identification, as advised by several studies to be used instead of CT [280, 313]. In this study, we described that LPT segmentation based on CBCT was relatively different from CT. In a letter to the editor by Rincon *et al.* triggered by our work, the contribution of new molecular and radiological imaging technologies like CBCT for a more accurate SIRT planning plan was highlighted [314]. They mentioned: *"Any health institution that has these technologies should take advantage of them for the benefit of the patient and the development of the technique."*

6.1.5 Implementation of multi-modal image processing in predictive dosimetry and dose verification

In **chapter 4**, CBCT was examined to assist quantitative assessment of predicted and measured absorbed doses. Although in most centers post-treatment dosimetry is not routinely performed, it may be desirable for: **(1)** prompt safety assessment to predict the liver toxicity risk, **(2)** early efficacy evaluation to consider possible additional complementary clinical efforts, *e.g.* treatment with other modality of under-dosed lesions, **(3)** gain insight into the TV and NTV dose-effect for SIRT.

This study included 31 patients (67 tumors) treated with resin microspheres. The voxel-level predicted and delivered absorbed dose was calculated from [^{99m}Tc]Tc-MAA-SPECT and ^{90}Y-TOF-PET images, respectively. Liver perfusion territories and tumors have been delineated on contrast-enhanced CBCT images. Our proposed registration algorithm was used to align CBCT to [^{99m}Tc]Tc-MAA-SPECT/CT and post-treatment ^{90}Y-PET/CT or ^{90}Y-PET/MR. Based on that alignment, the LPTs and TVs defined on the CBCT images were propagated to all pre- and post-treatment images.

Several DVH parameters, together with the mean dose of liver perfusion territories, non-tumoral and tumoral compartments, were evaluated. In this study, we report:

- **consistent liver and LPT volume:** for liver and LPT, the ratio of volumes propagated to the post- and pre-treatment imaging had a median (first and third interquartile range) of 1.01 ([0.99, 1.04] and 1.03 ([0.84, 1.35]), respectively.
- **comparable NTV absorbed dose:** a strong correlation between the predicted and measured mean dose for non-tumoral volume was observed (r=0.937). The predicted and measured absorbed dose difference was never beyond 11 Gy. Also, comparable DVH parameters (*e.g.* $V40_{NTV}$ and $D30_{NTV}$) were noticed.
- **moderate TV dose correlation:** the correlation between measured and predicted mean dose to the tumor was moderate (r=0.623), with a mean difference of -9.3 Gy. The ratio of measured and predicted tumor mean dose had a median of 1.01, but the first and third interquartile ranges of 0.58 and 1.59 revealed a poorer agreement between predicted and measured absorbed dose compared to NTV. The correlation of DVH parameters (*e.g.* $V100_{TV}$ and $D500_{TV}$) in this compartment was also weaker than for NTV, which showed an inconsistency between TV dose distribution between simulation and treatment.
- **predicted and measured doses associated with a fixed safety and efficiency thresholds:** our results implied that [^{99m}Tc]Tc-MAA-based dosimetry could predict under- or overdosing of the non-tumoral liver parenchyma for almost all cases, when applying 50 Gy as the safety threshold. For more than two-thirds of the tumors, by using 70 Gy as the basis for tumor response, a predictive absorbed dose correctly indicated either good tumor dose coverage or under-dosing of the tumor.

– **comparing predicted and projected (planned) dose:** for patients with PM-based activity prescription based on so-called personalized projected or planned doses, an extra analysis was performed to investigate whether our voxel-level predictive dosimetry was close to the partition model in clinical routine. Predictive and planned NTV and TV absorbed doses had a median (first and third interquartile range) relative difference of 6% ([-42, 21]%) and -3% ([-38, 25]%). As these results were obtained using the same IA and image ([^{99m}Tc]Tc-MAA-SPECT for predicted dose and ^{90}Y-PET for post-treatment dosimetry), any difference in absorbed doses to the TV and NTV solely reflects the influence of different practiced VOI definition technique, *i.e.* activity thresholding in PM and anatomical (on CBCT) tumor segmentation in voxel-level dosimetry. So, it shows that VOI segmentation may dramatically alter both TV and NTV doses.

In this study, we demonstrated the value of CBCT imaging in tumor detection and LPT segmentation. Recently, O'Connor *et al.* published the feasibility of adopting CBCT as a reliable alternative to MR imaging [52]. They affirmed the advantage of employing this modality in planning as it presents supplementary knowledge about tumor and tissue perfusion (which are not currently detectable by other imaging modalities) for dose computations.

Our results showed that the [^{99m}Tc]Tc-MAA-based dose estimate is a good predictor of the non-tumor tissue irradiation. This is of particular importance if the treatment aim is to administer the maximum dose that can be tolerated by the non-tumoral liver parenchyma. In contrast, [^{99m}Tc]Tc-MAA-SPECT was found to be a poorer predictor of the tumor irradiation, which perhaps reflects a better overall similarity in larger volumes than smaller regions. In recent investigations, when comparing [^{99m}Tc]Tc-MAA-SPECT and ^{90}Y-PET, similar results were obtained by defining tumors on ceCT for glass microspheres [294], ceCT or MR for glass microspheres [312], and 3-phase CT for both glass and resin microspheres [296]. Gnesin *et al.* noticed more solid tumor dose agreement (particularly for bulky tumors, *e.g.* bigger than 150 ml), when segmenting tumors manually or semi-automatically for both glass and resin microsphere [243].

Despite a possible discrepancy, when relating the TV and NTV predicted and measured absorbed doses to the fixed safety and efficiency dose levels, we concluded that [^{99m}Tc]Tc-MAA may be used for PM-based treatment planning in most of the cases. In addition, we found that for PM, the calculated absorbed doses depend heavily on the VOI segmentation technique.

6.1.6 Prospective implementation of the proposed software in clinical workflow and interesting cases

Ultimately, the internal dosimetry workflow investigated in this thesis was utilized prospectively (and was shared with the treatment team) to estimate patient-specific absorbed dose (30+ sessions) and post-treatment dose measurement (20+ sessions). Some patients required particular consideration in terms of dosimetry which was addressed by voxel-level dosimetry. **Chapter 5** presents some interesting examples of these cases: **(i)** considering intrahepatic dose distribution in treatment planning for a patient with substantial LSF, **(ii)** a case that confirmed the advantage of CBCT-based VOI definition in reporting a deviation between projected and measured absorbed dose, **(iii)** a case with increasing prescribed activity by practicing predictive dosimetry. Also, we discussed a preliminary report on the impact of tumor segmentation technique on dosimetry by comparing CBCT-based tumor delineation and [^{99m}Tc]Tc-MAA-SPECT tumor definition using different activity threshold levels, and **(iv)** introductory inclusion of the [^{99m}Tc]Tc-mebrofenin (BrIDA) SPECT scan (to investigate the liver function) in treatment planning. In this case, voxel-level dosimetry was used for the first time in our department as the primary method for prescribing.

Thus, our personalized dosimetry software has not only demonstrated its value as a research tool (by taking into account the detailed specific anatomy of the patient), it pro-

vided results that were of valuable input for the patient treatment planning. Therefore, in the near future, this imaging platform and dosimetric analysis suite may become a comprehensive tool capable of carefully executing each step of a personalized dosimetric approach to SIRT.

6.2 Limitations and opportunities of the developed software

Although the newly developed multi-modal image analysis software offers a great deal of promise, a few limitations need to be recognized, fully understood, and tackled in the future.

The software aimed to provide a comprehensive workflow for SIRT dosimetry. As detailed before, generating an absorbed dose distribution, as deposited energy per unit of mass, required activity distribution (provided by [^{99m}Tc]Tc-MAA-SPECT and ^{90}Y-PET for predictive and post-treatment dosimetry, respectively) in the numerator, and defined volumes (provided by other imaging modalities) in the denominator of the absorbed dose definition. For that, images representing the activity distribution ([^{99m}Tc]Tc-MAA-SPECT and ^{90}Y-PET) need to be quantitative and other images are solely employed to define clinically relevant VOIs:

- In our procedure, activity images are assumed to be relatively quantitative. Any uncertainty in capturing the activity distribution (*e.g.* partial volume effect) could directly affect the dosimetry accuracy. This is discussed in the first point in the future perspective in the following section.
- For VOI segmentation on different modalities and aligning them to the activity maps, different tools and a non-rigid registration routine were developed. It supports different image modalities that may be acquired on different cameras, with different protocols, and suffering from different levels of noises and artifacts. The variability of the image characteristics obtained from the different modalities could introduce inaccuracies of the new tools (*e.g.* misregistration of tumor VOIs, truncation of activity due to spill over, inclusion of extra-hepatic activity in liver VOI). This could affect the entire process as well as final reports, which is detailed below.

The CT component of the [^{99m}Tc]Tc-MAA study is used for liver delineation and as the reference for registration in the predictive dose assessment. In the clinical workflow, this image is principally acquired for attenuation correction of the SPECT component. Therefore, the CT tube current is lower than in a high dose diagnostic CT, and a contrast-agent is not administered. This might influence our liver segmentation based on either region-growing technique or CNN. As a result, in some cases, extensive manual corrections may be required. Besides, in most cases, no intrahepatic component is visible in this CT (*e.g.* vessels, malignancies, ...). So, there are virtually no intra-hepatic feature to guide liver non-rigid registration. This might affect the final alignment of the activity map and segmented intra-hepatic VOIs (*e.g.* tumors). This is discussed in more detail in the second point of the future perspectives.

CBCT images provide useful information about perfused liver volume and hypervascularity of the tumors. These images usually suffer from several types of artifacts (*e.g.* metal artifact, unreliable imaging timing regarding contrast administration, so-called ring artifact, etc) and have a narrow FOV (not even including the entire liver in most cases). So, both VOI segmentation and image registration for these images are challenging:

- Our experience suggests that CBCT to CT registration performance is poorer than registration for other modalities. To improve image registration, when necessary (*e.g.* visible misalignment), a tool is provided to define fiducial markers on both reference and floating images to guide the registration.
- LPT segmentation on CBCT is challenging when a low contrast signal or a dominant artifact is observed. We currently separate different LPTs, by defining separation lines in a set of selected slices and interpolating them to create a separation plane. So, accurate curvature of the LPT is not preserved.

Aligning MR images, either from stand-alone MR systems or from the MR component of a post-treatment PET/MR study, to CT from [^{99m}Tc]Tc-MAA study is also challenging. In chapter 4, our results suggest the feasibility of using our registration technique for MR to CT alignment. Further improvement (as described in the second point of the future perspective) would improve the robustness.

Finally, tumor segmentation on an "independent" imaging modality rather than on the microspheres activity maps is prone to introduce additional error (registration) in tumor dose assessment. Even a small misregistration between defined tumor (*e.g.* on [^{18}F]FDG-PET, CT, MR or CBCT) and the activity map (a hot spot in [^{99m}Tc]Tc-MAA-SPECT or ^{90}Y-PET) could have a devastating effect on tumor DVH. This could be considered as a factor in observing a more or less weak correlation between predictive and measured doses for tumors in chapter 4. This could be investigated by improving registration (see the second point in future perspective), using fiducial markers for tumors in registration, manually correcting the tumor VOI on activity maps after registration, or providing an additional tumor rigid registration step as is implemented in our workflow (see section 4.3.3.3).

6.3 Future perspective

Although we have extensively investigated the opportunities of using multi-modal image analysis for SIRT, which successfully answered several research questions, it must be admitted that our findings showed certain gaps, and further research is surely needed. Many interesting research topics can be identified, and a few of those are listed below:

1. **Dosimetry error estimation:** historically, one of the main barriers to image-based radionuclide dosimetry was the large error on the estimated absorbed doses. In this thesis, we have investigated to reduce the dosimetry error by developing a dedicated multi-model image processing chain. Now, the error contribution of each workflow step could be investigated and possibly improved: image registration and VOI segmentation (tumor, liver, and target volume) as specified in points 2 and 3, the predictive power of the employed surrogate which is discussed in points 4 and 5, activity measurement (respiratory motion during image acquisition [283], activity calibration and residual activity in the administration equipment, quantitative pre-treatment and post-treatment imaging [315] *e.g.* by addressing partial volume effect [316]), and converting the activity map to the dose distribution (local deposition model, dose-point kernels, and MC simulation [107]).
2. **Combined liver segmentation and image registration:** as declared earlier, image registration and VOI delineation are critical steps in dose reporting and these steps may introduce considerable uncertainties into the estimated absorbed doses. In our group, a new Ph.D. study is running dedicated to advancing image registration and VOI segmentation in SIRT by applying novel techniques, such as using CNN to improve liver segmentation on both (contrast-enhanced and non contrast-enhanced) CT [211] and MR images and joined liver segmentation/registration. Image segmentation and registration are related problems and therefore it is better to solve them together. By having an image with multiple complementary values per voxel (*i.e.* explicit definition of the liver boundaries for both floating and reference image), it should be possible to make a better segmentation. Moreover, defining any other relevant image feature inside the liver (*e.g.* tumors and other lesions) in reference and floating imaging modalities could be used to strengthen the registration algorithm to align voxels within the liver better.
3. **Improving tumor segmentation by separating viable and necrotic tissue:** one of the limitations of this thesis is the absence of large-scale study about the role of tumor segmentation on dosimetry. There is not a gold standard in this step. In **chapter 3**, [^{18}F]FDG-PET was used to segment the tumor. In **chapter 4**, CBCT was explored for segmenting hypervascular tumors. Also, in **chapter 5**, one example of the effect of [^{99m}Tc]Tc-MAA-SPECT thresholding was discussed. In many

dosimetry papers, this approach was preferred to segment the tumor. One problem with thresholding the [^{99m}Tc]Tc-MAA-SPECT (or ^{90}Y-PET) is that it assumes that MAA (or microsphere) uptake accurately identifies viable tumors, which may not be true. Defining tumor VOIs based on [^{99m}Tc]Tc-MAA (or ^{90}Y) uptake will hide problems in case of poor targeting.
However, variability in the thresholding methods resulted in potentially a large volume over- or underestimation, which can be considered as a cause of the wide variation between reported data for TV and NTV dose-response relationship [71]. In a study by Mikell *et al.* a considerable inconsistency between morphologically driven and semi-automated gradient-based tumor segmentations was observed (even for large tumors, *e.g.* larger than 200 ml) in terms of tumor volume, mean dose, and more pronounced in DVH parameters (*e.g.* $D70_{\mathrm{TV}}$, $D90_{\mathrm{TV}}$) [308]. They highlighted *"the need for standardizing segmentation methods for reporting of lesion dosimetry on post-therapy ^{90}Y-PET by the SIRT community."* Garin *et al.* proposed a hybrid method to detect tumors on anatomical imaging and delineate the viable tumors on [^{99m}Tc]Tc-MAA-SPECT. On the other hand, Ilhan et al. [317] reported a high variation of uptake within the different tumor entities [180]. A recent study described a fairly good inter-observer reproducibility of the evaluation of tumor irradiation, but they mentioned significant variations in some patients [309].
Thanks to our multi-modal image registration framework, comparing different tumor segmentation methods, *e.g.* anatomical (contrast-enhanced MR or ceCT),CBCT-based, functional ([^{18}F]FDG- or [^{68}Ga]Ga-DOTA-TATE-PET) and activity-based ([^{99m}Tc]Tc-MAA-SPECT or ^{90}Y-PET thresholding) on a large number of patients can be used to estimate the role of tumor segmentation in TV (and NTV) dosimetry.

4. **Catheter position:** in several studies, the difference in catheter position and catheterization very close to a major artery bifurcation were quantified as a primary cause of a mismatch between [^{99m}Tc]Tc-MAA and ^{90}Y-microsphere distribution [158, 312]. Sometimes this is even a deliberate result of the chosen treatment strategy, where a more restricted volume is treated than the one injected during simulation. Registration of 3D angiography images to 2D fluoroscopic images [318] and CT to 2D fluoroscopic images [319] have been proposed to improve catheterization guidance for intra-arterial treatments. A similar approach could be beneficial for early prediction of undesired activity deposition. By using this approach, we could **(a)** automatically recognize the mismatch between catheter tip position through the pre-treatment workup and treatment sessions by employing 2D/2D image-based registration between pre-treatment and treatment fluoroscopic images, and **(b)** a 2D/3D registration between 2D fluoroscopic images and CBCT (or ceCT) could be used to project the hepatic vasculature on intra-operative fluoroscopic images.
5. **Detailed comparison between predicted and measured doses using γ-index:** we implemented the γ-index method that was introduced by Ferreira et al. [216] to compare dose distributions obtained from [^{99m}Tc]Tc-MAA-SPECT and ^{90}Y-PET. In the γ-index, the agreement between two absorbed dose maps is computed using passing rate values by considering a distance agreement level (for small alignment errors) and a dose difference agreement level (for small dosimetry errors). The clinical case provided in **chapter 2** covers the results of γ-index. We believe that the γ-index is a promising metric for comparing predicted and measured absorbed doses but needs further investigations.
6. **Hepatobiliary imaging:** including hepatobiliary imaging (*e.g.* BrIDA scan), as one of the most reliable measures of absolute liver function and its regional distribution [320] can improve the evaluation of the NTV irradiation in both global and regional strategies. Willowson *et al.*, recently introduced a sigmoidal relationship between change in fractional functional involvement and NTV absorbed dose [310]. One example of registering BrIDA-SPECT/CT to the [^{99m}Tc]Tc-MAA-SPECT/CT was discussed in **chapter 5**. In the future, functional liver image-guided treatment planning and evaluation may be suitable for patients with limited liver function, such as patients with cirrhosis or previously heavily treated with chemotherapy [305], and the planning of radiation lobectomy [311]. Also, it can be

applied after treatment for early identification of potential REILD.

7. **Patient follow-up and exploring the dose-effect relationship**: finally, one of the major concerns that needs to be investigated in more detail is the relationship between absorbed dose and tumor response/liver toxicity (which are usually estimated by TCP/NTCP models) and implementing these models into treatment planning [75]. Although patient follow-up was not covered (and was not the purpose) in this work, this could be investigated in future work, as illustrated in figure 6.1. Follow-up information should support both SIRT radiobiological mechanisms and important dosimetric parameters (*e.g.* mean dose or DVH parameters) [76,200]. Once these parameters are known for each tumor type and microsphere type, they can be incorporated in the pre-treatment dosimetric model for activity planning and in treatment evaluation, to see if the tumor will be destroyed and healthy tissue spared as intended. Tumor response is hard to measure accurately and many classical response evaluation methods (based on tumor volume or size) are not adequate because metabolically non-active lesions (*e.g.* necrosis) could remain visible in anatomical images. Our workflow can be employed to extract functional or metabolic parameters such as contrast-enhancement on CT, diffusion-restriction on MR or FDG-avidity on PET to improve tumor response assessment.
8. **Overall survival analysis for different activity planning scenarios:** although a linkage between treatment planning methods and OS was identified from our meta-analysis in section 2.1.3, this finding needs more affirmations and exploration in the future to remove risk of bias due to other confounding factors as much as possible.
9. **Supporting different types of microsphere:** our current workflow was validated for resin microspheres. Most of the steps are generic and could be surely extended to glass microspheres. The most crucial difference between glass and resin microspheres is the difference in specific activity, which results in a different dose-response relationship.
   On the other hand, supporting the use of QuiremSpheres needs more adjustments in several perspectives: **(a)** This new device is labelled with holmium-166, which has a different decay scheme, energy deposition pattern, and dose rate and dose-response relationships [321]. **(b)** A new concept of "scout dose" instead of "surrogate particle" is proposed as an improvement in the QuiremSpheres design. Instead of [^{99m}Tc]Tc-MAA, a scout dose consists of a smaller number of the very same therapeutic microspheres (with lower specific activity) used to simulate the intrahepatic distribution during treatment and to indicate any extrahepatic activity deposition [322]. **(c)** The distribution of Quirem-microspheres can be quantified using a SPECT camera. In addition, because of the highly paramagnetic nature of holmium-166, MR-based activity measurement and dosimetry is also possible for this device [323].
10. **Interaction with other software and automation:** recently, SIRT dosimetry has grown as a hot topic in nuclear medicine. During this study, several commercial softwares (*e.g.* SurePlan™ by MIM software, PLANET Dose by DOSIsoft, Simplicit^{90}Y™ by Mirada for glass microspheres, Q-Suite™ for QuiremSpheres, and STRATOS Dosimetry Solution by Philips) were introduced. Currently, MIM software is used in our department for both research and in clinical routine. Our physicians prefer our research software for image registration, CNN-based liver segmentation, and dosimetry reporting. But MIM is favored for manual liver, tumor and LPT segmentation, and VOI editing. Fortunately, several tools have been developed in our group to import/export images and contours in DICOM format. This is practiced to exchange images and contours between our research software and MIM software. Our group is currently sketching a comprehensive semi-automatic workflow to merge MIM workflows and our software tools to facilitate the dosimetry steps based on user choice.
11. **A standard dosimetry workflow for different clinical scenarios:** our proposed workflow is generic and can be utilized for different tumor types and different conditions. However, every patient has unique characteristics and needs, which ne-

cessitate flexibility of the dosimetry workflow. In a next step, one should consider a flowchart and step-by-step dosimetry workflow instructions that concern tumor characteristics (tumor type, vascularity, visibility on different imaging modality, ...), liver status (*e.g.* cirrhosis), availability of different pre- and post-treatment image modalities (*e.g.* contrast-enhanced CT and MR), treatment aim (radiation segmentectomy or lobectomy, whole liver, lobar, and bi-lobar SIRT), limiting organ for projected absorbed dose (TV, NTV, and lung), etc.
More research and continuous prospective implementation of our workflow are needed to reach a consensus "standard operating procedure" for employing our proposed dosimetry tool. A side effect would be a better insight into the limitations of our software in different clinical scenarios.

6.4 Final conclusion

In this dissertation, we demonstrated the feasibility of using multi-modal image processing in SIRT dosimetry. We mainly focused on improving image processing methods for quantitative analysis of the images performed before and after SIRT. Such an advanced image processing pipeline is expected to improve the dosimetry of ^{90}Y-microsphere therapy and, thus, adequately predict the treatment outcome and can guide the requirement for adjuvant therapy. The proposed framework is generic and can be easily adapted and extended. Therefore, our workflow can become a fundamental tool for providing new insights into SIRT dosimetry.

6.5 A final comment

Concerning the validation and integration of the multi-modal image processing for SIRT dosimetry in the clinical workflow, some technical and conceptual dilemmas are yet to be solved. However, we are convinced that the number of cases in which this tool can aid the physician to tailor the therapy planning will continue to grow.

In addition, post-treatment dosimetry and evaluating the predictive value of [^{99m}Tc]Tc-MAA for each case could be beneficial to address "technical success" and "technique effectiveness", as proposed by Salem *et al.* [324]. This could be viewed as a learning curve for all stakeholders within the treatment/research team. Also, with further implementation of the dosimetry and follow-up image analysis, a better understanding of dose-response can be accomplished. To grasp this opportunity, a close collaboration between research and clinical practice becomes ever more crucial. Additionally, physicians and medical physicists should assess and process the clinical data side by side. Their different background and point of view are essential to consider the best approach for each patient to improve patient outcome. It was a pleasure to have been part of it as well.

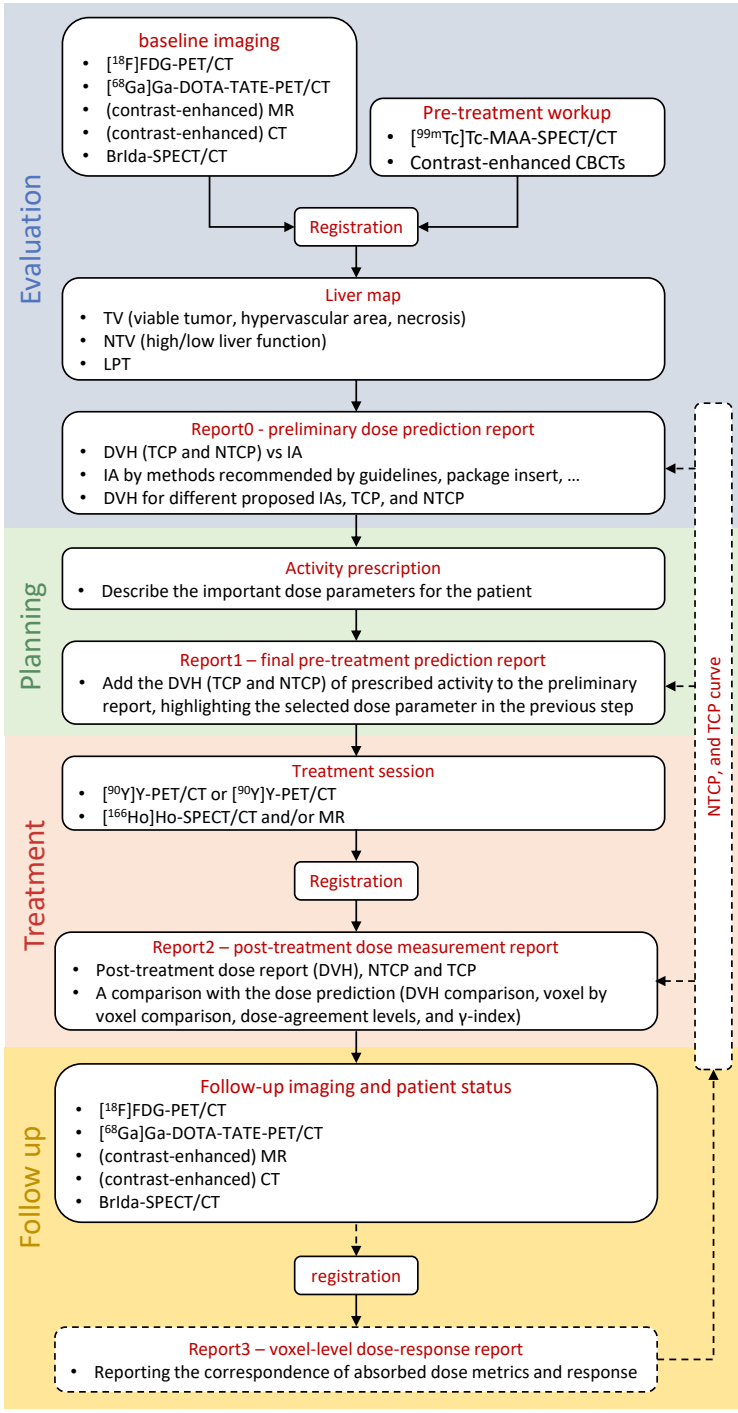

Figure 6.1: An overview of the design of the proposed dosimetry workflow for SIRT. The research questions are indicated in the boxes with the dashed boarders. This workflow is aligned with proposed procedure by several experts [293]

Bibliography

[1] Kaplan JB, Kalra A, Biggins SW. Liver Anatomy and Function. In: Radiation Therapy for Liver Tumors. Springer International Publishing; 2017. p. 3–11.

[2] Cross T, Palmer DH, editors. Liver Cancers. Springer International Publishing; 2019.

[3] Wessels BW, Konijnenberg MW, Dale RG, Breitz HB, Cremonesi M, Meredith RF, et al. MIRD Pamphlet No. 20: The Effect of Model Assumptions on Kidney Dosimetry and Response–Implications for Radionuclide Therapy. Journal of Nuclear Medicine. 2008 oct;49(11):1884–1899.

[4] Shoup M, Gonen M, D'Angelica M, Jarnagin WR, DeMatteo RP, Schwartz LH, et al. Volumetric Analysis Predicts Hepatic Dysfunction in Patients Undergoing Major Liver Resection. Journal of Gastrointestinal Surgery. 2003 apr;7(3):325–330.

[5] Couinaud C. Liver Anatomy: Portal (and Suprahepatic) or Biliary Segmentation. Digestive Surgery. 1999;16(6):459–467.

[6] Michels NA. Newer Anatomy of the Liver and Its Variant Blood Supply and Collateral Circulation. The American Journal of Surgery. 1966 sep;112(3):337–347.

[7] Kobayashi S, Otsubo T, Koizumi S, ichi Ariizumi S, Katagiri S, Watanabe T, et al. Anatomic Variations of Hepatic Artery and New Clinical Classification Based on Abdominal Angiographic Images of 1200 Cases. Hepato-gastroenterology. 2014;61(136):2345–2348.

[8] Bray F, Ferlay J, Soerjomataram I, Siegel RL, Torre LA, Jemal A. Global Cancer Statistics 2018: GLOBOCAN Estimates of Incidence and Mortality Worldwide for 36 Cancers in 185 Countries. CA: A Cancer Journal for Clinicians. 2018 sep;68(6):394–424.

[9] Guglielmi A, Ruzzenente A, Conci S, Valdegamberi A, Iacono C. How Much Remnant Is Enough in Liver Resection? Digestive Surgery. 2012;29(1):6–17.

[10] Sodergren MH, Sharma D. The Role of Liver Resection for the Treatment of Hepatocellular Carcinoma. In: Liver Cancers. Springer International Publishing; 2018. p. 83–97.

[11] Cardona K, Maithel SK, editors. Primary and Metastatic Liver Tumors. Springer International Publishing; 2018.

[12] Lo CM, Ngan H, Tso WK, Liu CL, Lam CM, Poon RTP, et al. Randomized Controlled Trial of Transarterial Lipiodol Chemoembolization for Unresectable Hepatocellular Carcinoma. Hepatology. 2002 may;35(5):1164–1171.

[13] Llovet JM, Real MI, Montaña X, Planas R, Coll S, Aponte J, et al. Arterial Embolisation or Chemoembolisation Versus Symptomatic Treatment in Patients with Unresectable Hepatocellular Carcinoma: A Randomised Controlled Ttrial. The Lancet. 2002 may;359(9319):1734–1739.

[14] Lee SY, , Ou HY, Yu CY, Huang TL, Tsang LLC, et al. Drug-eluting Bead Transarterial Chemoembolization for Hepatocellular Carcinoma: Does Size Really Matter? Diagnostic and Interventional Radiology. 2020 may;26(3):230–235.

[15] Westerly DC, Goodman KA. External Beam Radiation Therapy for Liver Tumors: Simulation, Treatment Planning, and Advanced Delivery Techniques. In: Radiation Therapy for Liver Tumors. Springer International Publishing; 2017. p. 91–105.

[16] Chan LS, Sze DY, Poultsides GA, Louie JD, Mohammed MAA, Wang DS. Yttrium-90 Radioembolization for Unresectable Combined Hepatocellular-Cholangiocarcinoma. CardioVascular and Interventional Radiology. 2017 apr;40(9):1383–1391.

[17] Brunt E, Aishima S, Clavien PA, Fowler K, Goodman Z, Gores G, et al. cHCC-CCA: Consensus Terminology for Pprimary Liver Carcinomas with Bboth Hepatocytic and Cholangiocytic Differentation. Hepatology. 2018 may;68(1):113–126.

[18] Galle PR, Forner A, Llovet JM, Mazzaferro V, Piscaglia F, Raoul JL, et al. EASL Clinical Practice Guidelines: Management of Hepatocellular Carcinoma. Journal of Hepatology. 2018 jul;69(1):182–236.

[19] Njei B, Rotman Y, Ditah I, Lim JK. Emerging Trends in Hepatocellular Carcinoma Incidence and Mortality. Hepatology. 2014 nov;61(1):191–199.

[20] Forner A, Reig ME, de Lope CR, Bruix J. Current Strategy for Staging and Treatment: The BCLC Update and Future Prospects. Seminars in Liver Disease. 2010 feb;30(01):061–074.

[21] Ryan MJ. Ablation Techniques for Primary and Mmetastatic Lliver Tumors. World Journal of Hepatology. 2016;8(3):191.

[22] Ganten TM, Stauber RE, Schott E, Malfertheiner P, Buder R, Galle PR, et al. Sorafenib in Patients with Hepatocellular Carcinoma—Results of the Observational INSIGHT Study. Clinical Cancer Research. 2017 jul;23(19):5720–5728.

[23] Klompenhouwer EG, Dresen RC, Verslype C, Laenen A, Hertogh GD, Deroose CM, et al. Safety and Efficacy of Transarterial Radioembolisation in Patients with Intermediate or Advanced Stage Hepatocellular Carcinoma Refractory to Chemoembolisation. CardioVascular and Interventional Radiology. 2017 jul;40(12):1882–1890.

[24] Vilgrain V, Pereira H, Assenat E, Guiu B, Ilonca AD, Pageaux GP, et al. Efficacy and Safety of Selective Internal Radiotherapy with Yttrium-90 Resin Microspheres Compared with Sorafenib in Locally Advanced and Inoperable Hepatocellular Carcinoma (SARAH): An Open-Label Randomised Controlled Phase 3 Trial. The Lancet Oncology. 2017 dec;18(12):1624–1636.

[25] Gupta A, Dixon E. Epidemiology and Risk Factors: Intrahepatic Cholangiocarcinoma. HepatoBiliary Surgery and Nutrition. 2017 apr;6(2):101–104.

[26] Buettner S, van Vugt JLA, IJzermans J, Koerkamp BG. Intrahepatic Cholangiocarcinoma: Current Perspectives. OncoTargets and Therapy. 2017 feb;10:1131–1142.

[27] Edeline J, Touchefeu Y, Guiu B, Farge O, Tougeron D, Baumgaertner I, et al. Radioembolization Plus Chemotherapy for First-line Treatment of Locally Advanced Intrahepatic Cholangiocarcinoma - A Phase 2 Clinical Trial. JAMA Oncology. 2020 jan;6(1):51.

[28] Al-Adra DP, Gill RS, Axford SJ, Shi X, Kneteman N, Liau SS. Treatment of Unresectable Intrahepatic Cholangiocarcinoma with Yttrium-90 Radioembolization: A Systematic Review and Pooled Analysis. European Journal of Surgical Oncology (EJSO). 2015 jan;41(1):120–127.

[29] Levillain H, Derijckere ID, Ameye L, Guiot T, Braat A, Meyer C, et al. Personalised Radioembolization Improves Outcomes in Refractory Intra-Hepatic Cholangiocarcinoma: A Multicenter Study. European Journal of Nuclear Medicine and Molecular Imaging. 2019 jul;46(11):2270–2279.

[30] Poston GJ, Adam R, Alberts S, Curley S, Figueras J, Haller D, et al. OncoSurge: A Strategy for Improving Resectability With Curative Intent in Metastatic Colorectal Cancer. Journal of Clinical Oncology. 2005 oct;23(28):7125–7134.

[31] Saxena A, Bester L, Shan L, Perera M, Gibbs P, Meteling B, et al. A Systematic Review on the Safety and Efficacy of Yttrium-90 Radioembolization for Unresectable, Chemorefractory Colorectal Cancer Liver Metastases. Journal of Cancer Research and Clinical Oncology. 2013 dec;140(4):537–547.

[32] Cutsem EV, Cervantes A, Adam R, Sobrero A, Krieken JHV, Aderka D, et al. ESMO Consensus Guidelines for the Management of Patients with Metastatic Colorectal Cancer. Annals of Oncology. 2016 aug;27(8):1386–1422.

[33] van Hazel GA, Heinemann V, Sharma NK, Findlay MPN, Ricke J, Peeters M, et al. SIRFLOX: Randomized Phase III Trial Comparing First-Line mFOLFOX6 (Plus or Minus Bevacizumab) Versus mFOLFOX6 (Plus or Minus Bevacizumab) Plus Selective Internal Radiation Therapy in Patients With Metastatic Colorectal Cancer. Journal of Clinical Oncology. 2016 may;34(15):1723–1731.

[34] Garlipp B, Gibbs P, Hazel GAV, Jeyarajah R, Martin RCG, Bruns CJ, et al. Secondary Technical Resectability of Colorectal Cancer Liver Metastases After Chemotherapy With or Without Selective Internal Radiotherapy in the Randomized SIRFLOX Trial. BJS. 2019 aug;.

[35] Garlipp B, Gibbs P, van Hazel G, Jeyarajah R, Martin R, Bruns C, et al. REsect: Blinded Assessment of Resectability of Previously Unresectable Colorectal Cancer Liver Metastases Following Chemotherapy±Y90-RadioEmbolization. HPB. 2019;21:S637.

[36] Winter H, Rassam J, Virdee PS, Goldin R, Pitcheshwar P, Weaver K, et al. Hepatic Resection Following Selective Internal Radiation Therapy for Colorectal Cancer Metastases in the FOXFIRE Clinical Trial: Clinical Outcomes and Distribution of Microspheres. Cancers. 2019 aug;11(8):1155.

[37] Frilling A, Sotiropoulos GC, Li J, Kornasiewicz O, Plöckinger U. Multimodal Management of Neuroendocrine Liver Metastases. HPB. 2010 aug;12(6):361–379.

[38] Tomozawa Y, Jahangiri Y, Pathak P, Kolbeck KJ, Schenning RC, Kaufman JA, et al. Long-Term Toxicity after Transarterial Radioembolization with Yttrium-90 Using Resin Microspheres for Neuroendocrine Tumor Liver Metastases. Journal of Vascular and Interventional Radiology. 2018 jun;29(6):858–865.

[39] Coldwell DM, Vyleta M, Samman M. Treatment of Neuroendocrine Tumors with Selective Internal Radiation Therapy. In: Liver Radioembolization with 90Y Microspheres. Springer Berlin Heidelberg; 2013. p. 151–155.

[40] Devcic Z, Rosenberg J, Braat AJA, Techasith T, Banerjee A, Sze DY, et al. The Efficacy of Hepatic 90Y Resin Radioembolization for Metastatic Neuroendocrine Tumors: A Meta-Analysis. Journal of Nuclear Medicine. 2014 jul;55(9):1404–1410.

[41] Yang TX, Chua TC, Morris DL. Radioembolization and Chemoembolization for Unresectable Neuroendocrine Liver Metastases – A Systematic Review. Surgical Oncology. 2012 dec;21(4):299–308.

[42] Braat AJAT, Ahmadzadehfar H, Kappadath SC, Stothers CL, Frilling A, Deroose CM, et al. Radioembolization with 90Y Resin Microspheres of Neuroendocrine Liver Metastases After Initial Peptide Receptor Radionuclide Therapy. CardioVascular and Interventional Radiology. 2019 oct;43(2):246–253.

[43] Braat AJAT, Bruijnen RCG, van Rooij R, Braat MNGJA, Wessels FJ, van Leeuwaarde RS, et al. Additional Holmium-166 Radioembolisation After Lutetium-177-dotatate in Patients with Neuroendocrine Tumour Liver Metastases (HEPAR PLuS): A Single-Centre, Single-Arm, Open-Label, Phase 2 Study. The Lancet Oncology. 2020 apr;21(4):561–570.

[44] Braat AJAT, Kappadath SC, Ahmadzadehfar H, Stothers CL, Frilling A, Deroose CM, et al. Radioembolization with 90Y Resin Microspheres of Neuroendocrine Liver Metastases: International Multicenter Study on Efficacy and Toxicity. CardioVascular and Interventional Radiology. 2019 jan;42(3):413–425.

[45] Jia Z, Jiang G, Zhu C, Wang K, Li S, Qin X. A Systematic Review of Yttrium-90 Radioembolization for Unresectable Liver Metastases of Melanoma. European Journal of Radiology. 2017 jul;92:111–115.

[46] Ponti A, Denys A, Digklia A, Schaefer N, Hocquelet A, Knebel JF, et al. First-Line Selective Internal Radiation Therapy in Patients with Uveal Melanoma Metastatic to the Liver. Journal of Nuclear Medicine. 2019 sep;61(3):350–356.

[47] Schima W, Hammerstingl R, Catalano C, Marti-Bonmati L, Rummeny EJ, Montero FT, et al. Quadruple-Phase MDCT of the Liver in Patients with Suspected Hepatocellular Carcinoma: Effect of Contrast Material Flow Rate. American Journal of Roentgenology. 2006 jun;186(6):1571–1579.

[48] Bapst B, Lagadec M, Breguet R, Vilgrain V, Ronot M. Erratum to: Cone Beam Computed Tomography (CBCT) in the Field of Interventional Oncology of the Liver. CardioVascular and Interventional Radiology. 2015 aug;38(5):1381–1381.

[49] Jafargholi Rangraz E, Coudyzer W, Maleux G, Baete K, Deroose CM, Nuyts J. Multi-Modal Image Analysis for Semi-Automatic Segmentation of the Total Liver and Liver Arterial Perfusion Territories for Radioembolization. EJNMMI Research. 2019 feb;9(1).

[50] Miyayama S, Yamashiro M, Shibata Y, Hashimoto M, Yoshida M, Tsuji K, et al. Variations in Feeding Arteries of Hepatocellular Carcinoma Located in the Left Hepatic Lobe. Japanese Journal of Radiology. 2012 apr;30(6):471–479.

[51] Miyayama S, Yamashiro M, Yoshie Y, Nakashima Y, Ikeno H, Orito N, et al. Hepatocellular Carcinoma in the Caudate Lobe of the Liver: Variations of Its Feeding Branches on Arteriography. Japanese Journal of Radiology. 2010 oct;28(8):555–562.

[52] O'Connor PJ, Pasik SD, van der Bom IM, Bishay V, Radaelli A, Kim E. Feasibility of Yttrium-90 Radioembolization Dose Calculation Utilizing Intra-procedural Open Trajectory Cone Beam CT. CardioVascular and Interventional Radiology. 2019 oct;43(2):295–301.

[53] Louie JD, Kothary N, Kuo WT, Hwang GL, Hofmann LV, Goris ML, et al. Incorporating Cone-beam CT into the Treatment Planning for Yttrium-90 Radioembolization. Journal of Vascular and Interventional Radiology. 2009 may;20(5):606–613.

[54] Pellerin O, Pereira H, Ty CVN, Moussa N, Giudice CD, Pernot S, et al. Is Dual-Phase C-Arm CBCT Sufficiently Accurate for the Diagnosis of Colorectal Cancer Liver Metastasis During Liver Intra-Arterial Treatment? European Radiology. 2019 apr;29(10):5253–5263.

[55] Zech CJ, Herrmann KA, Dietrich O, Horger W, Reiser MF, Schoenberg SO. Black-Blood Diffusion-Weighted EPI Acquisition of the Liver with Parallel Imaging. Investigative Radiology. 2008 apr;43(4):261–266.

[56] Alis D, Durmaz ESM, Gulsen F, Bas A, Kabasakal L, Sager S, et al. Prognostic Value of ADC Measurements in Predicting Overall Survival in Patients Undergoing 90Y Radioembolization for Colorectal Cancer Liver Metastases. Clinical Imaging. 2019 sep;57:124–130.

[57] Youk JH, Lee JM, Kim CS. MRI for Detection of Hepatocellular Carcinoma: Comparison of Mangafodipir Trisodium and Gadopentetate Dimeglumine Contrast Agents. American Journal of Roentgenology. 2004 oct;183(4):1049–1054.

[58] Ljungberg M. Absolute Quantitation of SPECT Studies. Seminars in Nuclear Medicine. 2018 jul;48(4):348–358.

[59] Ritt P, Vija H, Hornegger J, Kuwert T. Absolute quantification in SPECT. European Journal of Nuclear Medicine and Molecular Imaging. 2011 apr;38(S1):69–77.

[60] Takahashi A, Himuro K, Yamashita Y, Komiya I, Baba S, Sasaki M. Monte Carlo Simulation of PET and SPECT Imaging of 90Y. Medical Physics. 2015 mar;42(4):1926–1935.

[61] Attarwala AA, Molina-Duran F, Büsing KA, Schönberg SO, Bailey DL, Willowson K, et al. Quantitative and Qualitative Assessment of Yttrium-90 PET/CT Imaging. PLoS ONE. 2014 nov;9(11):e110401.

[62] Conti M, Bendriem B. The New Opportunities for High Time Resolution Clinical TOF PET. Clinical and Translational Imaging. 2019 feb;7(2):139–147.

[63] Townsend DW. Combined Positron Emission Tomography–Computed Tomography: The Historical Perspective. Seminars in Ultrasound, CT and MRI. 2008 aug;29(4):232–235.

[64] Seo Y, Mari C, Hasegawa BH. Technological Development and Advances in Single-Photon Emission Computed Tomography/Computed Tomography. Seminars in Nuclear Medicine. 2008 may;38(3):177–198.

[65] Grimes J. Patient-Specific Internal Dose Calculation Techniques for Clinical Use in Targeted Radionuclide Therapy. University of British Columbia; 2013.

[66] Marinelli LD, Quimby EH, Hine GJ. Dosage Determination with Radioactive Isotopes; Practical Considerations in Therapy and Protection. The American journal of roentgenology and radium therapy. 1948 feb;59(2):260–281.

[67] Grief WR, McDougall IR, Halnan KE. Treatment with Unsealed Radioisotopes. British Medical Bulletin. 1973 jan;29(1):63–68.

[68] MIRD committee of the Society of Nuclear Medicine;. Accessed: 2020-06-12. `http://www.snmmi.org/AboutSNMMI/CommitteeContent.aspx?ItemNumber=12475&navItemNumber=763`.

[69] Bolch WE, Eckerman KF, Sgouros G, Thomas SR. MIRD Pamphlet No. 21: A Generalized Schema for Radiopharmaceutical Dosimetry–Standardization of Nomenclature. Journal of Nuclear Medicine. 2009 feb;50(3):477–484.

[70] Lanconelli N, Pacilio M, Meo SL, Botta F, Dia AD, Aroche LAT, et al. A Free Database of Radionuclide Voxel S Values for the Dosimetry of Nonuniform Activity Distributions. Physics in Medicine and Biology. 2012 jan;57(2):517–533.

[71] Cremonesi M, Chiesa C, Strigari L, Ferrari M, Botta F, Guerriero F, et al. Radioembolization of Hepatic Lesions from a Radiobiology and Dosimetric Perspective. Frontiers in Oncology. 2014 aug;4.

[72] Petitguillaume A, Bernardini M, Broggio D, de Labriolle Vaylet C, Franck D, Desbrée A. OEDIPE, A Software for Personalized Monte Carlo Dosimetry and Treatment Planning Optimization in Nuclear Medicine: Absorbed Dose and Biologically Effective Dose Considerations. Radioprotection. 2014 sep;49(4):275–281.

[73] Bastiaannet R, Kappadath SC, Kunnen B, Braat AJAT, Lam MGEH, de Jong HWAM. The Physics of Radioembolization. EJNMMI Physics. 2018 nov;5(1).

[74] Walrand S, Hesse M, Jamar F, Lhommel R. A Hepatic Dose-Toxicity Model Opening the Way Toward Individualized Radioembolization Planning. Journal of Nuclear Medicine. 2014 jun;55(8):1317–1322.

[75] Strigari L, Sciuto R, Rea S, Carpanese L, Pizzi G, Soriani A, et al. Efficacy and Toxicity Related to Treatment of Hepatocellular Carcinoma with 90Y-SIR Spheres: Radiobiologic Considerations. Journal of Nuclear Medicine. 2010 aug;51(9):1377–1385.

[76] Willowson KP, Hayes AR, Chan DLH, Tapner M, Bernard EJ, Maher R, et al. Clinical and Imaging-Based Prognostic Factors in Radioembolisation of Liver Metastases from Colorectal Cancer: A Retrospective Exploratory Analysis. EJNMMI Research. 2017 may;7(1).

[77] Bierman HR, Byron RL, Kelley KH, Grady A. Studies on the Blood Supply of Tumors in Man. iii. Vascular Patterns of the Liver by Hepatic Arteriography in Vivo. JNCI: Journal of the National Cancer Institute. 1951 aug;.

[78] Breedis C, Young G. The Blood Supply of Neoplasms in the Liver. The American journal of pathology. 1954;30(5):969–77.

[79] Ariel IM. Treatment of Inoperable Primary Pancreatic and Liver Cancer by the Intra-Arterial Administration of Radioactive Isotopes (Y Radiating Microspheres). Annals of Surgery. 1965 aug;162(2):267–278.

[80] Grady ED, Sale WT, Rollins LC. Localization of Radioactivity by Intravascular Injection of Large Radioactive Particles. Annals of Surgery. 1963 jan;157(1):97–114.

[81] Blanchard RJ, Lafave JW, Kim YS, Frye CS, Ritchie WP, Perry JF. Treatment of Patients with Advanced Cancer Utilizing Y90 Microspheres. Cancer. 1965 mar;18(3):375–380.

[82] Eipel C. Regulation of Hepatic Blood Flow: The Hepatic Arterial Buffer Response Revisited. World Journal of Gastroenterology. 2010;16(48):6046.

[83] Tchelebi L, Sharma NK. Selective Internal Radiation Therapy in the Multidisciplinary Management of Liver Metastases From Colorectal Carcinoma. Seminars in Nuclear Medicine. 2019 may;49(3):182–188.

[84] Vouche M, Lewandowski RJ, Atassi R, Memon K, Gates VL, Ryu RK, et al. Radiation Lobectomy: Time-Dependent Analysis of Future Liver Remnant Volume in Unresectable Liver Cancer as a Bridge to Resection. Journal of Hepatology. 2013 nov;59(5):1029–1036.

[85] Reinders MTM, Mees E, Powerski MJ, Bruijnen RCG, van den Bosch MAAJ, Lam MGEH, et al. Radioembolisation in Europe: A Survey Amongst CIRSE Members. CardioVascular and Interventional Radiology. 2018 may;41(10):1579–1589.

[86] Riaz A, Gates VL, Atassi B, Lewandowski RJ, Mulcahy MF, Ryu RK, et al. Radiation Segmentectomy: A Novel Approach to Increase Safety and Efficacy of Radioembolization. International Journal of Radiation Oncology∗Biology∗Physics. 2011 jan;79(1):163–171.

[87] Lau WY, Kennedy AS, Kim YH, Lai HK, Lee RC, Leung TWT, et al. Patient Selection and Activity Planning Guide for Selective Internal Radiotherapy With Yttrium-90 Resin Microspheres. International Journal of Radiation Oncology∗Biology∗Physics. 2012 jan;82(1):401–407.

[88] Jia Z, Wang C, Paz-Fumagalli R, Wang W. Radiation Segmentectomy for Hepatic Malignancies: Indications, Devices, Dosimetry, Procedure, ClinicalOutcomes, and Ttoxicity of Yttrium-90 Microspheres. Journal of Interventional Medicine. 2019 feb;2(1):1–4.

[89] Salem R, Padia SA, Lam M, Bell J, Chiesa C, Fowers K, et al. Clinical and Dosimetric Considerations for Y90: Recommendations from an International Multidisciplinary Working Group. European Journal of Nuclear Medicine and Molecular Imaging. 2019 may;46(8):1695–1704.

[90] Padia SA, Johnson GE, Horton KJ, Ingraham CR, Kogut MJ, Kwan S, et al. Segmental Yttrium-90 Radioembolization versus Segmental Chemoembolization for Localized Hepatocellular Carcinoma: Results of a Single-Center, Retrospective, Propensity Score–Matched Study. Journal of Vascular and Interventional Radiology. 2017 jun;28(6):777–785.e1.

[91] Vouche M, Habib A, Ward TJ, Kim E, Kulik L, Ganger D, et al. Unresectable Solitary Hepatocellular Carcinoma not Amenable to Radiofrequency Ablation: Multicenter Radiology-Pathology Correlation and Survival of Radiation Segmentectomy. Hepatology. 2014 may;60(1):192–201.

[92] Fernández-Ros N, Silva N, Bilbao JI, Iñarrairaegui M, Benito A, D'Avola D, et al. Partial Liver Volume Radioembolization Induces Hypertrophy in the Spared Hemiliver and no Major Signs of Portal Hypertension. HPB. 2014 mar;16(3):243–249.

[93] Teo JY, Allen JC, Ng DC, Choo SP, Tai DWM, Chang JPE, et al. A Systematic Review of Contralateral Liver Lobe Hypertrophy After Unilobar Selective Internal Radiation Therapy with Y90. HPB. 2016 jan;18(1):7–12.

[94] Braat MNGJA, Samim M, van den Bosch MAAJ, Lam MGEH. The Role of 90Y-Radioembolization in Downstaging Primary and Secondary Hepatic Malignancies: A Systematic Review. Clinical and Translational Imaging. 2016 apr;4(4):283–295.

[95] Palard X, Edeline J, Rolland Y, Sourd SL, Pracht M, Laffont S, et al. Dosimetric Parameters Predicting Contralateral Liver Hypertrophy After Unilobar Radioembolization of Hepatocellular Carcinoma. European Journal of Nuclear Medicine and Molecular Imaging. 2017 nov;45(3):392–401.

[96] Kennedy A, Nag S, Salem R, Murthy R, McEwan AJ, Nutting C, et al. Recommendations for Radioembolization of Hepatic Malignancies Using Yttrium-90 Microsphere Brachytherapy: A Consensus Panel Report from the Radioembolization Brachytherapy Oncology Consortium. International Journal of Radiation Oncology∗Biology∗Physics. 2007 may;68(1):13–23.

[97] Bé M, Chisté V, Dulieu C, Browne E, Baglin C, Chechev V, et al. Table of Radionuclides (vol. 3–A= 3 to 244). Bureau International des Poids et Mesures; Sevres (France); 2006.

[98] Lhommel R, van Elmbt L, Goffette P, den Eynde MV, Jamar F, Pauwels S, et al. Feasibility of 90Y TOF PET-Based Dosimetry in Liver Metastasis Therapy Using SIR-Spheres. European Journal of Nuclear Medicine and Molecular Imaging. 2010 apr;37(9):1654–1662.

[99] Lhommel R, Goffette P, den Eynde MV, Jamar F, Pauwels S, Bilbao JI, et al. Yttrium-90 TOF PET Scan Demonstrates High-Resolution Biodistribution After Liver SIRT. European Journal of Nuclear Medicine and Molecular Imaging. 2009 jul;36(10):1696–1696.

[100] Rault E. Yttrium-90 Bremsstrahlung SPECT Imaging. Ghent University; 2011.

[101] Krishna M. Microscopic Anatomy of the Liver. Clinical Liver Disease. 2013 mar;2(S1):S4–S7.

[102] Doherty JO. A rReview of 3D Image-Based Dosimetry, Technical Considerations and Emerging Perspectives in 90Y Microsphere Therapy. Journal of Diagnostic Imaging in Therapy. 2015 apr;2(2):1–34.

[103] Sarrut D, Bardiès M, Boussion N, Freud N, Jan S, Létang JM, et al. A Review of the Use and Potential of the GATE Monte Carlo Simulation Code for Radiation Therapy and Dosimetry Applications. Medical Physics. 2014 may;41(6Part1):064301.

[104] Strigari L, Menghi E, D'Andrea M, Benassi M. Monte Carlo Dose Voxel Kernel Calculations of Beta-Emitting and Auger-Emitting Radionuclides for Internal Dosimetry: A Comparison Between EGSnrcMP and EGS4. Medical Physics. 2006 aug;33(9):3383–3389.

[105] Bolch WE, Bouchetand LG, Robertson JS, Wessels BW, Siegel JA, Howell R, et al. MIRD Pamphlet no. 17: The Dosimetry of Nonuniform Activity Distributions - Radionuclide S Values at the Voxel Level. Journal of Nuclear Medicine. 1999 1;40(1).

[106] Pasciak AS, Erwin WD. Effect of Voxel Size and Computation Method on Tc-99m MAA SPECT/CT-Based Dose Estimation for Y-90 Microsphere Therapy. IEEE Transactions on Medical Imaging. 2009 nov;28(11):1754–1758.

[107] Mikell JK, Mahvash A, Siman W, Mourtada F, Kappadath SC. Comparing Voxel-Based Absorbed Dosimetry Methods in Tumors, Liver, Lung, and at the Liver-Lung Interface for 90Y Microsphere Selective Internal Radiation Therapy. EJNMMI Physics. 2015 jul;2(1).

[108] Pirayesh E, Amoui M, Akhlaghpoor S, Tolooee S, Khorrami M, PoorBeigi H, et al. Technical Considerations of Phosphorous-32 Bremsstrahlung SPECT Imaging after Radioembolization of Hepatic Tumors: A Clinical Assessment with a Review of Imaging Parameters. Radiology Research and Practice. 2014;2014:1–7.

[109] Tsai SC, Hung GU, Lee JC, Huang YS, Lin WY, Lin YC. Direct Injection of 188Re-Microspheres in the Treatment of Hepatocellular Carcinoma. Nuklearmedizin. 2005;44(03):76–80.

[110] Hwang H, Kim KI, Kwon J, Kim BS, Jeong HS, Jang SJ, et al. 131 I-Labeled Chitosan Hydrogels for Radioembolization: A Preclinical Study in Small Animals. Nuclear Medicine and Biology. 2017 sep;52:16–23.

[111] Ferreira MCM, Podder TK, Rasmussen KH, Jung JW. Praseodymium-142 Microspheres for Brachytherapy of Nonresectable Hepatic Tumors. Brachytherapy. 2013 nov;12(6):654–664.

[112] Lewandowski RJ, Riaz A, Ryu RK, Mulcahy MF, Sato KT, Kulik LM, et al. Optimization of Radioembolic Effect with Extended-shelf-life Yttrium-90 Microspheres: Results from a Pilot Study. Journal of Vascular and Interventional Radiology. 2009 dec;20(12):1557–1563.

[113] Sangro B, Iñarrairaegui M, Bilbao JI. Radioembolization for Hepatocellular Carcinoma. Journal of Hepatology. 2012 feb;56(2):464–473.

[114] Rhee TK, Lewandowski RJ, Liu DM, Mulcahy MF, Takahashi G, Hansen PD, et al. 90Y Radioembolization for Metastatic Neuroendocrine Liver Tumors. Annals of Surgery. 2008 jun;247(6):1029–1035.

[115] Burrill J, Hafeli U, Liu DM. Advances in Radioembolization - Embolics and Isotopes. Journal of Nuclear Medicine & Radiation Therapy. 2011;01(01).

[116] Ho S, Lau WY, Leung TWT, Johnson PJ. Internal Radiation Therapy for Patients with Primary or Metastatic Hepatic Cancer. Cancer. 1998 nov;83(9):1894–1907.

[117] Braat AJAT, Kappadath SC, Bruijnen RCG, van den Hoven AF, Mahvash A, de Jong HWAM, et al. Adequate SIRT Activity Dose Is As Important As Adequate Chemotherapy Dose. The Lancet Oncology. 2017 nov;18(11):e636.

[118] Salem R, Gilbertsen M, Butt Z, Memon K, Vouche M, Hickey R, et al. Increased Quality of Life Among Hepatocellular Carcinoma Patients Treated With Radioembolization, Compared With Chemoembolization. Clinical Gastroenterology and Hepatology. 2013 oct;11(10):1358–1365.e1.

[119] Chow PKH, Gandhi M, Tan SB, Khin MW, Khasbazar A, Ong J, et al. SIRveNIB: Selective Internal Radiation Therapy Versus Sorafenib in Asia-Pacific Patients With Hepatocellular Carcinoma. Journal of Clinical Oncology. 2018 jul;36(19):1913–1921.

[120] Ricke J, Klümpen HJ, Amthauer H, Bargellini I, Bartenstein P, de Toni EN, et al. Impact of Combined Selective Internal Radiation Therapy and Sorafenib on Survival in Advanced Hepatocellular Carcinoma. Journal of Hepatology. 2019 dec;71(6):1164–1174.

[121] Wasan HS, Gibbs P, Sharma NK, Taieb J, Heinemann V, Ricke J, et al. First-Line Selective Internal Radiotherapy Plus Chemotherapy Versus Chemotherapy Alone in Patients with Liver Metastases from Colorectal Cancer (FOXFIRE, SIRFLOX, and FOXFIRE-Global): A Combined Analysis of Three Multicentre, Randomised, Phase 3 Trials. The Lancet Oncology. 2017 sep;18(9):1159–1171.

[122] Hawkins NS, Ross PJ, Palmer DH, Chatellier G, Pereira H, Vilgrain V. Overall Survival of Patients with Hepatocellular Carcinoma Receiving Sorafenib Versus Selective Internal Radiation Therapy with Predicted Dosimetry in the SARAH Trial. Annals of Oncology. 2019 oct;30:v282.

[123] Sposito C, Mazzaferro V. The SIRveNIB and SARAH Trials, Radioembolization vs. Sorafenib in Advanced HCC Patients: Reasons for a Failure, and Perspectives for the Future. HepatoBiliary Surgery and Nutrition. 2018 dec;7(6):487–489.

[124] Garin E, Rolland Y, Campillo-Gimenez B, Edeline J. Negative Phase 3 Study of 90Y Microspheres Versus Sorafenib in HCC. The Lancet Oncology. 2018 feb;19(2):e70.

[125] Scientific Boston - Dosisphere results;. Accessed: 2020-06-12. https://www.bostonscientific.com/en-US/products/cancer-therapies/therasphere-y90-glass-microspheres/dosisphere-trial.html.

[126] Garin E, Tzelikas L, Guiu B, Chalaye J, Edeline J, Baere TD, et al. Major Impact of Personalized Dosimetry Using 90Y Loaded Glass Microspheres SIRT in HCC: Final Overall Survival Analysis of a Multicenter Randomized Phase II Study (DOSISPHERE-01). Journal of Clinical Oncology. 2020 feb;38(4_suppl):516–516.

[127] Sangro B, Carpanese L, Cianni R, Golfieri R, Gasparini D, Ezziddin S, et al. Survival After Yttrium-90 Resin Microsphere Radioembolization of Hepatocellular Carcinoma Across Barcelona Clinic Liver Cancer Stages: A European Evaluation. Hepatology. 2011 jun;54(3):868–878.

[128] White J, Carolan-Rees G, Dale M, Morgan HE, Patrick HE, See TC, et al. Analysis of a National Programme for Selective Internal Radiation Therapy for Colorectal Cancer Liver Metastases. Clinical Oncology. 2019 jan;31(1):58–66.

[129] Kennedy A, Cohn M, Coldwell DM, Drooz A, Ehrenwald E, Kaiser A, et al. Updated Survival Outcomes and Analysis of Long-Term Survivors from the MORE Study on Safety and Efficacy of Radioembolization in Patients with Unresectable Colorectal Cancer Liver Metastases. Journal of Gastrointestinal Oncology. 2017 aug;8(4):614–624.

[130] Lewandowski RJ, Memon K, Mulcahy MF, Hickey R, Marshall K, Williams M, et al. Twelve-Year Experience of Radioembolization for Colorectal Hepatic Metastases in 214 Patients: Survival by Era and Chemotherapy. European Journal of Nuclear Medicine and Molecular Imaging. 2014 jun;41(10):1861–1869.

[131] Salem R, Gabr A, Riaz A, Mora R, Ali R, Abecassis M, et al. Institutional Secision to Adopt Y90 As Primary Treatment for Hepatocellular Carcinoma Informed by a 1,000-Patient 15-Year Experience. Hepatology. 2018 jan;68(4):1429–1440.

[132] Sangro B. The ENRY Analysis: A 325-Patient European Multicentre Analysis. European Journal of Cancer Supplements. 2012 aug;10(3):23–26.

[133] Vogel A, Cervantes A, Chau I, Daniele B, Llovet JM, Meyer T, et al. Hepatocellular Carcinoma: ESMO Clinical Practice Guidelines for Diagnosis, Treatment and Follow-Up. Annals of Oncology. 2018 oct;29:iv238–iv255.

[134] Benson AB, D'Angelica MI, Abbott DE, Abrams TA, Alberts SR, Anaya DA, et al. NCCN Guidelines Insights: Hepatobiliary Cancers, Version 1.2017. Journal of the National Comprehensive Cancer Network. 2017 may;15(5):563–573.

[135] NICE guidline[IPG460] Selective internal radiation therapy for primary hepatocellular carcinoma;. Accessed: 2020-06-12. https://www.nice.org.uk/guidance/ipg460/chapter/1-Guidance.

[136] Marrero JA, Kulik LM, Sirlin CB, Zhu AX, Finn RS, Abecassis MM, et al. Diagnosis, Staging, and Management of Hepatocellular Carcinoma: 2018 Practice Guidance by the American Association for the Study of Liver Diseases. Hepatology. 2018 aug;68(2):723–750.

[137] Omata M, Cheng AL, Kokudo N, Kudo M, Lee JM, Jia J, et al. Asia–Pacific Clinical Practice Guidelines on the Management of Hhepatocellular Carcinoma: A 2017 Update. Hepatology International. 2017 jun;11(4):317–370.

[138] Haydar AA, Nasr LA, Hussain HK. Imaging Characteristics of Normal Liver and Liver Tumors. In: Radiation Therapy for Liver Tumors. Springer; 2017. p. 13–29.

[139] Patil PG, Reddy P, Rawat S, Ananthasivan R, Sinha R. Multimodality Approach in Detection and Characterization of Hepatic Metastases. Journal of Gastrointestinal and Abdominal Radiology. 2020 may;.

[140] Tsurusaki M, Okada M, Kuroda H, Matsuki M, Ishii K, Murakami T. Clinical Application of 18F-Fluorodeoxyglucose Positron Emission Tomography for Assessment and Evaluation After Therapy for Malignant Hepatic Tumor. Journal of Gastroenterology. 2013 mar;49(1):46–56.

[141] Cheebsumon P, Yaqub M, van Velden FHP, Hoekstra OS, Lammertsma AA, Boellaard R. Impact of [18F]FDG PET Imaging Parameters on Automatic Tumour Delineation: Need for Improved Tumour Delineation Methodology. European Journal of Nuclear Medicine and Molecular Imaging. 2011 aug;38(12):2136–2144.

[142] Heimbach JK, Kulik LM, Finn RS, Sirlin CB, Abecassis MM, Roberts LR, et al. AASLD Guidelines for the Treatment of Hepatocellular Carcinoma. Hepatology. 2017 dec;67(1):358–380.

[143] Hoffmann RT, Diaz-Dorronsoro L, Bilbao JI. Complications and Side Effects. In: Liver Radioembolization with 90Y Microspheres. Springer; 2013. p. 171–175.

[144] Quirk M. Management of Hepatocellular Carcinoma with Portal Vein Thrombosis. World Journal of Gastroenterology. 2015;21(12):3462.

[145] Iñarrairaegui M, Thurston KG, Bilbao JI, D'Avola D, Rodriguez M, Arbizu J, et al. Radioembolization with Use of Yttrium-90 Resin Microspheres in Patients with Hepatocellular Carcinoma and Portal Vein Thrombosis. Journal of Vascular and Interventional Radiology. 2010 aug;21(8):1205–1212.

[146] Steel JL, Eton DT, Cella D, Olek MC, Carr BI. Clinically Meaningful Changes in Health-Related Quality of Life in Patients Diagnosed with Hepatobiliary Carcinoma. Annals of Oncology. 2006 feb;17(2):304–312.

[147] Rognoni C, Ciani O, Sommariva S, Bargellini I, Bhoori S, Cioni R, et al. Trans-Arterial Radioembolization for Intermediate-Advanced Hepatocellular Carcinoma: A Budget Impact Analysis. BMC Cancer. 2018 jul;18(1).

[148] Gersem RD, Maleux G, Vanbilloen H, Baete K, Verslype C, Haustermans K, et al. Influence of Time Delay on the Estimated Lung Shunt Fraction on 99mTc-Labeled MAA Scintigraphy for 90Y Microsphere Treatment Planning. Clinical Nuclear Medicine. 2013 nov;p. 1.

[149] Soldin OP, Braverman LE, Lamm SH. Perchlorate Clinical Pharmacology and Human Health: A Review. Therapeutic Drug Monitoring. 2001 aug;23(4):316–331.

[150] Mauxion T, Hobbs R, Herman J, Lodge M, Yue J, Du Y, et al. Comparison of Lung Shunt Fraction (LSF) from Pre-Therapy 99mTc MAA and Post-Therapy Quantitative 90Y Imaging in Microsphere (MS) Radioembolization. Journal of Nuclear Medicine. 2015;56(supplement 3):104–104.

[151] Gill H, Bian J, Gabriel M, Molvar C, Wagner R, Halama J. 99mTc-MAA SPECT/CT Imaging for Quantitative Assessment of Lung Shunt Fraction Prior to 90Y Transarterial Radioembolization. Journal of Nuclear Medicine. 2019;60(supplement 1):265–265.

[152] Bastiaannet R, van der Velden S, Lam MGEH, Viergever MA, de Jong HWAM. Fast and Accurate Quantitative Determination of the Lung Shunt Fraction in Hepatic Radioembolization. Physics in Medicine & Biology. 2019 nov;64(23):235002.

[153] Dezarn WA, Cessna JT, DeWerd LA, Feng W, Gates VL, Halama J, et al. Recommendations of the American Association of Physicists in Medicine on dosimetry, imaging, and quality assurance procedures for 90 Y microsphere brachytherapy in the treatment of hepatic malignancies. Medical Physics. 2011 aug;38(8):4824–4845.

[154] Giammarile F, , Bodei L, Chiesa C, Flux G, Forrer F, et al. EANM Procedure Guideline for the Treatment of Liver Cancer and Liver Metastases with Intra-Arterial Radioactive Compounds. European Journal of Nuclear Medicine and Molecular Imaging. 2011 apr;38(7):1393–1406.

[155] Darte L, Söderbom L, Persson BR. Quality Control and Testing of 99mTc-Macroaggregated Albumin. Nuklearmedizin Nuclear medicine. 1976 apr;15(2):80–85.

[156] Grosser OS, Ruf J, Kupitz D, Pethe A, Ulrich G, Genseke P, et al. Pharmacokinetics of 99mTc-MAA- and 99mTc-HSA-Microspheres Used in Preradioembolization Dosimetry: Influence on the Liver-Lung Shunt. Journal of Nuclear Medicine. 2016 feb;57(6):925–927.

[157] Jiang M, Fischman A, Nowakowski FS. Segmental Perfusion Differences on Paired Tc-99m Macroaggregated Albumin (MAA) Hepatic Perfusion Imaging and Yttrium-90 (Y-90) Bremsstrahlung Imaging Studies in SIR-Sphere Radioembolization: Associations with Angiography. Journal of Nuclear Medicine & Radiation Therapy. 2012;03(01).

[158] Wondergem M, Smits MLJ, Elschot M, de Jong HWAM, Verkooijen HM, van den Bosch MAAJ, et al. 99mTc-Macroaggregated Albumin Poorly Predicts the Intrahepatic Distribution of 90Y Resin Microspheres in Hepatic Radioembolization. Journal of Nuclear Medicine. 2013 jun;54(8):1294–1301.

[159] Flamen P, Vanderlinden B, Delatte P, Ghanem G, Ameye L, Eynde MVD, et al. Multimodality Imaging Can Predict the Metabolic Response of Unresectable Colorectal Liver Metastases to Radioembolization Therapy with Yttrium-90 Labeled Resin Microspheres. Physics in Medicine and Biology. 2008 oct;53(22):6591–6603.

[160] Kao YH, Steinberg JD, Tay YS, Lim GK, Yan J, Townsend DW, et al. Post-Radioembolization Yttrium-90 PET/CT - Part 2: Dose-Response and Tumor Predictive Dosimetry for Resin Microspheres. EJNMMI Research. 2013;3(1):57.

[161] Kao YH. A Clinical Dosimetric Perspective Uncovers New Evidence and Offers New Insight in Favor of 99mTc-Macroaggregated Albumin for Predictive Dosimetry in 90Y Resin Microsphere Radioembolization. Journal of Nuclear Medicine. 2013 nov;54(12):2191–2192.

[162] Dittmann H, Kopp D, Kupferschlaeger J, Feil D, Groezinger G, Syha R, et al. A Prospective Study of Quantitative SPECT/CT for Evaluation of Lung Shunt Fraction Before SIRT of Liver Tumors. Journal of Nuclear Medicine. 2018 jan;59(9):1366–1372.

[163] Allred JD, Niedbala J, Mikell JK, Owen D, Frey KA, Dewaraja YK. The Value of 99mTc-MAA SPECT/CT for Lung Shunt Estimation in 90Y Radioembolization: A Phantom and Patient Study. EJNMMI Research. 2018 jun;8(1).

[164] Ho S, Lau WY, Leung TWT, Chan M, Ngar YK, Johnson PJ, et al. Partition model for estimating radiation doses from yttrium-90 microspheres in treating hepatic tumours. European Journal of Nuclear Medicine. 1996;23(8):947–952.

[165] Gray BN, Burton MA, Kelleher DK, Anderson J, Klemp P. Selective Internal Radiation (SIR) Therapy for Treatment of Liver Metastases: Measurement of Response Rate. Journal of Surgical Oncology. 1989 nov;42(3):192–196.

[166] Kennedy AS, McNeillie P, Dezarn WA, Nutting C, Sangro B, Wertman D, et al. Treatment Parameters and Outcome in 680 Treatments of Internal Radiation With Resin 90Y-Microspheres for Unresectable Hepatic Tumors. International Journal of Radiation Oncology∗Biology∗Physics. 2009 aug;74(5):1494–1500.

[167] Vauthey JN, Abdalla EK, Doherty DA, Gertsch P, Fenstermacher MJ, Loyer EM, et al. Body Surface Area and Body Weight Predict Total Liver Volume in Western Adults. Liver Transplantation. 2002 mar;8(3):233–240.

[168] Bois DD, Eugene F. Clinical calorimetry:. Archives of Internal Medicine. 1916 jun;XVII(6_2):863.

[169] Gibbs P, Gebski V, Buskirk MV, Thurston K, Cade DN, Hazel GAV. Selective Internal Radiation Therapy (SIRT) with Yttrium-90 Resin Microspheres Plus Standard Systemic Chemotherapy Regimen of FOLFOX Versus FOLFOX Alone as First-Line Treatment of Non-Resectable Liver Metastases From Colorectal Cancer: the SIRFLOX Study. BMC Cancer. 2014 dec;14(1).

[170] Kao YH, Tan EH, Ng CE, Goh SW. Clinical Implications of the Body Surface Area Method versus Partition Model Dosimetry for Yttrium-90 Radioembolization Using Resin Microspheres: A Technical Review. Annals of Nuclear Medicine. 2011 jun;25(7):455–461.

[171] Lam MGEH, Louie JD, Abdelmaksoud MHK, Fisher GA, Cho-Phan CD, Sze DY. Limitations of Body Surface Area–Based Activity Calculation for Radioembolization of Hepatic Metastases in Colorectal Cancer. Journal of Vascular and Interventional Radiology. 2014 jul;25(7):1085–1093.

[172] Bernardini M, Smadja C, Faraggi M, Orio S, Petitguillaume A, Desbrée A, et al. Liver Selective Internal Radiation Therapy with 90Y Resin Microspheres: Comparison Between Pre-Treatment Activity Calculation Methods. Physica Medica. 2014 nov;30(7):752–764.

[173] Sangro B, Gil-Alzugaray B, Rodriguez J, Sola I, Martinez-Cuesta A, Viudez A, et al. Liver Disease Induced by Radioembolization of Liver Tumors. Cancer. 2008;112(7):1538–1546.

[174] van Roekel C, Braat AJAT, Smits MLJ, Bruijnen RCG, de Keizer B, Lam MGEH. Radioembolization. In: Clinical Nuclear Medicine. Springer International Publishing; 2020. p. 961–999.

[175] Garin E, Rolland Y, Laffont S, Edeline J. Clinical Impact of 99mTc-MAA SPECT/CT-Based Dosimetry in the Radioembolization of Liver Malignancies with 90Y-Loaded Microspheres. European Journal of Nuclear Medicine and Molecular Imaging. 2015 sep;43(3):559–575.

[176] Gulec SA, Mesoloras G, Dezarn WA, McNeillie P, Kennedy AS. Safety and Efficacy of Y-90 Microsphere Treatment in Patients with Primary and Metastatic Liver Cancer: The Tumor Selectivity of the Treatment as a Function of Tumor to Liver Fow Ratio. Journal of Translational Medicine. 2007 mar;5(1).

[177] Campbell JM, Wong CO, Muzik O, Marples B, Joiner M, Burmeister J. Early Dose Response to Yttrium-90 Microsphere Treatment of Metastatic Liver Cancer by a Patient-Specific Method Using Single Photon Emission Computed Tomography and Positron Emission Tomography. International Journal of Radiation Oncology∗Biology∗Physics. 2009 may;74(1):313–320.

[178] Kao YH, Tan AEH, Burgmans MC, Irani FG, Khoo LS, Lo RHG, et al. Image-Guided Personalized Predictive Dosimetry by Artery-Specific SPECT/CT Partition Modeling for Safe and Effective 90Y Radioembolization. Journal of Nuclear Medicine. 2012 feb;53(4):559–566.

[179] Arbizu J, Rodriguez-Fraile M, Martí-Climent JM, Domínguez-Prado I, Vigil C. Nuclear Medicine Procedures for Treatment Evaluation and Administration. In: Liver Radioembolization with 90Y Microspheres. Springer Berlin Heidelberg; 2013. p. 63–75.

[180] Garin E, Rolland Y, Lenoir L, Pracht M, Mesbah H, Porée P, et al. Utility of Quantitative 99mTc-MAA SPECT/CT for 90Yttrium-Labelled Microsphere Treatment Planning: Calculating Vascularized Hepatic Volume and Dosimetric Approach. International Journal of Molecular Imaging. 2011;2011:1–8.

[181] Garin E, Lenoir L, Rolland Y, Laffont S, Pracht M, Mesbah H, et al. Effectiveness of quantitative MAA SPECT/CT for the definition of vascularized hepatic volume and dosimetric approach. Nuclear Medicine Communications. 2011 dec;32(12):1245–1255.

[182] Grimes J, Celler A, Shcherbinin S, Piwowarska-Bilska H, Birkenfeld B. The Accuracy and Reproducibility of SPECT Target Volumes and Activities Estimated Using an Iterative Adaptive Thresholding Technique. Nuclear Medicine Communications. 2012 dec;33(12):1254–1266.

[183] Mikell JK, Mahvash A, Siman W, Baladandayuthapani V, Mourtada F, Kappadath SC. Selective Internal Radiation Therapy With Yttrium-90 Glass Microspheres: Biases and Uncertainties in Absorbed Dose Calculations Between Clinical Dosimetry Models. International Journal of Radiation Oncology∗Biology∗Physics. 2016 nov;96(4):888–896.

[184] Caruana CJ, Tsapaki V, Damilakis J, Brambilla M, Martín GM, Dimov A, et al. EFOMP Policy Statement 16: The Role and Competences of Medical Physicists and Medical Physics Experts Under 2013/59/EURATOM. Physica Medica. 2018 apr;48:162–168.

[185] Guibelalde E, Christofides S, Caruana CJ, Evan SH, Van der Putten W. European Guidelines on Medical Physics Expert. European Commission; 2014. May.

[186] Dezarn WA, Kennedy AS. Resin Y90 Microsphere Activity Measurements for Liver Brachytherapy. Medical Physics. 2007 may;34(6Part1):1896–1900.

[187] Vargas CS, Pérez SR, Baete K, Pommé S, Paepen J, Ammel RV, et al. Intercomparison of 99mTc, 18F and 111In Activity Measurements with Radionuclide Calibrators in Belgian Hospitals. Physica Medica. 2018 jan;45:134–142.

[188] Therasse P, Arbuck SG, Eisenhauer EA, Wanders J, Kaplan RS, Rubinstein L, et al. New Guidelines to Evaluate the Response to Treatment in Solid Tumors. JNCI: Journal of the National Cancer Institute. 2000 feb;92(3):205–216.

[189] Eisenhauer EA, Therasse P, Bogaerts J, Schwartz LH, Sargent D, Ford R, et al. New Response Evaluation Criteria in Solid Tumours: Revised RECIST Guideline (Version 1.1). European Journal of Cancer. 2009 jan;45(2):228–247.

[190] Lencioni R, Llovet J. Modified RECIST (mRECIST) Assessment for Hepatocellular Carcinoma. Seminars in Liver Disease. 2010 feb;30(01):052–060.

[191] Bruix J, Sherman M, Llovet JM, Beaugrand M, Lencioni R, Burroughs AK, et al. Clinical Management of Hepatocellular Carcinoma. Conclusions of the Barcelona-2000 EASL Conference. Journal of Hepatology. 2001 sep;35(3):421–430.

[192] Lauenstein TC, Schelhorn J, Kinner S. Assessment of Tumor Response with MRI and CT After Radioembolization. In: Clinical Nuclear Medicine. Springer International Publishing; 2020. p. 1001–1009.

[193] Young H, Baum R, Cremerius U, Herholz K, Hoekstra O, Lammertsma AA, et al. Measurement of Clinical and Subclinical Tumour Response Using [18F]-Fluorodeoxyglucose and Positron Emission Tomography: Review and 1999 EORTC Recommendations. European Journal of Cancer. 1999 dec;35(13):1773–1782.

[194] Wahl RL, Jacene H, Kasamon Y, Lodge MA. From RECIST to PERCIST: Evolving Considerations for PET Response Criteria in Solid Tumors. Journal of Nuclear Medicine. 2009 apr;50(Suppl_1):122S–150S.

[195] Gordic S, Wagner M, Zanato R, Hectors S, Besa C, Kihira S, et al. Prediction of Hepatocellular Carcinoma Response to 90Yttrium Radioembolization Using Volumetric ADC Histogram Quantification: Preliminary Results. Cancer Imaging. 2019 may;19(1).

[196] Haug A, Schmidt GP. Evaluation of the Response by Multimodality Imaging. In: Liver Radioembolization with 90Y Microspheres. Springer Berlin Heidelberg; 2013. p. 91–103.

[197] Johnson DT, Kesner AL. Yttrium-90 Selective Internal Radiation Therapy. In: Radiation Therapy for Liver Tumors. Springer International Publishing; 2017. p. 121–131.

[198] Maccauro M, Lorenzoni A, Boni G, Chiesa C, Spreafico C, Romito R, et al. Multiagent Imaging of Liver Tumors with Reference to Intra-Arterial Radioembolization. Clinical and Translational Imaging. 2013 dec;1(6):423–432.

[199] Macapinlac HA. Assessing Response to Therapy. In: Silverman PM, editor. Oncologic Imaging: A Multidisciplinary Approach. Philadelphia: Elsevier; 2012. p. 25–33.

[200] Kappadath SC, Mikell J, Balagopal A, Baladandayuthapani V, Kaseb A, Mahvash A. Hepatocellular Carcinoma Tumor Dose Response After 90Y-radioembolization With Glass Microspheres Using 90Y-SPECT/CT-Based Voxel Dosimetry. International Journal of Radiation Oncology∗Biology∗Physics. 2018 oct;102(2):451–461.

[201] European Society of Radiology (ESR and others). Summary of the European Directive 2013/59/Euratom: Essentials for Health Professionals in Radiology. Insights into Imaging. 2015 may;6(4):411–417.

[202] Heinemann A, Wischhusen F, Püschel K, Rogiers X. Standard Liver Volume in the Caucasian Population. Liver Transplantation and Surgery. 1999 sep;5(5):366–368.

[203] Gil-Alzugaray B, Chopitea A, Iñarrairaegui M, Bilbao JI, Rodriguez-Fraile M, Rodriguez J, et al. Prognostic Factors and Prevention of Radioembolization-Induced Liver Disease. Hepatology. 2013 feb;57(3):1078–1087.

[204] Samim M, Lam MGEH. Safety and Efficacy of Y-90 Radioembolization After Prior Major Hepatic Resection: Dosimetric Consideration. CardioVascular and Interventional Radiology. 2017 may;40(8):1293–1294.

[205] Selwyn R, Micka J, DeWerd L, Nickles R, Thomadsen B. Technical Note: The Calibration of Y90-Labeled SIR-Spheres® Using a Nondestructive Spectroscopic Assay. Medical Physics. 2008 mar;35(4):1278–1279.

[206] Caribé PRRV, Koole M, D'Asseler Y, Deller TW, Laere KV, Vandenberghe S. NEMA NU 2–2007 Performance Characteristics of GE Signa Integrated PET/MR for Different PET Isotopes. EJNMMI Physics. 2019 jul;6(1).

[207] Mo L, Avci B, James D, Simpson B, Wyngaardt WMV, Cessna JT, et al. Development of Activity Standard for 90Y Microspheres. Applied Radiation and Isotopes. 2005 aug;63(2):193–199.

[208] Directive Council. 59/Euratom of 5 December 2013 laying down basic safety standards for protection against the dangers arising from exposure to ionising radiation, and repealing Directives 89/618/Euratom, 90/641/Euratom, 96/29/Euratom, 97/43/Euratom and 2003/122/Euratom. Euratom; 2013.

[209] De Moor K, Nuyts J, Plessers L, Stroobants S, Maes F, Dupont P. Non-Rigid Registration with Position Dependent Rigidity for Whole Body PET Follow-Up Studies. In: 2006 IEEE Nuclear Science Symposium Conference Record. IEEE; 2006. p. 3502–3506.

[210] Kamnitsas K, Ledig C, Newcombe VFJ, Simpson JP, Kane AD, Menon DK, et al. Efficient Multi-Scale 3D CNN with Fully Connected CRF for Accurate Brain Lesion Segmentation. Medical Image Analysis. 2017 feb;36:61–78.

[211] Tang X, Jafargholi Rangraz E, Coudyzer W, Bertels J, Robben D, Schramm G, et al. Whole Liver Segmentation Based on Deep Learning and Manual Adjustment for Clinical Use in SIRT. European Journal of Nuclear Medicine and Molecular Imaging. 2020 apr;46(SUPPL 1):S763—-S763.

[212] Firouzian A, Kelly MD, Declerck JM. Insight on Automated Lesion Delineation Methods for PET Data. EJNMMI Research. 2014 dec;4(1).

[213] Low DA, Harms WB, Mutic S, Purdy JA. A Technique for the Quantitative Evaluation of Dose Distributions. Medical Physics. 1998 may;25(5):656–661.

[214] Hussein M, Clark CH, Nisbet A. Challenges in Calculation of the Gmma Index in Radiotherapy – Towards Good Practice. Physica Medica. 2017 apr;36:1–11.

[215] Li H, Dong L, Zhang L, Yang JN, Gillin MT, Zhu XR. Toward a Better Understanding of the Gamma Index: Investigation of Parameters with a Surface-Based Distance Method. Medical Physics. 2011 nov;38(12):6730–6741.

[216] Ferreira P, Parafita R, Canudo A, Oliveira C, Rosa L, Correia PL, et al. Gamma-Index and Dose-Volume Histograms (Based on Voxel Dosimetry) to Evaluate the Predictive Power of 99mTc-MAA SPECT Maps in Comparison with Post-Radioembolization 90Y PET Maps. In: 2017 IEEE 5th Portuguese Meeting on Bioengineering (ENBENG). IEEE; 2017. p. 1–4.

[217] Ferreira P, Parafita R, Girão PS, Correia PL, Costa DC. Radioembolization with 90Y-Labeled Glass Microspheres: Analytical Methods for Patient-Personalized Voxel-Based Dosimetry. In: VipIMAGE 2017. Springer International Publishing; 2017. p. 185–191.

[218] Chansanti O, Jahangiri Y, Matsui Y, Adachi A, Geeratikun Y, Kaufman JA, et al. Tumor Dose Response in Yttrium-90 Resin Microsphere Embolization for Neuroendocrine Liver Metastases: A Tumor-Specific Analysis with Dose Estimation Using SPECT-CT. Journal of Vascular and Interventional Radiology. 2017 nov;28(11):1528–1535.

[219] Choi E, Lin MH, Saboury B, Le Q, D'Emic N, Sharma NK, et al. Liver Toxicity Versus Dose Volume Parameters of Normal Liver for Yttrium-90 Radioembolization of Hepatic Tumors. International Journal of Radiation Oncology∗Biology∗Physics. 2015 nov;93(3):E179.

[220] Kafrouni M, Allimant C, Fourcade M, Vauclin S, Delicque J, Ilonca AD, et al. Retrospective Voxel-Based Dosimetry for Assessing the Ability of the Body-Surface-Area Model to Predict Delivered Dose and Radioembolization Outcome. Journal of Nuclear Medicine. 2018 mar;59(8):1289–1295.

[221] Hendlisz A, den Eynde MV, Peeters M, Maleux G, Lambert B, Vannoote J, et al. Phase III Trial Comparing Protracted Intravenous Fluorouracil Infusion Alone or With Yttrium-90 Resin Microspheres Radioembolization for Liver-Limited Metastatic Colorectal Cancer Refractory to Standard Chemotherapy. Journal of Clinical Oncology. 2010 aug;28(23):3687–3694.

[222] Rognoni C, Ciani O, Sommariva S, Facciorusso A, Tarricone R, Bhoori S, et al. Trans-Arterial Radioembolization in Intermediate-Advanced Hepatocellular Carcinoma: Systematic Review and Meta-Analyses. Oncotarget. 2016 aug;7(44):72343–72355.

[223] Lobo L, Yakoub D, Picado O, Ripat C, Pendola F, Sharma R, et al. Unresectable Hepatocellular Carcinoma: Radioembolization Versus Chemoembolization: A Systematic Review and Meta-analysis. CardioVascular and Interventional Radiology. 2016 sep;39(11):1580–1588.

[224] Kolligs FT, Bilbao JI, Jakobs T, Iñarrairaegui M, Nagel JM, Rodriguez M, et al. Pilot Randomized Trial of Selective Internal Radiation Therapy vs. Chemoembolization in Unresectable Hepatocellular Carcinoma. Liver International. 2015 jan;35(6):1715–1721.

[225] Ricke J, Bulla K, Kolligs F, Peck-Radosavljevic M, Reimer P, Sangro B, et al. Safety and Toxicity of Radioembolization Plus Sorafenib in Advanced Hepatocellular Carcinoma: Analysis of the European Multicentre Trial SORAMIC. Liver International. 2014 jul;35(2):620–626.

[226] Lewandowski RJ, Andreoli JM, Hickey R, Kallini JR, Gabr A, Baker T, et al. Angiogenic Response Following Radioembolization: Results from a Randomized Pilot Study of Yttrium-90 with or without Sorafenib. Journal of Vascular and Interventional Radiology. 2016 sep;27(9):1329–1336.

[227] Padia SA, Lewandowski RJ, Johnson GE, Sze DY, Ward TJ, Gaba RC, et al. Radioembolization of Hepatic Malignancies: Background, Quality Improvement Guidelines, and Future Directions. Journal of Vascular and Interventional Radiology. 2017 jan;28(1):1–15.

[228] Ibrahim SM, Lewandowski RJ, Ryu RK, Sato KT, Gates VL, Mulcahy MF, et al. Radiographic Response to Yttrium-90 Radioembolization in Anterior Versus Posterior Liver Segments. CardioVascular and Interventional Radiology. 2008 may;31(6):1124–1132.

[229] Mahnken AH, Spreafico C, Maleux G, Helmberger T, Jakobs TF. Standards of Practice in Transarterial Radioembolization. CardioVascular and Interventional Radiology. 2013 mar;36(3):613–622.

[230] Minarik D, Gleisner KS, Ljungberg M. Evaluation of Quantitative90Y SPECT Based on Experimental Phantom Studies. Physics in Medicine and Biology. 2008 sep;53(20):5689–5703.

[231] Selwyn RG, Nickles RJ, Thomadsen BR, DeWerd LA, Micka JA. A New internal Pair Production Branching Ratio of 90Y: The Development of a Non-Destructive Assay for 90Y and 90Sr. Applied Radiation and Isotopes. 2007 mar;65(3):318–327.

[232] Maughan NM, Eldib M, Faul D, Conti M, Elschot M, Knešaurek K, et al. Multi Institutional Quantitative Phantom Study of Yttrium-90 PET in PET/MRI: the MR-QUEST Study. EJNMMI Physics. 2018 apr;5(1).

[233] Yue J, Mauxion T, Reyes DK, Lodge MA, Hobbs RF, Rong X, et al. Comparison of Quantitative Y-90 SPECT and Non-Time-of-Flight PET Imaging in Post-Therapy Radioembolization of Liver Cancer. Medical Physics. 2016 sep;43(10):5779–5790.

[234] Wright CL, Binzel K, Zhang J, Wuthrick EJ, Knopp MV. Clinical Feasibility of 90Y Digital PET/CT for Imaging Microsphere Biodistribution Following Radioembolization. European Journal of Nuclear Medicine and Molecular Imaging. 2017 apr;44(7):1194–1197.

[235] Gray BN, Burton MA, Kelleher D, Klemp P, Matz L. Tolerance of the Liver to the Effects of Yttrium-90 Radiation. International Journal of Radiation Oncology∗Biology∗Physics. 1990 mar;18(3):619–623.

[236] Welsh JS, Kennedy AS, Thomadsen B. Selective Internal Radiation Therapy (SIRT) for Liver Metastases Secondary to Colorectal Adenocarcinoma. International Journal of Radiation Oncology∗tBiology∗Physics. 2006 oct;66(2):S62–S73.

[237] Garin E, Lenoir L, Rolland Y, Edeline J, Mesbah H, Laffont S, et al. Dosimetry Based on 99mTc-Macroaggregated Albumin SPECT/CT Accurately Predicts Tumor Response and Survival in Hepatocellular Carcinoma Patients Treated with 90Y-Loaded Glass Microspheres: Preliminary Results. Journal of Nuclear Medicine. 2012 feb;53(2):255–263.

[238] Kao YH. General Theory of Predictive Dosimetry for Yttrium-90 Radioembolization to Sites Other than the Liver. CardioVascular and Interventional Radiology. 2013 nov;37(4):1114–1117.

[239] Högberg J, Rizell M, Hultborn R, Svensson J, Henrikson O, Mölne J, et al. Increased Absorbed Liver Dose in Selective Internal Radiation Therapy (SIRT) Correlates with Increased Sphere-Cluster Frequency and Absorbed Dose Inhomogeneity. EJNMMI Physics. 2015 apr;2(1).

[240] Flamen P, Hendlisz A, Vanderlinden B. Selective Internal Radiation Therapy Simulation Using 99mTc-Labelled Macroaggregates of Albumin and SPECT-CT. European Journal of Cancer Supplements. 2012 aug;10(3):54–56.

[241] Pacilio M, Ferrari M, Chiesa C, Lorenzon L, Mira M, Botta F, et al. Impact of SPECT Corrections on 3D-Dosimetry for Liver Transarterial Eadioembolization Using the Patient Relative Calibration Methodology. Medical Physics. 2016 jun;43(7):4053–4064.

[242] Pasciak AS, Bourgeois AC, Bradley YC. A Comparison of Techniques for 90Y PET/CT Image-Based Dosimetry Following Radioembolization with Resin Microspheres. Frontiers in Oncology. 2014 may;4.

[243] Gnesin S, Canetti L, Adib S, Cherbuin N, Monteiro MS, Bize P, et al. Partition Model-Based 99mTc-MAA SPECT/CT Predictive Dosimetry Compared with 90Y TOF PET/CT Posttreatment Dosimetry in Radioembolization of Hepatocellular Carcinoma: A Quantitative Agreement Comparison. Journal of Nuclear Medicine. 2016 jun;57(11):1672–1678.

[244] Ljungberg M, Sjögreen-Gleisner K. The accuracy of Absorbed Dose Estimates in Tumours Determined by Quantitative SPECT: A Monte Carlo Study. Acta Oncologica. 2011 jul;50(6):981–989.

[245] Giammarile F, Muylle K, Bolton RD, Kunikowska J, Haberkorn U, Oyen W. Dosimetry in Clinical Radionuclide Therapy: The Devil is in the Detail. European Journal of Nuclear Medicine and Molecular Imaging. 2017 sep;44(12):1–3.

[246] Flux GD, Sjögreen-Gleisner K, Chiesa C, Lassmann M, Chouin N, Gear J, et al. From Fixed Activities to Personalized Treatments in Radionuclide Therapy: Lost in Translation? European Journal of Nuclear Medicine and Molecular Imaging. 2017 oct;45(1):152–154.

[247] Sjögreen-Gleisner K, Spezi E, Solny P, Gabina PM, Cicone F, Stokke C, et al. Variations in the Practice of Molecular Radiotherapy and Implementation of Dosimetry: Results from a European Survey. EJNMMI Physics. 2017 dec;4(1).

[248] Smits MLJ, Elschot M, Sze DY, Kao YH, Nijsen JFW, Iagaru AH, et al. Radioembolization Dosimetry: The Road Ahead. CardioVascular and Interventional Radiology. 2014 dec;38(2):261–269.

[249] Luu HM, Klink C, Niessen W, Moelker A, van Walsum T. Non-Rigid Registration of Liver CT Images for CT-Guided Ablation of Liver Tumors. PLOS ONE. 2016 sep;11(9):e0161600.

[250] Carvalho LE, Sobieranski AC, von Wangenheim A. 3D Segmentation Algorithms for Computerized Tomographic Imaging: a Systematic Literature Review. Journal of Digital Imaging. 2018 jun;31(6):799–850.

[251] Moghbel M, Mashohor S, Mahmud R, Saripan MIB. Review of Liver Segmentation and Computer Assisted Detection/Diagnosis Methods in Computed Tomography. Artificial Intelligence Review. 2017 mar;50(4):497–537.

[252] Lim SJ, Jeong YY, Ho YS. Automatic Liver Segmentation for Volume Measurement in CT Images. Journal of Visual Communication and Image Representation. 2006 aug;17(4):860–875.

[253] Campadelli P, Casiraghi E, Esposito A. Liver Segmentation from Computed Tomography Scans: A survey and a New Algorithm. Artificial Intelligence in Medicine. 2009 feb;45(2-3):185–196.

[254] Liao M, qian Zhao Y, Wang W, zhan Zeng Y, Yang Q, Shih FY, et al. Efficient Liver Segmentation in CT Images Based on Graph Cuts and Bottleneck Detection. Physica Medica. 2016 nov;32(11):1383–1396.

[255] Wu W, Zhou Z, Wu S, Zhang Y. Automatic Liver Segmentation on Volumetric CT Images Using Supervoxel-Based Graph Cuts. Computational and Mathematical Methods in Medicine. 2016;2016:1–14.

[256] Moghbel M, Mashohor S, Mahmud R, Saripan MIB. Automatic Liver Segmentation on Computed Tomography Using Random Walkers for Treatment Planning. EXCLI Journal. 2016;50:497–537.

[257] Massoptier L, Casciaro S. Fully Automatic Liver Segmentation through Graph-Cut Technique. In: 2007 29th Annual International Conference of the IEEE Engineering in Medicine and Biology Society. IEEE; 2007. p. 5243–5246.

[258] Ruskó L, Bekes G, Fidrich M. Automatic Segmentation of the Liver from Multi- and Single-Phase Contrast-Enhanced CT Images. Medical Image Analysis. 2009 dec;13(6):871–882.

[259] Wang J, Cheng Y, Guo C, Wang Y, Tamura S. Shape–Intensity Prior Level Set Combining Probabilistic Atlas and Probability Map Constrains for Automatic Liver Segmentation from Abdominal CT Images. International Journal of Computer Assisted Radiology and Surgery. 2015 dec;11(5):817–826.

[260] Chartrand G, Cresson T, Chav R, Gotra A, Tang A, DeGuise J. SEMI-Automated Liver CT Segmentation Using Laplacian Meshes. In: 2014 IEEE 11th International Symposium on Biomedical Imaging (ISBI). IEEE; 2014. p. 641–644.

[261] Shi C, Cheng Y, Liu F, Wang Y, Bai J, Tamura S. A Hierarchical Local Region-Based Sparse Shape Composition for Liver Segmentation in CT Scans. Pattern Recognition. 2016 feb;50:88–106.

[262] Slagmolen P, Elen A, Seghers D, Loeckx D, Maes F, Haustermans K. Atlas based liver segmentation using nonrigid registration with a B-spline transformation model. In: Proceedings of MICCAI workshop on 3D segmentation in the clinic: a grand challenge. Citeseer; 2007. p. 197–206.

[263] Okada T, Shimada R, Hori M, Nakamoto M, Chen YW, Nakamura H, et al. Automated Segmentation of the Liver from 3D CT Images Using Probabilistic Atlas and Multilevel Statistical Shape Model. Academic Radiology. 2008 nov;15(11):1390–1403.

[264] Heimann T, Wolf I, Meinzer HP. Active Shape Models for a Fully Automated 3D Segmentation of the Liver – An Evaluation on Clinical Data. In: Medical Image Computing and Computer-Assisted Intervention – MICCAI 2006. Springer Berlin Heidelberg; 2006. p. 41–48.

[265] Erdt M, Kirschner M. Fast automatic liver segmentation combining learned shape priors with observed shape deviation. In: 2010 IEEE 23rd International Symposium on Computer-Based Medical Systems (CBMS). IEEE; 2010. p. 249–254.

[266] Li C, Li A, Wang X, Feng D, Eberl S, Fulham M. A New Statistical and Dirichlet Integral Framework Applied to Liver Segmentation from Volumetric CT Images. In: 2014 13th International Conference on Control Automation Robotics & Vision (ICARCV). IEEE; 2014. p. 642–647.

[267] Christ PF, Elshaer MEA, Ettlinger F, Tatavarty S, Bickel M, Bilic P, et al. Automatic Liver and Lesion Segmentation in CT Using Cascaded Fully Convolutional Neural Networks and 3D Conditional Random Fields. In: Medical Image Computing and Computer-Assisted Intervention – MICCAI 2016. Springer International Publishing; 2016. p. 415–423.

[268] Lu F, Wu F, Hu P, Peng Z, Kong D. Automatic 3D Liver Location and Segmentation via Convolutional Neural Network and Graph Cut. International Journal of Computer Assisted Radiology and Surgery. 2016 sep;12(2):171–182.

[269] Dou Q, Chen H, Jin Y, Yu L, Qin J, Heng PA. 3D Deeply Supervised Network for Automatic Liver Segmentation from CT Volumes. In: Medical Image Computing and Computer-Assisted Intervention – MICCAI 2016. Springer International Publishing; 2016. p. 149–157.

[270] Ben-Cohen A, Diamant I, Klang E, Amitai M, Greenspan H. Fully Convolutional Network for Liver Segmentation and Lesions Detection. In: Deep Learning and Data Labeling for Medical Applications. Springer International Publishing; 2016. p. 77–85.

[271] Monsky WL, Garza AS, Kim I, Loh S, Lin TC, Li CS, et al. Treatment Planning and Volumetric Response Assessment for Yttrium-90 Radioembolization: Semiautomated Determination of Liver Volume and Volume of Tumor Necrosis in Patients with Hepatic Malignancy. CardioVascular and Interventional Radiology. 2010 aug;34(2):306–318.

[272] Goryawala M, Guillen MR, Cabrerizo M, Barreto A, Gulec S, Barot TC, et al. A 3-D Liver Segmentation Method with Parallel Computing for Selective Internal Radiation Therapy. IEEE Transactions on Information Technology in Biomedicine. 2012 jan;16(1):62–69.

[273] Goryawala M, Gulec S, Bhatt R, McGoron AJ, Adjouadi M. A Low-Interaction Automatic 3D Liver Segmentation Method Using Computed Tomography for Selective Internal Radiation Therapy. BioMed Research International. 2014;2014:1–12.

[274] Wang X, Li C, Fulham M, Eberl S, Feng D. PET-Enhanced Liver Segmentation for CT Images from Combined PET-CT Scanners. In: 2009 IEEE Nuclear Science Symposium Conference Record (NSS/MIC). IEEE; 2009. p. 2756–2759.

[275] Li C, Wang X, Chen J, Yin Y, Feng D. PET-Guided Liver Segmentation for Low-Contrast CT via Regularized Chan-Vese Model. In: Proceedings of 2012 IEEE-EMBS International Conference on Biomedical and Health Informatics. IEEE; 2012. p. 816–819.

[276] Li C, Wang X, Xia Y, Eberl S, Yin Y, Feng DD. Automated PET-Guided Liver Segmentation from Low-Contrast CT Volumes Using Probabilistic Atlas. Computer Methods and Programs in Biomedicine. 2012 aug;107(2):164–174.

[277] Mendes D, Ferreira N, Silva J, Caramelo F. 3D Liver Segmentation in Computed Tomography and Positron Emission Tomography Exams Through Active Surfaces. In: 2015 IEEE 4th Portuguese Meeting on Bioengineering (ENBENG). IEEE; 2015. p. 1–6.

[278] Spahr N, Schilling P, Thoduka S, Abolmaali N, Schenk A. Predictive SIRT Dosimetry Based on a Territorial Model. EJNMMI Physics. 2017 oct;4(1).

[279] Floridi C, Radaelli A, Abi-Jaoudeh N, Grass M, Lin MD, Chiaradia M, et al. C-Arm Cone-Beam Computed Tomography in Interventional Oncology: Technical Aspects and Clinical Applications. La radiologia medica. 2014 jul;119(7):521–532.

[280] Derbel H, Kobeiter H, Pizaine G, Ridouani F, Luciani A, Radaelli A, et al. Accuracy of a Cone-Beam CT Virtual Parenchymal Perfusion Algorithm for Liver Cancer Targeting during Intra-arterial Therapy. Journal of Vascular and Interventional Radiology. 2018 feb;29(2):254–261.e2.

[281] Limited SM. SIR-Spheres microspheres (training program / Physicians and Instituions). Sirtex; 2015.

[282] Zeintl J, Vija AH, Yahil A, Hornegger J, Kuwert T. Quantitative Accuracy of Clinical 99mTc SPECT/CT Using Ordered-Subset Expectation Maximization with 3-Dimensional Resolution Recovery, Attenuation, and Scatter Correction. Journal of Nuclear Medicine. 2010 may;51(6):921–928.

[283] Bastiaannet R, Viergever MA, de Jong HWAM. Impact of Respiratory Motion and Acquisition Settings on SPECT Liver Dosimetry for Radioembolization. Medical Physics. 2017 aug;44(10):5270–5279.

[284] Christensen GE, Joshi SC, Miller MI. Volumetric Transformation of Brain Anatomy. IEEE Transactions on Medical Imaging. 1997;16(6):864–877.

[285] Oliveira FPM, Tavares JMRS. Medical Image Registration: A Review. Computer Methods in Biomechanics and Biomedical Engineering. 2012 mar;17(2):73–93.

[286] Temmerman F, Ho TA, Vanslembrouck R, Coudyzer W, Billen J, Dobbels F, et al. Lanreotide Reduces Liver Volume, But Might Not Improve Muscle Wasting or Weight Loss, in Patients With Symptomatic Polycystic Liver Disease. Clinical Gastroenterology and Hepatology. 2015 dec;13(13):2353–2359.e1.

[287] Taha AA, Hanbury A. Metrics for Evaluating 3D Medical Iimage Segmentation: Analysis, Selection, and Tool. BMC Medical Imaging. 2015 aug;15(1).

[288] Heimann T, van Ginneken B, Styner MA, Arzhaeva Y, Aurich V, Bauer C, et al. Comparison and Evaluation of Methods for Liver Segmentation From CT Datasets. IEEE Transactions on Medical Imaging. 2009 aug;28(8):1251–1265.

[289] Richetta E, Pasquino M, Poli M, Cutaia C, Valero C, Tabone M, et al. PET-CT Post Therapy Dosimetry in Radioembolization with Resin 90Y Microspheres: Comparison with Pre-Treatment SPECT-CT 99mTc-MAA Results. Physica Medica. 2019 aug;64:16–23.

[290] Bilic P, Ferdinand PC, Vorontsov E, Chlebus G, Chen H, Dou Q, et al. The Liver Tumor Segmentation Benchmark (LiTS); 2019.

[291] Simpson AL, Antonelli M, Bakas S, Bilello M, Farahani K, van Ginneken B, et al. A Large Annotated Medical Image Dataset for the Development and Evaluation of Segmentation Algorithms; 2019.

[292] Pasciak AS, Bourgeois AC, McKinney JM, Chang TT, Osborne DR, Acuff SN, et al. Radioembolization and the Dynamic Role of 90Y PET/CT. Frontiers in Oncology. 2014;4.

[293] Kim SP, Cohalan C, Kopek N, Enger SA. A Guide to 90Y Radioembolization and Its Dosimetry. Physica Medica. 2019 dec;68:132–145.

[294] Haste P, Tann M, Persohn S, LaRoche T, Aaron V, Mauxion T, et al. Correlation of Technetium-99m Macroaggregated Albumin and Yttrium-90 Glass Microsphere Biodistribution in Hepatocellular Carcinoma: A Retrospective Review of Pretreatment Single Photon Emission CT and Posttreatment Positron Emission Tomography/CT. Journal of Vascular and Interventional Radiology. 2017 may;28(5):722–730.e1.

[295] Elschot M, Nijsen JFW, Lam MGEH, Smits MLJ, Prince JF, Viergever MA, et al. 99mTc-MAA Overestimates the Absorbed Dose to the Lungs in Radioembolization: A Quantitative Evaluation in Patients Treated with 166Ho-Microspheres. European Journal of Nuclear Medicine and Molecular Imaging. 2014 may;41(10):1965–1975.

[296] Jadoul A, Bernard C, Lovinfosse P, Gérard L, Lilet H, Cornet O, et al. Comparative Dosimetry Between 99mTc-MAA SPECT/CT and 90Y PET/CT in Primary and Metastatic Liver Tumors. European Journal of Nuclear Medicine and Molecular Imaging. 2019 aug;47(4):828–837.

[297] Chiesa C, Maccauro M. 166Ho Microsphere Scout Dose for More Accurate Radioembolization Treatment Planning. European Journal of Nuclear Medicine and Molecular Imaging. 2019 dec;47(4):744–747.

[298] Walrand S, Hesse M, Chiesa C, Lhommel R, Jamar F. The Low Hepatic Toxicity per Gray of 90Y Glass Microspheres Is Linked to Their Transport in the Arterial Tree Favoring a Nonuniform Trapping as Observed in Posttherapy PET Imaging. Journal of Nuclear Medicine. 2013 dec;55(1):135–140.

[299] Walrand S, Hesse M. PET/CT Specificities in 90Y Imaging Post Radioembolization. PET Clinics. 2019 oct;14(4):469–476.

[300] Niemierko A. Reporting and Analyzing Dose Distributions: A Concept of Equivalent Uniform Dose. Medical Physics. 1997 jan;24(1):103–110.

[301] Cremonesi M, Ferrari M, Botta F, Guerriero F, Garibaldi C, Bodei L, et al. Planning Combined Treatments of External Beam Radiation Therapy and Molecular Radiotherapy. Cancer Biotherapy and Radiopharmaceuticals. 2014 aug;29(6):227–237.

[302] Chiesa C, Mira M, Maccauro M, Spreafico C, Romito R, Morosi C, et al. Radioembolization of hepatocarcinoma with 90Y glass microspheres: development of an individualized treatment planning strategy based on dosimetry and radiobiology. European Journal of Nuclear Medicine and Molecular Imaging. 2015 jun;42(11):1718–1738.

[303] d'Abadie P, Hesse M, Jamar F, Lhommel R, Walrand S. 90Y TOF-PET Based EUD Reunifies Patient Survival Prediction in Resin and Glass Microspheres Radioembolization of HCC Tumours. Physics in Medicine & Biology. 2018 dec;63(24):245010.

[304] Chiesa C, Maccauro M, Romito R, Spreafico C, Pellizzari S, Negri A, et al. Need, Feasibility and Convenience of Dosimetric Treatment Planning in Liver Selective Internal Radiation Therapy with 90Y Microspheres: The Experience of the National Cancer Institute of Milan. Quarterly Journal of Nuclear Medicine and Molecular Imaging. 2011;55(2):168–197.

[305] Braat MNGJA, de Jong HW, Seinstra BA, Scholten MV, van den Bosch MAAJ, Lam MGEH. Hepatobiliary Scintigraphy May Improve Radioembolization Treatment Planning in HCC Patients. EJNMMI Research. 2017 jan;7(1).

[306] Mörk H, Ignee A, Schuessler G, Ott M, Dietrich CF. Analysis of Neuroendocrine Tumour Metastases in the Liver Using Contrast Enhanced Ultrasonography. Scandinavian Journal of Gastroenterology. 2007 jan;42(5):652–662.

[307] Pasciak AS, McElmurray JH, Bourgeois AC, Heidel RE, Bradley YC. The Impact of an Antireflux Catheter on Target Volume Particulate Distribution in Liver-Directed Embolotherapy: A Pilot Study. Journal of Vascular and Interventional Radiology. 2015 may;26(5):660–669.

[308] Mikell JK, Kaza RK, Roberson PL, Younge KC, Srinivasa RN, Majdalany BS, et al. Impact of 90Y PET Gradient-Based Tumor Segmentation on Voxel-Level Dosimetry in Liver Radioembolization. EJNMMI Physics. 2018 nov;5(1).

[309] Meyers N, Jadoul A, Bernard C, Delwaide J, Lamproye A, Detry O, et al. Inter-Observer Variability of 90Y PET/CT Dosimetry in Hepatocellular Carcinoma After Gglass Microspheres Transarterial Radioembolization. EJNMMI Physics. 2020 may;7(1).

[310] Willowson KP, Schembri GP, Bernard EJ, Chan DL, Bailey DL. Quantifying the Effects of Absorbed Dose from Radioembolisation on Healthy Liver Function with [99mTc]TcMebrofenin. European Journal of Nuclear Medicine and Molecular Imaging. 2020 jan;47(4):838–848.

[311] Van Der Velden S, Braat MNGJA, Labeur TA, Scholten MV, Van Delden OM, Bennink RJ, et al. A Pilot Study on Hepatobiliary Scintigraphy to Monitor Regional Liver Function in 90Y Radioembolization. Journal of Nuclear Medicine. 2019 apr;60(10):1430–1436.

[312] Kafrouni M, Allimant C, Fourcade M, Vauclin S, Guiu B, Mariano-Goulart D, et al. Analysis of Differences Between 99mTc-MAA SPECT- and 90Y-Microsphere PET-Based Dosimetry for Hepatocellular Carcinoma Selective Internal Radiation Therapy. EJNMMI Research. 2019 jul;9(1).

[313] Grözinger G, Kupferschläger J, Dittmann H, Maurer M, Grosse U, la Fougère C, et al. Assessment of the Parenchymal Blood Volume by C-Arm Computed Tomography for Radioembolization Dosimetry. European Journal of Radiology. 2016 sep;85(9):1525–1531.

[314] Rincón JO, Regi AR, Leyte MG, Martín LC, Pascual RP, Farto JCA. Hepatic Supraselective Radioembolization, Today and New Horizons. European Journal of Nuclear Medicine and Molecular Imaging. 2019 aug;46(12):2412–2413.

[315] Gear JI, Cummings C, Craig AJ, Divoli A, Long CDC, Tapner M, et al. Abdo-Man: a 3D-Printed Anthropomorphic Phantom for Validating Quantitative SIRT. EJNMMI Physics. 2016 aug;3(1).

[316] Willowson KP, , Tapner M, Bailey DL, The QUEST Investigator Team. A Multicentre Comparison of Quantitative 90Y PET/CT for Dosimetric Purposes After Radioembolization with Resin Microspheres. European Journal of Nuclear Medicine and Molecular Imaging. 2015 may;42(8):1202–1222.

[317] Ilhan H, Goritschan A, Paprottka P, Jakobs TF, Fendler WP, Bartenstein P, et al. Systematic Evaluation of Tumoral 99mTc-MAA Uptake Using SPECT and SPECT/CT in 502 Patients Before 90Y Radioembolization. Journal of Nuclear Medicine. 2015 feb;56(3):333–338.

[318] Ambrosini P, Ruijters D, Niessen WJ, Moelker A, van Walsum T. Continuous Roadmapping in Liver TACE Procedures Using 2D–3D Catheter-Based Registration. International Journal of Computer Assisted Radiology and Surgery. 2015 may;10(9):1357–1370.

[319] Duménil A, Kaladji A, Castro M, Göksu C, Lucas A, Haigron P. A Versatile Intensity-Based 3D/2D Rigid Registration Compatible with Mobile C-Arm for Endovascular Treatment of Abdominal Aortic Aneurysm. International Journal of Computer Assisted Radiology and Surgery. 2016 may;11(9):1713–1729.

[320] van Roekel C, Reinders MTM, van der Velden S, Lam MGEH, Braat MNGJA. Hepatobiliary Imaging in Liver-directed Treatments. Seminars in Nuclear Medicine. 2019 may;49(3):227–236.

[321] Bastiaannet R, van Roekel C, Smits MLJ, Elias SG, van Amsterdam WAC, Doan D, et al. First Evidence for a Dose–Response Relationship in Patients Treated with 166Ho Radioembolization: A Prospective Study. Journal of Nuclear Medicine. 2019 oct;61(4):608–612.

[322] Smits MLJ, Dassen MG, Prince JF, Braat AJAT, Beijst C, Bruijnen RCG, et al. The Superior Predictive Value of 166Ho-Scout Compared with 99mTc-Macroaggregated Albumin Prior to 166Ho-Microspheres Radioembolization in Patients with Liver Metastases. European Journal of Nuclear Medicine and Molecular Imaging. 2019 aug;47(4):798–806.

[323] Smits MLJ, Elschot M, van den Bosch MAAJ, van de Maat GH, van het Schip AD, Zonnenberg BA, et al. In Vivo Dosimetry Based on SPECT and MR Imaging of 166Ho-Microspheres for Treatment of Liver Malignancies. Journal of Nuclear Medicine. 2013 oct;54(12):2093–2100.

[324] Salem R, Lewandowski RJ, Gates VL, Nutting CW, Murthy R, Rose SC, et al. Research Reporting Standards for Radioembolization of Hepatic Malignancies. Journal of Vascular and Interventional Radiology. 2011 mar;22(3):265–278.

Chapter 7

Acknowledgment, Personal Contribution, and Conflict of Interest statements

7.1 Scientific acknowledgment

I would like to thank my leading promoter (*Johan Nuyts*), and co-promoters (*Christophe Deroose* and *Kristof Baete*) for conceptualizing the projects, their ideas, and patient feedback, mentorship, and scientific/clinical supervision.

We thank members of the examination committee (*Geert Maleux*, *Patrick Dupont*, *Stephan Walrand*, and *Marnix Lam*) and thesis advisory committee (*Ghislain Opdenakker*, *Steven Dymarkowski*, *Lieven Dupont*, and *Inge Depoortere*) for their guidance and support on this journey.

I would like to acknowledge the following persons for their contributions, which may or may not be listed as co-authors in the published/submitted articles:

- We wish to thank *Johan Nuyts' Group* for their creative input during group meetings, particularly *Georg Schramm* and *Ahmadreza Rezaei*, for their contribution to the improvement of the developed software and critical discussions.
- We acknowledge the CNN software developed by *Xikai Tang* and *Johan Nuyts* for liver segmentation. His software generated the automatic liver segmentations in **chapter 4** and **chapter 5**. The assistance of *Jeroen Bertels* and *David Robben* (Medical Image Computing-ESAT/PSI- KU Leuven, Leuven, Belgium) in implementing CNN in liver segmentation is much appreciated.
- We would like to thank the radiology team (University Hospitals Leuven); *Walter Coudyzer* engaged in manual VOI segmentation in **chapter 3**, *Geert Maleux* provided feedback throughout the study design and research process and co-authored different papers. We wish to thank *Vincent Vandecaveye* and *Frederik De Keyzer* for valuable discussions about MR imaging and protocols, and *Stijn De Buck* and *Janne Vignero* for the technical support.
- We would also like to acknowledge the Nuclear Medicine department (University Hospitals Leuven), especially *Christelle Terwinghe*, *Wies Deckers*, and *Nathalie Mertens*, for their excellent technical skills and guidance. We wish to thank *Michel Koole* for helpful discussions in **chapter 3** and yttrium-90 phantom study.

Funding

This project was supported by *the Research Foundation- Flanders (FWO, grant G082418N)* and by the *European H2020 MSCA-ITN-2017 project (HYBRID, id 764458)*.

Christophe Deroose is a Senior Clinical Investigator for *the Research Foundation- Flanders (FWO)*

Personal contribution

I state that my personal contributions to this dissertation covered (but were not limited to):

- collecting and interpreting clinical data
- collecting and analyzing experimental data
- performing development and management of dosimetry software for SIRT (*e.g.* liver segmentation using multi-modal region growing, LPT and tumor segmentation, image registration, and dose reporting) and analyzing patient data prospectively and retrospectively, which are presented in several publications (*e.g.* presented in international conferences or published in peer-reviewed journals) and also in clinical routine (*e.g.* pre-treatment activity planning and post-treatment dose evaluation).
- conceiving, planning and carrying out the experiments, analyzing the results, and writing this manuscript in consultation with the supervisors and co-authors.

The author's contributions for each published chapter of this manuscript are listed below.

Chapter 3

All authors contributed to the study design and manuscript editing and reviewing.

- *Johan Nuyts*, *Christophe Deroose*, and *Kristof Baete* were the main investigators of the research and were involved in revising the manuscript critically for important intellectual content.
- ***Esmaeel Jafargholi Rangraz*** and *Johan Nuyts* did the software development.
- ***Esmaeel Jafargholi Rangraz*** was involved in the data collection, image analysis, statistical analysis, and the manuscript drafting.
- *Walter Coudyzer* performed manual liver perfusion territory and liver segmentation.
- *Christophe Deroose* scored the registration results.
- *Kristof Baete* designed the acquisition of [^{99m}Tc]Tc-MAA-SPECT/CT and [^{18}F]FDG-PET/CT scans.
- *Geert Maleux* performed and analyzed the CBCT scans.

Chapter 4

All authors contributed to the study design and manuscript editing and reviewing.

- *Johan Nuyts*, *Christophe Deroose*, and *Kristof Baete* were the principal investigators of the research and have been involved in revising the manuscript critically for important intellectual content.
- ***Esmaeel Jafargholi Rangraz***, *Xikai Tang*, and *Johan Nuyts* did the software development.
- ***Esmaeel Jafargholi Rangraz*** was involved in data collection, image analysis, statistical analysis, and drafting the manuscript.
- *Christophe Deroose* performed manual VOI segmentation and validation.
- *Kristof Baete* designed the acquisition of [^{99m}Tc]Tc-MAA-SPECT/CT, ^{90}Y-PET/CT and [^{18}F]FDG-PET/CT scans.
- *Geert Maleux* performed the angiographical workups and angiographies during SIRT and performed the CBCTs.
- *Jeroen Dekervel*, *Eric Van Cutsem*, and *Chris Verslype* performed the patient selection, presentation at the multidisciplinary tumor board, and patient care during the pre-SIRT procedure and post-SIRT follow-up.
- *Charlotte Van Laeken* contributed in data collection and providing patient characteristics.

7.2 Conflict of interest statement

Christophe Deroose was a member of advisory boards for Novartis Pharma, Terumo, and Ipsen and has been a consultant for Sirtex, Novartis Pharma, and Bayer.

All other authors (including ***Esmaeel Jafargholi Rangraz***) do not have any conflicts of interest to disclose.

None of the funding sources stated above were involved in the study design, patient recruitment, data collection and analysis, or in the results interpretation.

Esmaeel Jafargholi Rangraz

Ph.D. candidate at KU Leuven from 2016 to present

Email: rangraz@icloud.com | Webpage: https://www.linkedin.com/in/rangraz/

Facts & figures

- Motivated multidisciplinary scientist with years of experience in medical physics (dosimetry, advanced image and data analysis) leading to developed software modules successfully implemented in clinical routines (e.g., pre-treatment dose estimation and post-treatment dosimetry for SIRT)
- Analytical problem solver with a solid background in advanced mathematics (bronze medal holder in National Mathematics Olympiad) and years of experience in teaching and writing textbook in this field
- Ability to plan, organize, prioritize, work independently; co-founder and project leader of educational institutes for 8+ years

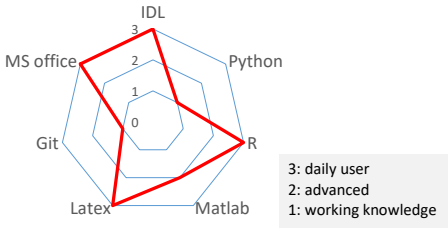

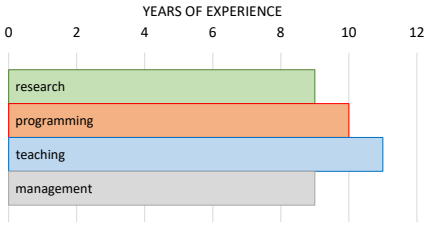

Academic education

Apr. 2014 – present | **predoc** and **Ph.D.** researcher in Nuclear Medicine, KU Leuven, Leuven, Belgium
Project: "Multi modal image analysis for radionuclide therapy (SIRT) dosimetry"

- **Area of research:** Medical imaging (CT, MR, PET, and SPECT), Image processing (image registration and segmentation), dosimetry, medical reporting, data collection, and analysis. *Promotor: Prof. Dr Johan Nuyts.*
- **Programming languages:** IDL (Interactive Data Language), Python, C and R
- Expertise in implementing principles of digital image processing and advanced medical physics using different programming languages to a novel technique for multimodal image analysis for radionuclide therapy (SIRT) dosimetry which is used for 50+ patients for research purposes
- Strategic planner with ability to make complex concepts understandable to the entire treatment team leading to reshaping developed software to be implemented in daily clinical routine; the software is used in the clinics for 20+ patients prospectively

Sep. 2007 – Jul. 2010 | **M.Sc.** in Biomedical Engineering-Biomaterials, Amirkabir University, Tehran, Iran
Project: "Classification of grades of cancer tumors with applications of fractal geometry"

- **Area of research:** Mathematical modelling, image processing, statistical analysis
- **Programming languages:** Matlab and R
- Developing an in-house platform to bring advanced mathematical techniques, e.g., "fractal analysis", into the pathologic evaluation of the breast cancer samples
- Ranked among the top 10% of the participants in the entrance exam

Sep 2003 – Sep. 2007 | **B.Sc.** in Biomedical Engineering-Biomechanics, Amirkabir University, Tehran, Iran
Project: "Study of morphological alterations of stem cells under cyclic loading"

- **Area of research:** Mathematical modelling, image processing, statistical analysis
- **Programming languages:** Matlab and R
- Designing a framework to study the morphological alteration of the stem cells under cyclic loading
- Among the top 0.2% in the entrance exam (around half a millions of participants)

Academic achievements

- Awarded a bronze medal for National Mathematics Olympiad-third round (2012); selected in the second round of Mathematics and Computer Olympiad (2012)
- Several published peer-reviewed papers, and conference talks and posters (available in my LinkedIn)
- Attending numerous training courses and seminars, including two courses on deep learning (see my LinkedIn)

Professional and research experience

2009 – 2011 | Granted project: **research assistant (image processing)**
Project:"Design of software for diagnosis of breast cancer"
Sazmane Gostaresh Sanaye Iran, Tehran, Iran

- **Programming languages:** Matlab, R
- Pragmatic team worker with experience in computer coding and image processing to extend the achievements of my M.Sc. project for two more years as a national granted project

Summer 2006 | Internship: **research assistant (image processing)**
Project:"connector of movement markers, designing of speed and acceleration code"
National Olympic and Paraolympic Academy of Iran, Tehran, Iran

- **Programming languages:** Matlab
- Software engineer who participates in implementing a program used to improve the training of the Karate National Team by analysing joints' movement of the athletes

2003 – 2014 | Co-founder and Head of training division of educational/publication institutes
advanced mathematics (Math Olympiad) tutor in highly ranked high schools
author of educational text books (advanced mathematics) in Persian

- Co-founder and manager of the training division of educational/publication institutes with the goal of "Bringing fresh air into the Iranian high-school system"; publishing 20+ textbooks mostly in the area of advanced mathematics and physics
- Author of 4 books and editor of 2 books
- Creative and enthusiastic tutor with 10+ years experience in teaching advanced mathematics (algebra, algorithm, combinatorics, and geometry) to high-school students; I am proud of my profoundly talented students who achieved national and international Mathematics and Computer Olympiad medals.

Fields of interest

- research and development
- computer vision and image processing
- medical imaging
- mathematical modelling
- medical physics
- machine learning

Technical skills

Programming Languages	IDL, Python, R and MatLab
Image Software	MevisLab, MIM, PACS-viewers, KWS, 3D slicer and ImageJ
Operation Systems	Microsoft Windows, Linux/Unix and Mac OS X
Medical data	DICOM, Nifti, RTstruct
General Software	Microsoft office, LaTeX and Git

Language skills

Language	Farsi/Persian: Mother tongue
	English: Fluent
	Dutch: Intermediate (in progress)

Hobbies and interests

- Big fan of kids, I always volunteer for designing creative games for them.
- An active member in advanced mathematics forums, especially problem-solving sub-forums.
- Super meme lover, I enjoy both scrolling and making internet memes.

Soft skills

I consider myself as an introspective thinker. Years of engaging myself as a tutor and manager sharpen my communication skills and power of motivating others. Like many other Ph.D. students, I am a result-oriented, strategic thinker, and able to work under pressure and tight deadlines.

Selected training courses and seminars

- 2^{st}-SUMM^{90}YT user meeting; **2019, Frankfurt, Germany**
- BTG IO Benelux meeting; **2019, Antwerp, Belgium**
- Simplicit^{90}Y advanced training; **2019, Leuven, Belgium**
- Moving Yttrium-90 therapy to tomorrow, 1^{st}-SUMM^{90}YT user meeting; **2019, Frankfurt, Germany**
- WOG meeting on model selection; **2018, KU Leuven, Belgium**
- MISS2018- medical imaging summer school, Medical imaging meets deep learning; **2018, Favignana, Italy**
- FLAMES @KU Leuven Colloquium, Neural Networks; **2018, KU Leuven, Belgium**
- 30^{th} Annual congress of the European Association of Nuclear Medicine- EANM; **2017, Vienna, Austria**
- Theranostics and molecular radiotherapy (IAEA, BELNUC and Jules Bordet); **2017, Brussels, Belgium**
- TheraSphere, Y-90 Glass Microsphere; **2016, Essen, Geramy**
- Advanced in nuclear therapy; **2016, Utrecht, The Nederlands**
- EFOMP summer school: Radiation dosimetry in radionuclide therapy; **2016, Prague, Czech Rep**
- Holmium, the next generation microspheres for radioembolization; **2016, Utrecht, The Nederlands**
- PET/MR symposium; **2016, Leuven, Belgium**
- Radiation Protection; **2015, KU Leuven , Leuven, Belgium**
- EFOMP summer school: Nuclear medicine and radiopharmaceutical dosimetry; **2015, Prague, Czech Rep**
- 17^{th} Symposium of the Belgian Society of Nuc. Med. (BELNUC); **2015, Maastricht, The Nederlands**

Publications

- **Jafargholi Rangraz E**, Tang X, Van Laeken C, Maleux G, Dekervel J, Van Cutsem E, Verslype E, Baete K, Nuyts J, Deroose CM. *"Quantitative comparison of pre-treatment predictive and post-treatment measured dosimetry for selective internal radiation therapy using cone-beam CT for tumor and liver perfusion territory definition."* EJNMMI research, 10(1), 1-20..
- Tang X, **Jafargholi Rangraz E**, Coudyzer W, Bertels J, Robben D, Schramm G, Deckers W, Maleux G, Baete K, Verslype C, Gooding MJ. *"Whole liver segmentation based on deep learning and manual adjustment for clinical use in SIRT."* European Journal of Nuclear Medicine and Molecular Imaging. 2020 Apr 20:1-1.
- **Jafargholi Rangraz E**, Coudyzer W, Maleux G, Baete K, Deroose CM, Nuyts J. *"Multi-modal image analysis for semi-automatic segmentation of the total liver and liver arterial perfusion territories for radioembolization."* EJNMMI research. 2019 Dec 1;9(1):19.
- Ghazanfari S, Tafazoli SM, Shokrgozar MA, Haghighipour N, Amirizadeh N, **Jafargholi Rangraz E.** *"Analysis of alterations in morphologic characteristics of mesenchymal stem cells by mechanical stimulation during differentiation into smooth muscle cells."* Yakhteh Medical Journal 12.1 (2010): 73-80.

Conference talks and posters

- Tang X, **Jafargholi Rangraz E**, Coudyzer W, Bertels J, Robben D, Schramm G, Deckers W, Deroose CM, Baete K, Gooding MJ, Nuyts J. *"Preliminary Results of Whole Liver Segmentation with Deep Learning for SIRT."* EUROPEAN JOURNAL OF NUCLEAR MEDICINE AND MOLECULAR IMAGING. 2019;46(SUPPL 1):S763.
- **Jafargholi Rangraz E**, Baete K, Koole M, Maleux G, Deroose C, J. Nuyts J. *"Multi-modal image analysis for optimized treatment safety and effectiveness of radioembolization of liver tumors"* Annual congress of the European Association of Nuclear Medicine- EANM'17. Vienna. 21-25 October 2017.
- **Jafargholi Rangraz E**, Baete K, Maleux G, Deroose C, Nuyts J. *"3D and Voxel level dosimetry to determine maximum injected activity in liver radioembolization with 90Y."* In17th national Congress of the Belgian Society of Nuclear Medicine, Date: 2015/05/09-2015/05/10, Location: Maastricht 2015.
- Ghazanfari S, Tafazzoli-Shadpour M, Shokrgozar MA, Amirizadeh N, **Jafargholi Rangraz E.** *"Morphological changes of mesenchymal stem cells by cyclic stretch."* International Conference on BioMedical Engineering and Informatics 2008 (Vol. 1, pp. 743-747). IEEE.